INFRARED THERMOGRAPHY INSPECTION OF FIBER-REINFORCED POLYMER COMPOSITES BONDED TO CONCRETE

By

JEFF ROBERT BROWN

A DISSERTATION PRESENTED TO THE GRADUATE SCHOOL
OF THE UNIVERSITY OF FLORIDA IN PARTIAL FULFILLMENT
OF THE REQUIREMENTS FOR THE DEGREE OF
DOCTOR OF PHILOSOPHY

UNIVERSITY OF FLORIDA

2005

Copyright 2005

by

Jeff Robert Brown

To my wife, Heather,
and daughter, Zoë

ACKNOWLEDGMENTS

This work would not have been possible without the help and contributions of others. First, I would like to thank my committee chair and advisor, Dr. Trey Hamilton, for his guidance and support throughout this effort. It was a truly an honor to work on this project and I will always appreciate the experience. Members of my dissertation advisory committee are also acknowledged for their efforts: Dr. Andrew Boyd (Cochair), Dr. Gary Consolazio, Dr. Ron Cook, and Dr. Elliot Douglas. Additional thanks goes to Dr. Kurt Gurley for his assistance with my research and teaching here at UF.

Chuck Broward provided essential support during the laboratory phase of this study. He has also been a wonderful friend. I can safely say that if it were not for Chuck and his passion for astronomy, I would never have seen the rings of Saturn or the transit of Venus. I would also like to thank Tony Murphy for providing excellent computer support.

My master's thesis advisor, Dr. Sashi Kunnath, was responsible for sparking my interest in research and also been a wonderful influence on my career. I cannot thank him enough for all of his help. Another colleague from UCF, Dr. Mark Williams, was also a major influence and helped to get me established here at the University of Florida.

I would like to thank a number of my friends and colleagues for their help and support. Tony Michael and Markus Kutarba were a tremendous help both in the lab and out in the field. We will always have some amazing stories to tell about two bridges in Jacksonville. Amber Paul assisted in the specimen construction and data collection for

Phase II of this study. This work would never have been completed on-time without her help. Finally, I would like to thank Gustavo Alvarez for his help in the early stages of this project.

My parents have also provided tremendous support over the years, and their contributions are gratefully acknowledged.

I have also been blessed with a family of my own, and none of this would have been possible without the support of my wife, Heather. Our daughter, Zoë, also contributed in more ways than can be mentioned. The only way I would do this again would be if we could do it together.

Finally, this material is based upon work supported under a National Science Foundation Graduate Research Fellowship.

TABLE OF CONTENTS

page

ACKNOWLEDGMENTS iv

LIST OF TABLES ix

LIST OF FIGURES xii

ABSTRACT xix

CHAPTER

1 INTRODUCTION 1

2 FIBER-REINFORCED POLYMER COMPOSITES USED TO STRENGTHEN REINFORCED CONCRETE 9

Constituent Materials 9
Fibers 9
Matrix Materials 11
Construction Methods and Application Procedures for FRP Composites 12
Composites Used in the Aerospace Industry 12
Composites Used to Strengthen RC 13
Locations of Defects in FRP Systems Bonded to Concrete 14
Quality Control Standards 15
Research Significance 17

3 NONDESTRUCTIVE EVALUATION USING INFRARED THERMOGRAPHY 18

Infrared Thermography Fundamentals 18
Detection of EM Radiation with an IR Camera 22
Thermal Imaging System Used in Current Study 24
Infrared Thermography Methods for NDE of Materials 25
Heating Methods 26
Image Acquisition 28
Data Analysis 29
Objectives of Current Research 35

4 PHASE I EXPERIMENTAL WORK AND FIELD STUDY 36

Introduction 36
Full-Scale AASHTO Girders 37
Description of AASHTO Girders and FRP Systems 37
Infrared Inspection Procedures 41
Initial IR Inspections 44
IR Inspections Performed During Load Testing 49
IR Inspections of Known Debonded Areas After Failure 49
Summary of IR Inspection Results for Each FRP System 54
Field Inspection: Chaffee Road 57
Summary of Findings for Phase I 61

5 PHASE II: EXPERIMENTAL SETUP 65

Introduction 65
Specimen Construction 66
FRP Composite Materials 67
Concrete Substrate 68
Surface Preparation 70
Surface Saturation and Tack-Coat 70
Application of FRP Composite to Concrete 73
Construction Details for Each Series 74
Heating Methods and Thermal Imaging 82
Flash Heating 83
Scan Heating 86
Long-Pulse Heating 90
Sinusoidal Heating 93
Comparison of Heating Configurations 94

6 PHASE II: DATA COLLECTION AND ANALYSIS 97

Introduction 97
Pulse Thermography: Series A 98
Specimen Heating and Data Collection 98
Image Preprocessing 99
Defect Analysis 101
Proposed Method for Characterizing Detectability 116
Experimental Results: Flash Heating (Series A) 118
Experimental Results: Scan Heating (Series A) 135
Experimental Results: Long-Pulse Heating (Series A) 143
Comparison of Heating Methods 145
General Detectability 146
Defect Characterization 152
Summary of Pulse Thermography Results 166
Step Thermography Analysis 167
Analysis Procedures 167

Summary of Step Thermography Results: Series A Specimens....188
Frequency Domain Analysis: Series A....190
Sinusoidal Heating (Lock-In IRT)....190
Pulse Phase Thermography....199
Comparison of Heating Methods and Analysis Techniques....207
General Detectability....207
Defect Characterization....210
Series B, C, D, and E Specimens....212
Data Collection....214
Series B....214
Series C....218
Series D....218
Series E....219

7 SUMMARY AND RECOMMENDATIONS FOR FUTURE RESEARCH....221

Summary....221
Phase I....222
Laboratory Study....222
Field Study....223
Phase II....223
Heating Methods....223
Data Analysis Methods....224
FRP System Properties and IRT Results....225
Recommendations for Deployment of IRT....225
Guidelines for Qualitative IRT Inspections....225
Quantitative Analysis....226
Future Research....227

APPENDIX

A TIME DOMAIN RESULTS: SERIES A....229

B SINUSOIDAL HEATING RESULTS: SERIES A....250

C SERIES B, C, D, AND E RESULTS....255

D COMPOSITE PROPERTIES FOR SMALL-SCALE SPECIMENS....265

LIST OF REFERENCES....268

BIOGRAPHICAL SKETCH....271

LIST OF TABLES

Table		page
2-1	Dry carbon-fiber properties used in aerospace industry	10
2-2	Properties of dry fibers for commercially available fiber-reinforced polymer systems used to strengthen reinforced concrete	11
2-3	Properties of epoxies used in commercially available fiber-reinforced polymer systems for strengthening reinforced concrete	12
4-1	Fiber-reinforced polymer system properties for full-scale AASHTO girders	38
4-2	Summary of scanning speed and uniformity of heating	47
5-1	Overview of Specimen Matrix	67
5-2	Material properties for fibers, epoxy, and lamina	68
5-3	Concrete mix proportions used for Series A to E	70
5-4	Series A details	76
5-5	Series B details	79
5-6	Series C details	80
5-7	Series D details	81
5-8	Series E details	82
5-9	Surface temperature increase results for different heating methods	96
6-1	Summary of data collected for pulse analysis study	99
6-2	Parameters computed for defect area at each time step	104
6-3	Parameters extracted from ΔT_{def} vs. time plot for each defect	109
6-4	Detectability classification based on ΔCOV of computed radii	118

6-5 Flash heating results for Specimen A-1 120
6-6 Gradient area method results for Specimen A-1: flash heating 122
6-7 Summary of Results for Specimen A-2: flash heating 126
6-8 Summary of results for Specimen A-3: flash heating 128
6-9 General detectability results for flash heating 131
6-10 Signal to boundary noise ratio (SBR) results for flash heating 132
6-11 Ratio of parameters for air and epoxy-filled defects 135
6-12 General detectability results for scan heating 139
6-13 Signal to boundary noise ratio (SBR) results for scan heating 139
6-14 Ratio of parameters for air and epoxy-filled defects (scan heating) 142
6-15 General detectability results for long-pulse heating 144
6-16 Defect data and predicted depth for defects shown in Figure 6-48 162
6-17 Predicted and actual properties of defects in Figure 6-48 165
6-18 Typical thermal properties for materials of interest 169
6-19 Summary statistics for defect-free areas (Series A) 175
6-20 Parameters of interest for characterizing defects from step thermography data 190
6-21 Frequencies investigated during sinusoidal heating experiments 191
6-22 Recommended pulse durations and detection limits for sinusoidal heating (carbon-FRP systems) 198
6-23 Normalized temperature response @ t = 60 sec for properly saturated specimens 216
A-1 Flash heating results for Series A 233
A-2 Scan heating results for Series A 237
A-3 Long-pulse (30 sec) heating results for Series A 241
A-4 Long-pulse (45 sec) heating results for Series A 245

A-5 Long-pulse (60 sec) heating results for Series A 249

B-1 Sinusoidal heating results: ΔΦ vs. frequency plot parameters 254

C-1 Series B (low saturation) summary statistics for defect-free areas 259

C-2 Series C (surface prep) summary statistics for defect-free areas 261

C-3 Series D (fiber saturation methods) summary statistics for defect-free areas 262

D-1 Series A composite properties 266

D-2 Series B composite properties 266

D-3 Series C composite properties 266

D-4 Series D composite properties 267

D-5 Series E composite properties 267

LIST OF FIGURES

Figure		page
1-1	Strengthening reinforced concrete beams	2
1-2	Prestressed AASHTO girder damaged by over height vehicle	3
1-3	Application of FRP composite to strengthen existing structure	4
1-4	Reinforced concrete column wrapped with FRP	5
1-5	Vehicle impact damage to FRP composites that occurred after installation	5
1-6	Damage to FRP composite due to corrosion of internal reinforcing steel	6
1-7	Surface temperature response due to external radiant heating	7
1-8	Infrared thermography inspection of FRP composite system	8
2-1	Location of potential unbonded, debonded, and delaminated areas in FRP systems	15
3-1	Incident radiation (Φ_i) is reflected, transmitted or absorbed	20
3-2	Electromagnetic emission curves for objects at different temperatures.	21
3-3	Atmospheric emission in the MWIR and LWIR spectral bands	23
3-4	General schematic of a focal plane array (FPA) and associated optics	24
3-5	Application of IR thermography to FRP composite bonded to concrete	25
3-6	Surface heating and defect detection for pulse thermography	31
3-7	Defect detection with lock-in thermography	34
4-1	Full-scale AASHTO type II girder and load test setup	37
4-2	Cross-section views of FRP systems	39
4-3	Data collection for full-scale AASHTO girders	43

4-4 Subsurface defect found on Girder 3 44
4-5 Subsurface defects found on Girder 3....45
4-6 Non-uniform surface heating of Girder 4 46
4-7 Thermal images collected for full-scale AASHTO girders 47
4-8 Background temperature increase vs. position along length of girder....48
4-9 Failure modes for full-scale AASHTO girders....50
4-10 Defect signal strength (ΔT_{defect}) vs. time for known debonded area....51
4-11 Debonded area after failure for Girder 6....53
4-12 Series of thermal images for air and epoxy filled defects....54
4-13 Polyurethane matrix shown after debonding from concrete (Girder 4)....56
4-14 Vehicle impact damage sustained after FRP strengthening....58
4-15 Visual and thermal images of vehicle impact damage....59
4-16 Infrared thermography inspection of undamaged girder 60
4-17 Damaged girder before new FRP system was applied....61
5-1 TYFO SCH-41 carbon-fibers....69
5-2 TYFO SEH-51 glass-fibers....69
5-3 Surface preparation before FRP placement 70
5-4 Application of epoxy saturant and tack-coat 71
5-5 Fiber saturation 73
5-6 Completed specimen....74
5-7 Defect configuration for Series A specimens 76
5-8 Defect configuration for Series B specimens....80
5-9 Lap-splice configuration for Series E 82
5-10 Heat source and camera configuration for pulse heating experiments 84
5-11 Typical thermal image collected during pulse heating experiment 84

5-12 Surface temperature profile due to pulse heating 87
5-13 Heat source used in scan heating experiments....88
5-14 Thermal images collected during scan heating experiment....88
5-15 Thermal image collected during scan heating experiment 89
5-16 Surface temperature profile for scan heating....89
5-17 Heat source and camera configuration for long-pulse heating 91
5-18 Thermal image collected at t = 1 sec during long-pulse heating 91
5-19 Laboratory setup for long-pulse heating experiments 92
5-20 Surface temperature profile for long-pulse heating (30 sec pulse)....92
5-21 Surface temperature profile for long-pulse heating (60 sec pulse)....93
5-22 Diagram for sinusoidal heating control and data acquisition....96
6-1 Application of 3x3 averaging filter applied to each pixel in thermal image....102
6-2 Area identification for defect analysis 104
6-3 Constructing ΔT_{def} vs. time plots from area parameters 105
6-4 Thermal images and ΔT_{def} vs. time plot for Defect IB 106
6-5 Non-uniform heating and weak signals for defects 107
6-6 Identification of important parameters for weak signals 108
6-7 Signal for undetected defect....109
6-8 Defect area computations using boundary trace method 111
6-9 Surface temperature profile and gradient used to approximate the boundary of detected defects 112
6-10 Reduced accuracy in area computations due to a weak signal 114
6-11 Coefficient of variation for ellipse radii (computed with NP = 250)....115
6-12 Reduced accuracy in area computations due to non-uniform heating 115
6-13 Reduced accuracy in area computations due to low image resolution 116

6-14 Detectability classification based on ΔT_{def} vs. time plot 118
6-15 Flash heating results for Specimen A-1 120
6-16 Gradient images for defects. 122
6-17 Specimen A-1: Important parameters for defects 123
6-18 Thermal images for Specimen A-2: flash heating 124
6-19 Flash heating results for Specimen A-2 : temperature vs. time data 126
6-20 Unintentional defects between layers in Specimen A-2 126
6-21 Specimen A-2: important parameters for defects 127
6-22 Thermal images and ΔT_{def} vs. time plots for Specimen A-3 128
6-23 Specimen A-3: important parameters for defects 129
6-24 Thermal images and ΔT_{def} vs. time plots for Specimen A-4 130
6-25 Normalized ΔT_{max} for flash heating 133
6-26 Time to maximum signal for flash heating 134
6-27 Signal half-life for flash heating 134
6-28 Standard deviation of Defect IB perimeter 136
6-29 Data for Defects A25 and E25 (6.4 mm diameter) 137
6-30 Thermal images for Defect IB (Specimen A-2) 138
6-31 Normalized ΔT_{max} for scan heating 140
6-32 Time to maximum signal for scan heating 141
6-33 Signal half-life for scan heating 142
6-34 Normalized ΔTmax for long-pulse heating 144
6-35 Time to maximum signal for long-pulse heating 145
6-36 Signal half-life for long-pulse heating 145
6-37 Legend for Figure 6-38 146
6-38 Summary of general detectability for flash, scan, and long-pulse heating 147

6-39 Comparison of ΔT_{max} for different heating methods. 149

6-40 Comparison of normalized ΔT_{max} for different heating methods. 151

6-41 Coefficient of variation (COV) of computed radii for different heating methods. 153

6-42 Maximum signal vs. radii COV for all detected defects in Series A 154

6-43 Time to maximum signal for different pulse durations 155

6-44 Defect circumference (C) x depth (d) vs. t_{max} for flash experiments 156

6-45 Signal half-life for different pulse durations 158

6-46 Plot of defect circumference C x depth D vs. $t_{1/2}$ for all heating methods 159

6-47 Plot of defect circumference C x depth D vs. $t_{1/2}$ for all heating methods 160

6-48 Thermal image from long-pulse experiment (Series B and C specimens) 161

6-49 Defect signal vs. time plot for defects shown in Figure 6-48 161

6-50 Characterization of Defect A3 163

6-51 Characterization of Defect A4 164

6-52 Temperature increase for select areas 166

6-53 Surface temperature increase due to uniform heat flux 170

6-54 Normalizing ΔT for two points on Specimen A-1 173

6-55 ΔT image for Series A specimens 173

6-56 Normalized ΔT image for Series A specimens 174

6-57 Defect-free areas for Series A specimens 176

6-58 Mean value of ΔT_{norm} for defect-free areas on Series A 176

6-59 One-dimensional model of FRP systems 177

6-60 Computation of ΔT_{def} from normalized temperature data 179

6-61 Determining point at which defect is detected in ΔT_{def} plots 180

6-62 Surface plots of Defect A50 (Specimen A-2) 181

6-63 Two-dimensional correlation coefficient, R, for Defect A50 182

6-64 Defect signal vs. $t^{1/2}$ for Specimen A-1 183

6-65 Two-dimensional correlation coefficient vs. $t^{1/2}$ for Specimen A-1 184

6-66 Defect signal vs. $t^{1/2}$ for Specimen A-2 185

6-67 Two-dimensional correlation coefficient vs. $t^{1/2}$ for Specimen A-2 186

6-68 Normalized ΔT images for Defect IB (Specimen A-2) 186

6-69 Defect signal vs. $t^{1/2}$ for Specimen A-3 187

6-70 Two-dimensional correlation coefficient vs. $t^{1/2}$ for Specimen A-3 188

6-71 Normalized temperature image for Specimen A-4 (t = 60 sec) 188

6-72 Data analysis for sinusoidal heating (pulse duration = 500 sec) 193

6-73 Sinusoidal heating results for Series A specimens (Pulse Duration = 8.33 sec) 194

6-74 Sinusoidal heating results for Series A specimens (Pulse Duration = 25 sec) 195

6-75 Sinusoidal heating results for Series A specimens (Pulse Duration = 125 sec) 196

6-76 Sinusoidal heating results for Series A specimens (Pulse Duration = 500 sec) 197

6-77 Application of PPT method to Specimen A-3 204

6-78 Comparison of time domain and frequency domain (PPT) results for Specimen A-3 205

6-79 Comparison of time domain and frequency domain (PPT) results for Specimen A-4 205

6-80 Defect signal (phase) vs. frequency plots for air-filled defects 206

6-81 Frequency domain results for Specimen A-3 207

6-82 Comparison of heating methods for Specimen A-4 209

6-83 Comparison of data analysis techniques for Specimen A-3 212

7-1 Field inspection (scan heating method) of FRP system 226

A-1 Flash heating results: Thermal images for Series A. 230

A-2 Flash heating results: ΔT_{def} vs. time plots for Series A. 231
A-3 Scan heating results: Thermal images for Series A. 234
A-4 Scan heating results: ΔT_{def} vs. time plots for Series A. 235
A-5 Long-pulse (30 sec) heating results: Thermal images for Series A. 238
A-6 Long-pulse (30 sec) heating results: ΔT_{def} vs. time plots for Series A. 239
A-7 Long-pulse (45 sec) heating results: Thermal images for Series A. 242
A-8 Long-pulse (45 sec) heating results: ΔT_{def} vs. time plots for Series A. 243
A-9 Long-pulse (60 sec) heating results: Thermal images for Series A. 246
A-10 Long-pulse (60 sec) heating results: ΔT_{def} vs. time plots for Series A. 247
B-1 Sinusoidal heating results: Phase images for Series A. 251
B-2 Sinusoidal heating results: $\Delta\Phi$ vs. frequency plots for Series A. 252
C-1 Low matrix saturation (Series B carbon-fibers)....256
C-2 Medium matrix saturation (Series B carbon-fibers) 256
C-3 High matrix saturation (Series B carbon-fibers)....257
C-4 Low matrix saturation (Series B glass-fibers) 257
C-5 Medium matrix saturation (Series B glass-fibers) 258
C-6 High matrix saturation (Series B glass-fibers)....258
C-7 No surface preparation (Series C carbon-fibers) 260
C-8 Light blast surface preparation (Series C carbon-fibers) 260
C-9 Heavy blast surface preparation (Series C carbon-fibers) 261
C-10 Different fiber saturation methods (Series D carbon-fibers) 262
C-11 Specimen E-1 (1-layer/3-layer/2-layer) 263
C-12 Specimen E-2 (2-layer/3-layer/2-layer) 263
C-13 Specimen E-3 (3-layer/4-layer/2-layer) 264

Abstract of Dissertation Presented to the Graduate School
of the University of Florida in Partial Fulfillment of the
Requirements for the Degree of Doctor of Philosophy

INFRARED THERMOGRAPHY INSPECTION OF
FIBER-REINFORCED POLYMER COMPOSITES
BONDED TO CONCRETE

By

Jeff Robert Brown

August 2005

Chair: H.R. Hamilton III
Cochair: Andrew J. Boyd
Major Department: Civil and Coastal Engineering

The use of fiber-reinforced polymer (FRP) composites to strengthen existing civil infrastructure is expanding rapidly. Many FRP systems used to strengthen reinforced concrete are applied using a "wet layup" method in which dry fibers are saturated on-site and then applied to the surface. Air voids entrapped between the FRP system and concrete as a result of improper installation reduce the integrity of the repair.

The objective of this study was to investigate the use of infrared thermography (IRT) for evaluating bond in FRP composites applied to reinforced concrete. Phase I of this study examined FRP strengthening systems that were applied to full-scale bridge girders. IRT inspections were performed on four AASHTO type II girders with simulated impact damage that were loaded to failure. Phase I also contained a field inspection of an in-service bridge that was strengthened with FRP composites. The results of the field studies indicated that as the overall thickness of the FRP system

increased the detectability of defects was diminished. In addition the installation procedures influenced IRT results. The use of excessive epoxy tack-coat was shown to reduce detectability and increase the required observation time.

A second experimental study (Phase II) was conducted in which 34 small-scale specimens (15 cm x 30 cm) containing fabricated defects were inspected in a laboratory environment. These specimens were constructed using different FRP composite thicknesses (1mm to 4 mm) and matrix saturation levels. Four heating methods were investigated (flash, scan, long-pulse, and sinusoidal), and quantitative analyses were performed on the thermal data using currently available techniques.

Data were used to establish detection limits for air and epoxy-filled voids in carbon FRP composites. It was shown that IRT is capable of detecting 19 mm diameter and larger defects in carbon FRP composites up to 4 mm thick. Quantitative data analysis techniques were also used to estimate the depth and material composition of defects up to 2 mm below the surface. These data analysis techniques were also effective for enhancing detection of defects up to 4 mm below the surface.

CHAPTER 1
INTRODUCTION

Fiber reinforced polymer (FRP) composites are currently used to repair and strengthen existing reinforced concrete structures. Several types of FRP repair systems are commonly encountered: surface bonded, near surface mounted (NSM), and FRP bars. Surface mounted systems consist of dry fibers that are saturated on-site with a matrix material and applied directly to the surface before the composite cures. NSM systems involve pre-cured FRP laminates that are bonded to the structure using an intermediate bonding agent. One advantage of pre-cured laminates is that they are manufactured in a factory setting. The resulting laminates are typically of high quality and possess uniform material properties. FRP bars are also pre-cured composites that are intended to serve as additional reinforcement in reinforced concrete (RC) structures. These systems are installed by cutting a groove in the surface of the concrete just large enough to accommodate the FRP bar. An intermediate bonding agent, typically a thickened epoxy, is then used to grout the bar in place.

The advantages of using FRP composites for strengthening and repair include the high strength to weight ratio of FRP materials, ease of installation, and resistance to corrosion. Prior to the availability of composite materials, traditional repair and retrofit techniques involved attaching steel plates to members or outright replacement. This type of repair is often difficult to implement and requires the mobilization of heavy equipment simply to handle the repair materials.

The American Concrete Institute (ACI) committee 440 has produced a document that engineers can use to specify FRP system requirements based on design objectives (ACI 440-R02 2002).

FRP composites are used primarily to:

- Increase flexural capacity of a member
- Increase shear capacity
- Provide additional confinement to increase concrete ductility

For flexural strengthening, the fibers are oriented along the length of the beam axis to serve as added tensile reinforcement (Figure 1-1A). The FRP composite is typically applied to the tension face. To increase the shear capacity of a member, unidirectional FRP composite is applied to the web with the fibers oriented transverse to the beam axis (Figure 1-1B). Bi-directional FRP composites are also used with the goal of providing additional reinforcement in areas of high diagonal tension.

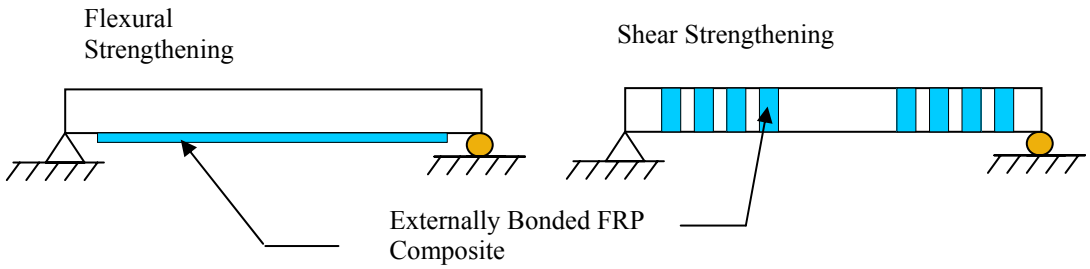

Figure 1-1. Strengthening reinforced concrete beams. A) For flexure. B) For shear.

A common thread with these two approaches is that they rely entirely on bond to transfer stresses between the concrete beam and fibers. These applications are considered "bond-critical". The adhesive and concrete substrate must be sound and of sufficient strength to transfer stress to the fibers. The bond is critical because there are no redundant load paths for stress to follow should the bond fail.

A practical example of these types of repairs is shown in Figure 1-2. In this case, an AASHTO girder was hit by an over height vehicle and was subsequently repaired with FRP composites. In addition to the heavy concrete spalling, a number of the girder's prestressing strands were cut. The FRP composite was applied to restore both flexural and shear capacity. Figure 1-3(a) demonstrates the relative ease with which FRP composites can be applied to existing structures. FRP composites are easily conformed to the member and the orientation of fibers can be adjusted depending on the particular strengthening application.

Figure 1-2. Prestressed AASHTO girder damaged by over height vehicle. Girder was repaired with FRP composites.

The third approach, improving concrete confinement, is popular in seismically active regions and is generally referred to as "column-wrapping". Figure 1-4 shows the use of column-wrapping at the base of a column or pier where a plastic hinge is expected to form during extreme ground shaking. The FRP composite wrap confines the concrete, which improves the ductility and apparent strength as well as improving lap splice performance. Bond is not considered critical in this application since the fibers are continuously wound around the member. Column wrapping is commonly referred to as "contact-critical".

A B

Figure 1-3. Application of FRP composite to strengthen existing structure. A) Workers applying carbon-fiber composite. B) completed project.

If the composite is not installed properly and air-bubbles are present at the FRP/concrete interface, the system may not perform as desired. Figure 1-4 shows the severity of installation defects that can occur in FRP composite systems. Another issue that can affect the overall performance of an FRP system is durability. Numerous researchers have cited durability of FRP composite systems as a major challenge confronting the industry (CERF 2001, Kharbari et al 2003, Nanni 2003). A number of factors can contribute to the degradation of an FRP composite system during its service life:

- Environmental exposure (moisture, temperature cycles)
- Overloading resulting in partial debonding
- Vehicle impact
- Corrosion of internal reinforcing steel

A number of the FRP repairs initiated by the Florida Department of Transportation (FDOT) to mitigate vehicle impact damage have also been struck and damaged by over height vehicles (Lammert 2003). Figure 1-5 provides two examples of damage to FRP systems resulting from vehicle impact.

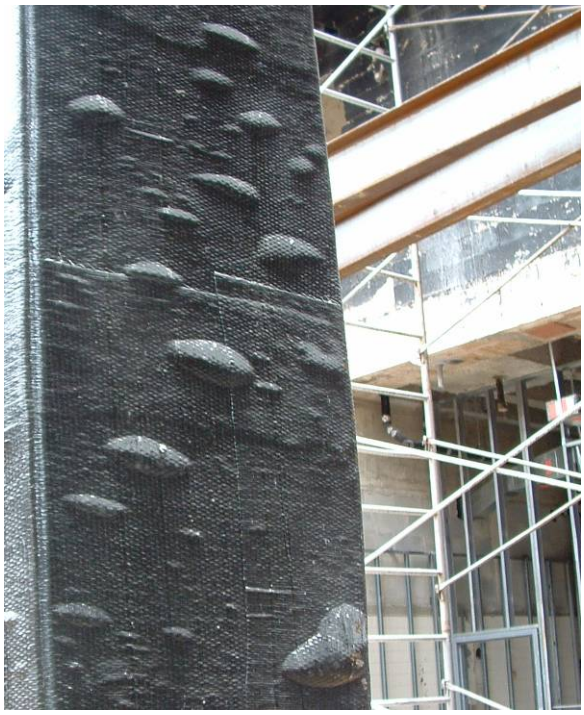

Figure 1-4. Reinforced concrete column wrapped with FRP. The large air bubbles are a result of installation defects.

A B

Figure 1-5. Vehicle impact damage to FRP composites that occurred after installation. A) Chaffee Rd./I-10 overpass near Jacksonville, Florida. B) 45th St./Florida Turnpike overpass in West Palm Beach, Florida.

The expansive nature of corrosion byproducts result in cracking of the concrete substrate. If an FRP system is applied to a member experiencing active corrosion, subsequent cracking of the concrete substrate can lead to debonding or rupture of the FRP composite. This scenario was observed on an FRP repair that was applied to a US

Highway 100 bridge spanning the intracoastal waterway in Melbourne, Florida (Figure 1-6). This damage led to the removal and replacement of the entire FRP system

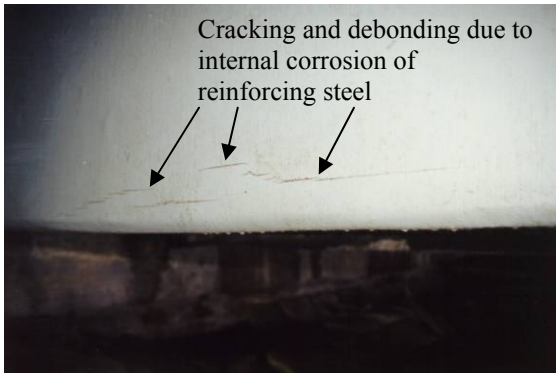

Figure 1-6. Damage to FRP composite due to corrosion of internal reinforcing steel

After an extensive survey on defects in FRP composites, Kaiser and Kharbari (2001a) concluded that the performance and expected lifetime of FRP repairs are largely dependent on the quality of installation and the presence of defects. This work also highlights a need for long-term monitoring of performance and durability. Kaiser and Kharbari (2001b) also provide a description of NDE techniques that can be used to evaluate FRP composites.

It is apparent that FRP composites are increasingly used to repair and strengthen reinforced concrete structures. Because this is a relatively new construction technique, methods of evaluating the installation quality and long-term efficacy are needed. ACI 440 cites acoustic sounding, ultrasonics, laser shearography, and infrared thermography (IRT) as methods that can be used to evaluate these critical aspects of FRP composites.

The objective of this research is to develop IRT techniques to evaluate bond quality in FRP composites applied to concrete. IRT is a non-contact remote sensing technique that can be used to measure the surface temperature of an object. The fundamental approach is shown in Figure 1-7. If the surface of a homogeneous material is heated

using an external heat source, the increase in temperature on the surface will be uniform. If, however, the thermal front traveling from the surface into the material encounters an air-void or other discontinuity (defect), the relative rate of surface temperature increase above the defect will change. Depending on the size and material characteristics of the subsurface defect, it may be possible to detect this change in temperature using an infrared camera. A sample application of IRT is shown in Figure 1-8. In this example, the surface of a carbon-fiber/epoxy FRP system was heated using a 500 W halogen lamp. The thermal image provided in Figure 1-8(a) indicates that a portion of the FRP is not bonded to the concrete substrate. The light colors in the thermal image indicate higher temperatures. Portions of the FRP composite that are well bonded to the concrete substrate appear darker in the thermal image.

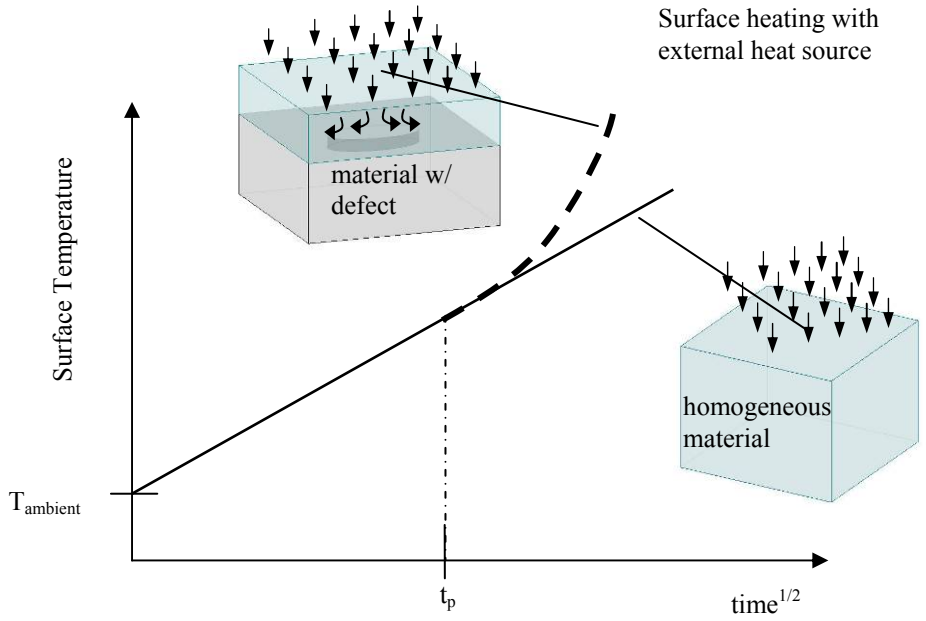

Figure 1-7. Surface temperature response due to external radiant heating for homogeneous materials and materials with subsurface imperfections.

This research investigated the use of IRT for detecting defects in FRP systems bonded to concrete. Specifically, a major goal was to use IRT data to provide the following information about detected defects:

- Size
- Depth below the surface
- Material composition

Other items that are addressed include:

- Detection limits
- Heating methods
- Data analysis procedures

Previous research in this field has focused on the inspection of FRP composites that are commonly used in the aerospace industry. A number of data analysis techniques have been developed that can assist in using IRT results to characterize defects. None of these methods have been calibrated for use on FRP systems bonded to concrete.

A B

Figure 1-8. Infrared thermography inspection of FRP composite system. A) Thermal image. B) Visual image.

CHAPTER 2
FIBER-REINFORCED POLYMER COMPOSITES USED TO STRENGTHEN REINFORCED CONCRETE

Constituent Materials

The term composite is used to describe any material that is created by combining two or more materials on a macroscopic level. In the current study, the term composite will refer to a combination of a polymer matrix and fibers. The primary function of the fiber material is to carry load. The matrix serves as a binder that holds the composite together and transfers stress between fibers.

Fibers

The following fiber materials are commonly used in FRP composites (Gibson 1994):

- Glass
- Carbon
- Aramid
- Boron

The type of fiber chosen for a specific application depends on the specific requirements for strength, toughness, stiffness, and service temperature. Glass (E-glass) and carbon-fibers are widely used for strengthening reinforced concrete.

It is interesting to note the wide array of material properties that are found amongst different types of carbon-fibers. The strength, stiffness and thermal conductivity of carbon-fiber materials are highly dependent on the manufacturing process and on the base material from which the fibers are extruded. Carbon-fibers can be divided into two general categories: PAN based fibers, which are extruded from a polyacrlyonitrile

precursor, and pitch based fibers, which are extruded from a petroleum based pitch precursor. PAN based fibers tend to have a lower modulus of elasticity (207 to 310 GPa) and a higher ultimate tensile strength (3.8 to 5.2 GPa) than pitch based fibers (Table 2-1). Pitch based fibers are noted for their relatively high stiffness and can have a modulus of elasticity of ranging 379 to 965 GPa.

A wide range of thermal conductivity values is associated with different carbon-fiber types. Callister (1997) provides a thermal conductivity for low modulus PAN based fibers of 8.5 W/m-k. The ASM Materials Handbook (Vol. 21, 2005) provides a thermal conductivity of 20 W/m-K for standard modulus PAN based carbon-fibers and values as high as 1100 W/m-K for ultra-high modulus pitch based carbon-fibers. All quantities cited for thermal conductivity represent values in the longitudinal direction of the fibers.

The glass-fibers used in structural engineering applications are typically E-glass, with a thermal conductivity of 1.3 W/m-K which is lower than all forms of carbon-fibers.

Table 2-1. Dry carbon-fiber properties used in aerospace industry

Manufacturer	Designation	Organic precursor	Tensile strength (GPa)	Modulus of elasticity (GPa)
Hexcel[a]	AS4	PAN	4.27	228
Hexcel	IM7	PAN	5.17	276
Cytec[b]	Thornel-P55s	Pitch	1.90	379
Cytec	Thornel-P120s	Pitch	2.41	827
Cytec	K-1100	Pitch	3.10	965

[a] Hexcel (2005). http://www.hexcel.com/Products. 6400 West 5400 South, Salt Lake City, UT
[b] Cytec Industries (2005) http://www.cytec.com/business/EngineeredMaterials/CFInternet/cfthornelpitch.shtm. Cytec Industries Inc., 5 Garret Mountain Plaza, West Paterson, NJ

Mechanical properties of dry carbon and glass-fibers commonly used in structural engineering applications are provided in Table 2-2. Only one of the FRP system manufacturers listed in the table (VSL) explicitly identifies their carbon-fibers as PAN based. The modulus of elasticity of all carbon-fibers provided in Table 2-2 is relatively

consistent between the different FRP system manufacturers. These modulus values suggest that a PAN precursor is common amongst the different carbon-fiber systems.

Table 2-2. Properties of dry fibers for commercially available fiber-reinforced polymer systems used to strengthen reinforced concrete

Manufacturer	Designation	Fiber type	Tensile strength (GPa)	Modulus of elasticity (GPa)	Area density (g/m^2)	Percent elongation @break
Fyfe Co.[a]	SCH-41	Carbon	3.79	230	644	1.7
Fyfe Co.	SCH-41S	Carbon	3.79	230	644	1.7
Edge Composites[b]	VelaCarb 335	Carbon	4.48	234	335	1.9
Edge Composites	VelaCarb 600	Carbon	4.48	234	600	1.9
VSL[c]	V-Wrap C100	Carbon	3.79	228	300	1.5
VSL	V-Wrap C150	Carbon	3.79	228	440	1.0
VSL	V-Wrap C200	Carbon	3.79	228	600	1.5
Fyfe Co.	SEH-51A	E-Glass	3.24	72	915	4.5
Edge Composites	Vela-Glass	E-Glass	2.28	72	875	4.0
VSL	V-Wrap EG-50	E-Glass	2.28	72	900	4.0

[a] Fyfe Co. LLC (2005). http://www.fyfeco.com/products/compositesystems.html. Nancy Ridge Technology Center, 6310 Nancy Ridge Drive, Suite 103,San Diego, CA

[b] Edge Structural Composites (2005). http://www.edgest.com/edgedataintro.html. 145 Park Place Point, Richmond, CA

[c] VSL (2005). http://www.vsl.net/strengthening_products/vsl_frp_composites.html. 7455 New Ridge Road, Suite T, Hanover, MD.

Matrix Materials

A variety of matrix materials (resins) are commonly used in structural engineering applications: epoxy, polyester, vinylester, and polyurethane. Epoxies are commonly used in wet layup systems due to the relatively long pot-life (usually on the order of several hours depending on the temperature). Typical mechanical properties of epoxies commonly used in structural engineering applications are provided in Table 2-3. Polyester resins and vinylester resins are used in spray-up applications where chopped glass-fibers and matrix material are sprayed onto the surface. These materials tend to

cure more rapidly than epoxies. Polyurethane resin can be found in certain pre-impregnated (prepreg) systems. An interesting feature of this matrix material is that water can be used to activate the curing process.

Table 2-3. Properties of epoxies used in commercially available fiber-reinforced polymer systems for strengthening reinforced concrete

Manufacturer	Designation	Tensile strength (MPa)	Modulus of elasticity (GPa)	Density (g/cm^3)	Glass transition temperature (°C)
Fyfe Co.[a]	Tyfo S	72.4	3.2	1.1	82
Edge Composites[b]	Veloxx LR	44.8	2.1	NA	63
VSL[c]	V-Wrap C100	55.2	3.4	NA	NA

[a] Fyfe Co. LLC (2005)
[b] Edge Structural Composites (2005)
[c] VSL (2005)

The thermal conductivity associated with the different matrix materials ranges from 0.15 W/m-K to 0.2 W/m-K (Callister 1994).

Construction Methods and Application Procedures for FRP Composites

Composites Used in the Aerospace Industry

Major developments in the field of FRP composites occurred in the 1960s around the growth of the aerospace industry (Gibson 1994). A wide variety of fiber and matrix materials were developed along with a number of advanced manufacturing procedures. Today, most composites used in the aerospace industry consist of carbon-fibers and an epoxy matrix. Composite parts are typically constructed by placing layers of carbon-fibers that have been pre-impregnated with the matrix material onto a mold with the desired fiber orientation. Parts are then placed in a vacuum bag and cured in an autoclave under high pressures at an elevated temperature. The resulting parts have a high fiber volume fraction (typically from 0.5 to 0.8) and a low void content (0.001 to 0.01 by volume).

Composites Used to Strengthen RC

FRP composites applied to RC are typically installed using a wet layup method. This procedure involves saturating dry fibers on-site and then applying the wet composite directly to the surface being strengthened. The composite is then allowed to cure in-situ. The resulting composites typically have low fiber volume fractions (high matrix content) and a higher percentage of air voids than aerospace composites.

The concrete substrate must be properly cleaned and contain no sharp protrusions before the saturated composite is applied to the surface. The level of surface preparation that is performed can vary significantly between different applications. In some cases the surface will be sandblasted while in other cases the surface might be ground smooth with a grinding wheel.

Large imperfections in the concrete substrate must be repaired by backfilling the damaged area with a cementitious material. Smaller imperfections, such as “bug holes” and formwork joints, can be repaired by filling the void with putty or thickened epoxy. It is important that any remaining sharp edges are removed before the FRP composite is applied.

The next step in surface preparation involves saturating the surface with matrix material (epoxy). Concrete is a naturally porous material that can absorb epoxy. If the saturated fabric was applied directly to dry concrete, there would be a tendency for the concrete to pull matrix out of the fibers. This can result in air voids at the FRP/concrete interface. If the composite is being applied to an overhead surface, an additional layer of thickened epoxy tack-coat can be used to ensure that the saturated fabric does not fall down before the matrix material cures.

After the saturated fibers have been applied to the surface, a squeegee or roller is used to remove air bubbles and any excess matrix material from the FRP composite. If the specific application calls for more than one layer of composite, the layers are applied one at a time. Once the composite has cured, a final top-coat of epoxy is applied to provide an additional layer of protection for the composite.

Another common application involves bonding precured FRP laminates to the structure. The FRP laminates are manufactured in a controlled environment using similar procedures to those described for the aerospace composites. These precured laminates are then bonded to the structure using a thickened epoxy paste. Even though the composite material is not likely to contain defects such as air voids, there is a possibility that imperfections will exist along the thickened epoxy bond line if the material is not applied properly.

The wet layup method provides the most flexibility for RC strengthening applications. Different thicknesses can be obtained over critical areas and the fiber orientation can be easily adjusted depending on the strengthening requirements. It is also possible to span long distances across beams by splicing shorter pieces together.

Locations of Defects in FRP Systems Bonded to Concrete

Defects in FRP systems can result from improper installation or long-term degradation due to environmental factors. Defects in FRP systems can be classified in three ways: unbonded areas, debonded areas, and delaminated areas (adopted from Levar and Hamilton (2003)). The term “unbonded” refers to areas of the FRP system that were not properly bonded when the system first cured. The most common causes of unbonded areas are improper surface preparation of the concrete and attempting to apply material across sharp angles or re-entrant corners. Debonded areas are locations in which bond

that previously existed between the concrete and FRP has been destroyed. Debonded areas can occur at several locations in the composite/concrete interface region (Figure 2-1) and are usually a result of excessive loading or impact. If the debonded area occurs due to excessive loading, it is common for the failure plane to occur a few millimeters below the adhesive concrete interface. It is also possible for the entire layer of concrete cover to separate from the beam at the level of the reinforcing steel (Sebastian 2001). Delaminations are a lack of bond between different layers in a multi-layer FRP system. Delaminations can be a result of improper installation or excessive loading.

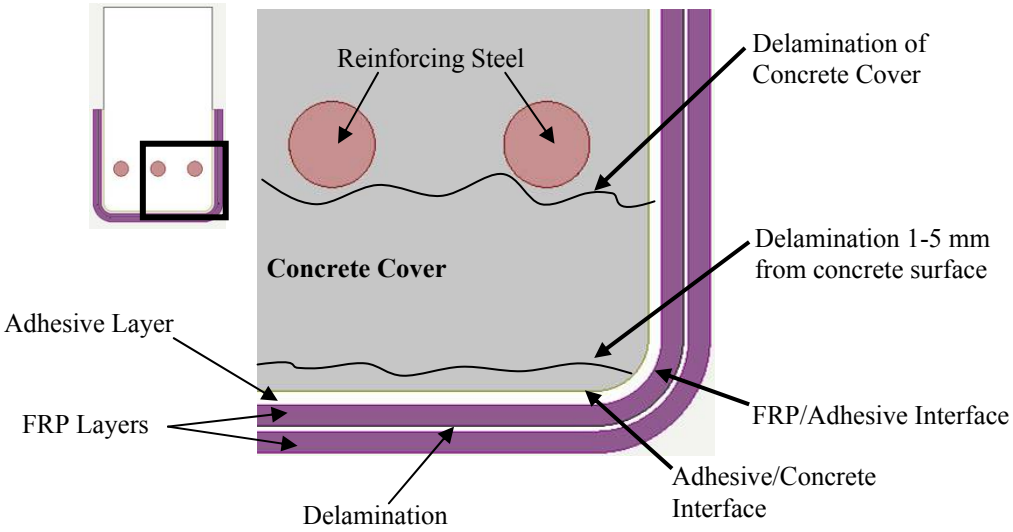

Figure 2-1. Location of potential unbonded, debonded, and delaminated areas in FRP systems

Quality Control Standards

Installation defects are likely to occur in FRP systems bonded to concrete. ACI document 440.2R-02 provides acceptance criteria for the allowable debonded area in wet layup FRP systems. These guidelines are intended to be applied to the installation of new FRP systems and may be summarized as follows:

- Small delaminations less than 12.9 cm^2 each are permissible as long as the delaminated area is less than 5% of the total laminate area and there are no more than 10 such delaminations per 0.93 m^2.
- Large delaminations, greater than 161 cm^2,can affect the performance of the installed FRP and should be repaired by selectively cutting away the affected sheet and applying an overlapping sheet patch of equivalent plies
- Delaminations less than 12.9 cm^2 may be repaired by resin injection or ply replacement, depending on the size and number of delaminations and their locations.

The ACI document also identifies three NDE techniques that can be used to evaluate bond: acoustic sounding (hammer sounding or coin-tap), ultrasonics, and thermography. No additional information is given regarding the deployment of a particular technique or the interpretation of results. In addition, the document does not provide any references or cite specific data to justify these guidelines.

NCHRP Report 514 (Mirmiran et al. 2004) also provides guidelines for the allowable debonded area in wet layup FRP systems. These requirements are more stringent than those prescribed by ACI. According to the NCHRP report, small debonded areas less than 6.4 mm in diameter are acceptable so long as there are less than five such defects in a 0.93 m^2 area. Debonded areas with diameters between 6.4 mm and 32 mm should be repaired by injecting the void with epoxy. Debonded areas with diameters between 32mm and 152 mm should be repaired by cutting out the defective area and replacing the removed material with a new FRP composite patch that extends a distance of one inch beyond the borders of the original defect. Larger defects (greater than 152 mm in diameter) are to be repaired in a similar manner except that the replacement patch should extend a distance of 152 mm beyond the defect area.

The NCHRP report also recommends acoustic sounding as the primary NDE technique. The report states that “if an air-pocket is suspected, an acoustic tap test will be

carried out with a hard object to identify delaminated areas by sound with at least one strike per 929 cm^2." This report also acknowledges infrared thermography, microwave detection, and ultrasonics as additional NDE testing that may be performed.

Guidelines provided by the International Conference of Building Officials (ICBO) in document AC125 (ICC Evaluation Services 2003) are similar to the standards laid out by ACI. This document recognizes that small diameter defects (1.6 to 3.2 mm in diameter) are naturally occurring and do not require any attention. Defects smaller than 12.9 cm^2 are acceptable so long as there are fewer than 10 per 0.93 m^2. Specific requirements for repair procedures are not provided, but the document does describe backfilling with epoxy and replacement of small areas as acceptable. The AC125 document also recommends a visual inspection of the cured FRP system in combination with acoustic sounding using a ball peen hammer to identify debonded areas.

Research Significance

The overall effect that defects have on the short and long-term performance of FRP systems bonded to concrete is not well understood. ACI, NCHRP, and ICBO have all recognized that defects are an important issue that must be addressed. The most common NDE method that is currently used to inspect FRP systems is acoustic sounding (coin tapping). This method is subjective and may not accurately identify or characterize defects. The focus of the current research effort was to develop a NDE technique for evaluating FRP composites bonded to concrete using infrared thermography (IRT). This technique can be used to evaluate bond in FRP systems immediately after installation and throughout the service life of the repair.

CHAPTER 3
NONDESTRUCTIVE EVALUATION USING INFRARED THERMOGRAPHY

This chapter contains background information about infrared thermography (IRT) and a review of previous research. The first section deals with the fundamentals of IRT and describes some of the basic technology used in thermal imaging systems. The following section addresses IRT as a nondestructive evaluation (NDE) technique.

Infrared Thermography Fundamentals

All objects at a temperature greater than 0 K emit electromagnetic (EM) radiation. Furthermore, this radiation is emitted across a range of wavelengths. Max Planck formally quantified the EM emissions of a blackbody (perfect emitter) in 1900 with the following relationship describing intensity of the emitted radiation as a function of wavelength and temperature of the object (Maldague 2001):

$$I(\lambda,T)=\frac{2hc}{\lambda^5\left[\exp(hc/\lambda KT)-1\right]} \qquad (3\text{-}1)$$

I = spectral radiance (W m^2 sr^{-1} μm)
λ = wavelength of emitted radiation (μm)
T = temperature of the object (K)
h = Planck's constant (6.63 x 10^{-34} J s)
K = Boltzmann constant (1.38 x 10^{-23} J/K)
c = speed of light in a vacuum (m/s)

The wavelength at which the peak intensity occurs is given by the Wien displacement law:

$$\lambda_{\max}=\frac{c_3}{T} \qquad (3\text{-}2)$$

λ_{max} = wavelength of peak intensity (μm)
T = Temperature of the object (K)
c_3 = a radiation constant (2898 μm K)

This formula is obtained by taking the derivative of Plank's law (Equation 3-1) with respect to wavelength, λ, and setting the result equal to zero. Another useful formula when considering EM emissions is the Stefan-Boltzmann Law. This law states that the total amount of radiation per unit area, M, emitted by an object can be described by:

$$M = \varepsilon \sigma T^4 \qquad (3\text{-}3)$$

M = total radiant power emitted by object (W/m^2)
ε = emissivity of objects' surface
T = Temperature of the object (K)
σ = Stefan-Boltzmann constant (5.67×10^{-8} $W/m^2\text{-}K^4$)

The Stefan-Boltzmann law is simply the integration of Planck's law over all wavelengths. This relationship also contains a factor to account for the surface characteristic of the object: emissivity. Emissivity can be summarized by the following relationship:

$$\varepsilon(\lambda, T) = \frac{I_o(\lambda, T)}{I_b(\lambda, T)} \qquad (3\text{-}4)$$

ε = emissivity of the objects' surface
I_o = Intensity of the radiation emitted by the surface
I_b = Intensity of radiation emitted by a black body (perfect emitter)

Another useful relationship describes what happens to the total radiation flux incident on an object. The total incident flux is the sum of the reflected, transmitted, and absorbed radiation. The behavior is illustrated in Figure 3-1 and is defined as:

$$\Phi_i = \Phi_r + \Phi_t + \Phi_a \qquad (3\text{-}5)$$

Φ_i = Total incident flux
Φ_r = Total flux reflected by the surface

Φ_t = Total flux transmitted
Φ_a = Total flux absorbed

Equation 3-5 is often expressed as a fraction of the total incident flux and can be re-written as follows:

$$1 = \rho + \tau + \alpha \qquad (3\text{-}6)$$

ρ = % of flux reflected by the surface (reflectivity)
τ = % of total flux transmitted (transmissivity)
α = % of total flux absorbed (absorptivity)

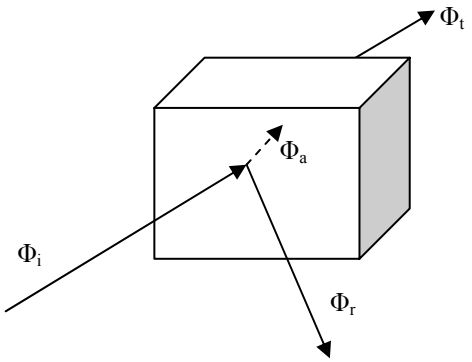

Figure 3-1. Incident radiation (Φ_i) is reflected, transmitted or absorbed (Maldague 2001)

For simplicity, the discussion will now be limited to opaque objects that do not transmit incident radiation. If this is the case, Equation 3-6 can be simplified as:

$$1 = \rho + \alpha \qquad (3\text{-}7)$$

ρ = % of flux reflected by the surface (reflectivity)
α = % of total flux absorbed (absorptivity)

Finally, the relationship between absorptivity and emissivity can be expressed by Kirchoff's law which states that the two quantities are equal.

Figure 3-2 A shows the electromagnetic (EM) radiation emission curves for several common objects at different temperatures. The curves illustrate that the intensity (brightness) of the EM emissions increase with the object's temperature and that the wavelength containing the peak intensity increases as temperature decreases.

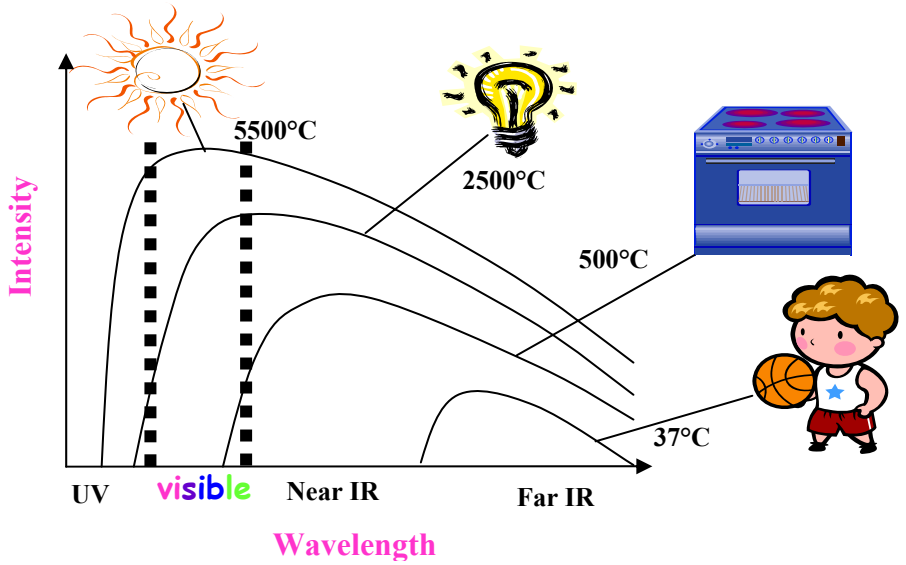

Figure 3-2. Electromagnetic emission curves for objects at different temperatures

Equation 3-1 to Equation 3-6 serve as the foundation for both visible light imaging (photography) and thermal imaging (IR thermography). The importance of these relationships is best demonstrated with several examples. First, consider the largest emitter of EM radiation that humans on earth are likely to experience: the sun. The surface temperature of the sun is approximately 5800 K, which, when substituted into Equation 3-1 results in relatively high intensities across the entire EM spectrum. The wavelength at which the peak intensity occurs, 0.5 μm, can be determined using the Wien Displacement law. This turns out to be very convenient for humans since 0.5 μm (500 nanometers) happens to fall very close to the center of the visible spectrum. When visible light from the sun strikes an object, a portion of that light is absorbed and a portion is reflected (assuming the object is opaque). Visual imaging devices, including the human eye, are designed to capture this *reflected* energy and measure the intensity of the radiation that occurs within the visible spectrum.

Next, consider an object with a temperature of 300 K (27°C or 80°F). The EM radiation emitted by an object at this temperature is limited to longer wavelengths outside

of the visible spectrum. Using the Wien displacement law, the peak intensity is found to occur at 9.7 μm (9700 nanometers). This value falls within the infrared (IR) region of the EM spectrum. Thermal imaging devices are designed to capture and record the radiation *emitted* by an object in the IR region of the EM spectrum. Additional information about thermal imaging systems is provided in the following section.

Detection of EM Radiation with an IR Camera

The IR region is commonly divided into five categories based on wavelength:

- Near IR (NIR) (0.7 – 1.4 μm)
- Short wavelength IR (SWIR) (1.4 – 3 μm)
- Mid wavelength IR (MWIR) (3 – 8 μm)
- Long wavelength IR (LWIR) (8 – 15 μm)
- Far IR (FIR) (15 – 1000 μm)

IR cameras measure surface temperature using EM radiation emitted by an object. The two primary regions of interest of the EM spectrum for IR cameras are referred to as mid-wavelength IR (MWIR) and long-wavelength IR (LWIR). MWIR cameras are sensitive to wavelengths between 3 and 5 μm (this range can vary slightly depending on the particular detector and optics used) while LWIR cameras are primarily sensitive to wavelengths between 8 and 13 μm. Figure 3-3 shows why sensors are banded in this manner. The figure plots the EM emissions of the earth's atmosphere, which shows very high levels between 5 and 8 μm. Based on Kirchoff's law, this translates into very high absorption. IR radiation emitted by the subject is effectively blocked by the atmosphere.

MWIR cameras are typically more sensitive than LWIR cameras. However, both MWIR and LWIR cameras can accurately measure surface temperatures within the range of interest for IR inspections of composites bonded to concrete. A fundamental difference between the two types of cameras is that MWIR detectors often require some

type of cryogenic cooling to avoid signal noise due to the EM emissions from the detector and surrounding electronics. This adds to the overall complexity of the thermal imaging system and requires an additional level of maintenance as compared to uncooled detectors.

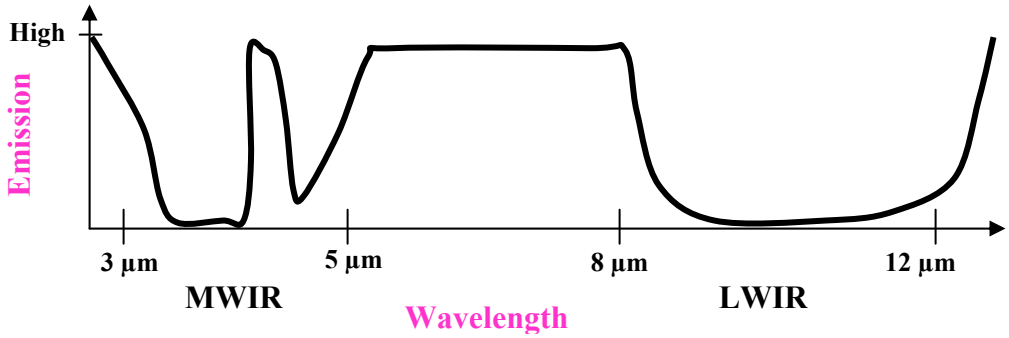

Figure 3-3. Atmospheric emission in the MWIR and LWIR spectral bands

Many IR cameras made today operate in the LWIR region and use microbolometer focal plane array (FPA) technology. A bolometer is a type of thermal detector made of a material whose electrical conductivity varies with temperature change due to incident radiation. A microbolometer FPA is simply an array of extremely small bolometers (50 µm x 50 µm) onto which an image is projected (similar to a CCD digital camera). Typical FPA detectors might include a 320x240 array of microbolometers.

The electrical signal that is developed by each bolometer is converted to a single pixel containing temperature data by applying an appropriate calibration factor. The electrical signal must be corrected to ensure that the temperature determined from the incident EM radiation matches the actual surface temperature of the object. Factors that must be corrected for include:

- Emissivity of the object's surface
- Background temperature of any objects that might reflect off the surface of interest
- Distance to the object
- Atmospheric temperature
- Relative humidity

The optical lenses for LWIR cameras are typically made of germanium because of its high index of refraction (around 4.0) for wavelengths between 2 and 12 µm and its high opacity to wavelengths outside of the 2 to 20 µm band. This allows the lens to serve as a filter for the visible and UV radiation that would otherwise be incident on the detector (resulting in noise). The remaining wavelengths outside of the 8-12 µm band are removed using in-line spectral filters. This is important since EM radiation emissions by the atmosphere in the 5-8 µm band would result in additional background noise. A general schematic of an FPA camera and associated optics is provided in Figure 3-4.

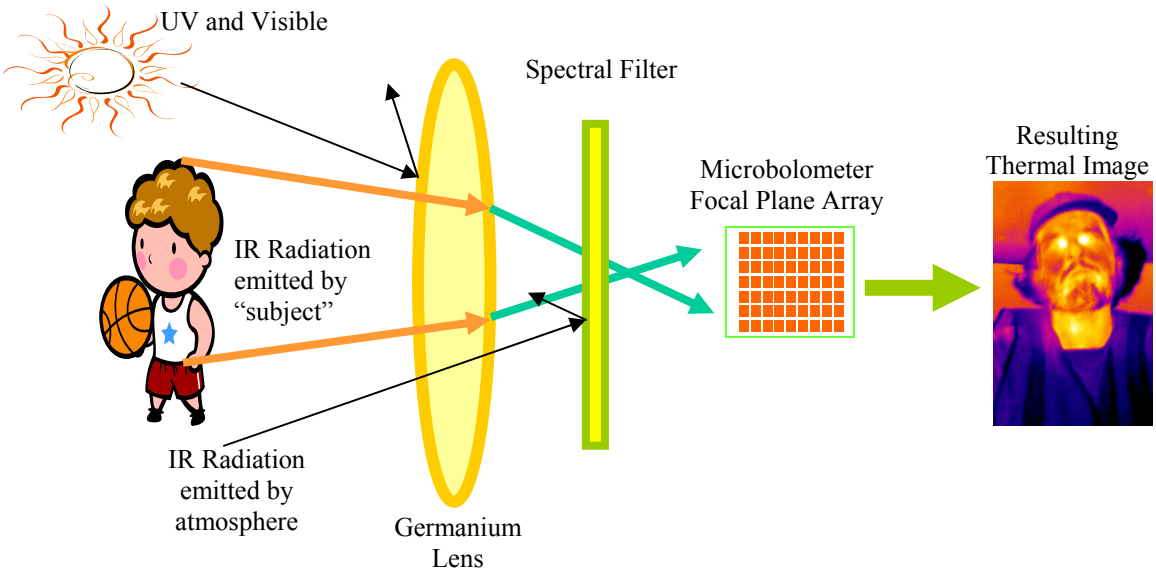

Figure 3-4. General schematic of a focal plane array (FPA) and associated optics

Thermal Imaging System Used in Current Study

A FLIR ThermaCAM PM 695 infrared camera was used in this study. This thermal imaging system operates in the 8 – 12 µm (LWIR) wavelength band of the electromagnetic spectrum. An important feature of this camera is the ability to save thermal images digitally. Each pixel in the thermal image (320x240) is stored as a temperature value. This allows for easy post-processing of collected images using

proprietary software. The maximum image save rate for this thermal imaging system is 5 frames per sec (5 Hz).

Infrared Thermography Methods for NDE of Materials

The fundamental concept behind using IRT as an NDE technique is to apply heat to the surface of an object and generate a thermal front that travels into the material. The increase in surface temperature should be uniform if the material is homogeneous. If the material contains defects below the surface, such as air voids, "hot-spots" will develop since the flow of heat from the surface to the substrate is interrupted. These "hot-spots" can be detected with an IR camera. The thermal image provided in Figure 3-5A demonstrates this concept for an FRP system applied to RC. The "hot-spots" in the image result from very small air voids at the FRP concrete interface. The visual image provided in Figure 3-5B was taken after a saw-cut was made through the composite to examine the cross-section. The thickness of the FRP layer in this system was approximately 1 mm. The sizes of the air voids detected in this FRP system were extremely small (less than 6.4 mm across for the smallest dimension and less than 0.25 mm thick).

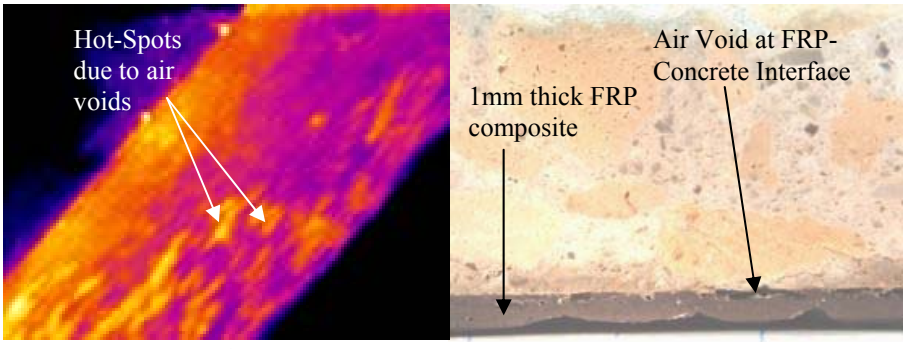

Figure 3-5. Application of IR thermography to FRP composite bonded to concrete A Thermal image of FRP surface showing defects and B cross-section view showing air voids

This technique has been applied by numerous researchers to a wide variety of materials. There are currently ASTM standards available that describe procedures for detecting pavement delaminations in bridge-decks due to corrosion (ASTM 2003) and for identifying wet insulation in roofing systems (ASTM 1997). A recent search of the ASTM standards database indicated that a new document is currently being drafted to address the NDE of polymer matrix composites used in aerospace applications. Work item summary WK8211 cites IRT as an "… emerging NDT [method] that [has] yet to be validated…"

Considerable work does exist in the literature that investigates the use of IRT for identifying subsurface defects in materials. Much of the work on composites has focused on aerospace applications, though several researchers have addressed the issue of FRP composites applied to concrete. This work will be discussed in greater detail in the following sections.

There are three fundamental issues that must be addressed when using IRT as an NDE tool:

- Heating methods
- Image acquisition
- Data analysis

Heating Methods

A wide variety of heating methods can be used when inspecting FRP composites. Short duration heat pulses can be applied using a photography flash. Longer duration heat pulses can be generated with halogen or IR heating lamps. These heat sources transfer energy to the surface being inspected by radiation. The resulting surface

temperature increase is dependent on the intensity of the heat source and the configuration of the heat source with respect to the surface.

Photography flashes offer a great deal of flexibility with regards to controlling the intensity of the heat pulse. Different f-stop settings can be used to regulate the amount of energy released during each flash. A wide variety of models are also available with different maximum output capabilities. Flash systems are typically rated in terms of the amount of energy that can be stored in the system's capacitors. This quantity is measured in Joules or Watt-seconds. Models with relatively low output for IRT applications are typically rated from 500 to 1000 W-s. Models with relatively high output can be rated as high as 6400 W-s. As a general rule, higher intensity will translate into better IRT results since the difference in temperature between defects and defect free regions is proportional to the intensity of the applied heat. The cost of photography flash systems, however, is proportional to their maximum output capabilities. The overall cost of these systems can range from $1000 to $10000 depending on the maximum output and time required to recharge the capacitors after each flash.

Infrared heating lamps and halogen lamps are also efficient means for heating samples during IRT inspections. The output of these lamps is measured in Watts and can range from 250 to 1000 W. A wide variety of lamp configurations are available. Most IR heating lamps are designed to project a narrow beam of energy. Halogen lamps are usually designed to illuminate large areas and tend to disperse the energy over a wider field.

The specific requirements for surface temperature increase depend on the thermal properties of the material under consideration and the depth below the surface that

defects occur. Heating methods that work well for one material may not be appropriate for another. A major focus of the current study is to determine the required heat source intensity and configuration for inspecting FRP composites bonded to concrete.

Image Acquisition

IR cameras capture and record data in two basic formats:

- Intensity images
- Radiometric images

Intensity images provide information about the relative temperature difference between objects or areas within the IR camera's field of view. Before intensity images are collected, the user is required to specify the level and span of temperatures that will be encountered. The total span is typically divided into 255 bins. In a standard grayscale image, the highest temperatures will appear as white and the coolest temperatures will appear as black. Depending on the sophistication of the thermal imaging system, the intensity image may or may not contain a temperature scale in physical units. Another important thing to note about intensity images is that any intensity values that are greater than the specified level and span will be assigned a value of 255, and any values less than the preset level and span will be assigned 0. If the span and level are not set properly, the image may appear underdeveloped (excessively dark) or overdeveloped (washed out).

Radiometric images involve storing a temperature value for each pixel in the thermal image, eliminating any requirements for presetting the span and level. This format facilitates post processing since thermal images can be viewed with any desired grayscale or color scale limits. It is also possible to access a specific temperature value in an image by specifying the coordinates of the point in terms of the row and column

number. If a series of images are saved at a specified time interval, the temperature vs. time history for a single point (or series of points) can be extracted and analyzed.

The image save rate is also a distinguishing feature of thermal imaging systems. The most sophisticated research grade cameras can save thermal images at rates up to 120 frames per second. Specific image save rate requirements depend on the nature of the material being inspected. If the thermal diffusivity of the material is high and defects are located very close to the surface, a higher image save rate is required. Conversely, a lower image save rate is sufficient if the thermal diffusivity is low and defects occur deep beneath the surface.

Data Analysis

There are two primary types of IRT analysis techniques: qualitative and quantitative. Qualitative inspections involve collecting thermal images and searching for any signs of non-uniformity in the resulting images. The thermal image provided in Figure 3-5 represents a qualitative analysis in that the thermal image indicates something of interest is occurring in the composite. Without additional information or an accompanying destructive test to reveal the source of the hot-spots, very little can be said about the true nature of the defects.

Levar and Hamilton (2003) conducted a study involving qualitative IRT inspections of FRP composites bonded to RC. In this study, small-scale RC beams were strengthened in flexure and shear using CFRPs and loaded to failure in laboratory testing. IRT inspections were performed after the FRP systems were installed and areas that appeared unbonded in the thermal images were recorded directly on the specimen. IRT inspections were also performed at various stages of loading and patterns of debonding were monitored. Important observations from these experiments were as follows: the

total debonded area increased as the load was increased up to failure; and certain debonded areas appeared to have different thermal signal strengths.

The objective of quantitative IRT analysis is to use time dependent temperature data to assess defect characteristics. The properties of interest in the current study include:

- Defect size (in physical units)
- Depth of the defect below the surface
- Material composition of the defect

During a quantitative IRT experiment, thermal images are collected at a predetermined interval while the surface of the object is being heated and then while the surface cools. Specific points of interest can then be identified in these images and the temperature variation can be monitored as a function of time. Careful analysis of the results can help to establish where the defect is located in the FRP system.

No standard test methods currently exist for performing quantitative IRT inspections. The following sections will highlight the basic principles behind some of the existing methods. Specific details regarding the implementation of each method for the current study will be presented in a later chapter.

Pulse IRT

Pulse IRT involves the application of a short burst of high intensity heat onto the surface of an object. The most common heat source is a photography flash apparatus. After the heat is applied to the surface, cooling will proceed as shown in Figure 3-6. If the thermal front encounters a defect as it travels into the object, the area above the defect will not cool as quickly. An important parameter to note is the time required for the perturbation to begin (t_p). This value is proportional to the defect depth (z_d). Another

important parameter is the observed thermal contrast (ΔT_{def}). This value is proportional to the size, depth, and thermal properties of the defect.

Pulse IRT is commonly used in the NDE of materials with high thermal conductivities containing defects near the surface. A good example of this application is the NDE of aerospace structures made from FRP composites and/or metals (Kulowitch et al. 1995). The required heating and observation time is short, which results in the ability to inspect large areas very quickly. This, however, requires very high image acquisition rates that can translate into higher equipment costs. Another disadvantage is that the small amount of heat deposited on the surface may not reveal deeper defects.

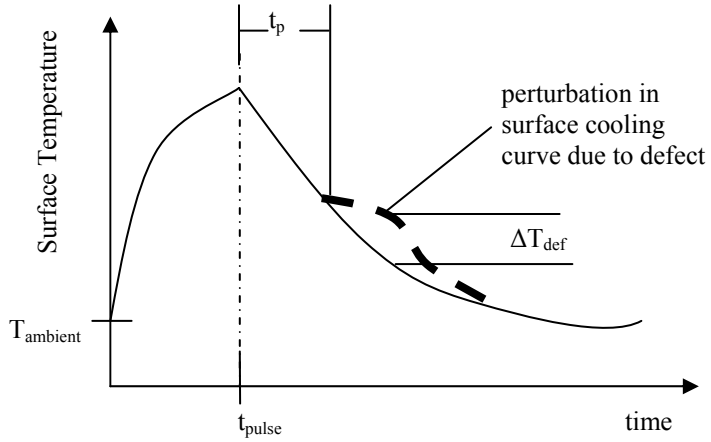

Figure 3-6. Surface heating and defect detection for pulse thermography (Maldague 2001)

Step heating

Step heating IRT involves a longer duration and lower energy heat input than pulse IRT. The temperature response on the surface of the specimen is monitored during heating and also after the heat source is removed. Materials with lower thermal diffusivities and deeper defects can often be evaluated with step heating IRT. Some advantages of this method include a low image acquisition rate and low cost heat sources (IR or halogen lamps). A disadvantage of this method is that it is sometimes difficult to

apply heat uniformly to the surface being inspected. An interesting study was reported by Maierhofer et al (2003) in which a large block of concrete (1.5 m x 1.5 m x 0.5 m) containing fabricated defects up to 3" below the surface was inspected using step heating IRT. The surface was heated using an array of three 2400 Watt IR radiators for up to 60 minutes. A computer controlled arm was required to move the radiators across the surface in a manner that resulted in uniform heating.

Starnes et al. (2003) used step heating IRT to identify and characterize defects in FRP systems bonded to concrete. Experimental results were presented for a small-scale specimen containing fabricated defects. The FRP system was comprised of a single 1.3 mm thick pre-cured carbon/epoxy lamina bonded to a concrete substrate with an epoxy adhesive. A total of 8 simulated defects were created by placing different materials between the lamina and the concrete. The first step in the experiment was to simply detect the subsurface defects. This was accomplished by passing a 250 Watt IR lamp across the surface at a rate of 15 cm/sec. The lamp was held at a distance of 5 cm from the surface. This technique easily revealed all of the implanted defects. Once the location of each defect was established, a quantitative step heating experiment was performed to characterize the defect. A single lamp was aimed toward the defect at a distance of 33 cm and heat was applied to the surface for 10 sec. This configuration resulted in a defect signal strength of 2.7°C for an air void.

Starnes et al. (2003) also used the finite element method to simulate the heat transfer process involved in step heating. It was difficult to establish an appropriate thermal conductivity (k) value for the carbon/epoxy lamina used in the experiment. This was due to the large range of fiber volume fractions that are commonly encountered in

FRP composites. For pre-cured laminates, fiber volume fractions are typically greater than 70%. Wet layup composites typically have much lower values (<50%). The matter is further complicated by the wide range of published k values for plain carbon-fibers. Textbook values range from 8 to 500 W/m-K depending on the modulus of the fiber and the type of precursor used (Pitch vs. PAN) (Callister 1997). A thermal conductivity of 2.9 W/m-k (perpendicular to the main fiber direction) was ultimately used in the finite element model. The finite element results were compared to experimental results from one fabricated defect and good agreement was observed.

Lock-in IRT

Both pulse and step heating IRT rely on the ability of the IR camera to detect temperature differences on the surface above defect and defect-free regions. In lock-in IRT, thermal images are recorded while a modulated heat source is used to heat the surface. Rather than monitor the temperature data at each pixel in a thermograph, lock-in thermography focuses on the phase shift of each pixel (see Figure 3-7). This technique results in "cleaner" thermal images and is also capable of detecting subsurface defects at greater depths.

The major advantage of lock-in IRT is that phase images are not as sensitive to non-uniform surface heating. Different values of surface emissivities and reflection of the heat source also have limited effect on phase images (Maldague 2001). An interesting study was presented by Carlomagno et al. (2002) which compared pulsed and lock-in IRT in the NDE of historic frescoes. An important finding was that lower net surface temperature increases are required for lock-in IRT than pulse or step-heating. This has implications for the current study since it is important to avoid heating the

surface beyond the glass transition temperature, T_g, of the FRP matrix (Kharbari et al 2003).

Pulse phase IRT

The experimental setup and data acquisition procedure used for pulse phase IRT (PPT) is similar to the pulse thermography procedure described above. After the series of thermal images is collected, a discrete Fourier transform operation is performed on each pixel of the images in the time domain. This operation results in a series of images in the frequency domain with each pixel consisting of an imaginary number. Phase images are obtained for each frequency by computing the inverse tangent of the imaginary part divided by the real part.

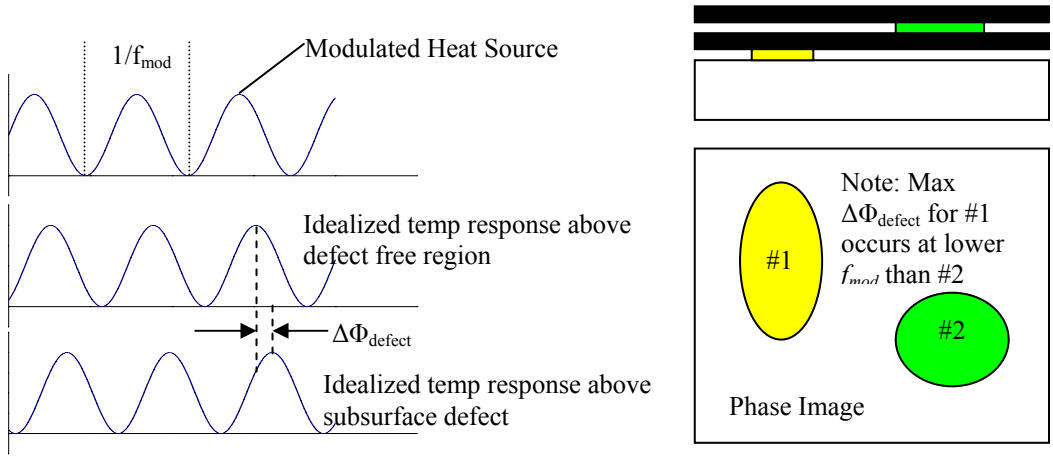

Figure 3-7. Defect detection with lock-in thermography

The advantage of this method is that the resulting phase images are relatively independent of non-uniform heating. There is also a strong relationship between the frequency at which a defect first appears in the phase images and the depth of the defect. Defects that are closer to the surface appear in higher frequency phase images while deeper defects only appear at lower frequencies. A major disadvantage of this method is

that the amplitude of the defect signal strength is significantly less than for long-pulse heating.

Objectives of Current Research

The overall objective of the current research was to develop IRT methods that could be used to detect defects in FRP systems bonded to concrete. Specifically, a major goal was to use IRT data to provide the following information about detected defects:

- Size
- Depth below the surface
- Material composition

Other items that are addressed include:

- Detection limits
- Heating methods
- Data analysis procedures

Previous research in this field has focused on the inspection of FRP composites that are commonly used in the aerospace industry. A number of data analysis techniques have been developed that can assist in using IRT results to characterize defects. None of these methods have been calibrated for use on FRP systems bonded to concrete.

The remainder of this dissertation is divided into two main sections: Phase I and Phase II. Results from Phase I of the current study are presented in Chapter 4. During Phase I, IRT was used to inspect FRP systems that were applied to full-scale AASHTO girders. Phase I contains a laboratory study and a field study. Findings from Phase I were used to develop a second laboratory study that was conducted in Phase II. Details of the Phase II experimental work are provided in Chapter 5 and Chapter 6.

CHAPTER 4
PHASE I EXPERIMENTAL WORK AND FIELD STUDY

Introduction

This chapter describes experimental work that was performed in conjunction with a Florida Department of Transportation (FDOT) project investigating the performance of FRP strengthening systems. The FDOT currently uses FRP composites to repair impact-damaged bridge girders. The objective of the FDOT study was to develop a "quality products list" (QPL) for FRP systems that are suitable for repairing impact damage suffered by bridges.

The FDOT study involved full-scale load testing of six AASHTO Type-II bridge girders at the FDOT's structural research facility in Tallahassee, Florida. Impact damage was simulated at the midspan of each girder by removing a section of concrete and cutting four prestressing strands. Four different FRP system manufacturers then had the opportunity to design and install an FRP system to restore the capacity of the damaged girder. These repairs were then validated by load testing each girder to failure.

This project represented an excellent opportunity to investigate the use of IRT for evaluating the installation and performance of FRP systems. Each FRP system was inspected prior to the load test and then again at various stages of loading. The first part of this chapter results from this research. It should be noted, however, that the objective is to describe the IRT results and not the results from the load testing. This information is available in Lammert (2003).

Full-Scale AASHTO Girders

Description of AASHTO Girders and FRP Systems

A typical AASHTO type II bridge girder that was used in this series of experiments is shown in Figure 4-1. The total depth of each girder was 122 cm (48 in.), which includes a 30.5 cm (12 in.) cast-in-place slab. The distance between supports for each load test was 12.2 m (40 ft.). The critical dimensions with regards to the infrared inspections were the width of the girder's tension face, 45.7 cm (18 in.), and the clearance between the girder and the laboratory floor, 50.8 cm (20 in.).

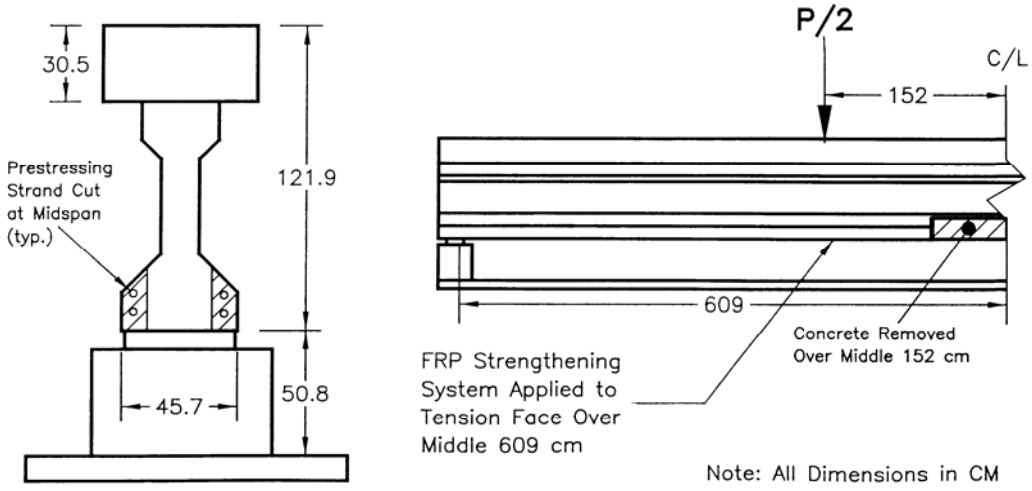

Figure 4-1. Full-scale AASHTO type II girder and load test setup

Before the installation of each FRP strengthening system, vehicle impact damage was simulated by removing a section of concrete and cutting four prestressing strands at midspan. This area was then patched with concrete to restore the original cross-section of the girder.

Four different FRP strengthening systems were evaluated in this study (applied to Girder 3, 4, 5, and 6). The properties of each system are shown in Table 1. Each FRP system was independently designed by the system manufacturer to restore the flexural capacity provided by the cut strands. The FRP system manufacturers also installed each

system. During installation, each girder was raised to a height of 122 cm above the laboratory floor. This provided a challenge for the FRP installers by limiting access to the girder's tension face.

Table 4-1. Fiber-reinforced polymer system properties for full-scale AASHTO girders

	FRP system					
Girder	Fiber	Matrix	Layers	Thickness (mm)[a]	Width of laminate (cm)	Anchorage
3	Carbon	Epoxy	4	4 / 7	40.6	None
4	Carbon	Polyurethane	4	3.1 / 6	30.5	2-ply carbon
5	E-Glass	Polyester Resin	1	12.7 / 3.5 – 9.8	45.7	12.7 mm
6	Carbon	Epoxy	3	1.75 / 4.34	45.7	2-ply carbon

[a] Data Sheet thickness / As-Built thickness

Girder 3

The FRP system applied to Girder 3 consisted of four layers of unidirectional carbon-fiber fabric (with aramid cross-fiber) and an epoxy matrix. Each layer extended over the entire middle 6.1 m of the girder. A tack-coat (epoxy thickened with silica fume) was first applied to the concrete surface followed by the first layer of saturated carbon-fiber fabric. During installation, there was a tendency for the saturated carbon sheets to fall from the tension face. This prompted the installers to apply an additional coat of thickened epoxy between each layer of fabric. The final step was the application of an epoxy gel coat to the surface of the system. The thick layer of gel coat combined with the overhead application resulted in drips forming before the matrix cured. These thickened areas affected the infrared inspections. There were also areas where the gel coat was thin, but no exposed unsaturated fibers were observed. Acoustic sounding (coin tap) indicated that the system was well bonded to the concrete substrate and there were no visible abnormalities that would indicate debonded areas.

The material data sheet (MDS) for this FRP system indicated a 1mm ply thickness resulting in a total laminate thickness of 4 mm. In order to verify this thickness, a small

area of the strengthening system and concrete substrate (2 cm x 7 cm x 1.5 cm thick) was removed from the girder after load testing. The total thickness of the laminate varied between 6 mm and 7 mm (62.5% thicker than the MDS thickness). A 2 mm layer of thickened epoxy was observed between the second and third layers of carbon-fiber (Figure 4-2).

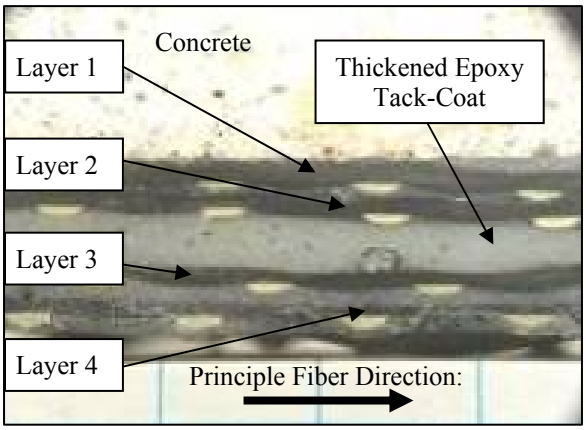

A

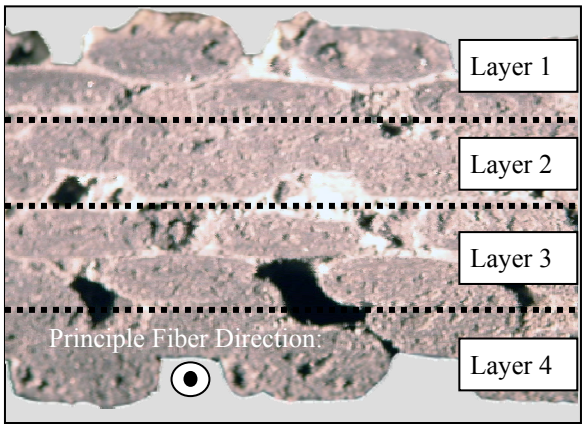

B

Figure 4-2. Cross-section views of FRP systems. A) Girder 3. B) Girder 4 (note: principle fiber direction is out of page for Girder 4)

Girder 4

The FRP system applied to Girder 4 consisted of multiple layers of unidirectional carbon-fiber fabric that was pre-impregnated with a water-activated polyurethane matrix. Four layers of carbon-fiber were applied to the middle 4.9 m of the girder; three layers

extended over the middle 7.3 m; 2 layers extended over the middle 9.75 m; and a single layer was applied over the entire length of 12.2 m. A polyurethane tack-coat was first applied to the concrete followed by the two longest layers of the pre-impregnated fabric. These layers were then sprayed with water to initiate the curing process. Finally, the two remaining layers were applied and sprayed with water. Anchorage for the FRP system was provided by two FRP stirrups (each was 2 plies oriented at 0 and 90 degrees) located at 12 feet on either side of midspan.

A coin tap inspection of the installed system did not indicate any debonded areas. The MDS thickness for this system was 0.78 mm per layer, which resulted in a total thickness at midspan of 3.1 mm. The measured thickness of the 4-ply laminate varied between 5 and 7 mm (Figure 4-2 B).

Girder 5

The FRP system applied to Girder 5 was a sprayed-on mixture of chopped E-glass-fibers and polyester resin. This process requires highly specialized equipment and is commonly employed in the fabrication of boat hulls. The application method worked extremely well on vertical surfaces (sides of the beam); however, it was difficult to apply material to the bottom of the girder. After a thin layer of glass and resin were applied with the spray gun, the material was pressed with a roller to condense the laminate. If too much glass and resin were sprayed onto the bottom, large sections tended to fall down. Sometimes this material would separate entirely and fall to the floor, and other times it would simply cure as small draped areas. This resulted in a large number of visible surface and subsurface defects in the laminate.

The laminate was extended over the middle 6.1 m of the girder and stirrups were also sprayed onto the sides of the girder where the laminate was terminated. The final

measured thickness of the FRP system on the girder's tension face varied between 3.5 mm and 9.8 mm. Additional material was also sprayed on the sides of the girder's bulb to an average thickness of 12.7 mm.

Girder 6

The FRP system applied to Girder 6 consisted of three layers of unidirectional carbon-fiber fabric and an epoxy matrix. All layers extended over the middle 6.1 m of the girder. The data sheet indicated 0.58 mm ply thickness resulting in a total laminate thickness of 1.75 mm. Two additional plies of unidirectional fabric were used to anchor the FRP system at the termination points. This resulted in a total laminate thickness of 2.9 mm on the tension face at the termination points. The as-built thickness of this FRP system was not verified.

Little or no excess matrix material was present on the surface of the installed system. A coin tap inspection indicated that the system was well bonded to the concrete substrate and there were no visible abnormalities.

Infrared Inspection Procedures

Thermal images were collected using the thermal imaging equipment described in Chapter 3. Heat sources used in this study included 125 Watt IR heating lamps and a 500 Watt halogen lamp. Limited access to the tension face of each girder along with the need for efficiency in evaluating the relatively large area prompted the development of two novel scanning procedures. In both procedures, the heat source and IR camera were mounted to a rolling cart. The heat source was positioned on the leading edge of the cart and placed a distance of 7.6 cm from the FRP surface. The camera was positioned to view the FRP surface just behind the area being heated. As the cart was pushed along the floor, the IR camera recorded a series of images as the surface cooled.

The cart configuration for the first procedure is shown in Figure 4-3 A. This resulted in a camera field of view (FOV) of only 22.9 cm x 17.1 cm. Consequently, two passes were required to inspect the entire 45.7 cm width of the girder's tension face. This image was also slightly distorted since the angle of incidence for the camera was not 90°. The cart configuration for the second procedure (shown in Figure 4-3 B) utilized first-surface mirrors located near the ground to increase the camera's FOV to 56.7 cm x 42.5 cm.

The image save rate for all inspections was set to one frame per two seconds (0.5 Hz). The fastest image save rate to the on-board PCMCIA storage card is approximately 1 Hz. This rate, however, produces an unmanageable amount of data (each thermal image is 158 Kb). An even faster rate of up to seven frames per second is possible, but this requires a direct link to a laptop computer. For the scanning speed used in these inspections, the rate of 0.5 Hz was found to be adequate. A typical series of thermal images containing a subsurface defect is shown in Figure 4-3 C. This particular series was recorded using the cart configuration shown in Figure 4-3 A.

To characterize defects detected during each inspection, the defect signal strength, ΔT_{def}, was calculated as follows:

$$\Delta T_{def} = T_{def} - T_{background} \qquad (4\text{-}1)$$

T_{def} = temperature above the defect
$T_{background}$ = temperature of adjacent defect free area

The magnitude of T_{def} was determined by identifying an appropriately sized area above the brightest portion of the defect and using the average temperature measured within that area. The standard deviation of temperature values within each area was

typically less than 0.5°C. A similar technique was used to determine the corresponding $T_{background}$.

A B

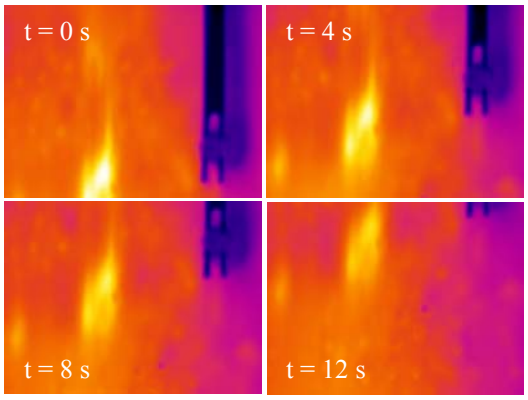

C

Figure 4-3. Data collection for full-scale AASHTO girders. A) Scanning cart configuration for Girder 3. B) Girders 4 to 6. C) Typical thermal images

To make a valid comparison between defect signal strengths, the amount of heat applied to the surface should be consistent during each inspection. Heating consistency for each scan was evaluated by monitoring $\Delta T_{background}$ along the leading edge (edge closest to the heat source, as shown in Figure 4-4) of each thermal image in a series:

$$\Delta T_{background} = T_{background} - T_{ambient} \qquad (4\text{-}2)$$

$T_{ambient}$ = ambient temperature of the girder prior to heating

This quantity was also monitored along the trailing edge (farthest away from the heat source) of each image in a series in order to evaluate the average cooling rate on the surface of the FRP.

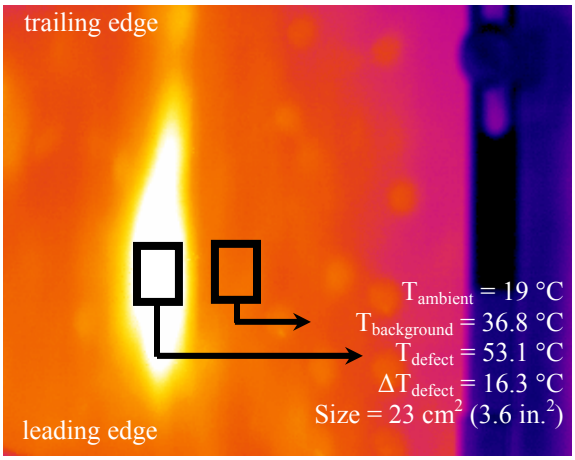

Figure 4-4. Subsurface defect found on Girder 3

Initial IR Inspections

An initial infrared inspection was performed on each girder prior to load testing. The objective was to identify any defects formed during the installation. Girder 3 was inspected using the cart configuration shown in Figure 4-3 A. Girders 4-6 were inspected using the configuration shown in Figure 4-3 B.

The inspection of Girder 3 revealed 11 minor subsurface defects (< 12.9 cm^2) and three moderate subsurface defects (> 12.9 cm^2 but less than 161 cm^2). Thermal images for two of these defects are shown in Figure 4-5. These images were recorded approximately six seconds after the area was heated.

The computed signal strength for defect 1 and defect 2 was 7.5°C and 15.1°C, respectively. The difference in signal strengths could be a result of several factors: defect depth, amount of heat applied to the surface, and the size of the defect. Stronger signal strengths are expected for defects that are closer to the surface (signal strength is

inversely proportional to defect depth). Applying more heat to the surface will also result in higher signal strengths. Finally, a larger surface area will result in higher defect signal strengths since the heat applied above the defect must travel farther before it is absorbed by the concrete.

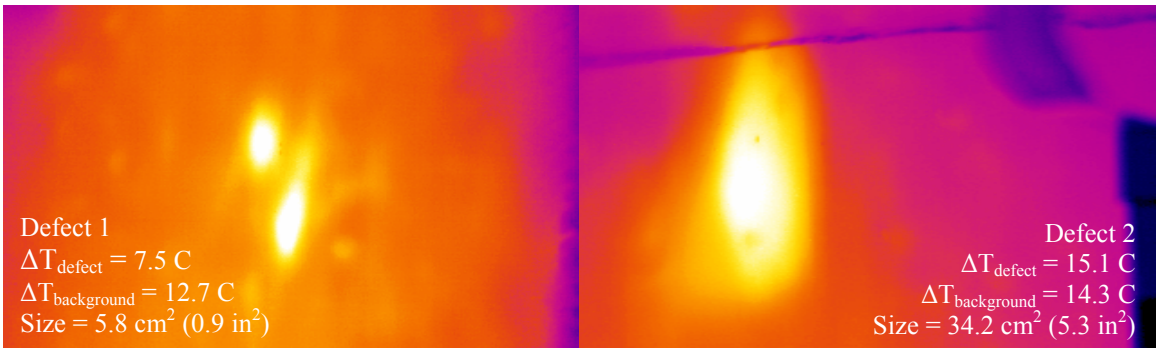

Figure 4-5. Subsurface defects found on Girder 3

The initial infrared inspection performed on Girder 4 did not reveal any defects similar to those observed in Girder 3. There were, however, two interesting observations made regarding the polyurethane matrix material and the uniformity of heating perpendicular to the girder's length. Some areas of the FRP surface were covered with excess polyurethane matrix. This excess matrix material had the appearance of a thin layer of foam. The color of this layer was also much lighter than adjacent areas, which appeared black. An example of this occurrence is shown in Figure 4-6. The resulting $\Delta T_{background}$ for the light colored area was 5.4°C while the $\Delta T_{background}$ for the dark color was 7.8°C. Another source of non-uniform heating was streaking due to the narrow beam width of the IR heat lamps. The resulting $\Delta T_{background}$ for the area directly in-line with the heat lamp was 9.7°C while the $\Delta T_{background}$ in the area between lamps was 7.7°C.

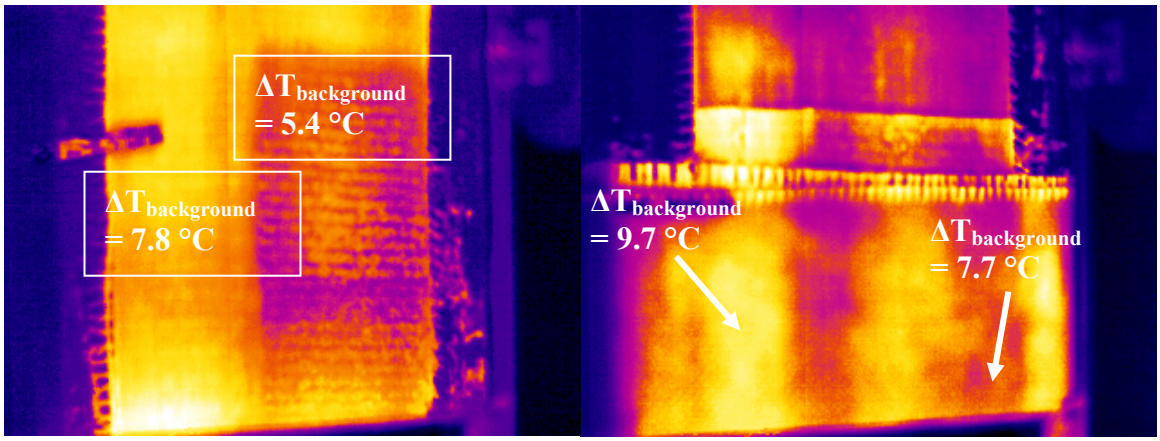

Figure 4-6. Non-uniform surface heating of Girder 4

A visual inspection of Girder 5 revealed numerous defects on the surface of the FRP system. These were a result chopped fibers falling down before the system fully cured. There were also a large number of defects visible just below the surface of the FRP, which were the result of improper saturation of the chopped glass-fibers. These large imperfections near the surface interfered with the IRT inspection. The thermal images were crowded with these imperfections and it was difficult to distinguish defects that occurred near the surface and defects that occurred below the surface. A typical thermal image is shown in Figure 4-7 A. All of the defects that were visible in the thermal image were also visible to the naked eye.

Only one subsurface defect was detected during the initial scan of Girder 6 (shown in Figure 4-7 B. The recorded defect signal strength was 7.4°C and $\Delta T_{background}$ was 8.5°C. This defect occurred on the edge of the laminate and was not considered to be significant.

A summary of the scanning speed for each initial inspection is presented in Table 2. $\Delta T_{background}$ was computed along the leading edge (closest to heat source) and trailing edge (farthest from heat source) of the series of thermal images that were collected as the cart was pushed along the beam. The average speed was computed by dividing the total

distance scanned by the total time required. These scanning rates are much slower than those reported by Starnes et al (2003). Their basic procedure for identifying subsurface defects involved passing a single 250 Watt IR heat lamp held a distance of 5 cm from the FRP surface at a speed of approximately 15 cm/s. This approach was adequate to detect defects beneath a 1.3 mm thick pre-cured CFRP laminate.

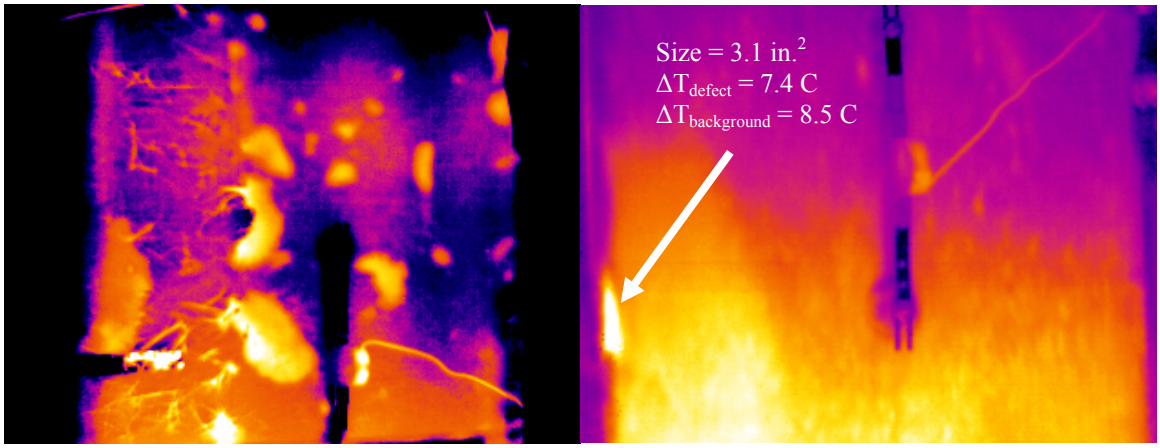

A B

Figure 4-7. Thermal images collected for full-scale AASHTO girders. A) Girder 5. B) Girder 6

Table 4-2. Summary of scanning speed and uniformity of heating

Girder	Scan Config.	Avg. Speed (cm/s)	Leading Edge[a] $\Delta T_{background}$ (°C)	Leading Edge Std. Dev. (°C)	Trailing Edge $\Delta T_{background}$ (°C)	Trailing Edge Std. Dev. (°C)	Avg. Cooling (°C/s)
3	Fig. 3 A	1.2	13	1.4	9.5	1.1	0.25
4	Fig. 3 B	2.77	11.3	2.4	6.0	1.8	0.35
5	Fig. 3 B	1.25	7.2	1.5	4.26	0.98	0.09
6	Fig. 3 B	2.1	10.4	1.9	1.67	0.88	0.44

[a] Leading Edge of image is closest to heat source

For the current series of inspections, the average cooling rate (ACR) on the surface of the FRP was computed as follows:

$$ACR = \frac{\Delta T_{background}(leading) - \Delta T_{background}(trailing)}{t'}$$

$$where: \qquad (4\text{-}3)$$

$$t' = \frac{FOV_{SD}}{Speed}$$

FOV_{SD} is the camera's field of view in the direction of scanning and speed is the average speed. This calculation assumes that the surface temperature cooling profile at every point is linear, which is not the case. The results are reported in this format for ease of comparison between FRP systems.

Controlling the speed of the cart during each scan was difficult. Figure 4-8 shows the resulting $\Delta T_{background}$ along the leading and trailing edge of each thermal image vs. position for Girder 3 and Girder 6. The leading edge curve represents $\Delta T_{background}$ measured just after an area enters the thermal image. The trailing edge curve represents $\Delta T_{background}$ measured just before the same area leaves the image. The average time between these two curves can be calculated as t` in equation 4. The significant fluctuation observed in each curve demonstrates the sensitivity of $\Delta T_{background}$ to cart speed. In areas where the cart was pushed slowly, there was an increase in $\Delta T_{background}$ while areas in which the cart was moved more quickly experienced a decrease in $\Delta T_{background}$. The standard deviation of $\Delta T_{background}$ along the leading edge for Girder 3, 4, 5, and 6 was 1.4, 2.4, 1.5, and 1.9°C, respectively.

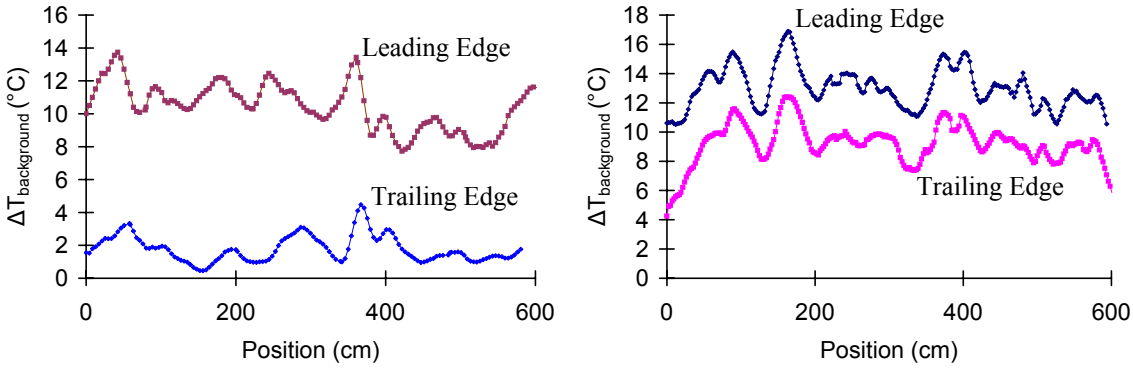

Figure 4-8. Background temperature increase vs. position along length of girder. A) Girder 6. B) Girder 3

IR Inspections Performed During Load Testing

Additional IR inspections were performed during the load test of each girder. For Girder 3, the load was removed during each inspection. Girders 4-6 were inspected while the specimen was under loading. Table 3 contains a summary of the load levels at which each IR inspection was performed. The purpose of these inspections was to monitor the subsurface defects detected in the initial scan as well as to detect any new debonded areas resulting from the applied load.

None of the additional inspections that were performed prior to failure revealed new defects or subsurface defect growth due to loading.

IR Inspections of Known Debonded Areas After Failure

The failure mode for Girder 3 was delamination of the concrete cover at the level of the girder's pre-stressing tendons (see Figure 4-9). There were no visual or audible indications of FRP debond during the loading. A 90 cm x 45 cm piece of the delaminated cover was recovered after load testing to perform a thorough IR inspection. This section did not contain any defects that were identified in the initial inspection, however, debonded areas were formed as a result of the delaminated cover concrete and FRP striking the floor after the girder failed.

A series of IR inspections were performed on this section using the same amount of heat that was applied during initial inspections prior to load testing. These inspections did not reveal any debonded areas even though coin-tap testing did indicate that large areas of the FRP had separated from the concrete. A very important observation was made regarding a large section of FRP on the edge of the sample that was no longer attached to any concrete (effectively an overhang). This area was expected to appear

extremely bright after being heated with the halogen lamp to a $\Delta T_{background}$ of 15°C. However, no thermal signal was detected.

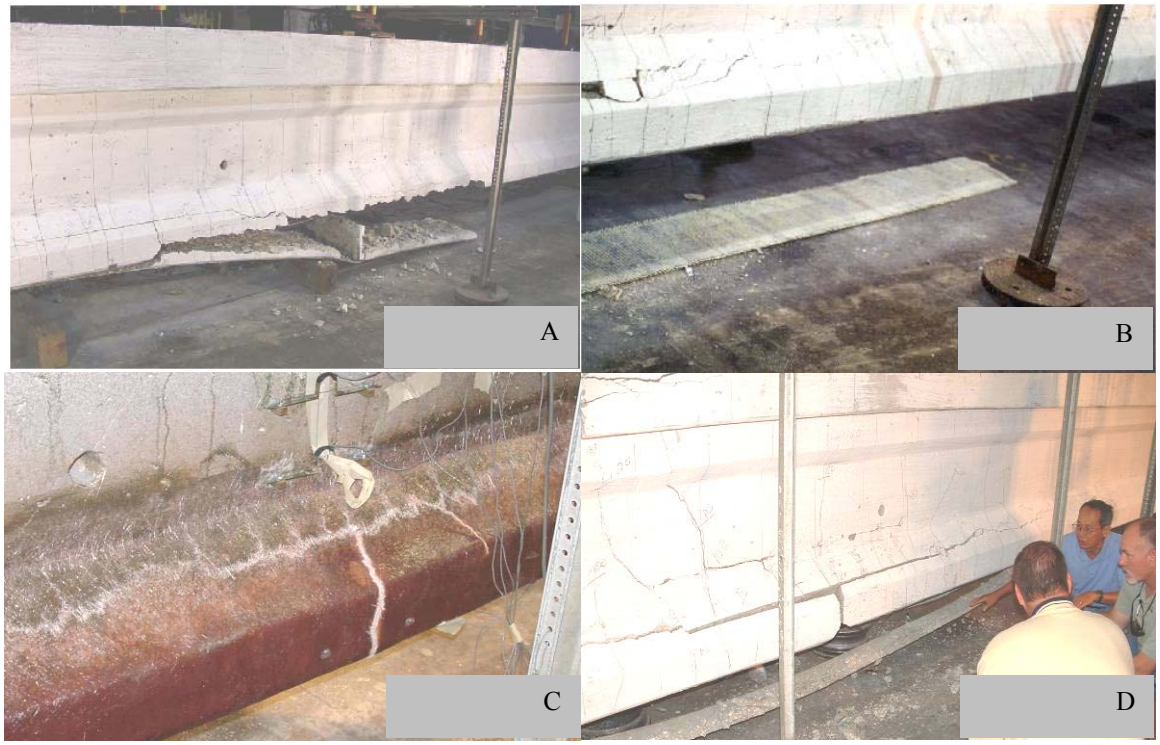

Figure 4-9. Failure modes for full-scale AASHTO girders. A) Girder 3. B) Girder 4. C) Girder 5. D) Girder 6.

Figure 4-10 shows results from an experiment in which a $\Delta T_{background}$ of 33.3°C was generated above the bonded area. Immediately following the removal of the heat source, the temperature increase above the debonded (non-bonded / overhanging) area was 28.6°C. This resulted in a thermal signal of – 4.61°C at t = 0 seconds. This initial negative temperature difference was likely due to improper lamp positioning that resulted in non-uniform heating of the surface. After 282 seconds of cooling, the thermal signal achieved its maximum value of 2.12°C. Measurements were terminated after 594 seconds with a thermal signal of 1.69°C.

If the sample had been heated uniformly, the maximum signal would likely have approached 6.7°C (2.12°C – (-4.61°C)). It is important to note that this would occur after

4.7 minutes of cooling. These results stand in sharp contrast to the measurements obtained during the initial IR inspections (defect signal strengths between 10°C and 15°C that were visible after less than 2 seconds of cooling).

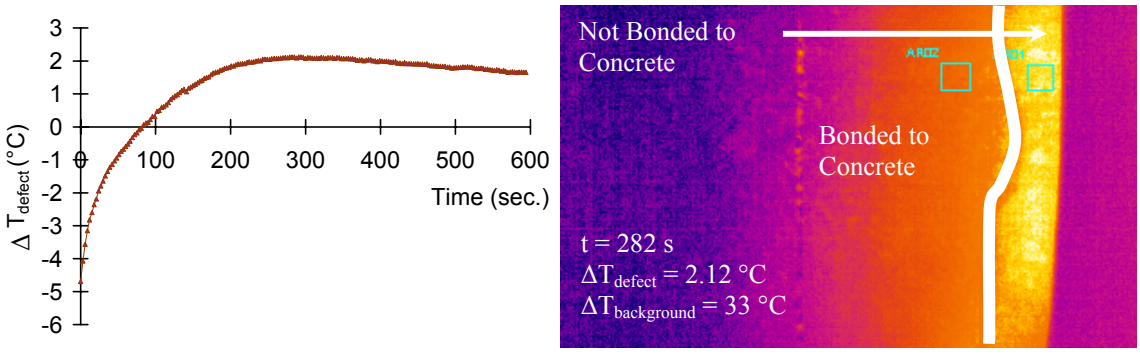

Figure 4-10. Defect signal strength (ΔT_{defect}) vs. time for known debonded area

The failure mode for Girder 4 was debonding of the FRP laminate. Debonding began in the middle of the specimen and progressed outward towards both ends of the girder. At the north end of the girder, debonding caused the anchorage FRP to rupture and then continued to end of the laminate. On the south end of the girder, the FRP system ruptured in tension before the debonding reached the anchorage point.

After the specimen failed, the majority of the FRP system was no longer bonded to the girder. There was, however, a short section on the south end that remained partially bonded. The line of demarcation between the bonded and debonded area of this section was easily recognized with a coin-tap inspection. An IR inspection of this debonded area was made using the same procedure outlined above (cart speed of approximately 3 cm/sec). This inspection did not reveal the debonded area. Another inspection was performed in which the lamp was passed over the debond line for 120 sec and the area was observed while cooling for 3 minutes. Again, the debonded area was not detected.

The failure mode for Girder 5 was tensile rupture of the FRP laminate at the girder's midspan. There were no audible indicators during loading that the FRP system ever debonded from the surface of the concrete.

The area around the rupture point of the FRP system was thoroughly inspected after the girder failed. A large debonded area (approx. 15.2 x 45.7 cm) was identified adjacent to the rupture point on the bottom of the girder. This area could not be identified with the scanning procedure that was used during the initial inspection of this girder.

The failure mode for Girder 6 was debonding of the FRP system. This debonding began at midspan and progressed outward towards the anchorage points (very similar to Girder 4). Audible indicators of the debonding were also present; however no IR scans were performed between the time they were first heard and failure of the specimen. At the ultimate load, a portion of the FRP slipped at the north anchorage point resulting in failure.

Results from an IR inspection performed on the tension face of the girder at the north anchorage point are shown in Figure 4-11. A thin strip (approx. 15 cm wide) in the center of the beam remained bonded to the concrete at the anchorage point. The adjacent debonded/delaminated areas are clearly distinguishable in the thermal image. The defect signal strength for the delaminated area varied from 5°C to 9°C.

A small FRP test patch (21.6 cm x 45.7 cm) was constructed on the side of Girder 6 near the support. This test patch consisted of a single layer of carbon-fiber fabric. The area chosen for the test patch contained numerous bug-holes and other surface imperfections. A single bug-hole near the center of the area was identified and filled with thickened epoxy paste prior to placement of the carbon-fiber. The remaining bug-holes

were left unfilled. The test patch area was heated for 18 seconds with an array of four 125 Watt IR heating bulbs. The resulting $\Delta T_{background}$ above the defect free area was 5°C. The bug-holes were visible immediately after the heat source was removed. The reference hole (unfilled), shown in Figure 4-12, had a defect signal strength of 9.5°C. The signal strength above the epoxy filled hole was only 5.25°C immediately after the heat was removed. After 8 seconds of cooling, the defect signal strengths above the filled and unfilled holes were equal at 5.0°C. As the area continued to cool, the signal strength above the unfilled hole decayed rapidly, and after 20 seconds only the epoxy filled hole continued to possess a significant thermal signal.

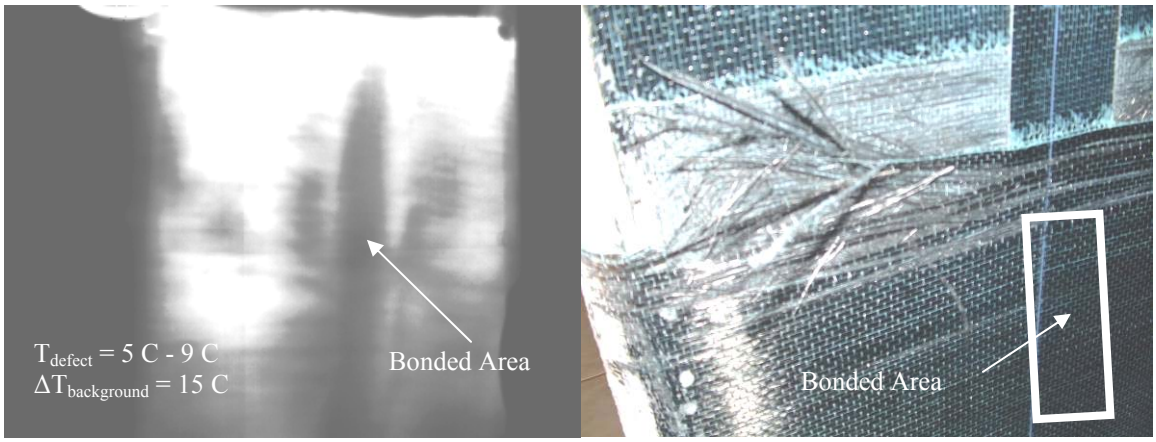

A B

Figure 4-11. Debonded area after failure for Girder 6. A) IR image. B) Visual image

This finding has several implications. Filling the hole with epoxy will ensure that the FRP is bonded to the concrete; however there is still a difference in thermal conductivity between the epoxy filler and concrete substrate. This results in the appearance of a debonded area in thermal images. Careful scrutiny of the thermal signal vs. time can differentiate the epoxy filled void from an air filled defect; however this requires a series of thermal images to be recorded with the camera in a static position.

Also, it might be difficult to differentiate between these two thermal signals if a particular image does not contain both types for reference.

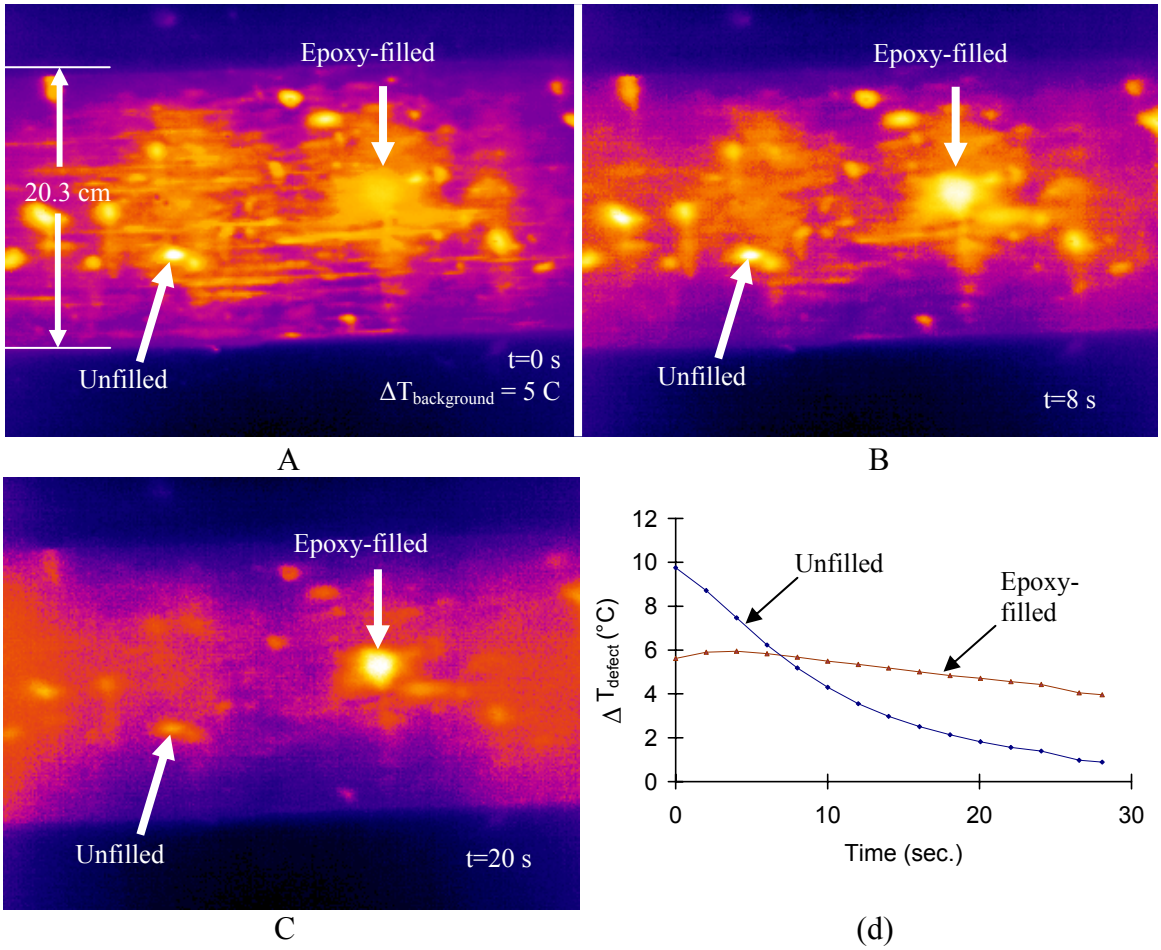

Figure 4-12. Series of thermal images for air and epoxy filled defects. A) t = 0 sec. B) t = 8 sec. C) t = 20 sec. D) ΔT_{defect} vs. time plot.

Summary of IR Inspection Results for Each FRP System

The FRP system applied to Girder 3 consisted of four layers of unidirectional carbon-fiber fabric with an epoxy matrix. Initial IR inspections performed after installation revealed three subsurface defects having an area greater than 12.9 cm^2. Defect signal strengths for these defects were greater than 10°C and resulted from a $\Delta T_{background}$ of approximately 13°C. These defects were visible immediately after the heat source was removed. Additional IR inspections performed on a section of the FRP

system with known debonded areas produced different results. A $\Delta T_{background}$ of 33°C resulted in T_{defect} measurements of only 2.1°C after 282 sec of cooling. The defects found during the initial inspection were very close to the surface signifying delaminations rather than debonded areas. The more important finding is that the initial scanning technique would not have detected debonded areas since the amount of heat applied to the surface was relatively low and the camera was not positioned to record images when the defect's maximum signal strength was reached.

The FRP system applied to Girder 4 consisted of four layers (gradually tapering down to a single layer) of unidirectional carbon-fiber fabric pre-impregnated with a polyurethane matrix. No subsurface defects were detected during IR inspections performed after the installation of the FRP system. An IR inspection was also performed on a known debonded area. This debonded area was located on a portion of the FRP system that was partially attached to the girder after failure. Results indicated that this particular FRP strengthening system is not well-suited to inspection with IRT. A closer inspection of this system after failure revealed a thin layer of polyurethane matrix between the FRP and concrete that resembled insulating foam (as shown in Figure 4-13). If this particular type of matrix material is effectively insulating the carbon-fibers from the concrete, subsurface defects will not result in hot spots on the surface after heating. Additional experiments under controlled laboratory conditions are needed to determine the limits of detection.

The FRP system applied to Girder 5 was a chopped glass / polyester resin mixture that was sprayed on the surface. Numerous surface and subsurface defects (also close to the surface) were clearly visible with the naked eye. IR inspections of this system clearly

revealed these defects. The thickness of the system, however, and possibly the insulating characteristic of the glass-fibers made the detection of debonded areas difficult.

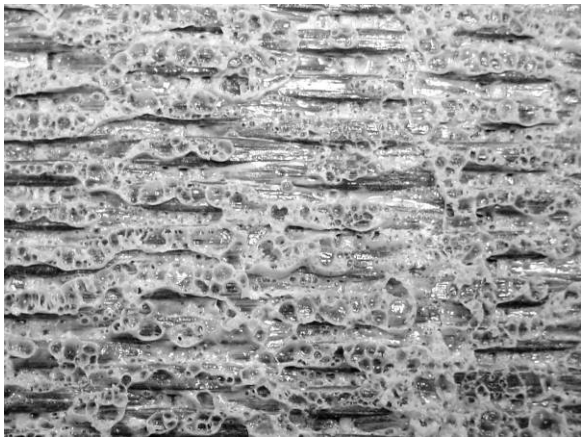

Figure 4-13. Polyurethane matrix shown after debonding from concrete (Girder 4)

The FRP system applied to Girder 6 consisted of three layers of unidirectional carbon-fiber fabric and an epoxy matrix. Initial IR inspections revealed only one subsurface defect. Additional IR inspections performed on a known delaminated area indicated that IR thermography was capable of detecting defects beneath at least two layers of the FRP system. It should be noted that the installation procedure for this girder was very different from Girder 3 even though the system specifications are similar. Excess matrix material that was present in the laminate on Girder 3 that was not observed on Girder 6. This reduction in matrix volume increased the effectiveness of the IR inspections. An IR inspection performed on a small test patch (single layer of carbon-fiber) containing numerous unfilled bug-holes demonstrated that IR thermography can be very effective at detecting defects under a single layer of FRP. This inspection also showed that epoxy-filled holes still possess a defect signal strength; however the rate of decay of this signal is much slower than a simple air void.

Field Inspection: Chaffee Road

The Chaffee Road/Interstate 10 overpass (located in Jacksonville, Florida) suffered severe vehicle impact damage in July of 2001 (see Figure 4-14). The impact dislodged large sections of concrete and ruptured a number of prestressing strands. The most severe damage occurred on the fascia girder that was hit first (east side of bridge). The exterior girder on the west side of the bridge also experienced similar damage. The interior girders were not significantly affected. Rather than replace these girders, the FDOT decided to repair the damaged concrete and then apply an externally bonded FRP strengthening system. This system was comprised of multiple layers of 0°-90° carbon fiber fabric and an epoxy matrix that fully encapsulated the middle 9 m of both exterior girders. The exact configuration of the FRP system was not available at the time of this study. Samples removed from the girder, however, contained two layers of the bidirectional fabric. There were no signs that excess epoxy was applied during the installation of the system.

Chaffee Road has the unfortunate distinction of being the lowest overpass on I-10 westbound out of Jacksonville. As a result, a number of minor vehicle impact events occurred between the time the FRP system was installed and July of 2002. In June of 2003, another serious vehicle impact occurred (shown in Figure 4-14). Clearly the FRP system was in need of repair and the strategy adopted by the FDOT was to completely remove the existing FRP and restore the cross-section of the girder with concrete. After this was completed, a new FRP system was applied to strengthen the girder.

Before the original system was removed, the author inspected the system using IRT. The primary goal of this inspection was to assess the affect of the vehicle impact damage on the FRP system (beyond what was clearly destroyed). This was also an

excellent opportunity to apply the IR inspection techniques developed during the full-scale AASHTO girder tests in a field situation.

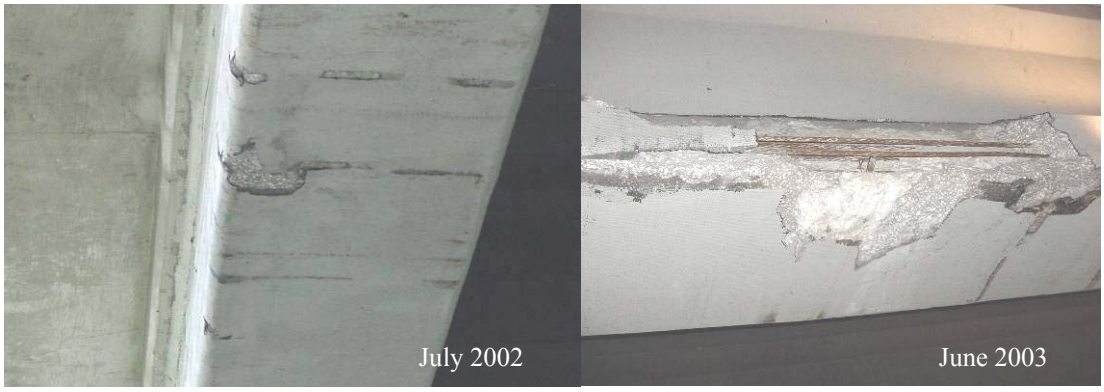

A B

Figure 4-14. Vehicle impact damage sustained after FRP strengthening. A) July 2002. B) June 2003.

Areas of the FRP system that were damaged by the vehicle impact were heated using four 125 Watt IR heat lamps. The inspection procedure required two people: one to operate the camera and one to heat the surface. The camera operator and the surface heater were lifted up to the girder in a mobile scissor lift positioned directly below the area being inspected. The surface was heated by passing the lamps over the surface at a distance of approximately 10 cm. The rate of motion of the heat lamps varied between scans, but the average $\Delta T_{background}$ generated by the heat lamps was 10°C. As the specimen was heated, the camera operator viewed the surface through the IR camera and directed the heat lamp operator.

While there was some evidence of debonding, thermal images indicated that significant damage was limited to the immediate area surrounding the point of impact (Figure 4-15). The debonded areas visible in the thermal images were verified with a coin tap inspection. This coin tap inspection also verified that areas which appeared bonded in the thermal images in fact were.

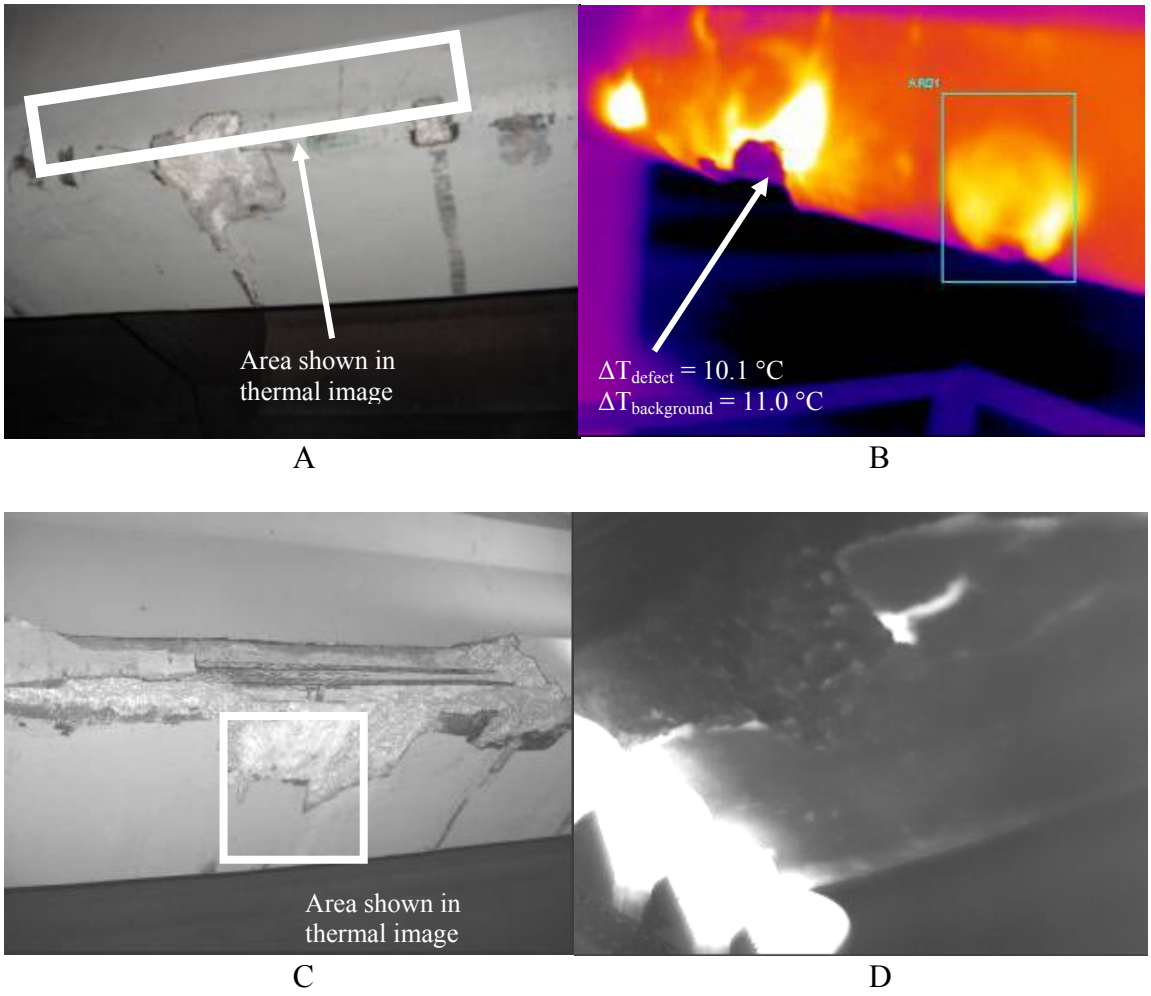

Figure 4-15. Visual and thermal images of vehicle impact damage. A) Damage to side of girder. B) Thermal image. C) Damage to tension face. D) Thermal image

While work was being done to apply the new FRP system to the east girder, the IR inspection team was able to evaluate the FRP system that was originally applied to the west girder. Access to the girder was achieved with a 2 m x 4 m scissor lift. The scanner cart configuration shown in Figure 4-3 B was deployed on the scissor lift in an attempt to duplicate the experiments performed on the full-scale girders in the laboratory. Unfortunately, this met with little success. Unevenness of the scissor lift platform meant that the height of the lamps were in constant need of adjustment as the cart was pushed

along the girder. Also the cart was not properly configured to account for the increased distance between the platform and the girder that was mandated by the platform's railing.

As an alternative to the scanner cart, the camera was placed on a tripod and the camera operator applied heat to the surface as the thermal images were recorded. This was effective at revealing subsurface defects in the FRP system; however this method required a significant amount of time for setup between shots. A typical thermal image collected during this inspection is shown in Figure 4-16. A number of small defects were detected throughout the inspected area. One area that was particularly prone to debonding was the re-entrant corner where the bulb intersects the shear face.

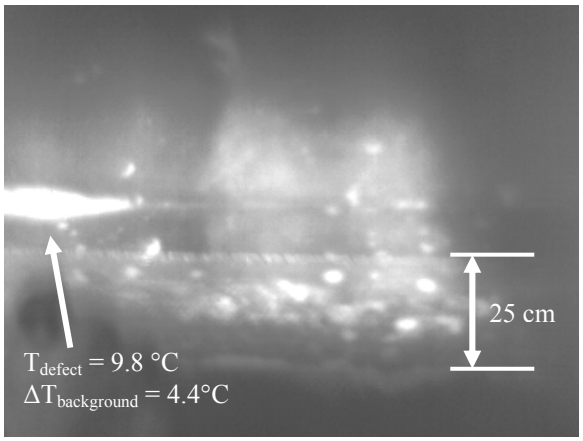

Figure 4-16. Infrared thermography inspection of undamaged girder

The IR inspection technique worked very well in this field inspection. A number of subsurface defects were identified in the original FRP system as well as a portion of the system that suffered additional vehicle impact damage. Overall, the IR inspection indicated that much of the FRP strengthening system was still bonded after the major impact damage. This was verified as the workers attempted to remove the existing FRP system with pneumatic jackhammers and encountered tremendous difficulty. Most of the system was so well bonded that it was left in place and the new system was installed over it (shown in Figure 4-17). An alternative repair procedure that might be considered is to

remove the debonded laminate around the damaged areas and patch the damaged concrete. Once the patch is cured, apply new FRP composite over the repaired area with an appropriate overlap onto the existing FRP system. It is not known, however, how this repair technique would affect the strengthened flexural capacity of the girder.

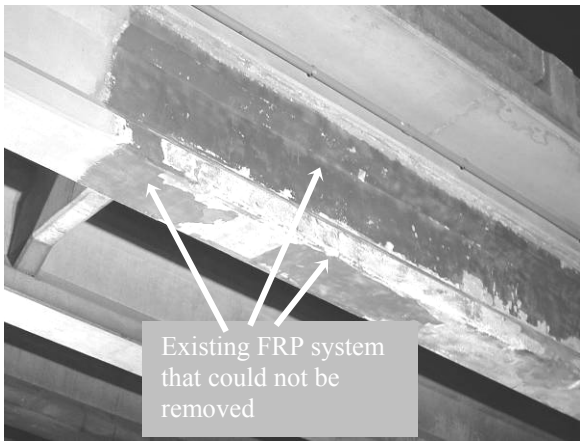

Figure 4-17. Damaged girder before new FRP system was applied

Summary of Findings for Phase I

Results from the full-scale AASHTO girder experiments and the field study conducted on the bridge at Interstate 10 and Chaffee Road provide insight into how IRT can and cannot be used to inspect FRP strengthening systems applied to civil infrastructure. The most important observation is that an IRT inspection procedure that is effective for one FRP system may not be applicable to another.

In the case of the AASHTO girder experiments, four independent FRP system manufacturers were given identical strengthening requirements for a damaged girder. The FRP systems that were installed on each girder varied significantly: different fiber types, different matrix materials, different thicknesses, and different installation procedures. In general, thicker FRP systems that contained more matrix material required longer heating times and longer observation times during cooling.

The IRT inspection performed on the bridge at Interstate 10 and Chaffee Road also raised some important issues. The IRT inspection procedure used for the original FRP system applied in 2001 did detect defects. These data, however, were not collected in a uniform manner and the heating process varied widely from one portion of the FRP system to the next. The general procedure involved heating an area with four IR heating lamps and watching the surface cool with the IR camera. If no defects were observed in the thermal images, the process was repeated by heating the area for a longer duration. This approach gave the inspectors a general idea of the required heating times for this specific FRP system. However, there was no rational basis for the heating time or the observation time with the IR camera.

The radiometric data were reported for select defects by identifying the relative surface temperature increase for the defect and the adjacent defect free areas. These data represent an improvement over basic intensity images. At the very least it is possible to state what the temperature difference is for the defect as opposed to stating the defect is "hotter" than the surroundings. Without a rational model or an extensive database of results to compare with these numbers, the radiometric temperature data do not provide additional information about the defect. It is not possible to determine the depth below the surface or the material composition of the defect.

Another finding of the Chafee Road study supports a conclusion made from the AASHTO girder experiments: the installation methods and resulting FRP thickness varies considerably and is not always known. The replacement system applied to the Chafee Road bridge was applied on top of significant portions of the original system. A large amount of thickened epoxy paste was also used to fill surface imperfections. There is

also a question about the final thickness of the replacement FRP system. The design for this system specified two layers of carbon/epoxy in the longitudinal direction and one layer of carbon/epoxy in the transverse direction for shear. However, installation of this system required a large number of lap splices and overlaps between successive layers. This installation procedure resulted in a composite thickness as high as five layers in certain locations. These five layers were in addition to any portions of the original system that were not removed.

Based on the findings of the Phase I experimental work, it was determined that additional laboratory work was needed. This work is described in the following chapters as Phase II experimental work. The objective of this work was to further investigate the effects of FRP system properties on IRT results. The properties that were investigated included thickness of the FRP system, fiber type, and matrix saturation levels.

Phase II experimental work also investigated different methods for applying heat to the surface of the FRP system. The objective of this work was to develop a standardized heating procedure that can be used to inspect FRP composites in the field. Phase I results highlighted the fact that FRP systems applied to concrete cover a large surface area. The heating methods that were investigated in Phase II were designed such that they could be practically implemented in the field.

Another significant finding from the Phase I experimental work was that thicker FRP systems require substantially longer heating times to reveal defects. From a practical standpoint, the heat flux applied to the surface of the FRP is not uniform. Longer heating times translate into large thermal gradients across the area of the composite. If the overall temperature difference that develops for a defect is small, the

defect signal may become lost in the thermal gradient that develops from non-uniform heating.

The data analysis techniques described in Chapter 3 were developed by other researchers to address the issue of non-uniform heating. These data analysis techniques were also developed to assist in using IRT data to characterize defects. The Phase II experimental work in the current study investigated some of these data analysis techniques and focused on calibrating the different methods for use with FRP composites bonded to concrete.

CHAPTER 5
PHASE II: EXPERIMENTAL SETUP

Introduction

The overall objective of the current research is to develop IRT methods that can be used to detect defects in FRP systems bonded to concrete. Specifically, a major goal is to use IRT data to provide the following information about detected defects:

- Size
- Depth below the surface
- Material composition

The results presented in Chapter 4 indicate that a standardized approach for collecting IRT data is needed. Although general heating methods and image capture techniques are available, the application of IRT to composites bonded to concrete has yet to be fully developed. Consequently, the following issues must be addressed before IRT can be used in the field environment:

- Heat intensity and duration
- Timing and duration of image capture
- Image capture rate
- Subject size in field of view of IR camera

The results presented in Chapter 4 also indicate that FRP system properties can vary significantly from one application to the next. A primary objective of the Phase II research was to investigate how the following FRP system properties can affect IRT results:

- Thickness of FRP composite
- Matrix saturation levels
- Fiber types

- Thickened epoxy tack-coat
- Lap splices

Small-scale specimens containing fabricated defects were constructed in a laboratory environment. Four experimental procedures were designed and implemented for heating the surface of the composite under consideration:

- Flash heating with a photographer's flash
- Scan heating with two 500 W halogen lamps
- Long-Pulse heating with four 500 W halogen lamps
- Sinusoidal heating with four 500 W halogen lamps

This chapter contains a description of the specimen matrix as well as the details of each heating method. Information regarding the noise characteristics of the IR camera used in the current study is also presented. Results and analysis are provided in Chapter 6.

Specimen Construction

A total of 34 small-scale specimens were constructed and grouped into the five categories shown in Table 5-1. Series A, B, and C contain fabricated defects of known size and location. Series A seeks to investigate the relationship between the smallest detectable defect and the thickness of the applied FRP composite system. Series B examines how different levels of fiber saturation and fiber type affect IRT results. Series C includes specimens that were prepared using different degrees of surface preparation (sandblasting) and tack-coat.

Series D and E were used to determine whether or not IRT is capable of providing any additional information about how an FRP composite system was constructed. Series D consists of three specimens that were constructed using different saturation methods for the fibers. Series E was used to investigate the effect of lap splices on IRT results.

Specific details regarding how each specimen was constructed are provided in a later section.

Table 5-1. Overview of specimen matrix

Series ID	Number of specimens	Variable investigated
A	4	Defect size and detection limits
B	18	Saturation levels and fiber type
C	6	Surface prep and tack coat
D	3	Saturation methods
E	3	Lap splices

A number of the steps and procedures that were used to construct each specimen are common to all of the specimens in each series. These general steps and procedures will be described first. Specific details for each series will be discussed after the general information has been provided.

FRP Composite Materials

All of the fiber and matrix materials used in this study were provided by Fyfe Co., LLC. These materials were chosen to represent common matrix and fiber types used in wet layup FRP strengthening systems. Pre-cured laminates were not addressed in this study. Two types of fiber materials were used in this study:

- Carbon (TYFO SCH-41)
- Glass (TYFO SEH-51A)

TYFO SCH-41 carbon fiber is a unidirectional, stitched carbon-fabric. The dry fibers are shipped in a large roll that is 61 cm wide and 91 m long. The surface of the fabric that is bonded to the concrete is covered with a very thin veil of multi-directional glass-fibers. These glass-fibers are held in place by the fabric's cross-stitching. The purpose of this veil is to keep the fabric intact during installation. These fibers also help to reinforce the matrix material at the FRP/concrete bond line and aid in shear transfer from the concrete into the composite. Figure 5-1 shows both the top and bottom surface

of the dry carbon fibers. TYFO SEH-51A glass fiber is a uni-directional, woven glass fabric (shown in Figure 5-2). The dry fibers are shipped in a large roll that is 137 cm wide and 46 m long. Important values are summarized in Table 5-2.

Table 5-2. Material properties for fibers, epoxy, and lamina

	Dry Fiber Properties		Epoxy Properties		Lamina Properties		
Fiber type	Area density (g/m^2)	Tensile strength (MPa)	Tg (°C)	Tensile strength (MPa)	Thickness (mm)	Tensile modulus (MPa)	Tensile strength (MPa)
Carbon	645	3790	82	72.4	1	82.0	834
Glass	915	3240	82	72.4	1.3	26.1	575

TYFO S epoxy was used as the matrix material for all of the FRP composites used in this study. This epoxy is a two-part system (component A and component B) that is shipped in two 19 L buckets. These buckets are typically pre-proportioned such that all of component B can be added directly into the bucket containing component A. Component B is non-viscous (similar to water) and can be moved from one container to another very easily while component A is very viscous. For this study, components A and B were proportioned by weight according to the manufacturer's guidelines (A:B = 100:34.5). Mixing was performed in a 1 L plastic mixing cup using a drill-powered mixing blade for a minimum of 3 minutes. Care was taken not to mix the epoxy too fast to prevent the formation of air-bubbles. Typical mixes were approximately 500 mL in total volume.

Concrete Substrate

The first step in specimen construction involved casting five 61 cm x 61 cm x 5 cm concrete slabs. Concrete mix proportions were taken directly from PCA's Design and Control of Concrete Mixtures (1994). This was a non air-entrained mix with a target slump of 7.6 to 10 cm. Mix proportions are provided in Table 5-3. Steel plates were used as the bottom surface of the concrete formwork and a thin layer of form-release oil

was applied to the surface of the steel before the concrete was placed. Prior to finishing, the concrete was consolidated in the formwork using a standard concrete vibrator. This was probably not the most effective means for consolidation considering the shallow depth of the slab (5 cm).

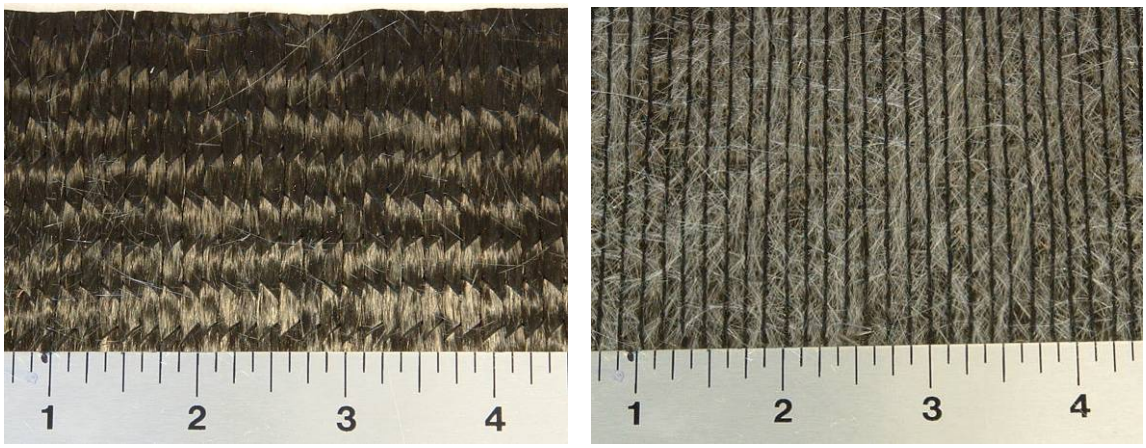

A B

Figure 5-1. TYFO SCH-41 carbon-fibers (scale shown in inches). A) Top surface. B) Surface bonded to concrete.

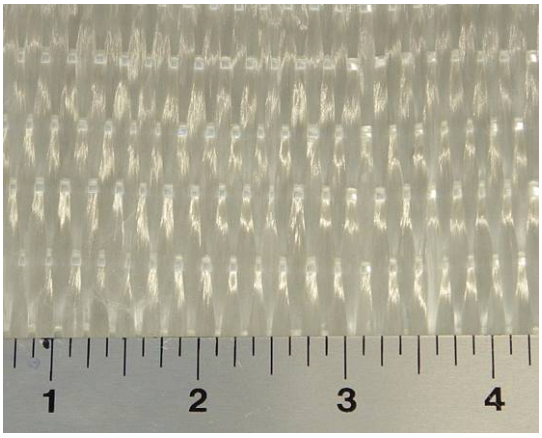

Figure 5-2. TYFO SEH-51 glass-fibers (scale shown in inches)

The concrete was allowed to cure in the forms for two days. No additional curing was provided after the forms were removed. The next step was to cut each of the large slabs into 30.5 cm x 15 cm x 5 cm concrete blocks. These blocks served as the base material for all 34 specimens that were constructed. The final thing to note about each

block was that the FRP composite was applied to the surface of the block that had been in direct contact with the steel formwork

Table 5-3. Concrete mix proportions used for Series A to E specimens

Concrete Mix Proportions	
Water/Cement Ratio	0.45
Water (kg/m^3)	217
Cement (kg/m^3)	481
Fine Aggregate (kg/m^3)	700
Coarse Aggregate (kg/m^3)	902
Max Aggregate Size (mm)	13

Surface Preparation

Each specimen received a light sandblasting prior to placement of the FRP composite. Figure 5-3A provides a visual reference for the level of sandblasting that was achieved. The objective of Series C specimens was to investigate the affect that level of surface preparation has on IR thermography results. Two samples of this series (C-5 and C-6) received additional sandblasting up to the level shown in Figure 5-3B. This will be referred to as "Heavy Blast" in the section describing Series C.

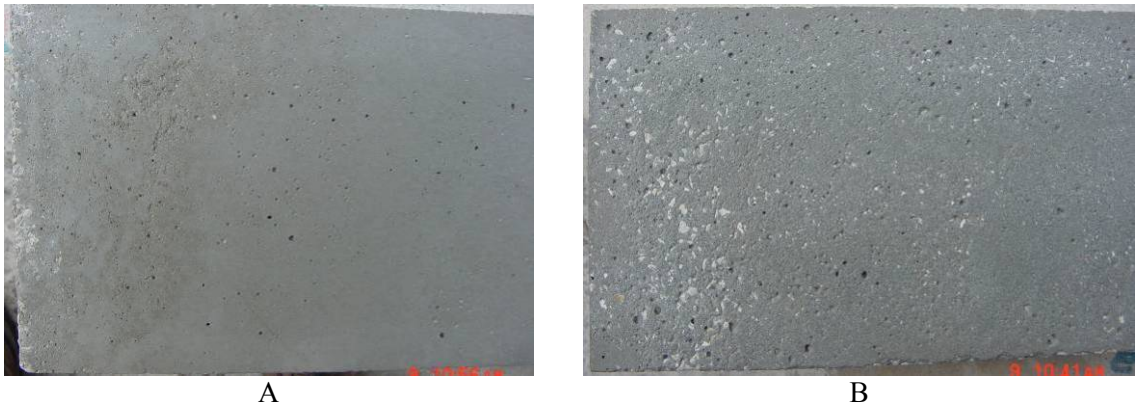

A B

Figure 5-3. Surface preparation before FRP placement. A) Light blast. B) Heavy blast.

Surface Saturation and Tack-Coat

After sandblasting, a 10 cm wide velour paint roller was used to apply a thin layer of epoxy saturant to the concrete surface. The amount of epoxy that was applied to each specimen was determined by weighing the paint tray containing the epoxy before and

after the surface was saturated. This epoxy (TYFO S) is the same epoxy that would later be used to saturate the fibers during composite construction.

The epoxy was allowed to sit on the surface for approximately one hour before a layer of thickened epoxy tack-coat was applied (TYFO TC). The same procedure that was used to apply the saturant epoxy was also used for the tack-coat (see Figure 5-4).

Figure 5-4. Application of epoxy saturant and tack-coat

There are two basic options available for saturating fibers in a wet layup application: (1) machine saturation and (2) hand saturation. Machine saturation involves a large piece of equipment that consists of an epoxy bath and two heavy rollers. The dry fabric is first passed through the epoxy bath and then pressed between the rollers in order to fully impregnate the fabric. This process also removes any excess epoxy from the composite. The gap distance between the two rollers can be controlled such that the resulting composite contains the desired amount of matrix material. The installation guidelines provided by the FRP system manufacturer (Fyfe Co. LLC 2001) include specific fiber to matrix proportions if a machine saturator is used: 1.0 lb. of fibers to 1.0 lb. of matrix for carbon-fiber systems and 1.0 lb. of fibers to 0.8 lb of matrix for glass-

fiber systems (allowable tolerance is +/- 10 %). It is common to use a machine saturator for large jobs in which hand saturation of the fibers using a roller would be impractical. The primary advantage of machine saturation is that the resulting composite is relatively uniform and contains the correct proportion of fibers and matrix.

For smaller jobs, it is very common to saturate the fibers using a hand-roller method. To give the reader some perspective on what might be considered a "large" or "small" job, it should be noted that the FRP system installed on the Chaffee Rd. bridge in 2003 was saturated by hand. Another project that the author was involved in required the application of 790 m of 15 cm wide by 4.6 m long carbon fiber strips. Again, all of the fibers were saturated by hand. Unfortunately, the hand-roller method is a very subjective procedure that may result in over/under/non-uniform saturation of the composite. The following steps are provided in the manufacturer's (Fyfe Co. LLC 2001) specification for hand saturation of fibers:

- Make a saturation bath frame out of a sheet of plywood and two-by-fours (or similar materials creating the same effect) using the two-by-fours for the sides of the bath and the plywood for the floor.
- Line the bath with plastic sheeting to create a non-permeable membrane for the epoxy.
- Pre-cut lengths and widths of fabric necessary for application.
- Place dry fabric sheets in the bath and add epoxy. Work epoxy into the fabrics using gloved hands, a trowel, paint roller, or similar.
- After the fabric has been completely saturated (both sides), remove excess epoxy by squeegying it out with the trowel or by blotting the excess resin with the next dry fabric sheet to be saturated. (NOTE: Properly saturated fabric is completely saturated with no visible dry fibers and minimal excess epoxy)

The hand-roller method was used to saturate all of the fibers in the current study. Each pre-cut 15 cm x 30.5 cm piece of dry fibers was laid on a piece of visqueen with the

surface to be bonded to the concrete facing up. TYFO S epoxy was then poured evenly over the surface. The amount of epoxy that was applied varied depending on the specimen being constructed (details for each specimen are provided below), but the 1:1 fiber to matrix ratio for carbon and 1.0:0.8 ratio for glass were chosen as the standard for a properly saturated composite. The same 10 cm velour roller (Figure 5-5B) that was used to saturate the surface and apply the tack coat was used to distribute the epoxy evenly throughout the fibers (Figure 5-5A). The total amount of epoxy that was used to saturate each layer was measured by weighing the dry fibers and then weighing the saturated composite.

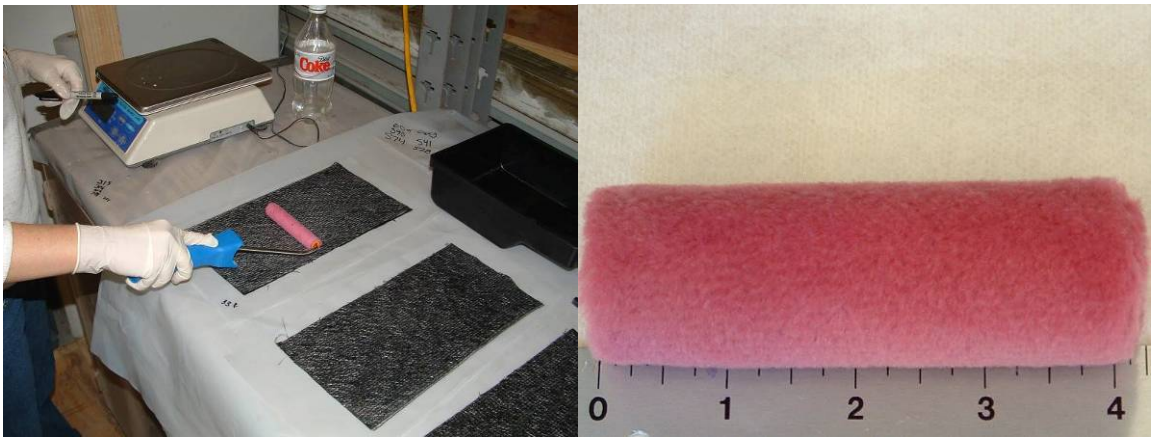

A B

Figure 5-5. Fiber saturation. A) The hand-roller method. B) 10 cm velour roller (scale shown in inches)

Application of FRP Composite to Concrete

After each layer of FRP composite was saturated on the visqueen, both the saturated fibers and the visqueen were placed on the surface of the specimen (visqueen side up). The visqueen was then peeled off leaving the saturated fibers attached to the specimen. Next, the piece of visqueen was weighed to account for any residual epoxy that did not become part of the final composite. The 10 cm velour roller was then used to smooth the composite onto the specimen and remove air bubbles. For multi-layer

systems, the process was repeated for each layer. After all of the layers were applied, the composite was allowed to cure for 24 hours. A final coat of TYFO S epoxy was then applied as a top-coat in accordance with the manufacturer's installation guidelines. The final step in the specimen preparation phase involved trimming the sharp edges where the composite extended beyond the edge of the concrete substrate. A finished specimen is provided in Figure 5-6.

Figure 5-6. Completed specimen

Construction Details for Each Series

Series A

The objective of this subset of specimens is to investigate how the following parameters affect IRT results:

- Composite Thickness
- Defect Size
- Defect Material Composition

A total of four specimens containing fabricated defects were constructed for this series. Specimens A-1, A-2, A-3, and A-4 were constructed using one, two, three, and four layers of TYFO SCH-41 carbon fiber composite, respectively. The target fiber to matrix saturation level for each layer of composite was 1:1. This level was achieved by

carefully adding epoxy and weighing the composite before and after the roller was used to saturate the fibers. The resulting weight volume fraction for layer of the composite was 0.50. Appendix C contains specific details regarding all quantities of saturant, tack-coat, composite matrix, fibers, and top-coat that was used for each specimen.

The fabricated defect configuration was the same for all four specimens. Defects were created by drilling a series of holes (3 @ 6.4 mm, 3 @ 12.7 mm, and 2 @ 19 mm) to a depth of 6.4 mm into the concrete substrate on the surface receiving the FRP composite. Several of the holes were backfilled with epoxy or insulating foam and the remaining holes were left empty. A detailed layout of the defects is provided in Figure 5-7.

An interface bubble was also implanted by inserting a small nylon machine screw (#8) into the surface of the concrete. The machine screw was cut such that it protruded 3 mm above the surface of the concrete before the FRP composite was applied. The exact size of the interface bubble was difficult to control while the composite was being rolled onto the surface of the concrete. It was also difficult to apply successive layers of composite material over the interface bubble and ensure that no air voids developed between layers. The final dimensions for each interface bubble were obtained by measuring the size on the surface of the cured composite. Two measurements were made: one parallel ($d_{\parallel}$) and one perpendicular ($d_{\perp}$) to the principle fiber direction. Results are summarized in Table 5-4.

Table 5-4. Series A details

Specimen ID	Fiber type	Surface prep	Weight vol. of fibers	Interface bubble	
				$d_{\parallel}$ (mm)	$d_{\perp}$ (mm)
A-1	Carbon	LB	0.50	51	18
A-2	Carbon	LB	0.50	57	29
A-3	Carbon	LB	0.50	57	25
A-4	Carbon	LB	0.50	51	32

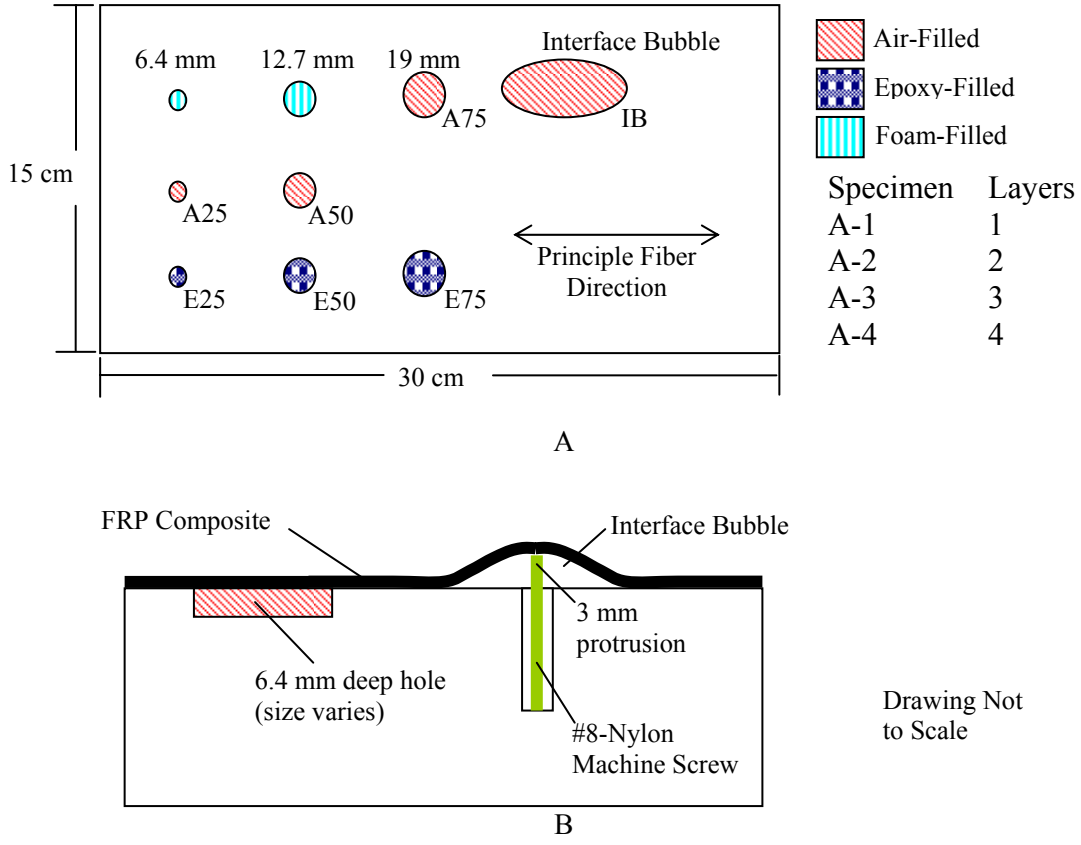

Figure 5-7. Defect configuration for Series A specimens. A) Plan view. B) Profile.

Series B

The objective of this subset of specimens was to investigate how the following parameters affect IRT results:

- Epoxy saturation levels
- Composite thickness
- Fiber type (carbon vs. glass)
- Inter-lamina defects vs. interface defects

A total of 18 specimens containing fabricated defects were constructed for this series. These 18 specimens are subdivided into three groups based on the amount of epoxy that was used to saturate the fibers: low saturation (6 specimens - designated "L"), medium saturation (6 specimens - designated "M"), and high saturation (6 specimens - designated "H"). Each of the six-specimen sub-groups contains four carbon-fiber systems (designated "C") and two glass-fiber systems (designated "G"). The final distinction to be made between each specimen of a sub-group is the number layers. The four carbon-fiber specimens each have 1, 2, 3, or 4 layers, and the two glass-fiber specimens have either 2 or 4 layers. To summarize, the specimen designated B-MC-3 is a three-layer carbon-fiber composite with medium epoxy saturation. B-LG-4 is a four-layer glass-fiber composite with low epoxy saturation.

The six specimens constructed using the low saturation level each had a fiber weight fraction (w_f) of approximately 0.67. For a carbon-fiber system, the 0.67 value represents one-half of the recommended amount of epoxy needed to saturate the fibers. For the glass-fiber system, one-half of the recommended epoxy would result in a w_f of 0.71. Attempts to saturate the glass fabric at this saturation level were unsuccessful, and it was clear that additional epoxy would be needed in order to create a composite that appeared close to saturated. The final value of w_f used for the glass-fiber composite was 0.67.

The medium saturation level was achieved using a target w_f of 0.5. This represents a properly saturated composite for the carbon-fiber systems and a slightly oversaturated composite for the glass-fiber systems.

The high saturation level specimens were constructed with a target w_f of 0.4. This w_f is obtained when the amount of epoxy used to saturate the composite exceeds the recommended level by 50%. Several trial specimens were constructed in which this excess epoxy was applied directly to the dry fibers during the saturation process. The resulting composites were too saturated and it became difficult to keep all of the epoxy on the visqueen as the fibers were being wetted-out. A more effective strategy was to first saturate the fibers to the medium saturation level and then apply the composite to the specimen. Next, additional thickened epoxy tack-coat (TYFO-TC) was applied to each layer using a roller. The amount of tack-coat applied was measured by weighing the pan and roller before and after each application. This quantity was assumed to be matrix material that was incorporated into the composite and was used in the w_f calculations.

All specimens in Series B contained at least one fabricated defect. This defect always occurred at the FRP/concrete interface and was created using the same procedure described for the interface bubble in Series A. After each system had cured, an estimate of the defect size was made by measuring the dimensions of the bubble with a ruler. For the carbon-fiber systems, each of the bubbles assumed an elliptical shape. The dimension of the ellipse in the direction of the fibers, $d_{\parallel}$, was typically larger than the dimension perpendicular to the fibers, $d_{\perp}$. For the glass-fiber systems, the shape of the interface bubble tended to be more round than elliptical.

For FRP systems containing more than 1 layer, an additional inter-lamina bubble was created by placing a #8 nylon nut beneath the top layer of composite. This nut resulted in a defect similar in size and shape to the interface bubble. Measured

dimensions for all of the fabricated defects are provided in Table 5-5. A schematic drawing of the defect configuration for this series is provided in Figure 5-8.

Table 5-5. Series B details

Specimen ID	Fiber type	Saturation level	wf	Inter-lamina bubble $d_{\parallel}$ (mm)	Inter-lamina bubble $d_{\perp}$ (mm)	Interface bubble $d_{\parallel}$ (mm)	Interface bubble $d_{\perp}$ (mm)
B-LG-2	Glass	Low	0.67	-	-	57	51
B-LG-4	Glass	Low	0.68	-	-	57	44
B-LC-1	Carbon	Low	0.67	-	-	57	19
B-LC-2	Carbon	Low	0.68	38	19	51	25
B-LC-3	Carbon	Low	0.67	51	29	57	19
B-LC-4	Carbon	Low	0.64	51	25	51	22
B-MG-2	Glass	Med	0.54	51	38	51	44
B-MG-4	Glass	Med	0.53	51	38	51	51
B-MC-1	Carbon	Med	0.52	-	-	76	25
B-MC-2	Carbon	Med	0.48	44	22	57	38
B-MC-3	Carbon	Med	0.50	51	22	57	35
B-MC-4	Carbon	Med	0.50	44	25	57	32
B-HG-2	Glass	High	0.44	-	-	57	57
B-HG-4	Glass	High	0.43	-	-	57	57
B-HC-1	Carbon	High	0.43	-	-	57	29
B-HC-2	Carbon	High	0.37	76	25	83	38
B-HC-3	Carbon	High	0.42	44	19	64	25
B-HC-4	Carbon	High	0.41	38	19	51	25

Series C

Series C contained a total of six specimens. The objective of this series was to investigate the effects of concrete surface preparation and the use of thickened epoxy tack-coat. Three different levels of surface preparation were used (two specimens for each method): none, light sandblasting, and heavy sandblasting. A visual reference for the light and heavy sandblasting was provided in Figure 5-3. For each of the surface preparation methods, one of the specimens received a layer of thickened epoxy tack-coat and the other did not. The specimen matrix for this series is summarized in Table 5-6.

Each of these specimens was constructed using one layer of carbon-fiber composite. One fabricated defected was implanted in each specimen using the interface

bubble procedure that was described above. In addition to investigating how surface preparation affects the IRT results for each defect, these specimens were also used to examine how surface preparation affects IRT results for non-defect areas.

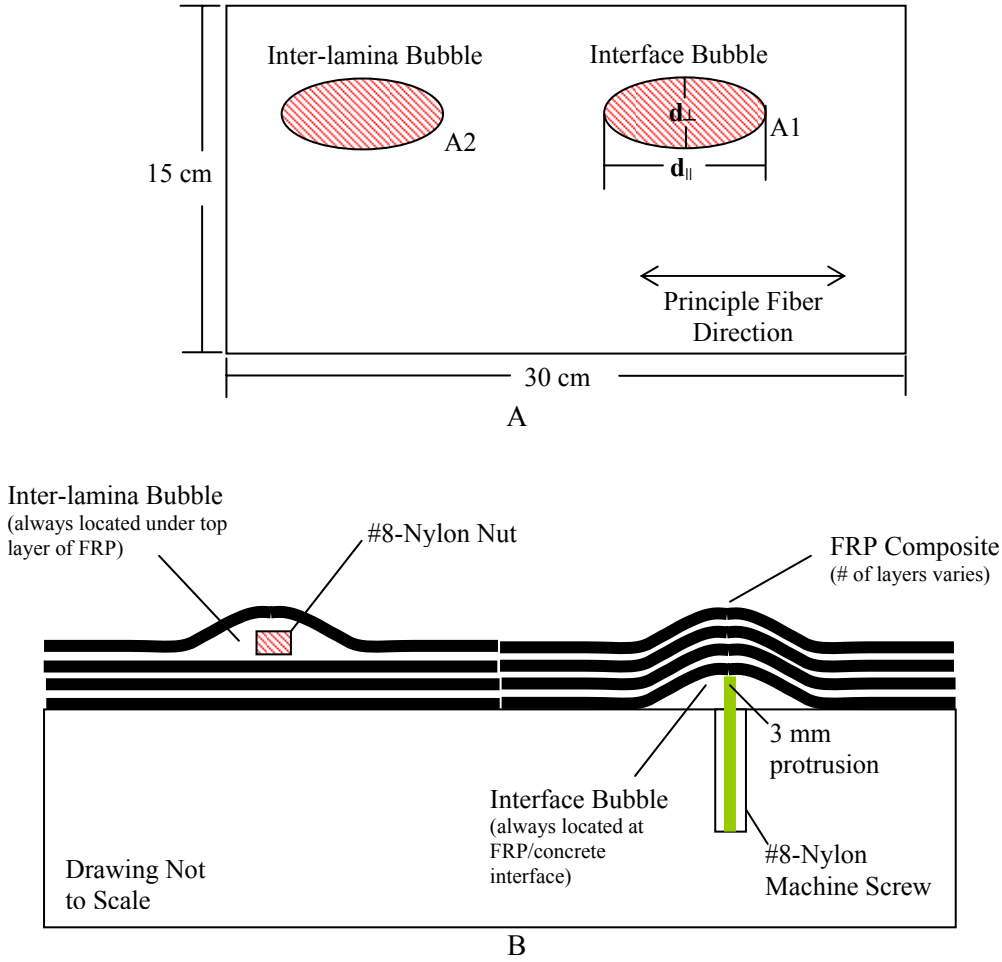

Figure 5-8. Defect configuration for Series B specimens. A) Plan view. B) Profile

Table 5-6. Series C details

Specimen ID	Surface prep	Tack-coat	w_f	Int. Bubble $d_{\parallel}$ (mm)	Int. Bubble $d_{\perp}$ (mm)
C-1	None	Yes	0.44	57	38
C-2	None	No	0.42	64	32
C-3	LB	Yes	0.45	57	32
C-4	LB	No	0.44	51	25
C-5	HB	Yes	0.46	64	32
C-6	HB	No	0.43	57	32

Series D

The objective of this series was to investigate how different fiber saturation techniques affect IRT results. Three different techniques were applied to three different specimens:

- D-1: Dry fibers were placed directly onto specimen (after tack-coat was applied). A 10 cm paint roller was dipped in epoxy and then rolled over composite until it appeared saturated.
- D-2: Dry fibers were placed on a sheet of visqueen and epoxy was pressed into the surface using a roller. Heavy pressure was applied such that all excess epoxy was removed. After the fibers were saturated, the composite was placed on the tack coat and the visqueen was peeled off.
- D-3: Similar to D-2 except that light pressure was applied with the roller and not all of the excess epoxy was removed. This resulted in a composite with more epoxy than D-2.

All specimens received a light sandblast and a layer of thickened epoxy tack-coat. Only one layer of carbon-fiber was applied to each specimen, and no fabricated defects were included. The specimen matrix for this series is summarized in Table 5-7

Table 5-7. Series D details

Specimen ID	Surface prep	Saturation method	wf
D-1	LB	Surface	0.50
D-2	LB	Heavy Roller	0.51
D-3	LB	Light Roller	0.40

Series E

The final series contained three specimens. These specimens were constructed to represent different configurations. Lap-splices are commonly encountered in the field when multiple strips of FRP are required to achieve the desired length for the composite system. The specimen labeled E-2/3/1 consists of 2 layers of carbon-fiber over the left 4

in., 3 layers of carbon-fiber over the middle 10 cm, and 1 layer of carbon-fiber over the right 7.6 cm Specimen E-2/3/2 consists of 2 layers, 3 layers, and 2 layers over the left, center and right sections, respectively. Finally, E-2/4/3 consists of 2 layers. 4 layers, and 3 layers. Table 5-8 provides a summary of the fiber w_f for each of the specimens. A detailed schematic showing the lap-splice configuration for each specimen is provided in Figure 5-9

Table 5-8. Series E details

Specimen ID	Surface prep	Fiber type	wf
E-2/3/1	LB	Carbon	0.56
E-2/3/2	LB	Carbon	0.51
E-2/4/3	LB	Carbon	0.46

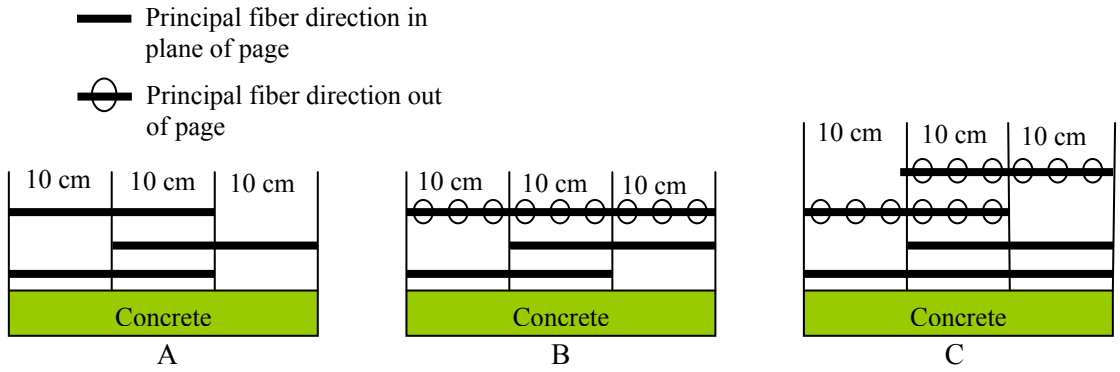

Figure 5-9. Lap-splice configuration for Series E. A) E-2/3/1. B) E-2/3/2. C) E-2/4/3

Heating Methods and Thermal Imaging

This section describes the four heating methods used in this study: flash heating, scan heating, long-pulse heating, and sinusoidal heating. Flash heating, scan heating, and long-pulse heating each involved a different geometric configuration for the heat source, specimens, and camera. The sinusoidal heating used the same configuration as the long-pulse heating.

Flash Heating

Flash heating experiments were conducted using two 3.3 kJ Godard photography flash systems. Each flash system consisted of a power pack (used to store the charge) and a lamp head (used to distribute the light energy). One of the power packs was established as the master unit and its lamp was fired with a manual trigger. The second power pack was established as a slave unit and was set to fire simultaneously with the master via a light sensor. The total pulse duration was 50 ms. A 17.8 cm diameter reflector shield was used on each lamp head.

The heat source and camera configuration used in the pulse heating experiments is provided in Figure 5-10. A number of different configurations were investigated in which the flash heads were moved further away from the specimen. This results in a larger area being heated by the flash (which is desirable in terms of efficiency). The tradeoff experienced for the increase in surface area is that the intensity of the heat deposited on the surface is reduced. The configuration shown in Figure 5-10 was ultimately chosen because it provided enough intensity to develop a signal for defects in multi-layer systems.

A typical thermal image collected for Specimen A-1 using the pulse heating configuration is provided in Figure 5-11. This image was saved one second after the flash was triggered (t = 1 sec). All future references regarding the time an image was saved will be made with respect to the end of heating. For example, an image saved at t = 0 sec refers to the thermal image collected immediately after the flash was fired. For these experiments, the image save rate was set to 5 frames per second (maximum rate for this thermal imaging system). Since there was no common trigger for the flash and IR camera, the actual time may differ by as much as 0.2 sec.

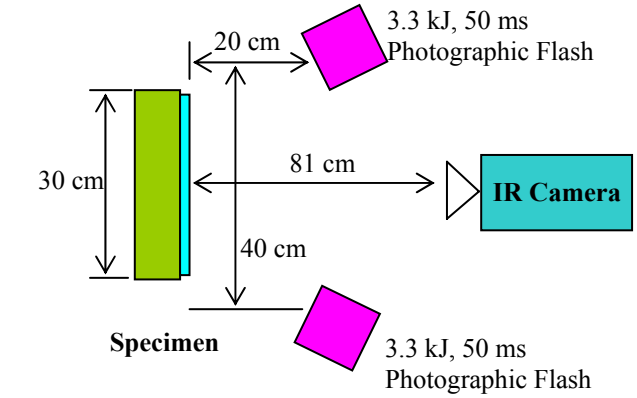

A

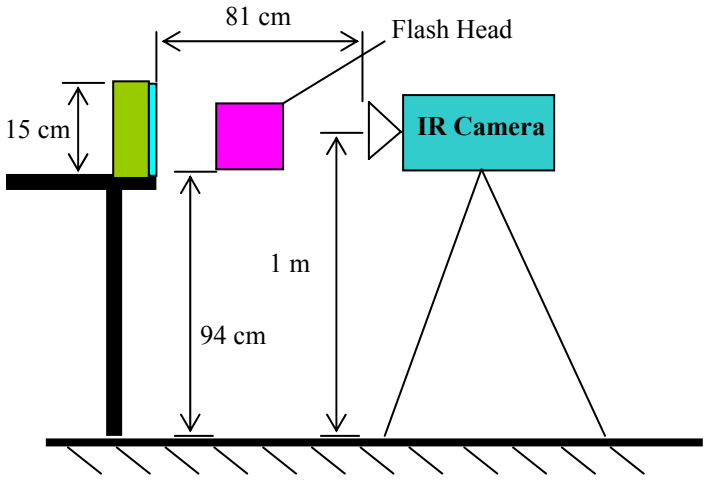

B

Figure 5-10. Heat source and camera configuration for pulse heating experiments. A) Plan view. B) Profile view.

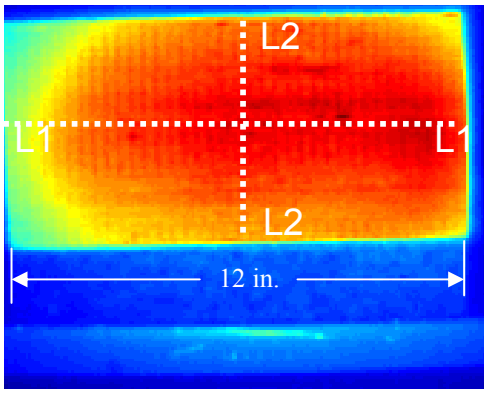

Figure 5-11. Typical thermal image collected during pulse heating experiment (Specimen A-1 @ t = 1 sec)

To characterize this heating configuration, the surface temperature profile was measured along two lines (L1 and L2 in Figure 5-11) at time values of 0, 1, 2, 3, 4, and 5 sec. The horizontal temperature profile, L1, is shown in Figure 5-12A. The values provided in this figure represent the surface temperature increase that was experienced by the specimen. The profile generated at t = 0 sec has a maximum value of 24.3°C and a mean value of 20.0°C. The profile generated at t = 1 sec has significantly lower values for the max (8.1°C) and mean (7.1°C). The subsequent profiles generated at t = 2, 3, 4, and 5 sec follow the same general trend that was established by the profile at t = 1 sec. A likely explanation for the large differences between the profiles at t = 0 and t = 1 is that the surface of the specimen can reflect a large amount of the heat energy from the flash. It is difficult to say exactly how much of the IR energy coming off of the surface at t = 0 is a result of the specimen's surface temperature or the reflected energy developed by the flash. For the purpose of comparison with other heating methods, only the surface temperature profile developed at t = 1 sec will be considered.

Figure 5-12B provides the normalized surface temperature profile for L1 at t = 1 sec. These values were obtained by dividing the temperature profile obtained at t = 1 sec and dividing by the maximum increase (ΔT_{max}). In a perfect setup, the maximum value (1) should occur in the middle of the specimen (d = 15.2 cm) and then experience little or no taper moving off in both directions towards the edges. For this case, the peak value occurs at a distance of 23 cm from the left of the specimen. A minimum value of approximately 0.5 was observed on the left hand side of the specimen and a minimum value of 0.75 was observed on the right had side. This unevenness can be attributed to a slight misalignment of the flash lamps.

Similar plots for the vertical profile, L2, are provided in Figure 5-12C and D. The peak and mean values obtained at t = 1 sec were 7.8°C and 6.9°C, respectively. The normalized temperature profile plot is relatively balanced with a peak value occurring at approximately 7 cm from the top of the specimen. The minimum values of normalized temperature increase obtained at the top and bottom were 0.8 and 0.75, respectively.

Scan Heating

One of the major limitations of the pulse heating setup is that only a small area can be heated and inspected at one time. The general concept behind scan heating is that the heat source is moved across the surface of the composite being inspected and the IR camera is positioned to record the surface temperature as the specimen cools. It is important to note that the camera position remains fixed throughout the duration of the experiment.

The heat source developed for this study is shown in Figure 5-13. Two 500 W halogen work lights were used as the energy source and were arranged as shown in the figure. It should be noted that the safety glass was removed. A thin heat shield was constructed using adhesive-backed sheet metal to help focus the energy from the lamps. The dimensions of the shield opening were 35.6 cm x 20.3 cm and the plane of the opening was offset a distance of 18.4 cm from the lamp bulb. This metal shield also helped to control reflections that were generated by the lamps.

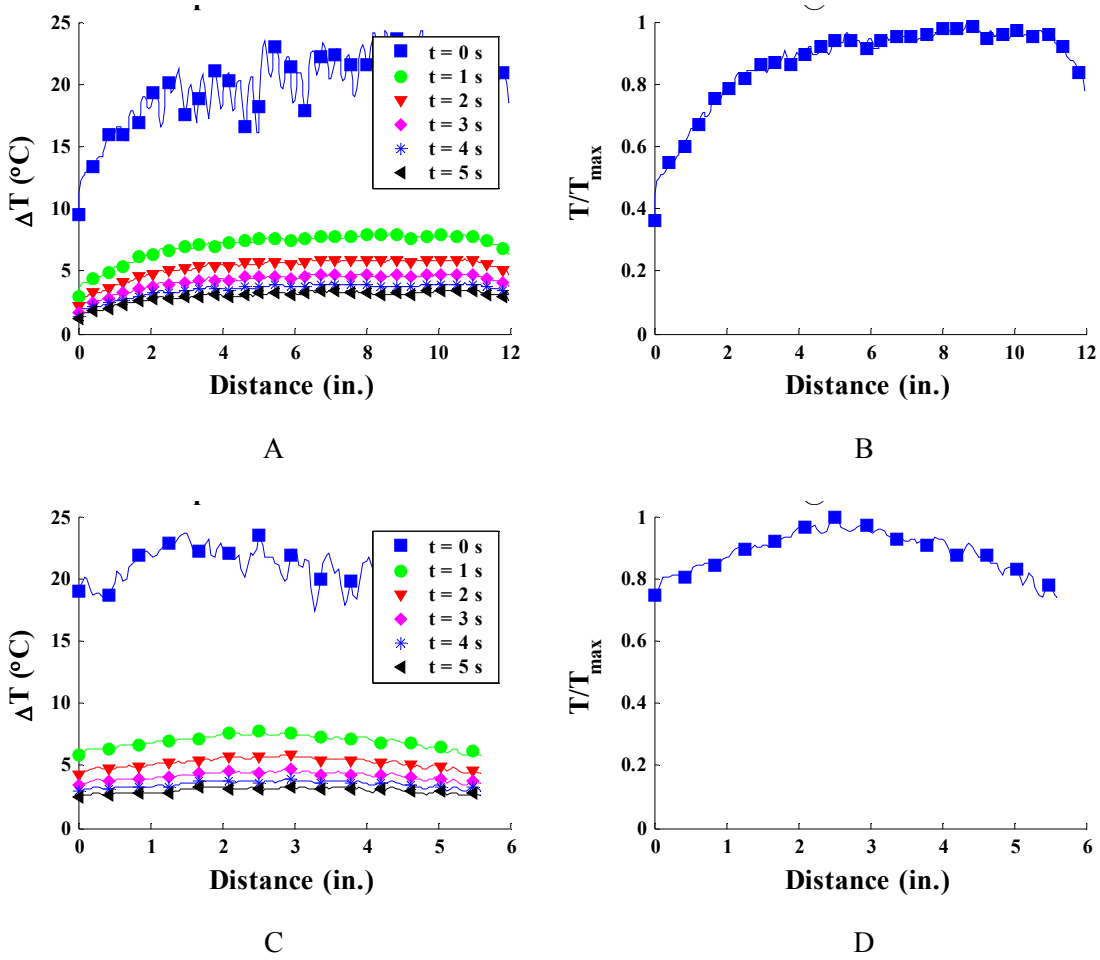

Figure 5-12. Surface temperature profile due to pulse heating. A) Horizontal profile for L1. B) L1 Normalized @ t = 1 sec. C) Vertical profile for L2. D) L2 Normalized @ t = 1 sec.

During each experiment, the heat shield opening was held at approximately 7.6 cm from the surface of the specimens. The heat source was moved from left to right at a constant rate of approximately 2.2 cm/sec. The total amount of time that any one point on a specimen was exposed to the heat source was 12 sec.

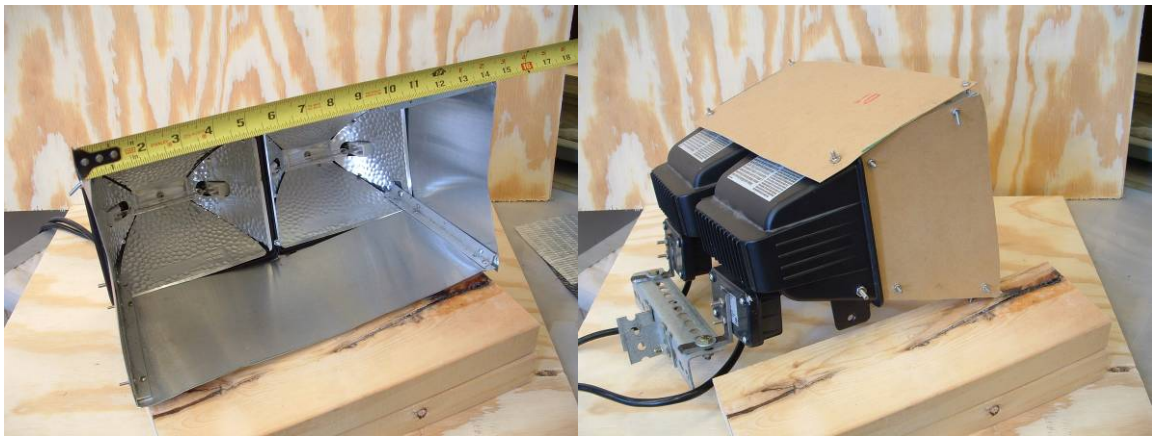

Figure 5-13. Heat source used in scan heating experiments (scale shown in inches)

A series of thermal images that were collected during a scan heating experiment is provided in Figure 5-14. The distance from the camera to the specimens was held fixed at 152 cm. This configuration allowed for the simultaneous inspection of up to 4 specimens (1858 cm^2).

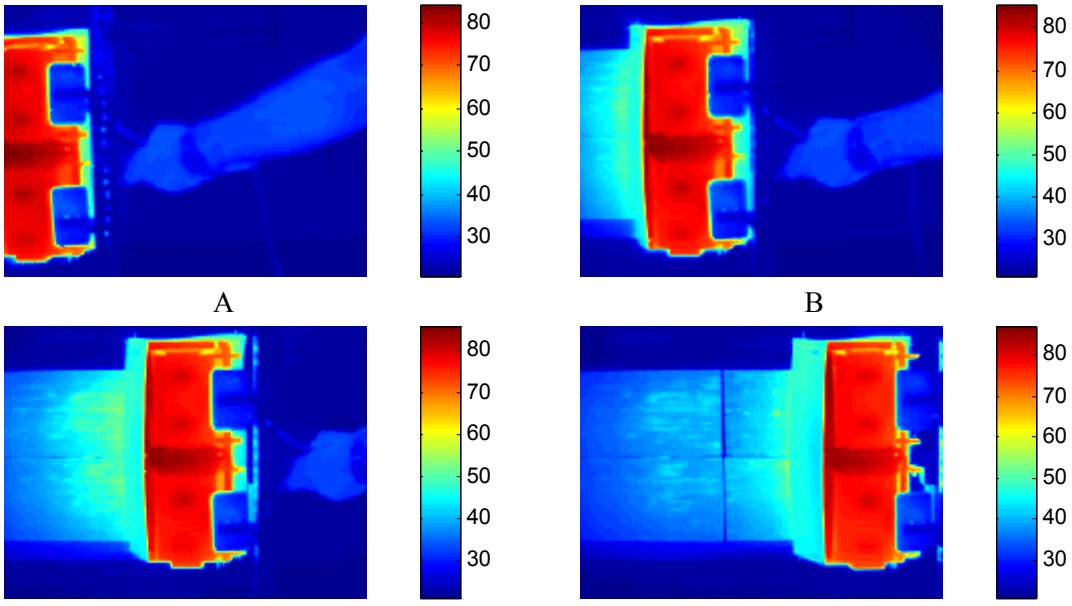

Figure 5-14. Thermal images collected during scan heating experiment. A) t = 0 sec. B) t = 5 sec. C) t = 10 sec. D) t = 15 sec

The surface temperature increase and uniformity analysis was conducted using the vertical line shown in Figure 5-15. This line passes through approximately the same

location on Specimen A-1 as line L2 shown in Figure 5-11. This image was collected one second after the edge of the heat shield passed over the line. The surface temperature increase profiles recorded at t = 0, 1, 2, 3, 4, and 5 sec are provided in Figure 5-16A. The maximum value recorded along this line at t = 1 sec was 25.0°C (mean value = 23.5°C).

The normalized temperature profile plot for t = 1 sec is provided in Figure 5-16B. The maximum value occurs near the bottom of the specimen which is located near the center of the heating apparatus. Near the top of the specimen, a normalized temperature increase of 0.85 was recorded.

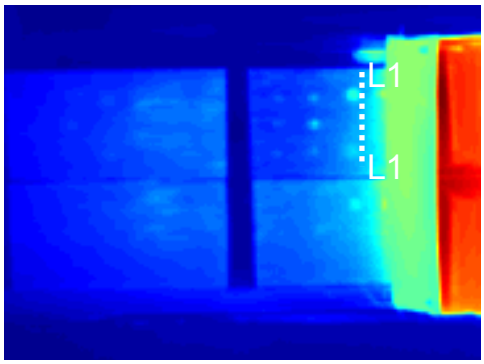

Figure 5-15. Thermal image collected during scan heating experiment for Series A (t = 1 sec for line L1)

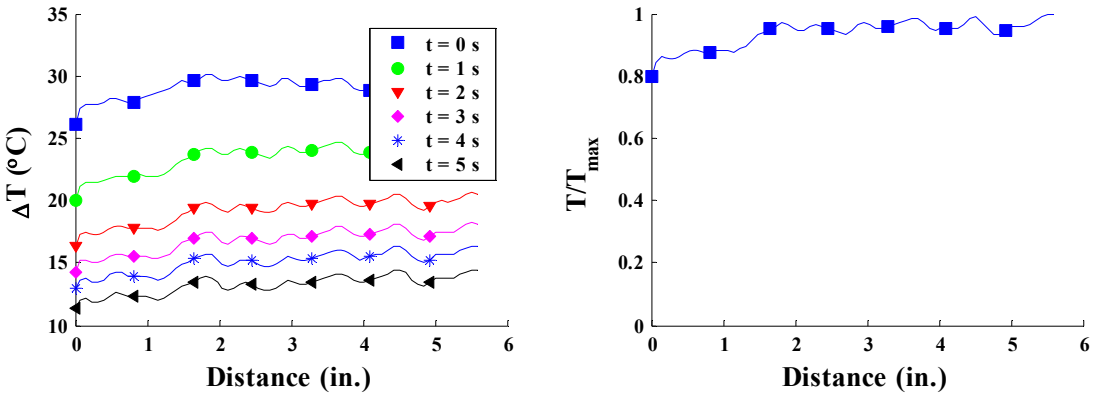

C B

Figure 5-16. Surface temperature profile for scan heating. A) Vertical Profile for L1. B) Normalized @ t = 1 sec

Long-Pulse Heating

The long-pulse heating configuration used in this study is provided in Figure 5-17. During each experiment, a total of four 500 W halogen lamps were used to provide a square heat pulse for a specified duration (30, 45, and 60 sec pulse durations were used in the preliminary investigations). The 500 W halogen lamps were similar to those used in the heat source for scan heating except that the safety glass was left in place. During each experiment, a maximum of six specimens (2787 cm^2) could be heated and observed simultaneously.

A thermal image collected for Series A at t = 1 sec following a 30 sec pulse is provided in Figure 5-18. The horizontal and vertical lines (L1 and L2) are located on Specimen A-1. The surface temperature increase profile for each of these lines is provided in Figure 5-20. Similar data for a pulse duration of 60 sec are provided in Figure 5-21.

This analysis yields similar results for the 30 and 60 sec pulse durations. The horizontal line, L1, experiences a significant decrease in surface temperature rise moving from right to left across the specimen. The minimum value of normalized surface temperature rise was 0.45 at the left edge (furthest away from the heat source). The vertical line, L2, experiences little or no taper from the top to the bottom of the specimen. It should be noted, however, that this is strictly a function of the specimen's position. The specimen positioned directly below A-1 does exhibit a temperature gradient along the vertical axis.

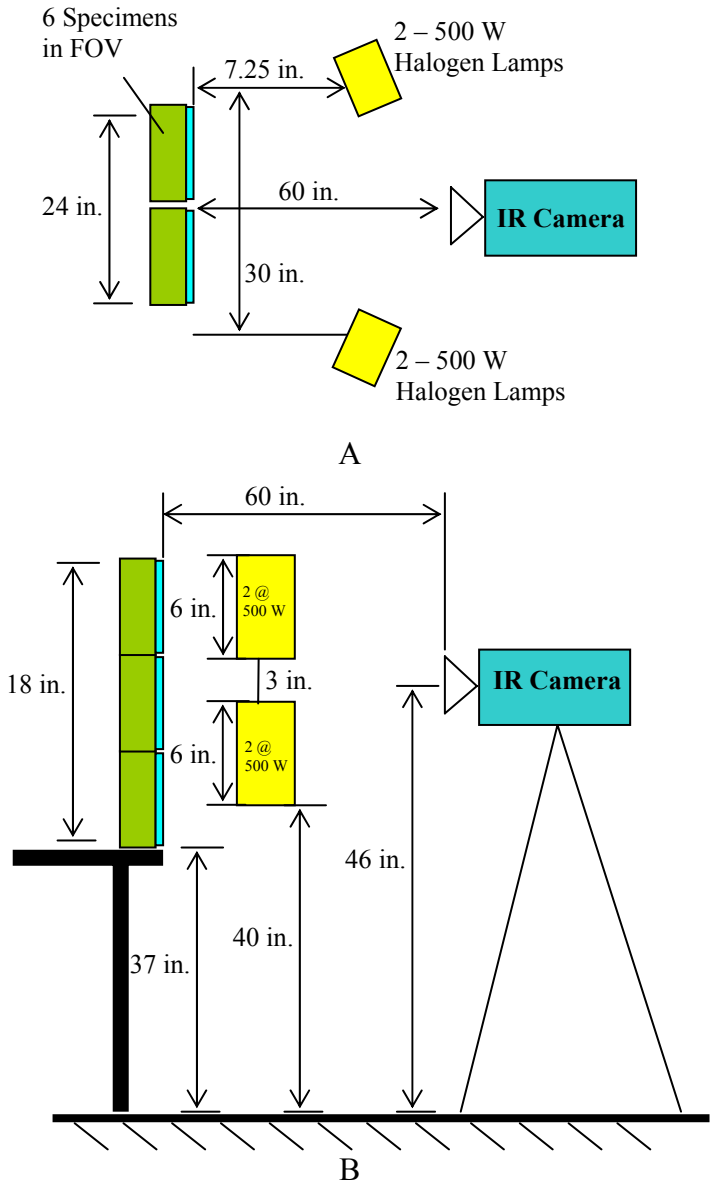

Figure 5-17. Heat source and camera configuration for long-pulse heating experiments. A) Plan view. B) Profile.

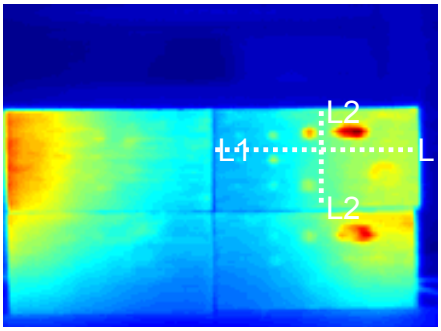

Figure 5-18. Thermal image collected at t = 1 sec during long-pulse heating experiment for Series A (30 second pulse)

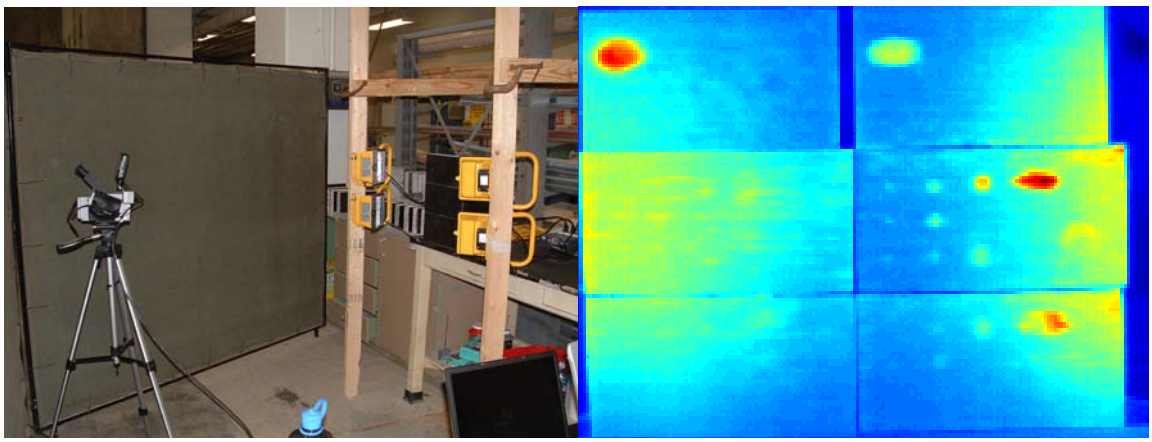

A B

Figure 5-19. Laboratory setup for long-pulse heating experiments. A) Halogen lamps and IR camera. B) Typical thermal image containing 6 specimens

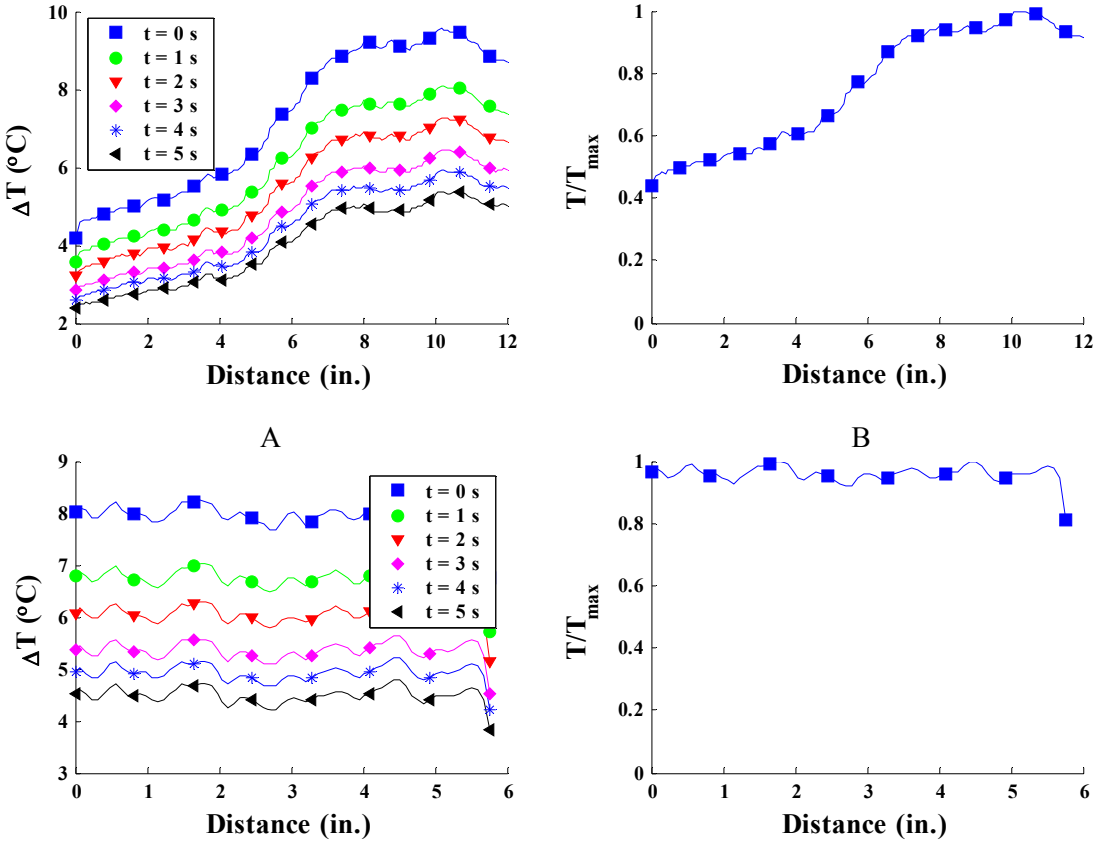

A B

C B

Figure 5-20. Surface temperature profile for long-pulse heating (30 sec pulse). . A) Horizontal profile for L1. B) L1 Normalized @ t = 1 sec. C) Vertical profile for L2. D) L2 Normalized @ t = 1 sec.

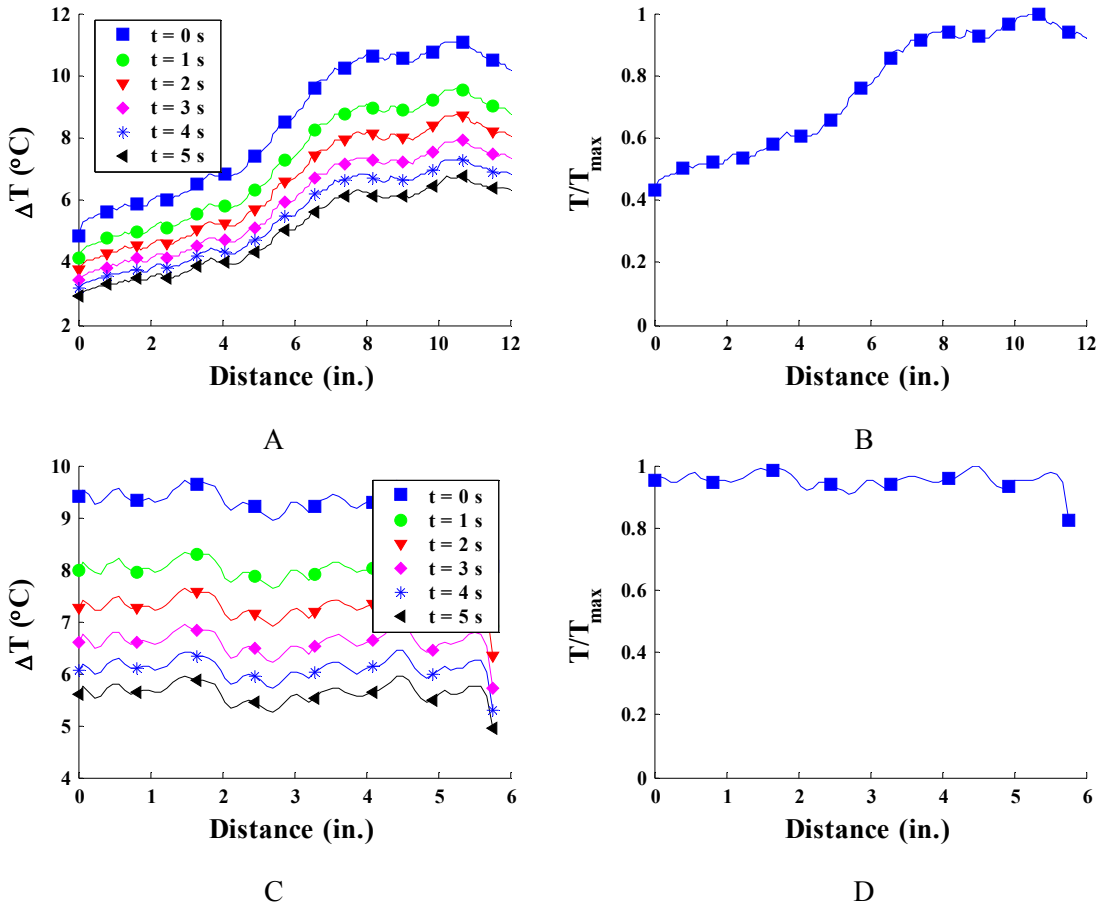

Figure 5-21. Surface temperature profile for long-pulse heating (60 sec pulse). A) Horizontal profile for L1. B) L1 Normalized @ t = 1 sec. C) Vertical profile for L2. D) L2 Normalized @ t = 1 sec.

Sinusoidal Heating

The sinusoidal heating experiments used the same heating and camera configuration that was described for the long-pulse heating. The only difference was that the shape of the heat pulse was sinusoidal in nature rather than square. The test setup for sinusoidal heating included an analog dimmer that was used to control the intensity of the four 500 W halogen lamps. The analog dimmer regulates the energy output of each lamp based on an input voltage (0 – 10 V). This voltage is supplied and manipulated by a laptop computer and an analog I/O data acquisition card. A Labview program was

created in which the user specifies the frequency and peak intensity of the desired sinusoidal pulse.

This Labview program was also used to control the image save rate on the IR camera. Since a broad range of pulse frequencies were investigated, it was important to have the ability to control how many images were saved during a given experiment. For the highest pulse frequency that was investigated, 0.2 Hz (total pulse duration = 5 sec)), an image save rate of 2 frames per second will yield a total of 10 images. The same image save rate applied the lowest frequency investigated, 0.002 Hz (total pulse duration = 5 sec), would yield over 1000 images. A block diagram representing the final test setup for sinusoidal heating is provided in Figure 5-22.

Comparison of Heating Configurations

A summary of the surface temperature profile results that were obtained for each heating method are provided in Table 5-9. These results are limited to the horizontal and vertical lines passing through the center of Specimen A-1. It should be noted that different specimens would produce different results based on the characteristics of the composite and the location of the specimen with respect to the heat source. The values for ΔT_{max} and ΔT_{mean} were computed for the profile obtained 1 sec after the heat source was removed. σ_{norm} was computed by taking the standard deviation of the normalized temperature increase profile at t = 1 sec.

The scan heating method provided the largest mean surface temperature increase (ΔT_{mean}=23.5°C). This increase was also relatively uniform with respect to the vertical axis (σ_{norm} = 4.4% perpendicular to the direction of movement by the heat source). The major downside to this heating method is that surface being inspected is not heated at the same time. The rate at which the heat source is moved will also affect the magnitude of

the temperature increase as well as the total duration of the heat pulse. A detailed investigation into these effects was not conducted.

From an efficiency standpoint, the scan heating method is also the most effective. The total area that was inspected in the original configuration (1858 cm^2) was limited by two factors: the width of the heat source (35.6 cm) and the distance from the camera to the target (152 cm). By moving the camera farther from the target, the total length of the 35.6 cm wide swath under consideration can be increased. Each of the other methods was limited by the total area the heat source was capable of illuminating. Moving the camera farther from the target does have implications for the image resolution. This parameter will be discussed further in Chapter 6 in the section on defect area analysis.

Another important observation stems from a comparison of long-pulse heating results for the 30 sec and 60 sec pulse durations. Even though the pulse duration was doubled, the mean surface temperature rise only increased from 8.1°C to 9.6°C. Another observation is that the degree of non-uniformity was the same for both pulse durations.

These results indicate that non-uniform heating is a variable that must be considered. For the long-pulse configuration, the maximum and minimum surface temperature increase across a single specimen can vary by as much as 55%. The implication of this finding is that defects located at different positions with respect to the heat source are subjected to a different intensity heat flux. A common strategy for limiting the effects of non-uniform heating is to reduce the size of the area under consideration. The heat sources described above could be reconfigured in such a way that a 15 cm x 15 cm area could be heated uniformly. A major goal of this research,

however, is to investigate techniques that will make IRT inspections practical on a large scale.

Table 5-9. Surface Temperature Increase Results for Different Heating Methods

Heating method	Total area heated (cm^2)	Horizontal profile (t=1sec)			Vertical profile (t=1sec)		
		ΔT_{max}	ΔT_{mean}	σ_{norm}	ΔT_{max}	ΔT_{mean}	σ_{norm}
Pulse	464	8.1	7.1	12.3%	7.8	6.9	6.4%
Scan	1858	NA	NA	NA	25.0	23.5	4.4%
Long-pulse (30 sec)	2787	8.1	6.1	18.9%	7.0	6.8	2.6%
Long-pulse (60 sec)	2787	9.6	7.2	18.8%	8.4	8.0	2.9%

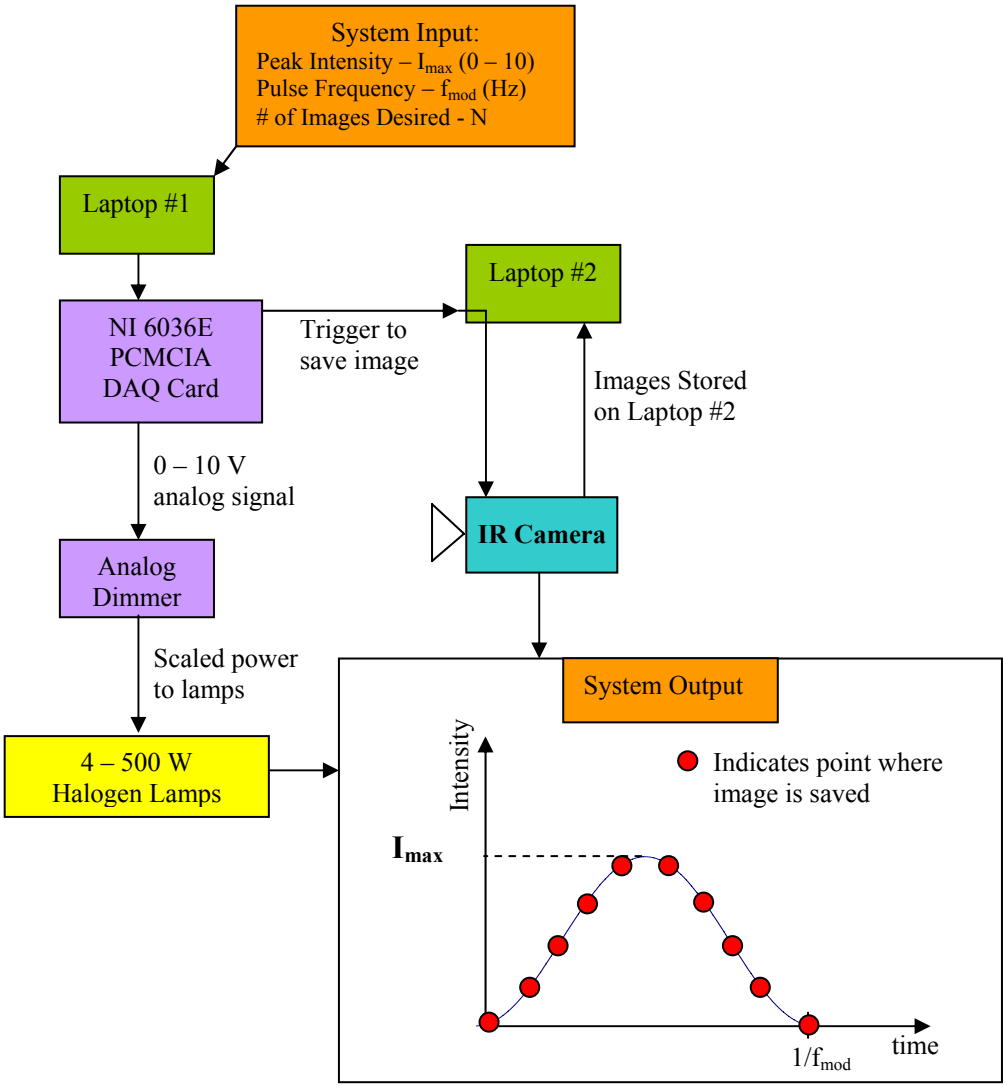

Figure 5-22. Diagram for sinusoidal heating control and data acquisition

CHAPTER 6
PHASE II: DATA COLLECTION AND ANALYSIS

Introduction

This chapter presents the data collection and processing techniques applied to Specimens A through E described in the previous chapter. The first step was to apply each of the following heating methods to the specimens in Series A:

- Flash heating
- Scan heating
- Long-pulse heating
- Sinusoidal heating

Four analysis techniques for processing thermal data were applied to the data collected for Series A:

- Pulse analysis (time domain)
- Step analysis (time domain)
- Lock-in analysis (frequency domain)
- Pulse phase analysis (frequency domain)

These analysis techniques are all currently available and have been utilized in some form in various IRT applications. None, as yet, have been adapted for use on FRP composites bonded to concrete. Consequently, the analysis techniques were adapted and calibrated using the data collected from the Series A specimens. The adjustments included modification of heating duration and data capture duration as well as filtering algorithms and defect characterization. The objective was to calibrate the techniques for varying composite thicknesses, defect sizes, and defect material compositions. Following the extensive calibration and adaptation, the techniques were compared to determine the best overall approach to use with the remainder of the specimens.

This chapter is divided into five main sections. The first two sections include results and discussion for the pulse and step analysis techniques. The third section examines the lock-in and pulse phase analysis techniques. The next section compares the different heating methods and analysis techniques that were applied to Series A. The last section covers results from Series B through E.

Pulse Thermography: Series A

During the pulse thermography experiments, a uniform heat flux was applied to the surface being inspected for a finite pulse duration, t_p. In the current study, five pulse durations were investigated: 15 ms, 12 sec, 30 sec, 45 sec, and 60 sec.

Specimen Heating and Data Collection

Three of the experimental setups described in Chapter 4 were used: flash, scan, and long-pulse.

Flash heating

The four specimens in Series A were heated with the flash system and thermal images were recorded at a rate of 5 frames/sec. Only one specimen was heated during each experiment. The first thermal image that was considered in the analysis was collected immediately after the flash was fired (t = 0 sec). Thermal images collected before the flash was fired were ignored.

Thermal images were recorded for 240 seconds while the surface of the specimen cooled. The image save rate of 5 frames per second generated an extremely large volume of data (1200 images = 720 MB). It was determined later that an image save rate of 1 frame per second was adequate. Once the start image was identified in a series of thermal images, the remaining set of images were decimated such that only 1 in 5 frames remained. This resulted in a total of 241 images for each specimen (F_s = 1 sec).

Scan heating

In the scan heating experiment, all four specimens were heated using the modified halogen lamps. The specimens were arranged such that all four could be observed at the same time. Thermal images were collected at a rate of 1 frame/sec while the heat source was being moved across the specimens. Images were saved for an additional 240 seconds while the specimens cooled.

Long-pulse heating

Data collection for these experiments was similar to scan heating in that all four specimens were heated at the same time. Three different pulse durations were investigated: 30 sec, 45 sec, and 60 sec. Thermal images were saved at a rate of 1 frame per second, and images were saved for 240 seconds while the specimens cooled.

Summary of data collection for pulse analysis

Five sets of data were collected. Each set contained a series of thermal images for each of the specimens in Series A. These five data sets are summarized in Table 6-1.

Table 6-1. Summary of data collected for pulse analysis study

Data set ID	Pulse duration (sec)	Experimental setup	Image save rate (1/sec)	Data collection begins	Number of images
P-0	0.015	Flash	1	end of heating	241
P-12	12	Scan	1	end of heating	241
P-30	30	Long-Pulse	1	end of heating	241
P-45	45	Long-Pulse	1	end of heating	241
P-60	60	Long-Pulse	1	end of heating	241

Image Preprocessing

The thermal images collected in each experiment were originally stored in a proprietary format. This file format is unique to the thermal imaging system and a stand-alone software package (Thermacam Researcher 2001) is required to view the thermal images. This software also allows the user to perform analysis functions on a series of

thermal images. These basic features include the ability to identify a single pixel of interest in a thermal image and extract the temperature vs. time response. A similar analysis can be performed by selecting an area of interest (squares or rectangles) and extracting user-specified parameters (maximum value, minimum value, average value, etc.) as a function of time. Unfortunately, this software package proved inadequate for the current study. The amount of time required to extract the necessary data to characterize a defect was prohibitive. This software package was also not capable of performing a frequency domain analysis.

These shortcomings led to the development of a new computer program using Matlab to analyze the data. The signal and image processing toolboxes that accompany Matlab make this platform well suited for a wide variety of matrix, data analysis and image processing related tasks. Matlab was also a convenient choice since the Thermacam Researcher 2001 software supports saving images in a standard Matlab format (*.mat). This new software program will be referred to as IMG_PROC in the text below.

Data pre-processing consisted of three steps:

- Convert images to Matlab format
- Generate series of thermal images for each specimen
- Spatial filtering to remove random noise

The images were converted to Matlab format using the Thermacam Researcher 2001 software. Once converted, the new image files could be opened and viewed in the IMG_PROC environment. The next step was to isolate each specimen in a series of thermal images by cropping away any extraneous pixels outside of the specimen boundary. Depending on the heating method being used, a series of thermal images may

contain data for more than one specimen. If this occurred, the cropping procedure was performed multiple times on the same series of images to generate a unique data set for each specimen. This operation provided two major advantages. First, the size of each image in a series was significantly reduced. This reduction in size leads to a reduction in the time required to process data for each specimen. Second, cropping the image ensures the entire range of the colormap is applied to the specimen of interest.

The next step in the pre-processing phase was to apply spatial filtering to each image to remove random noise. All of the thermal images that were collected in this study contain a random noise component. This random noise component was investigated and described in Chapter 5. An effective way to reduce the influence of this noise is to apply a 3x3 averaging filter to each pixel in a thermal image. The concept is illustrated in Figure 6-1A. The output value for each pixel is computed by averaging the original value of the pixel and the eight pixels that are immediately adjacent to the pixel of interest. Figure 6-1 B and C demonstrate the effects of spatial filtering on a 20x20 square pixel area. Figure 6-1 B provides a surface plot of this area before the filter was applied. Figure 6-1 C shows the same area after the filter was applied.

It is possible to increase the size of the averaging filter and obtain a smoother image. The danger in this approach, however, is that features of the image will be destroyed. A 3x3 filter was chosen since it is the smallest filter that can be applied on a two-dimensional basis.

Defect Analysis

The next step in the analysis was to extract quantitative information for the defects contained in the specimens. There are two objectives for this phase of the analysis:

- Generate a ΔT_{def} vs. time plot for each defect
- Estimate the area of the defect

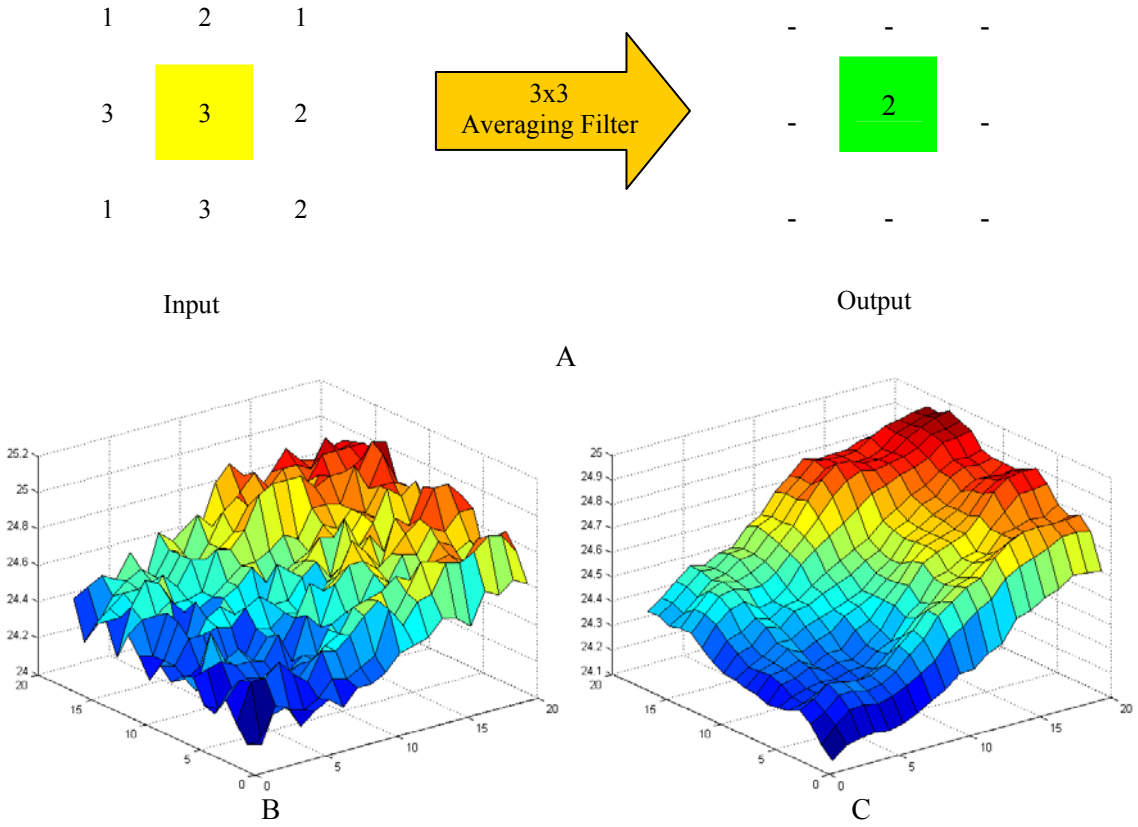

Figure 6-1. Application of 3x3 averaging filter applied to each pixel in thermal image. A) 3x3 Averaging Filter. B) Surface plot of 20x20 pixel area. C) Filtered Image (3x3).

Generating ΔT_{def} vs. time plots

ΔT_{def} is defined as the difference in temperature between the defect area and the surrounding defect-free area. The purpose of the ΔT_{def} vs. time plot is to monitor how this quantity changes as a function of time. There are two common options that were investigated for computing ΔT_{def} in a single thermal image:

- Select a single pixel above the defect and a single pixel adjacent to the defect (subtract the two values)
- Identify and average the temperature values in a small area above the defect and a small area adjacent to the defect (subtract the two values)

The first method immediately raises a very important issue: how are the points selected for the defect and defect free areas? The defect itself might occupy as many as 500 pixels in a typical thermal image. The location of the maximum value is not necessarily fixed and a point that is identified in one thermal image may not remain the maximum as time progresses. Choosing a defect-free location also introduces subjectivity. It was shown in Chapter 4 that the temperature profile along the surface varies considerably due to non-uniform heating. Furthermore, FRP composites are not homogeneous materials. Fiber patterns and matrix variation cause a certain amount of "texture" that will appear in the thermal images. The second method will reduce the influence of the variability. The areas to be averaged, however, still involve subjective choice.

In the current study, a new method for computing ΔT_{def} vs. time is proposed. The first step in the procedure is to identify an area around a defect and draw a rectangle on the thermal image. The width of the line defining the rectangle is one pixel. The only requirement for the location of this rectangle is that the sides are located a sufficient distance away from the defect. This concept is illustrated in Figure 6-2. Figure 6-2A shows an area drawn around Defect A75 on Specimen A-1. Figure 6-2C provides a surface plot of this area. The surface plot shows that the boundary of the rectangle is not influenced by the presence of the defect. Figure 6-2B shows a smaller rectangle for the same defect. The surface plot for this area (Figure 6-2D) indicates that the temperature profile of the defect does influence the temperature profile of the rectangle boundary. Based on this distinction, the area shown in Figure 6-2A is considered properly defined while the area shown in Figure 6-2B is considered poorly defined.

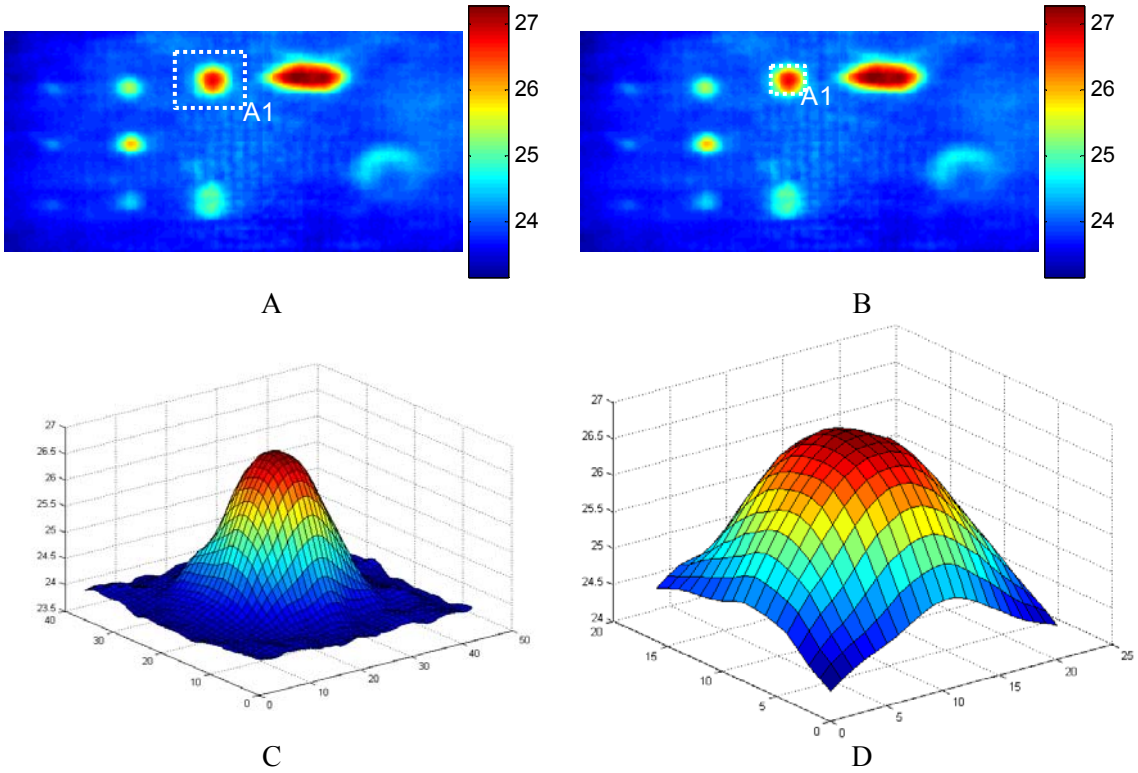

Figure 6-2. Area identification for defect analysis. A) Properly defined defect area. B) Poorly defined defect area. C) Surface plot of properly defined area. D) Surface plot of poorly defined area

Once this area was defined for each defect, the next step was to compute the parameters shown in Table 6-2 at each time step in the series of thermal images.

Table 6-2. Parameters computed for defect area at each time step

Parameter	Description
T_{max}	Maximum temperature bounded by the area
T_{per_avg}	Average temperature along the perimeter of the area
T_{per_max}	Maximum temperature on the perimeter
σ_{per}	Standard deviation of the temperature values on the perimeter

ΔT_{def} is computed at each time step using the following equation:

$$\Delta T_{def} = T_{max} - T_{per_avg} \qquad (6\text{-}1)$$

Figure 6-3A provides a plot of T_{max} and T_{per_avg} vs. time for the defect highlighted in Figure 6-2A. The corresponding ΔT_{def} vs. time plot is provided in Figure 6-3B. Once this ΔT_{def} vs. time plot has been generated, the next step is to extract additional

parameters from this plot that will be used to characterize the defect. Three parameters are shown in Figure 6-3B. ΔT_{max} is defined as the maximum value of ΔT_{def}. t_{max} is corresponding time at which the maximum value occurs. $t_{1/2}$ is the half-life of the ΔT_{def} signal and is defined as the time required for the signal to decay from ΔT_{max} to $\Delta T_{max} / 2$.

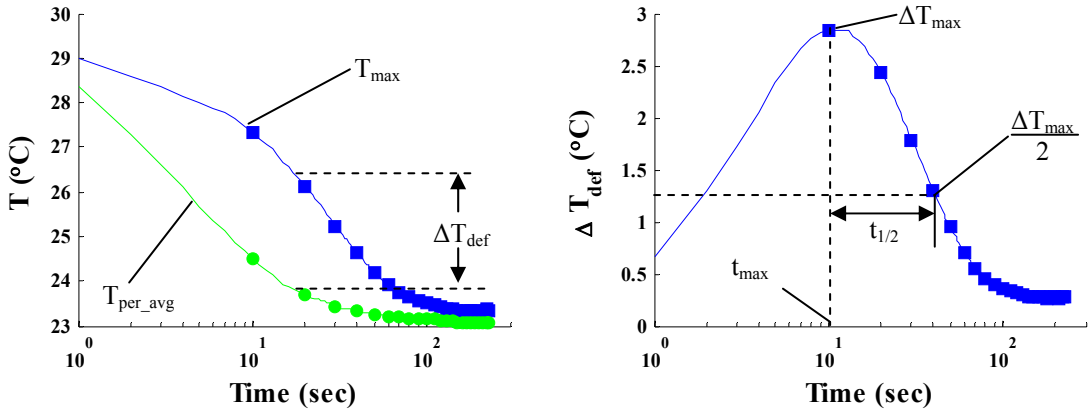

A B

Figure 6-3. Constructing ΔT_{def} vs. time plots from area parameters. A) T_{max} and T_{per_avg} vs. time. B) ΔTdef vs. time.

The example provided above describes the characterization procedure for a well-defined defect. A number of defects analyzed in this study produced markedly different ΔT_{def} vs. time plots. Figure 6-4A provides a ΔT_{def} vs. time plot for the interface bubble defect (IB) on Specimen A-3. This plot indicates a ΔT_{def} value of approximately 3.25°C at t = 0 sec. This signal slowly decays to a local minimum value of 2.5°C at t = 12 sec. At this time, the signal begins an upward trend until the absolute maximum value (ΔT_{max}) is reached at t = 40 sec. An examination of the thermal images taken at t = 0, t = 12, and t = 40 sec help to explain the ΔT_{def} vs. time plot (Figure 6-4B, C, and D respectively). The source of the signal between t = 0 and t = 12 sec is not the defect of interest that is bounded by the area IB. This false signal is a result of minor imperfections in the FRP system and non-uniform heating of the specimen. At t = 12 sec, there is a perceptible

shift in the location of the maximum value towards the center of Defect IB. At t = 40 sec, the dominant source of the ΔT_{def} signal is the defect of interest and the ΔT_{max} value has been achieved.

To characterize this ΔT_{def} vs. time plot, it is convenient to introduce a new parameter: t_b. t_b is defined as the time at which the ΔT_{def} signal reaches a local minimum and then begins an upward climb towards ΔT_{max}. In this situation, ΔT_{max} need not be greater in magnitude than the largest value of the false signal. ΔT_{max} is simply defined as the next local maximum after t_b.

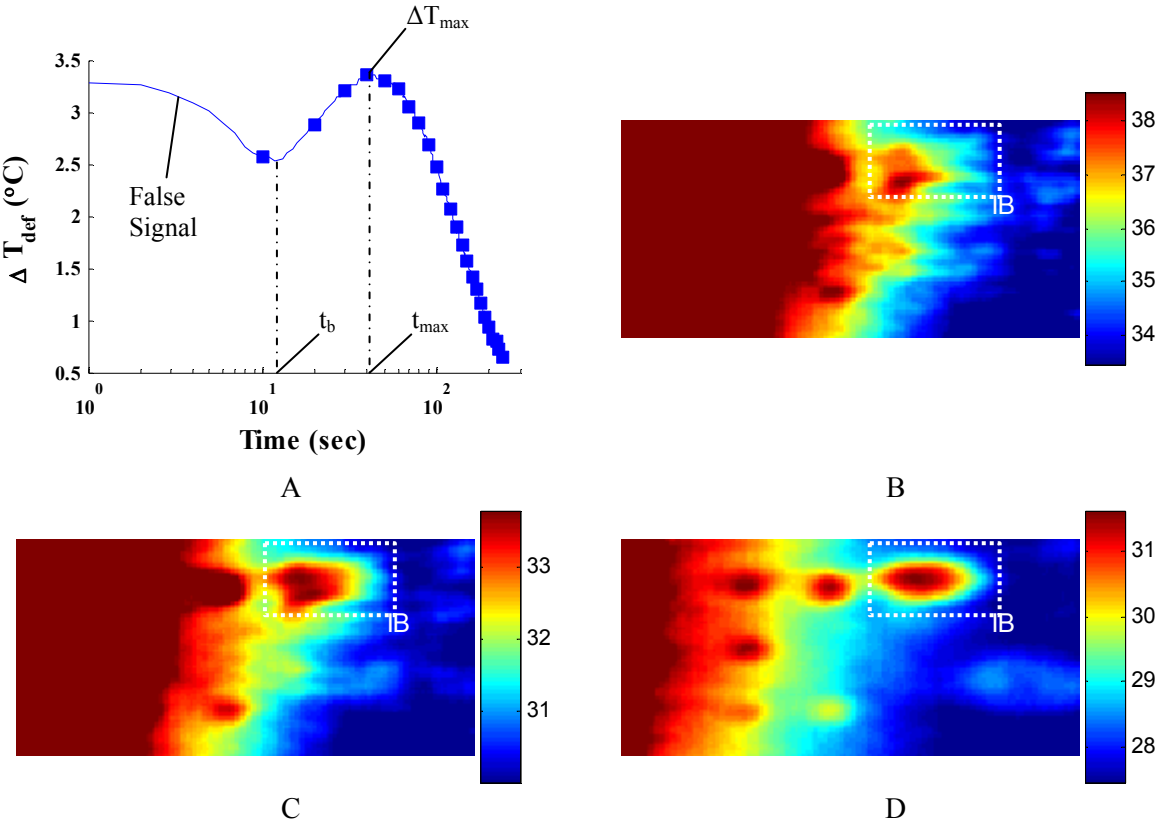

Figure 6-4. Thermal images and ΔT_{def} vs. time plot for Defect IB (Specimen A-3). A) ΔT_{def} vs. time. B) Thermal image @ t = 0 sec. C) Thermal image @ t = t_b (t = 12 sec). D) Thermal Image @ t = t_{max} (t = 40 sec)

Another distinct ΔT_{def} vs. time plot is provided in Figure 6-5. This plot was generated for Defect E75 in Specimen A-3. The plot begins with a false signal of 1.6°C

at t = 0 sec. This false signal is due to non-uniform heating. The signal decreases with a near linear slope (plotted on a log scale) up to t = 15 sec. Unlike the ΔT_{def} vs. time plot shown in Figure 6-4A, there is no distinct local minimum to indicate precisely when the defect begins to dominate the signal. The thermal image shown in Figure 6-4C clearly indicates that the defect is detected in the thermal image. However, it there is no well defined value for ΔT_{max}, t_{max}, or $t_{1/2}$.

An interesting observation was made during further investigation into the parameters that were measured for the E75 area. Recall that the maximum temperature on the perimeter of the area boundary (T_{per_max}) was also recorded at each time step. Figure 6-5B provides a plot of T_{per_max} minus T_{per_avg} (labeled "B" in the figure). The data series labeled "A" is the original ΔT_{def} vs. time plot. The interesting thing happens when series "B" is subtracted from "A" (result is labeled "C). This curve provides a very clear indication of when the defect begins to dominate the signal.

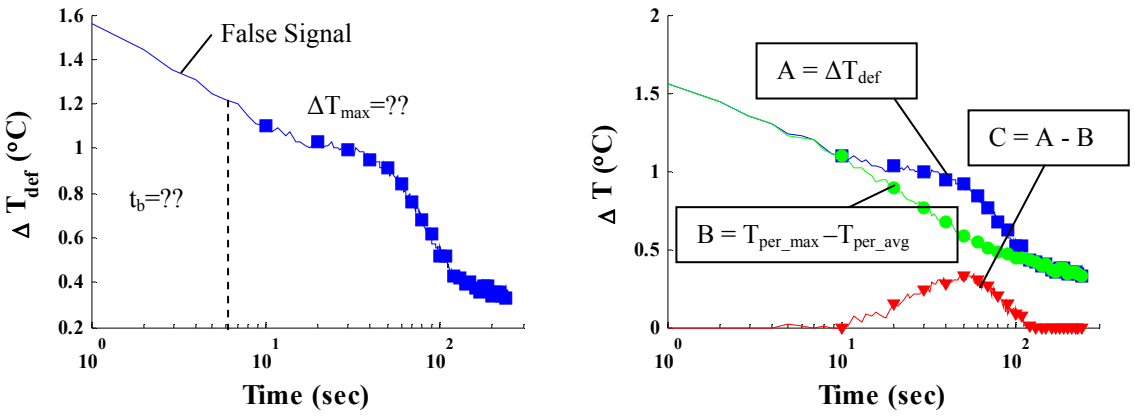

A B

Figure 6-5. Non-uniform heating and weak signals for defects. A) Plot of ΔT_{def} vs. time. B) Plot of ΔT_{def} vs. time with perimeter difference removed.

Figure 6-6 illustrates how this new curve can be used to identify t_b, t_{max}, and ΔT_{max}. t_b is simply the point at which the curve assumes a positive slope. t_{max} is chosen to be the

point at which curve "C" is maximum, and ΔT_{max} is the corresponding ΔT_{def} value measured at $t = t_{max}$ (from the original ΔT_{def} vs. time plot). Figure 6-6 also illustrates another very important quantity: ΔT_{thresh}. ΔT_{thresh} is defined as the threshold value of ΔT for curve "C". A value of 0.2°C was chosen for the current study. If the maximum value obtained by curve "C" is less than 0.2°C, the defect is considered to be undetected. Figure 6-7 provides an example of a ΔT_{def} vs. time plot for an undetected defect. This curve was generated for Defect A75 on Specimen A-3. Since the value of curve "C" never rises above the threshold value of 0.2°C, the defect is considered undetected in the ΔT_{def} vs. time plot.

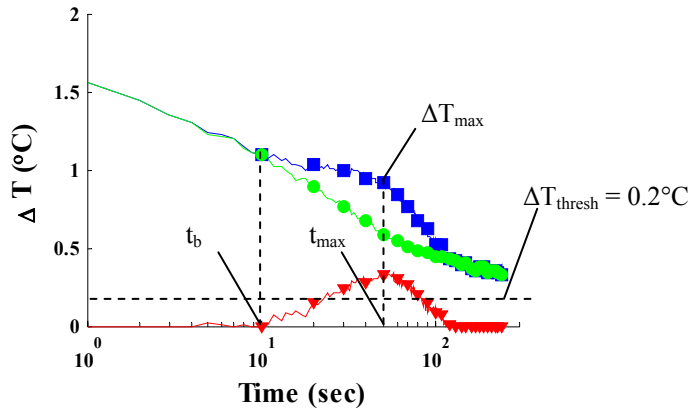

Figure 6-6. Identification of important parameters for weak signals

Another parameter that was measured for each defect was the signal to boundary noise ratio (SBR). This quantity is defined as the ratio of ΔT_{def} to the standard deviation of the temperature along the boundary of the area used to define the defect. A high SBR is indicative of a well-defined defect that is easy to detect in thermal images. Low SBR values are encountered when the computed ΔT_{def} is small or if the boundary of the area surrounding the defect lies in a region of the specimen that experienced non-uniform heating. The value of SBR that was extracted for each defect was measured at t_{max}.

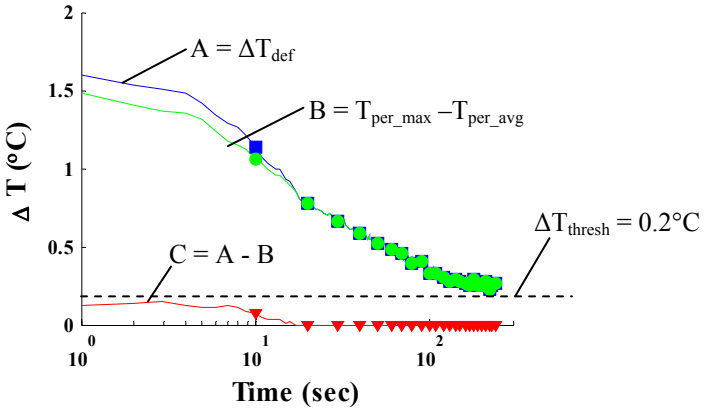

Figure 6-7. Signal for undetected defect

The only remaining parameter that was extracted for each area was ΔT_{per}. ΔT_{per} is defined as the average temperature rise experienced by the defect area boundary due to heating. This value was obtained by subtracting T_{avg_per} @ t = 240 sec from T_{avg_per} @ t = 0. Table 6-2 provides a summary of all the parameters that were extracted from each ΔT_{def} vs. time plot.

Table 6-3. Parameters extracted from ΔT_{def} vs. time plot for each defect

Parameter	Description
ΔT_{max}	Maximum defect signal strength
ΔT_{per}	Average temperature rise experienced by the perimeter of the defining area due to heating (T_{per_avg} @ t = 0 - T_{per_avg} @ t = 240)
t_b	Time at which ΔT_{def} becomes dominated by the defect of interest
t_{max}	Time at which ΔT_{max} occurs
$t_{1/2}$	Time required for ΔT_{max} to decay by a factor of two

Area computations

To determine the size of a defect from a thermal image, it is possible to draw a line around the boundary of the defect and count the number of pixels inside the boundary. This method will be referred to as the boundary trace method. The number of pixels can be converted to an area by applying a length factor that is obtained by identifying two points in a thermal image where the true separation distance is known (typically the two

bottom corners of a specimen). Matlab's 'improfile' command was then used to draw a line between these two points and the number of pixels this line passes through was counted. The known distance divided by the number of pixels can then be used as the length ratio for each pixel (measured in mm/pixel).

Figure 6-8 illustrates the boundary trace method applied to Defect A75 and Defect IB on Specimen A-1. The first step in the analysis procedure is to identify the image that was collected at t_{max} (time of maximum defect signal strength). The color scale of the image is then adjusted such that the entire scale is distributed across the range of temperature values encountered in the box used to define the defect. Next, Matlab's "roipoly" command is invoked and the user traces out the boundary of the defect in the thermal image. The results of this analysis for Defect A75 (19 mm diameter air-filled defect) are provided in Figure 6-8A. The total number of pixels bounded by the trace was 377. After applying the length factor for this image (1.1 mm/pixel or 1.2 mm^2/pixel), the area of the defect was estimated to be 4.4 cm^2. The true area for this defect was 2.8 cm^2. The same procedure applied to Defect IB on Specimen A-1 resulted in an estimated area of 10.6 cm^2. The true area for this defect was 1.2 cm^2.

Further experimentation with other defects of known size indicated that the boundary trace method consistently overestimates the size of the defect. It is conceivable that this bias error could be quantified and then considered in future computations. The fact remains, however, that selecting the boundary of the defect will always require some degree of human judgment. Maldague (2001) outlines a procedure for approximating the size of a defect by computing the magnitude of the maximum temperature gradient at each pixel in a thermal image. The underlying principle for this procedure is that the

location of maximum slope of the temperature field corresponds to the edge of the defect below the surface. This procedure will be referred to as the gradient area method in the text below.

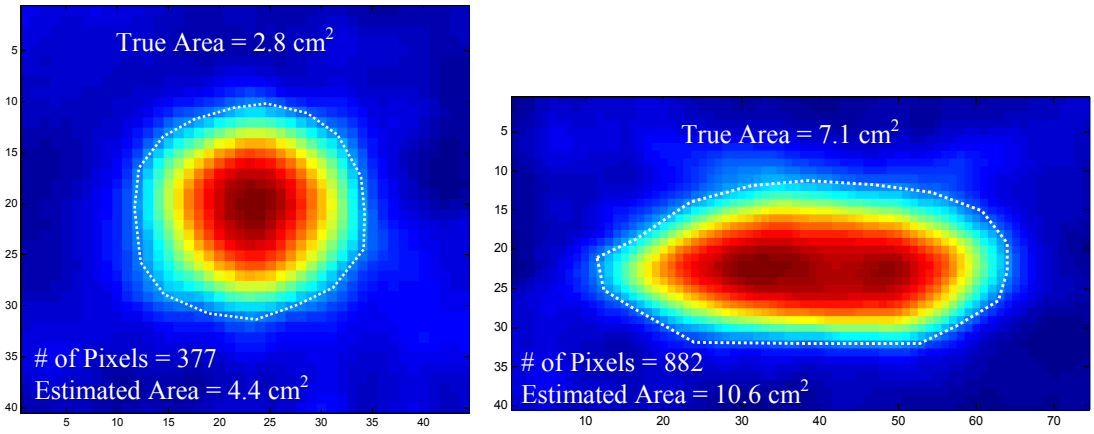

A B

Figure 6-8. Defect area computations using boundary trace method. A) Defect A75 (Specimen A-1). B) Defect IB (Specimen A-1)

A Matlab routine was developed to automate this procedure. The first step is to identify the thermal image collected at t_{max}. The next step is to compute a gradient image of the box area used to define the defect. The magnitude of the gradient for each pixel in this area is computed using Matlab's built-in gradient operator. The gradient image generated for Defect A75 (Specimen A-1) is provided in Figure 6-9A. Figure 6-9D provides a surface plot of the gradient image which illustrates the location of the defect boundary.

The next step is to locate the center of the defect by identifying the pixel with the smallest gradient near the center of the gradient image. Once the center of the defect has been identified, a line is constructed between the center and the upper left corner of the area containing the defect. The location of the maximum value along this line is determined and stored as one point on the defect's boundary. Next, a new line is constructed from the center point to the pixel on the border just below the upper left

pixel. The location of the maximum gradient is computed again and stored as the second point along the boundary of the defect. The process is repeated for a series of lines drawn from the center point to each pixel along the boundary of the area. The final defect boundary computed generated for Defect A75 is provided in Figure 6-9A. Once this boundary has been determined, the number of pixels contained within the boundary is summed. The number of pixels can then be converted into physical units by scaling with an appropriate factor.

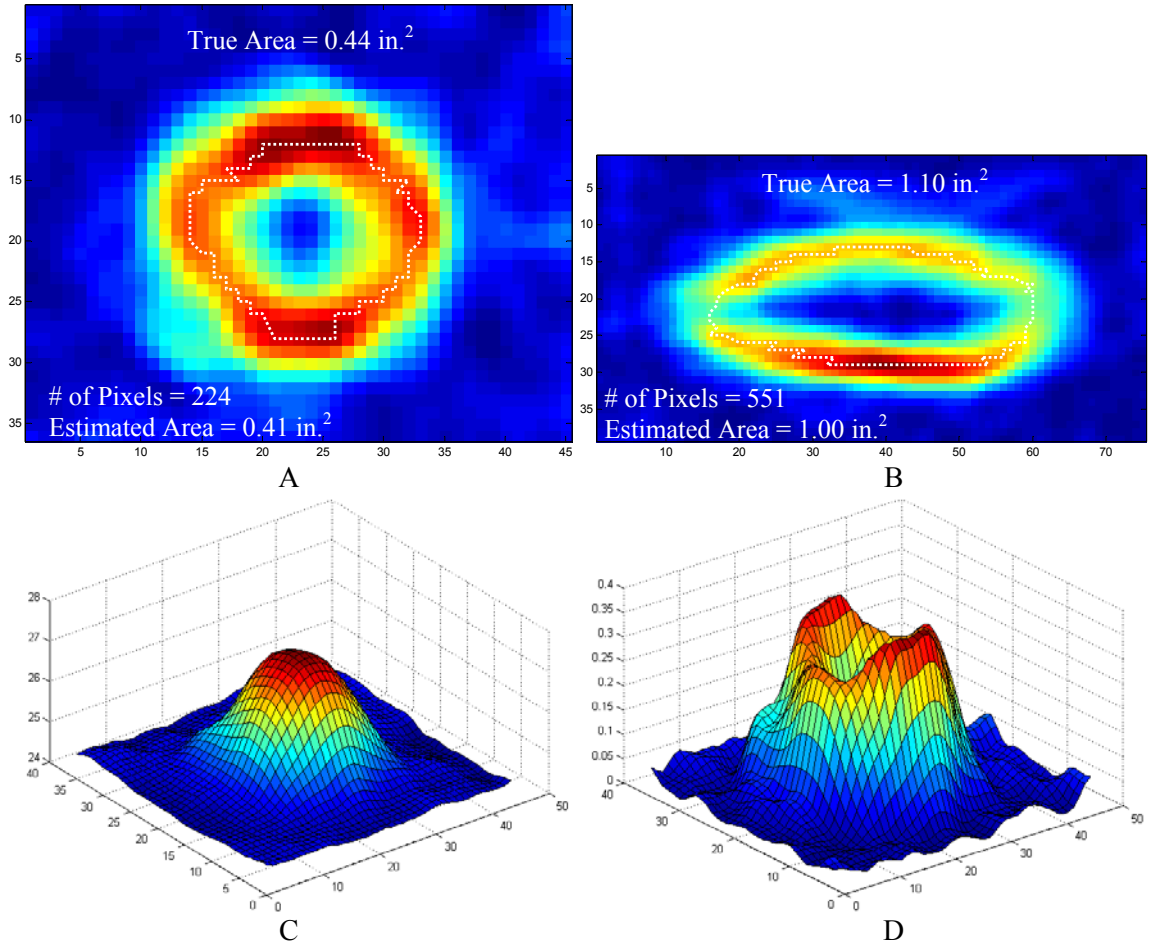

Figure 6-9. Surface temperature profile and gradient used to approximate the boundary of detected defects. A) Gradient intensity w/ defect boundary (A75). B) Gradient intensity w/ defect boundary (IB). C) Surface temperature profile (A75). D) Surface gradient profile (A75).

For Defect A75 and Defect IB on Specimen A-1, this procedure results in a better estimate for the defect area than the boundary trace method. The estimated area for Defect A75 was 2.6 cm^2 and the estimated area for Defect IB was 6.4 cm^2 (see Figure 6-9B). Unfortunately, the performance of the gradient area method is not always guaranteed. Results from the current study indicate several factors that can reduce accuracy in area computations using the gradient area method:

- Weak signal for the defect (low SBR value)
- High temperature gradient due to non-uniform heating
- Insufficient pixel resolution for small defects

An example of a defect which generated a weak signal is provided in Figure 6-10. This thermal image was collected for Defect A75 in Specimen A-3. The corresponding gradient image (shown in Figure 6-10B) does not provide a well-defined defect boundary. Oddly enough, the estimated area for this defect was 3.3 cm^2 which is within 14% of the actual value (2.8 cm^2). Based on observation of the gradient image, however, this estimate does not appear to be meaningful.

The coefficient of variation (COV) of the radius values generated by the gradient area method is a useful quantity for assessing the quality of the defect boundary. COV is defined as the standard deviation of a series of numbers divided by the mean value. When the gradient area method was applied using this center point, a total of 152 radius values were obtained. The apparent center point of the defect in Figure 6-10B is labeled "o". For the case shown in Figure 6-10B, the COV for these values was 0.54. The COV for the defect shown in Figure 6-9A, a well-defined defect, was 0.10.

In an ideal case, the COV for a circular defect should be zero. For an elliptical defect, however, there will always be variation in the computed radius values. The

magnitude of the COV will be dependant on the ratio of the primary axis dimensions of the ellipse. Figure 6-11 provides a graph of COV values plotted against the ratio of the radii of an ellipse. These COV values represent an ideal case for a perfectly defined boundary. This plot can be used to assess the quality of a defect boundary generated for an elliptical defect. Consider the defect boundary that is shown in Figure 6-9 (Defect IB in Specimen A-1). The approximate ratio of the principal axis dimensions for this defect is 0.35. This corresponds to an inherent COV of 0.35 on the graph in Figure 6-11. The computed COV for this defect was 0.33. This example illustrates that the absolute magnitude of COV should not be used to assess the quality of a computed defect boundary. Instead of the absolute magnitude, the difference between the computed COV and the inherent COV for the defect under consideration should be used.

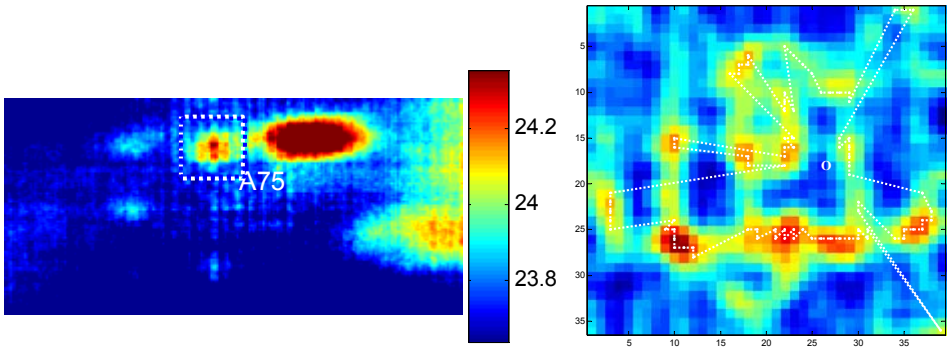

A B

Figure 6-10. Reduced accuracy in area computations due to a weak signal. A) Thermal image for weak signal. B) Gradient intensity.

The second source of reduced accuracy in area computations, non-uniform heating, is illustrated in Figure 6-12. The thermal image highlights the temperature gradient that develops across the box which was drawn around the defect. This thermal gradient is also apparent in the gradient image provided in Figure 6-12B. As a result, the defect boundary that was generated using the gradient area method is skewed to one side. The COV computed for the radius values was 0.25.

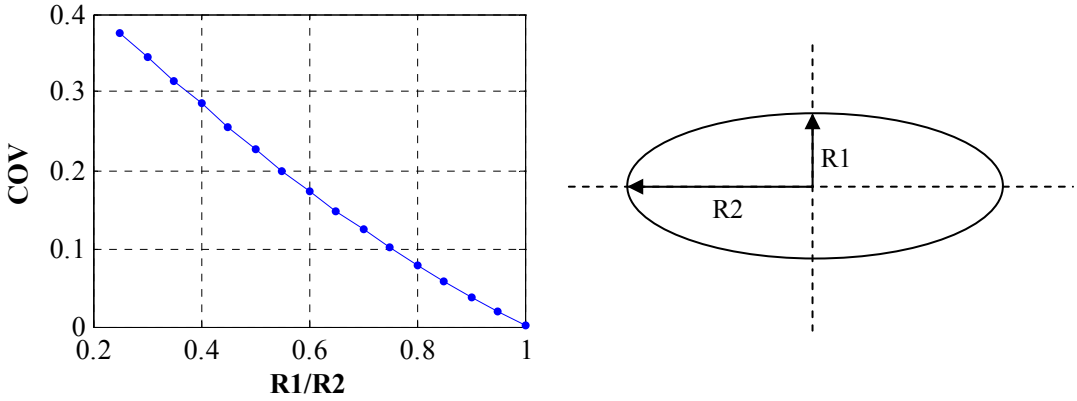

Figure 6-11. Coefficient of variation for ellipse radii (computed with NP = 250)

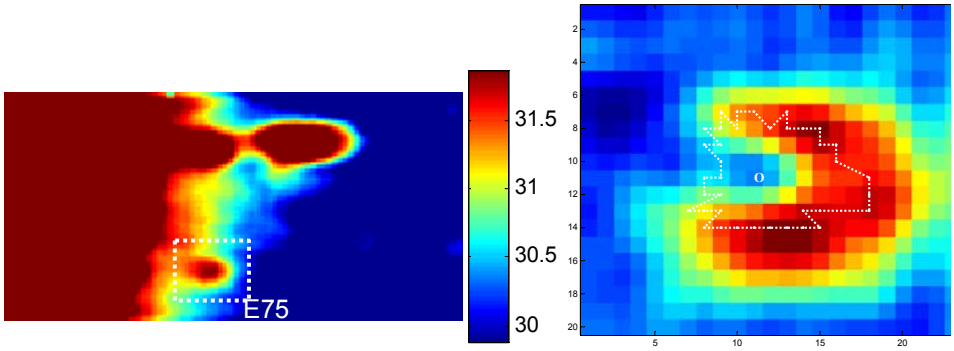

A B

Figure 6-12. Reduced accuracy in area computations due to non-uniform heating. A) Thermal image for non-uniform heating. B) Gradient intensity.

The final source of reduced accuracy encountered in the current study is illustrated in Figure 6-13. The thermal image shown in Figure 6-13A highlights Defect A75 on Specimen A-1. This thermal image was collected using the long-pulse heating setup in which the camera was a distance of 152 cm from the surface of the specimen. For this camera distance, the size of one pixel in the thermal image was determined to be 2 mm. Under these conditions, the entire diameter of Defect A75 (6.4 mm) is represented by just over three pixels. When the gradient image is generated at t_{max} for this defect, there are not enough pixels available for a well defined center point to develop. The resulting defect boundary is then based on a center point that often lies on the boundary edge. This

leads to a very high COV for the computed radii. A COV of 0.98 was computed for the defect boundary shown in Figure 6-13B.

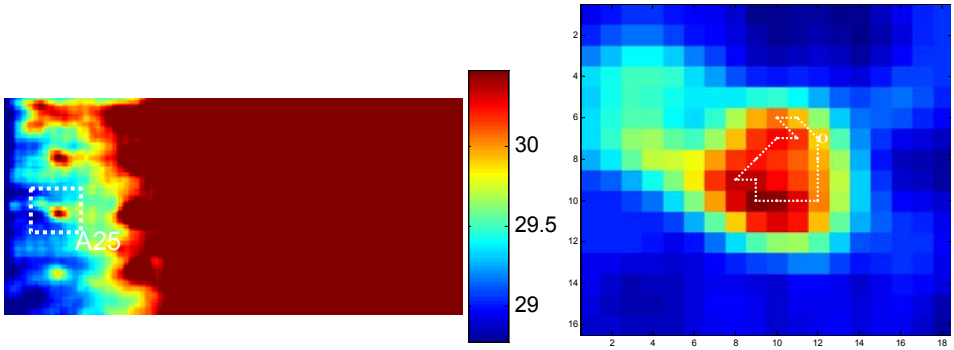

A B

Figure 6-13. Reduced accuracy in area computations due to low image resolution. A) Thermal image for small defect. B) Gradient intensity.

Proposed Method for Characterizing Detectability

This section outlines a proposed method for characterizing defect detectability. The first distinction that will be made is based on the shape of the ΔT_{def} vs. time plot. There were four basic shapes encountered during the IRT inspections of the Series A specimens. Each defect in these specimens will be classified Level I, Level II, Level III, or Level IV based on the shape of its ΔT_{def} vs. time plot. Level I defects assume a positive slope for $t > 0$ and achieve a single maximum value at $t = t_{max}$. Level II curves begin with a negative slope and reach a local minimum at $t = t_b$. After reaching the local minimum, the curve assumes a positive slope for $t > t_b$ until a distinct local maximum is reached at $t = t_{max}$. Level III curves begin with a negative slope and never assume a positive slope. There is, however, a distinct t_b that is recognizable when the difference in temperature on the perimeter of the defect's defining area is subtracted from the ΔT_{def} vs. time plot. This can also be recognized as an inflection point in the ΔT_{def} vs. time plot. The final classification, Level IV, is intended to describe defects that were not detected. A graphical depiction of each classification is provided in Figure 6-14.

A second distinction is made based on the COV of the computed radii of the defect using the gradient area method. A new quantity ΔCOV is introduced to describe the difference between the computed COV for the defect and the inherent COV for the shape of the defect. For circular defects, the computed COV and ΔCOV are equal since the inherent COV for a circle is zero. The inherent COV for an elliptical defect is obtained from the graph provided in Figure 6-11. The first category, A, is intended for well-defined defects whose ΔCOV values are less than 0.21. The second category, B, describes defects that are moderately defined by the gradient image and have ΔCOV values ranging between 0.21 and 0.4. The final category, C, is for poorly defined defects whose ΔCOV values are between 0.41 and 1.0. These categories are summarized in Table 6-4.

This classification system provides 12 unique categories to describe general defect detectability. Detectability is influenced by a number of factors: defect size, defect composition, defect depth below the surface, material properties of the composite, and the heating method employed during the inspection. This classification system will make it possible to discuss detectability from a broader perspective. For example, suppose that Defect E75 on Specimen A-3 was classified as Level III-C using the pulse heating method. During the step-heating method with a 60 sec pulse duration, however, the same defect was classified as a Level II-B. This would represent an improvement on the detectability scale. By repeating this process for all of the defects implanted in the Series A specimens (28 defects inspected using 5 heating methods = 140 observations), it will be possible to assess detectability for each heating method.

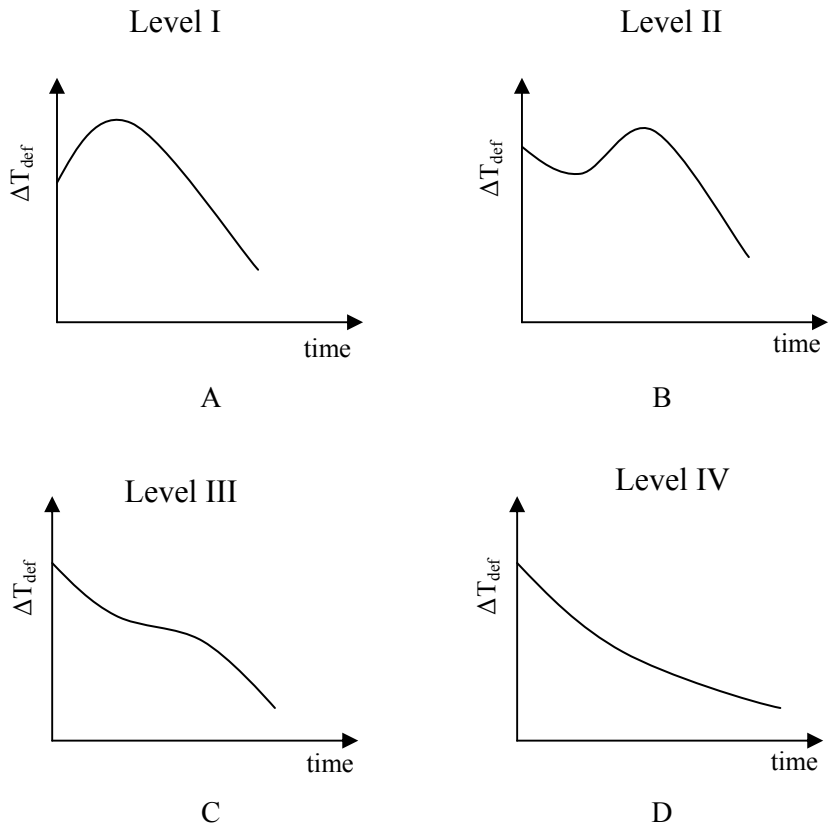

Figure 6-14. Detectability classification based on ΔT_{def} vs. time plot

Table 6-4. Detectability classification based on ΔCOV of computed radii

ΔCOV	Classification
0 – 0.20	A
0.21 – 0.40	B
0.41 – 1.0	C

Experimental Results: Flash Heating (Series A)

The following defects were considered in this analysis:

Air-filled

- Interface Bubble (IB)
- 19 mm diameter (A75)
- 12.7 mm diameter (A50)
- 6.4 mm diameter(A25)

Epoxy-filled

- 19 mm diameter(E75)
- 12.7 mm diameter(E50)
- 6.4 mm diameter(E25)

A ΔT_{def} vs. time plot was constructed for each of the defects and the important parameters identified above were extracted from each curve. The following sections contain specific results for each specimen.

Specimen A-1

Figure 6-15A provides a thermal image collected at t = 12 sec for Specimen A-1. The four air-filled defects are identified in this figure with boxes and the color scale for the thermal image is set to span the entire range of temperatures in the image. Figure 6-15B identifies the epoxy-filled defects. The color scale in this image has been set to span only the range of temperatures encountered in the box drawn around Defect E75 (19 mm diameter epoxy-filled).

All four of the air-filled defects were detected (Level I or Level II according to the classification system described in the previous section). The largest ΔT_{def} was obtained for the interface bubble (IB). The ΔT_{max} value for IB was 3.3°C and was recorded at t = 12 sec. The half-life for Defect IB was 38 sec. Defect A75 had a slightly lower ΔT_{max} (2.8°C) than IB. This value was also reached in a shorter amount of time after the heat was removed (t_{max} = 10 sec). The half-life of Defect A75 (28 sec) was also less than IB. Results for defects A50 and A25 are summarized in Table 6-5.

The three epoxy-filled defects were also detected. The ΔT_{max} value recorded for Defect E75 was 1.2°C. The corresponding t_{max} and $t_{1/2}$ for this defect were 14 sec and 47 sec, respectively. Defects E50 and E25 displayed a similar trend to that observed for the air-filled defects: as the area of the defect decreased, ΔT_{max}, t_{max} and $t_{1/2}$ also decreased.

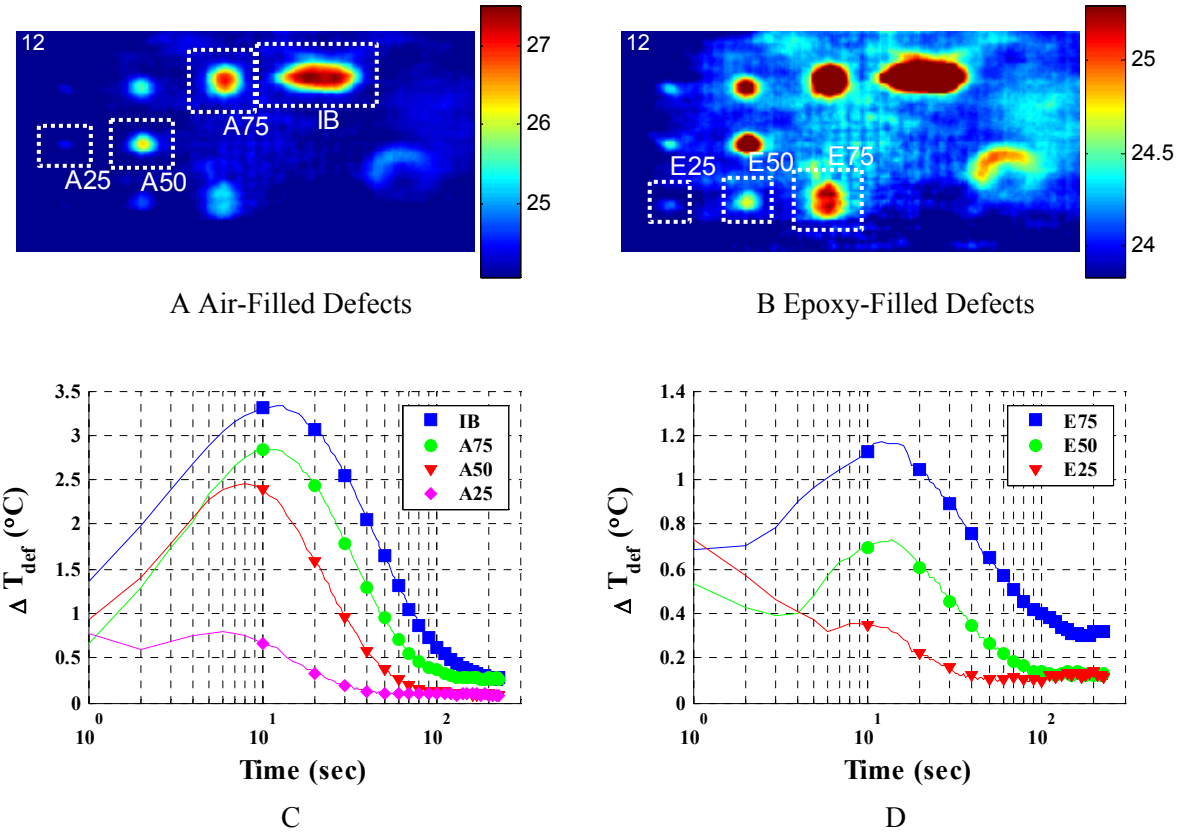

Figure 6-15. Flash heating results for Specimen A-1. A) Thermal image scaled for air-filled defects (t = 12 sec). B) Thermal image scaled for epoxy-filled defects (t = 12 sec). C) ΔT_{def} vs. time plot for air-filled defects. D) ΔT_{def} vs. time plot for epoxy-filled defects.

Table 6-5. Flash heating results for Specimen A-1

Defect	Defect Mat.	ΔT_{per} (°C)	ΔT_{max} (°C)	t_b (sec)	t_{max} (sec)	$t_{1/2}$ (sec)	SBR
IB	Air	7.1	3.3	0	12	38	40.9
A75	Air	7.0	2.8	1	10	28	33.5
A50	Air	7.0	2.5	0	8	18	23.3
A25	Air	5.8	0.8	2	6	12	3.5
E75	Epoxy	6.7	1.2	1	12	47	6.6
E50	Epoxy	6.4	0.7	3	14	25	6.2
E25	Epoxy	5.3	0.4	6	5	20	1.9

Area computations were performed for each defect following the procedure that was previously outlined and results are summarized in Table 6-6. The column labeled "Actual diameter" provides the true average diameter of the defect. For Defect IB, this was based on two length measurements: one in the direction of the fibers and one

perpendicular to the fibers. The column labeled "Actual Size" provides the true area of the defect based on the diameter measurements. The column labeled "Image Diameter" provides the average diameter computed for the defect using the gradient area method. For the camera configuration used in the pulse heating experiments, the length ratio for each pixel was 1.1 mm/pixel. For the circular shaped air-filled defects (A75, A50, and A25), the average diameter computed using the gradient area method was within the distance represented by 1 pixel of the true diameter.

The COV value computed for each of these defects varied considerably. The gradient images that were generated for defects A75, A25, E75 and E75 are provided in Figure 6-16. These four defects all fall within a different general detectability category based on the COV for the computed radii. The COV computed for Defect A75 was 0.10 (Category A) and the COV for Defect A25 was 0.28 (Category B). This difference in COV would indicate that the boundary generated for A75 was more consistent than the boundary determined for A25. This is not necessarily supported by visual inspection of the gradient images. The higher COV for Defect A25 can be attributed to a slight misalignment of the defect's center point. Defect E75 had a COV of 0.20 (technically a Category A). The largest source of variation in the defect's boundary occurs on the right side of the gradient image. This is likely due to a combination of weak signal and other imperfections in the composite above the defect. The gradient image generated for Defect E25 is provided in Figure 6-16D. This defect is poorly defined and the computed radius has a high COV of 0.79 (Category C).

These results demonstrate that COV can provide important insight into how well a defect's boundary has been defined by the gradient area method. It must be noted,

however, that a visual inspection of the generated defect boundary is still required when interpreting the results.

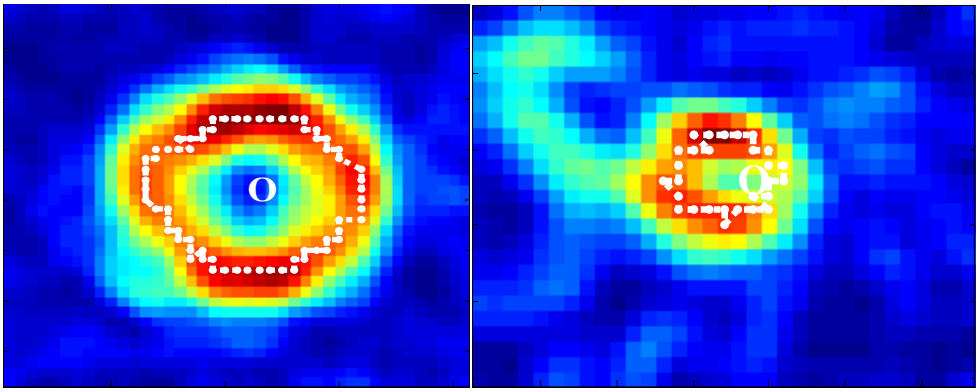

A A75: COV = 0.10 B A25: COV = 0.28

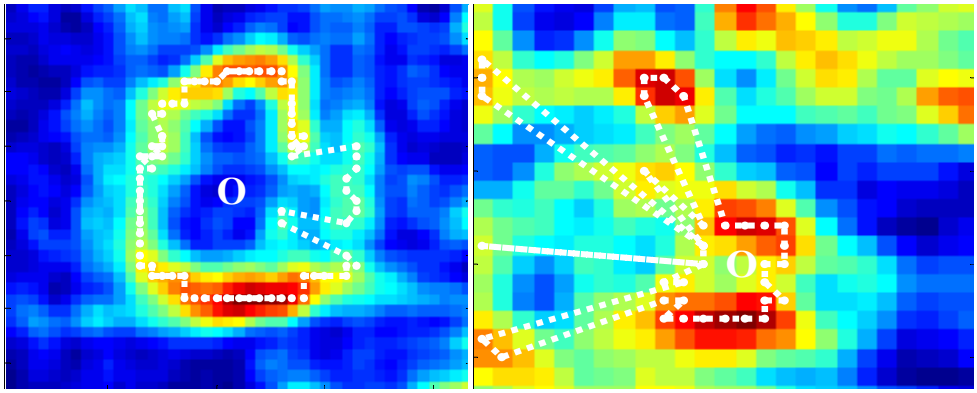

CE75: COV = 0.20 DE25: COV = 0.79

Figure 6-16. Gradient images for defects. A) A75 with COV = 0.10. B) A25 with COV = 0.28. B) E75 with COV = 0.20. D) E25 with COV = 0.79.

Table 6-6. Gradient area method results for Specimen A-1: flash heating

Defect	Actual diameter (mm)	Actual size (cm^2)	Image diameter (mm)	COV	Image area (pixels)	Image area (cm^2)
IB	34.0	7.1	29.2	0.33	542	6.3
A75	19.1	2.8	18.3	0.1	214	2.5
A50	12.7	1.3	12.2	0.11	91	1.0
A25	6.4	0.3	6.9	0.28	29	0.3
E75	19.1	2.8	21.3	0.2	312	3.6
E50	12.7	1.3	12.4	0.08	88	1.0
E25	6.4	0.3	8.6	0.79	54	0.6

Figure 6-17 provides bar charts for the important parameters listed in Table 6-5. Results for the largest defect (IB) are presented on the left side of the lower axis and

results for the smallest defect are shown on the right. Values for ΔT_{max} increase with respect to defect diameter. The air-filled defects also produced consistently larger values of ΔT_{max} than epoxy-filled defects of the same size. Figure 6-17B provides the normalized ΔT_{max} vs. defect diameter. This value was computed by dividing the maximum defect signal strength by the temperature increase experienced by the perimeter of the area used to define the defect (ΔT_{per} in Table 6-5).

Time to max and half-life of the signal also displayed an upward trend with increasing defect diameter. For these quantities, however, the epoxy-filled defects generated consistently larger values than air-filled defects of the same diameter.

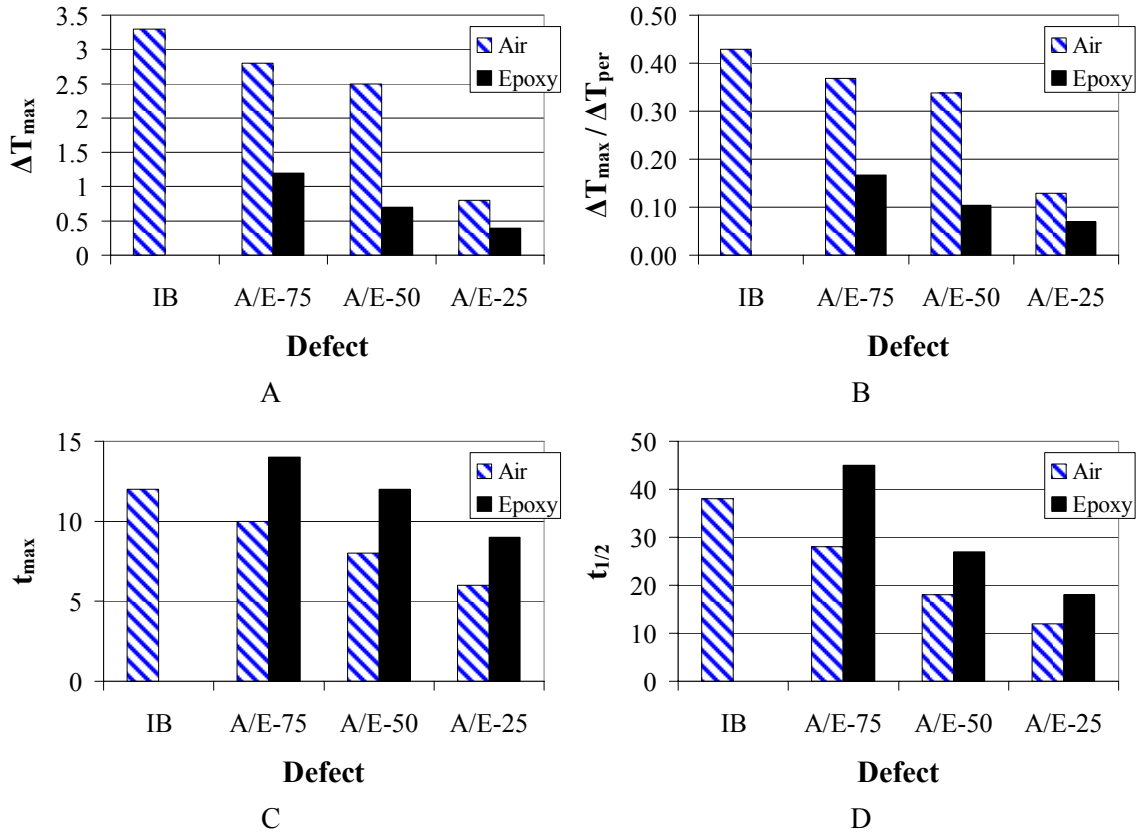

Figure 6-17. Specimen A-1: Important parameters for defects with different diameters. A) ΔT_{max}. B) Normalized ΔT_{max}. C) t_{max}. D) $t_{1/2}$.

Specimen A-2

Specimen A-2 was constructed using two layers of carbon-fiber composite. The thermal image shown in Figure 6-18B was recorded at t = 16 sec. At this point in time, the boundaries of defects IB, A75, and A50 are defined in the thermal image.

The exact time that Defect E75 becomes visible in the series of thermal images is not apparent. Figure 6-18C shows the thermal image at t = 16 sec with the color scale modified to encompass the temperature values encountered in the area defining E75. Some traces of the defect pattern are visible inside of area E75, but similar patterns can also be detected outside of the area. Figure 6-18D shows the thermal image taken at t = 38 sec. The boundaries of E75 and E50 are better defined at this time at it is possible to say that the defects have been detected.

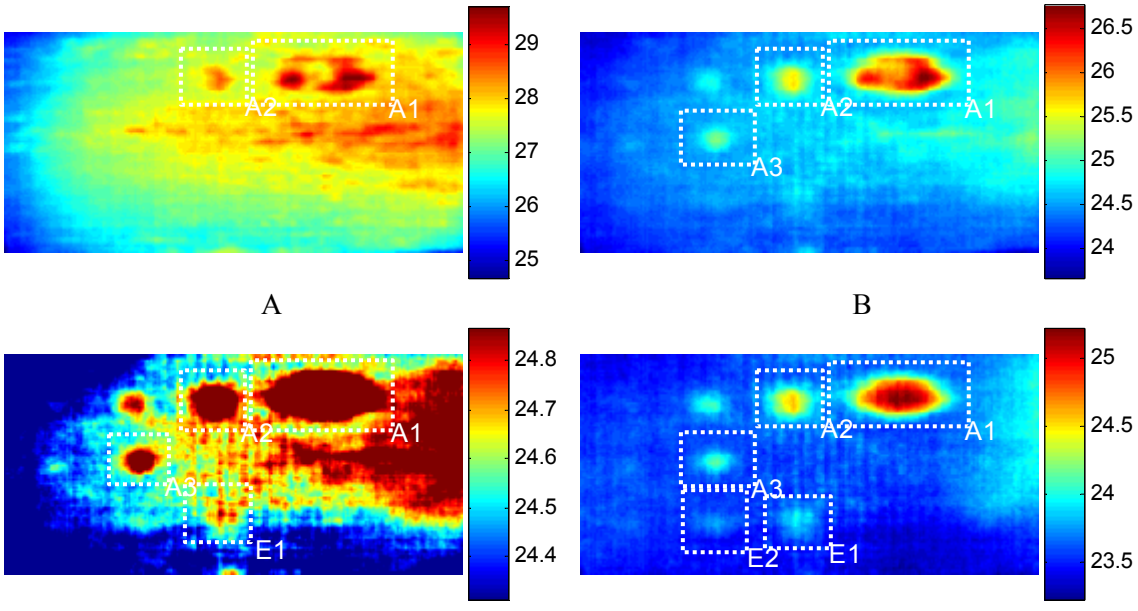

Figure 6-18. Thermal images for Specimen A-2: flash heating. A) t = 2 sec. B) t = 16 sec. C) t = 16 sec. D) t = 38 sec.

The ΔT_{def} vs. time plots for the seven defects of interest are provided in Figure 6-19. Data for the air-filled defects (shown in Figure 6-19A) provide additional insight into

the observations made while inspecting the thermal images. The curve for Defect IB assumes a positive slope at t = 0 sec and reaches a maximum value of 2.4°C at t = 7 sec. The curve generated for Defect A75 also begins with a positive slope at t = 0. A local maximum of 1.1°C occurs at t = 4 sec followed by a local minimum at t = 9 sec. From there, the curve begins climbing again until a final local maximum of 1.1°C is reached at t = 20 sec.

The curve for Defect A50 displays a noticeably different trend. The initial value for ΔT_{def} at t = 0 sec is 0.9°C. The initial slope for this curve is negative and a local minimum of 0.5°C is reached at t = 10 sec. At t = 23 sec, another local maximum is reached (0.7°C). The most likely explanation for the differences in these three curves is illustrated in Figure 6-20. During specimen construction, it is possible that several unintentional defects were created between the two layers of FRP composite. These unintentional defects, being closer to the surface than the interface defects, appear at earlier times in the thermal images. The maximum value for Defect IB and the initial local maximum experienced by A75 both occur at approximately the same time as the interface defects detected in Specimen A-1 (single-layer carbon).

Defects E75 and E50 were also detected. A ΔT_{def} vs. time plot is provided in Figure 6-19B. The ΔT_{max} recorded for E75 and E50 was 0.5°C (t = 40 sec) and 0.3°C (t = 38 sec), respectively. The two 6.4 mm diameter defects were not detected

Plots for ΔT_{max}, normalized ΔT_{max}, t_{max}, and $t_{1/2}$ are provided in Figure 6-21. The general trends observed for Specimen A-1 were also observed for Specimen A-2. The air-filled defects had consistently higher values for ΔT_{max} and normalized ΔT_{max} than the epoxy-filled defects. Three quantities that did not follow the expected trends: t_{max} and

$t_{1/2}$ for Defect IB and t_{max} for Defect A75. These discrepancies are explained by the fact that small inter-lamina defects developed between the first and second layers of the FRP composite.

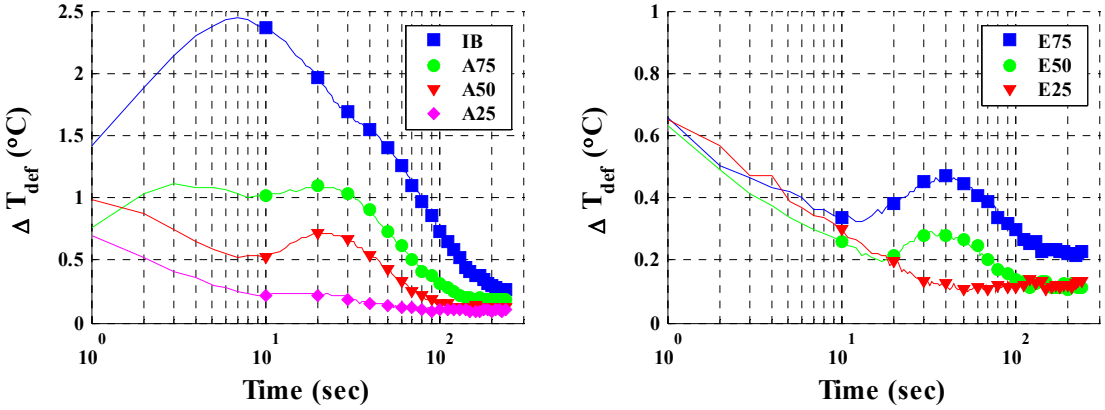

A B

Figure 6-19. Flash heating results for Specimen A-2: temperature vs. time data. A) Air-filled defects. B) Epoxy-filled defects.

Table 6-7. Summary of Results for Specimen A-2: flash heating

Defect	Defect Mat.	ΔT_{per} (°C)	ΔT_{max} (°C)	t_b (sec)	t_{max} (sec)	$t_{1/2}$ (sec)	SBR
IB	Air	7.3	2.4	0	7	55	19.1
A75	Air	7.1	1.1	8	20	47	12.4
A50	Air	7.1	0.7	7	23	35	16.4
A25	Air	5.8	-	-	-	-	-
E75	Epoxy	6.9	0.5	13	40	98	8.6
E50	Epoxy	6.5	0.3	17	38	50	6.7
E25	Epoxy	5.3	-	-	-	-	-

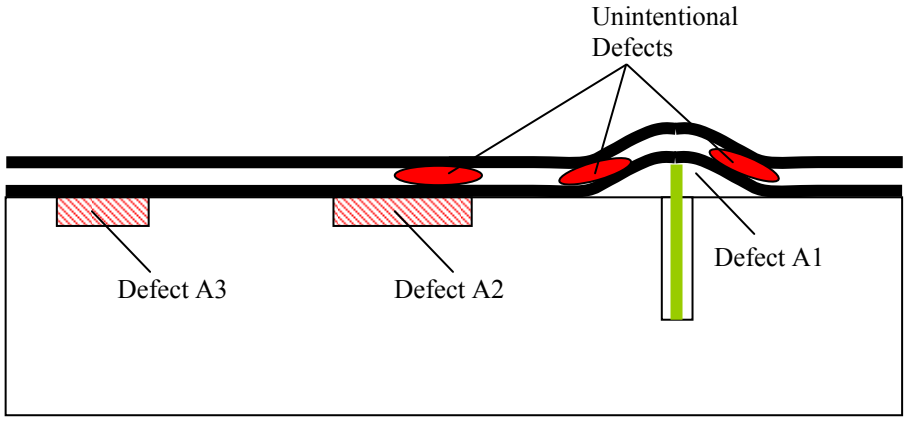

Figure 6-20. Unintentional defects between layers in Specimen A-2

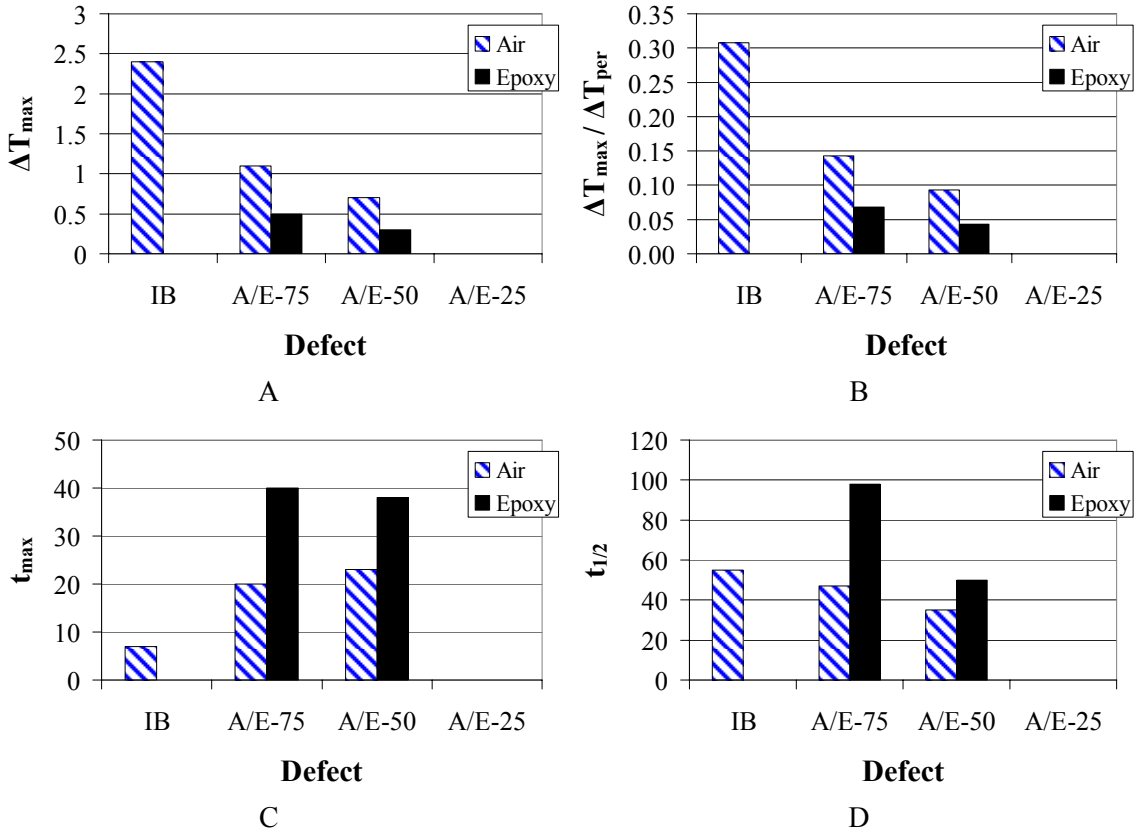

Figure 6-21. Specimen A-2: Important parameters for defects with different diameters. A) ΔT_{max}. B) Normalized ΔT_{max}. C) t_{max}. D) $t_{1/2}$

Specimen A-3

Specimen A-3 was constructed using three layers of FRP composite. Thermal images and ΔT_{def} vs. time plots are provided in Figure 6-22. Only the air-filled defects IB, A75, and A50 developed a significant signal in the ΔT_{def} vs. time plots. The ΔT_{max} value recorded for these defects was 0.9°C (t = 61 sec), 0.6°C (t = 54 sec), and 0.3°C (t = 36 sec), respectively.

The signal that developed for Defect E75 (19 mm dia. epoxy-filled) was very weak. The thermal image in Figure 6-22B does indicate a defect and the ΔT_{def} vs. time plot (Figure 6-22D) also indicates a small signal. Based on a ΔT_{thresh} value of 0.2°C (Figure 6-6), this defect was not detected.

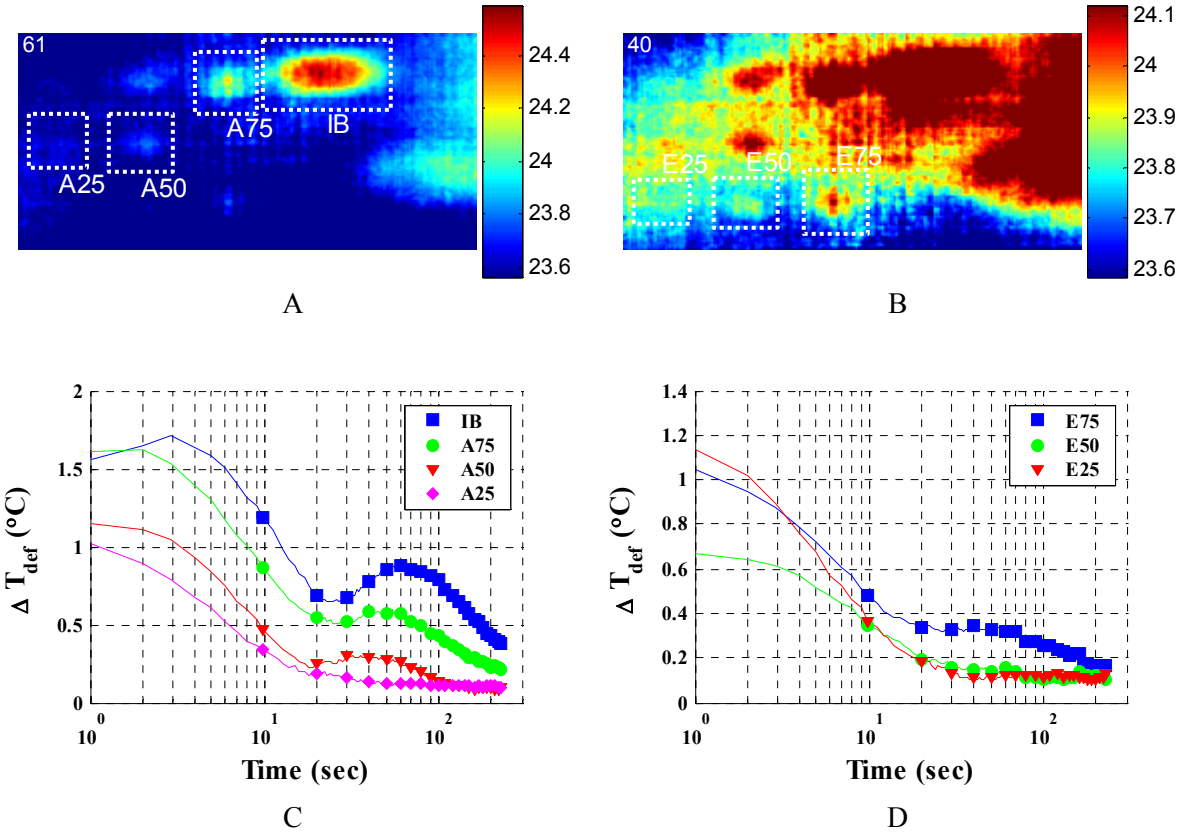

Figure 6-22. Thermal images and ΔT_{def} vs. time plots for Specimen A-3. A) Thermal image scaled for air-filled defects (t = 61 sec). B) Thermal image scaled for epoxy-filled defects (t = 40 sec). C) ΔT_{def} vs. time plot for air-filled defects. D) ΔT_{def} vs. time plot for epoxy-filled defects.

Table 6-8. Summary of results for Specimen A-3: flash heating

Defect	Defect Mat.	ΔT_{per} (°C)	ΔT_{max} (°C)	t_b (sec)	t_{max} (sec)	$t_{1/2}$ (sec)	SBR
IB	Air	6.1	0.9	25	61	136	12.7
A75	Air	6.0	0.6	27	54	91	9.5
A50	Air	5.9	0.3	18	36	60	7.3
A25	Air	4.9	-	-	-	-	-
E75	Epoxy	5.9	-	-	-	-	-
E50	Epoxy	5.4	-	-	-	-	-
E25	Epoxy	4.3	-	-	-	-	-

Important parameters from the ΔT_{def} vs. time plots are plotted against defect diameter in Figure 6-23. Since the epoxy-filled defects were not detected, no data are presented for defects E75, E50, or E25. ΔT_{max} and normalized ΔT_{max} both increase as the diameter of the defect increases. A similar trend is observed for t_{max} and $t_{1/2}$.

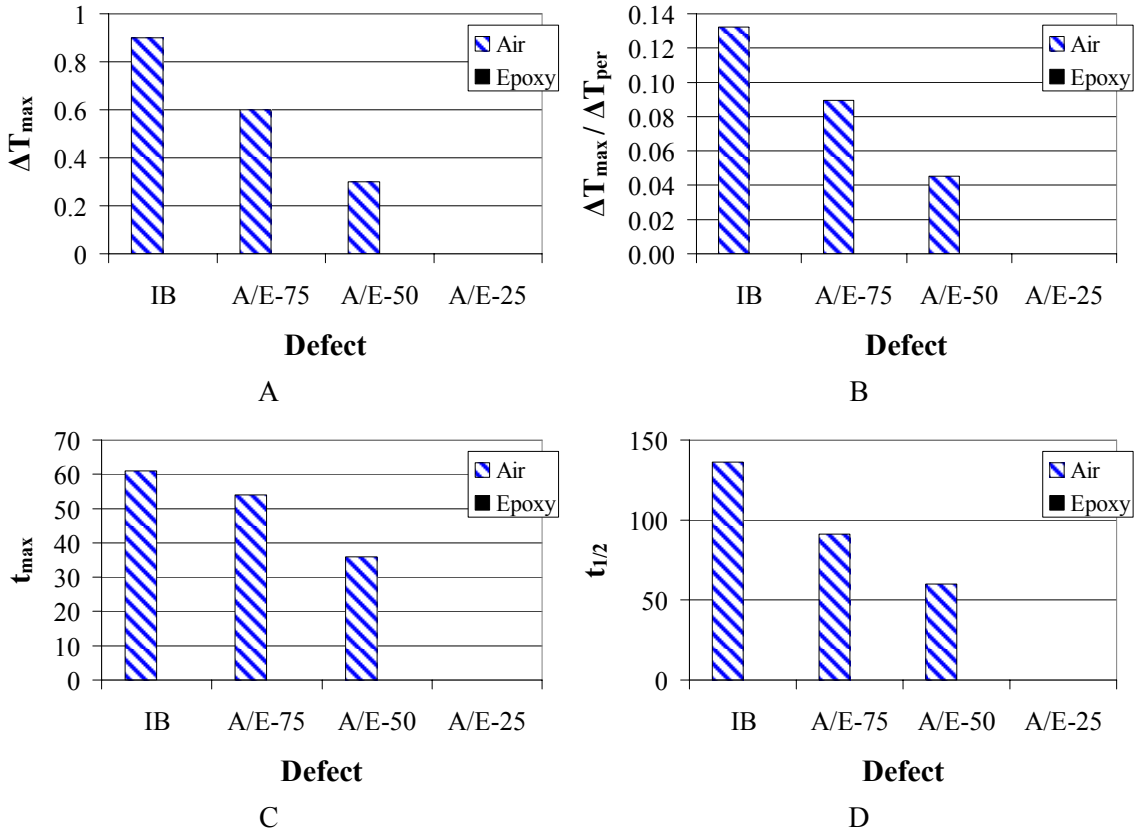

Figure 6-23. Specimen A-3: Important parameters for defects with different diameters. A) ΔT_{max}. B) Normalized ΔT_{max}. C) $t_{max.}$ D) $t_{1/2}$

Specimen A-4

Specimen A-4 was constructed using four layers of FRP composite. Thermal images and ΔT_{def} vs. time plots are provided in Figure 6-24. Only the air-filled defects IB and A75 developed a significant signal in the ΔT_{def} vs. time plots. The ΔT_{max} value recorded for these defects was 0.6°C (t = 86 sec) and 0.4°C (t = 72 sec). The half-life for Defect IB was not recorded since the value was not reached by the end of the data collection period. The half-life measured for Defect A75 was 146 sec. The gradient image that was generated for Defect IB was not sufficient to generate a suitable defect boundary.

Once again, the signal for the epoxy-filled Defect E75 was questionable. Based on the criteria described for Specimen A-3, none of the epoxy-filled defects were assumed to have been detected.

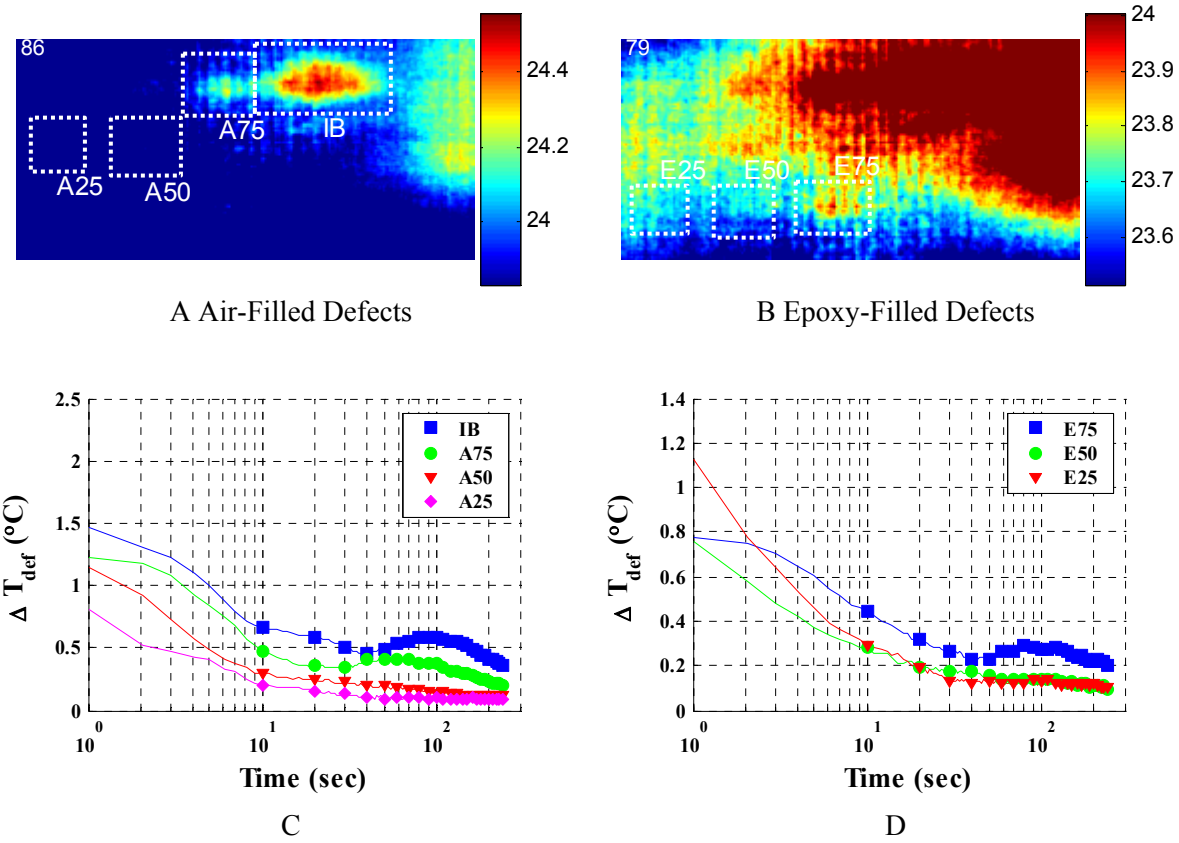

Figure 6-24. Thermal images and ΔT_{def} vs. time plots for Specimen A-4. A) Thermal image scaled for air-filled defects (t = 86 sec). B) Thermal image scaled for epoxy-filled defects (t = 79 sec). C) ΔT_{def} vs. time plot for air-filled defects. D) ΔT_{def} vs. time plot for epoxy-filled defects.

General detectability

Up to this point, the pulse heating method has been applied to all four specimens in series A. ΔT_{def} vs. time plots were constructed for the seven defects contained in each specimen resulting in a total of 28 unique plots. The previous sections for each specimen highlighted the differences between defects on the same specimen. The objective of this section is to condense these results into a manageable format and develop a basis for determining detectability.

The general detectability classification system was applied to each defect for the pulse heating method. Results are summarized in Table 6-9. For the single-layer carbon FRP system, all of the implanted defects received a Level I or Level II classification. This indicates that a quantifiable signal was generated in the ΔT_{def} vs. time plots for each defect. For the two-layer FRP composite system, all of the defects at least 12.7 mm in diameter or larger were considered Level I or Level II. The 6.4 mm diameter defects did not develop a significant signal in the ΔT_{def} vs. time plots. For the three-layer specimen, only air-filled defects with 12.7 mm diameters (or larger) developed a signal. Finally, only the IB and 19 mm diameter defect developed a significant signal in the four-layer specimen.

Detectability will likely improve with the use of a flash system capable of generating a higher intensity heat flux. It may also be possible to improve upon the quality of the thermal images by moving the camera closer to the specimen. This could lead to improvement in the classification based on the COV of the defect boundary.

Table 6-9. General detectability results for flash heating

Flash Heating Detectability		Defect						
		IB	A75	A50	A25	E75	E50	E25
Layers	1	I-A	I-A	I-A	II-B	I-A	II-A	II-C
	2	I-A	II-B	II-A	IV-C	II-C	II-C	IV-C
	3	II-A	II-C	II-C	IV-C	IV-C	IV-C	IV-C
	4	II-B	II-C	IV-C	IV-C	IV-C	IV-C	IV-C

Signal to boundary noise ratio (SBR) results for the pulse heating method are provided in Table 6-10. This quantity is calculated by dividing the maximum defect signal strength (ΔT_{max}) by the standard deviation of the temperature profile around the boundary of the area used to define the defect. Higher values of SBR indicate that a defect is well defined with respect to its surroundings. A low SBR indicates that the

temperature fluctuation resulting from the defect is closer in magnitude to temperature fluctuations resulting from noise or natural variations in the composite.

Table 6-10. Signal to boundary noise ratio (SBR) results for flash heating

Flash Heating SBR		Defect						
		IB	A75	A50	A25	E75	E50	E25
Layers	1	40.9	33.5	23.3	3.5	6.6	6.2	2.6
	2	19.1	12.4	16.4	-	8.6	6.7	-
	3	12.7	9.5	7.3	-	-	-	-
	4	10.8	5.1	-	-	-	-	-

Defect characterization

The objective of this analysis is to determine how well the parameters extracted from each ΔT_{def} vs. time plot can be used to characterize detected defects.

Figure 6-25A provides a bar chart with the normalized ΔT_{max} plotted for each of the air-filled defects. The four bars grouped together above the label "1" on the x-axis were obtained for defects IB, A75, A50, and A25 in the single-layer carbon specimen (A-1). Notice that there are only three bars provided for the two-layer specimen (defects IB, A75, and A50). This is because Defect A25 was not detected in the two-layer system. Results for the epoxy-filled defects are provided in Figure 6-25B. The general trend for all defects is that normalized ΔT_{max} decreases with FRP system thickness. Figure 6-25 also illustrates how normalized ΔT_{max} decreases as the size of the defect decreases for a given FRP system thickness.

How can this information be used to characterize a defect? Assume that an IRT experiment was performed using the pulse method and 19 mm diameter defect was detected. The normalized ΔT_{max} for this defect was measured to be 0.15. These data alone represent two possible scenarios: (1) the defect is air-filled and lies below 2 layers of FRP composite or (2) the defect is epoxy-filled and lies below 1 layer of FRP composite. A similar observation could be made for a 12.7 mm diameter defect with a

normalized ΔT_{max} of 0.1. If the system thickness is known, there will be little question about the material composition of the defect. If, however, the system thickness is not known a priori, additional information would be needed to characterize the defect.

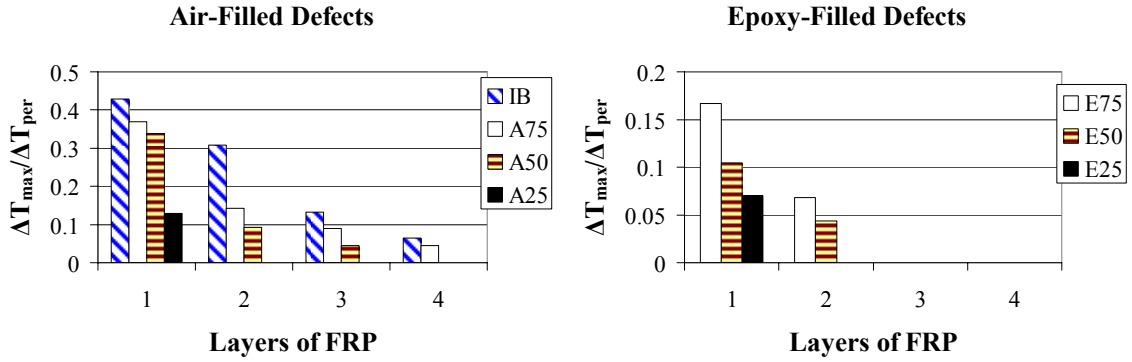

A B

Figure 6-25. Normalized ΔT_{max} for flash heating. A) Air-filled defects. B) Epoxy-filled defects.

Figure 6-26A provides a bar chart with t_{max} plotted for each of the air-filled defects. Recall that t_{max} is the time between when the heat source was removed and the maximum defect signal strength was obtained. The number of FRP layers is labeled on the x-axis. The general trend for the single-layer system is that t_{max} decreases as the size of the defect decreases. This trend is also observed for the three and four-layer systems. The air-filled defects for the two-layer system do not follow this general trend. This is a result of the unintentional air-filled defects that occurred between the first and second layer of the FRP system. Results for the epoxy-filled defects are provided in Figure 6-26B.

These data are also potentially useful for characterizing detected defects. Recall the previous example of a 19 mm diameter defect with a normalized ΔT_{max} of 0.15. Based on the measured value of normalized ΔT_{max} it was not possible to determine whether this represents Defect A75 on Specimen A-2 or Defect E75 on Specimen A-1 (both defects have the same size, but the composition and depth are unknown). Suppose

the t_{max} recorded for this defect was 15 sec (close to t_{max} for Defect E75, Specimen A-1). This result would suggest that the unknown defect is epoxy-filled and lies beneath one layer of FRP composite.

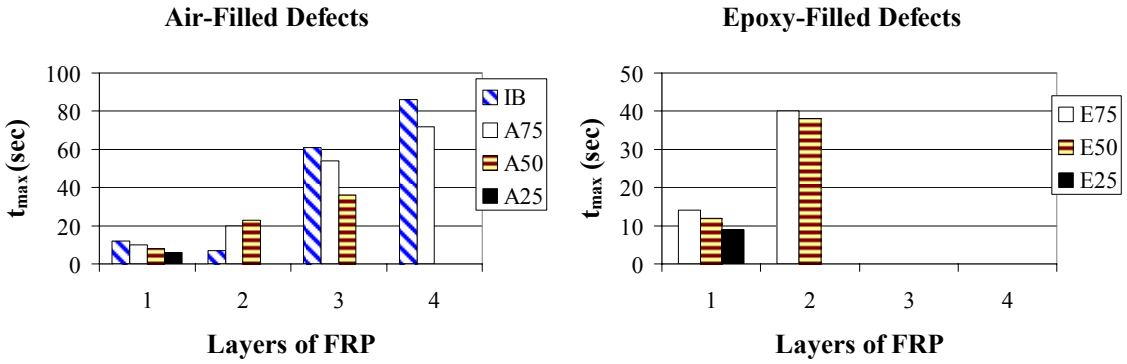

A B

Figure 6-26. Time to maximum signal for flash heating. A) Air-filled defects. B) Epoxy-filled defects

Data for signal half-life ($t_{1/2}$) displayed the same trend that was observed for t_{max}. Within each specimen, the values for $t_{1/2}$ decreased as the size of the defect decreased. As the thickness of the composite increased, the values for $t_{1/2}$ also increased. Data are provided in Figure 6-27 for the air and epoxy-filled defects.

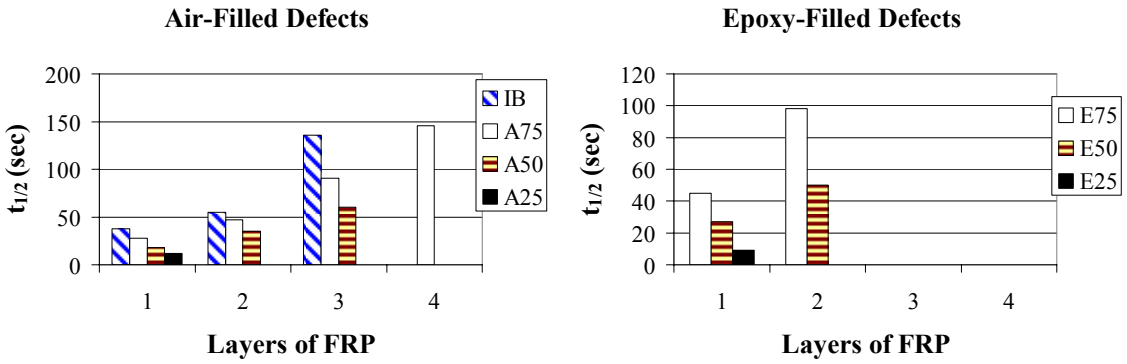

A B

Figure 6-27. Signal half-life for flash heating. A) Air-filled defects. B) Epoxy-filled defects

The bar charts provided above illustrate how defect size and FRP system thickness influence the parameters that were extracted from each ΔT_{def} vs. time plot. Table 6-11

contains the ratio of normalized ΔT_{max}, t_{max}, and $t_{1/2}$ for air-filled and epoxy-filled defects. Results are provided for the 19 mm diameter and the 12.7 mm diameter defects for the one and two layer composite systems. These ratios are omitted for the three and four layer specimens because the epoxy-filled defects were not detected using the pulse heating method.

Table 6-11. Ratio of parameters for air and epoxy-filled defects

		NDSS (Air:Epoxy)		tmax (Air:Epoxy)		t1/2 (Air:Epoxy)	
Pulse Heating		19 mm	12.7 mm	19 mm	12.7 mm	19 mm	12.7 mm
Layers	1	2.21	3.23	0.71	0.67	0.62	0.67
	2	2.09	2.15	0.50	0.61	0.48	0.70
	3	-	-	-	-	-	-
	4	-	-	-	-	-	-

Experimental Results: Scan Heating (Series A)

The scan heating procedure was outlined in Chapter 5. Since the entire surface area under consideration (all four specimens) was not heated at the same time, each defect was assigned a starting time (t=0) immediately after the heat source moved beyond the respective defect during the scan.

Complete ΔT_{def} vs. time results for each specimen are provided in Appendix A. Results from the scan heating experiment are summarized in the following sections.

Specimen A-1

All of the defects in Specimen A-1 were detected in the thermal images. The air-filled Defect IB generated a ΔT_{max} of 18.8°C. The smallest air-filled defect (A25) generated a ΔT_{max} of 4.0°C. These values are considerably higher than those observed in the pulse heating experiments: ΔT_{max} of 3.3°C and ΔT_{max} of 0.8°C for IB and A25, respectively. The three epoxy-filled defects also generated significantly higher ΔT_{max} values than were generated in the pulse heating experiments. The most likely explanation

for the increase in defect signal strength is the increase in background temperature due to the applied heat. Scan heating resulted in a ΔT_{per} value of 17.2°C for Defect IB while the pulse heating generated a ΔT_{per} of only 7.1°C.

The signal to perimeter noise ratio (SBR) for Defect IB was 14.9. This is considerably less than the value computed for pulse heating (40.9). The difference in SBR values is due to a higher standard deviation around the defect area perimeter in the scan heating results. The value of the perimeter standard deviation is plotted against time in Figure 6-28.

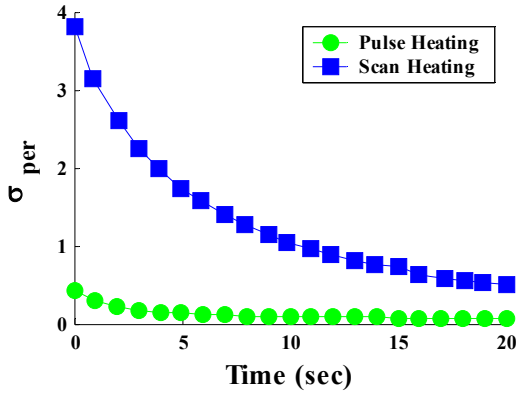

Figure 6-28. Standard deviation of Defect IB perimeter for pulse and scan heating

Area calculations were also performed for each defect using the gradient area method. The gradient images that were developed for defects A25 and E25 (both with 6.4 mm diameter) did not generate a well-defined defect boundary. This was not a result of weak signal or noise in surrounding pixels. Both the ΔT_{def} vs. time plots and thermal images indicate a strong signal for both defects (see Figure 6-29). The inability to estimate the size of these defects is a result of poor spatial resolution in the thermal image. Recall that the camera distance from the surface of the specimens was 60 in. This separation results in a length ratio of 2.2 mm/pixel. If this is the case, only three

pixels are required to span nearly the entire diameter of defects A25 and E25. The gradient image computed under these circumstances is insufficient to extract a reasonable defect boundary.

The gradient images generated for the larger defects contained did generate well-defined defect boundaries. However, there was more error in these calculated values than was observed in the pulse heating experiment. The computed area for Defect A75 (19 mm diameter) was 2.1 cm^2 (actual area = 2.8 cm^2). This represents an error in the area computation of 27.3%. In terms of diameter, however, the error is only 14.6%. The difference in the actual and computed diameter is 2.8 mm, which is less than the distance represented by two pixels in the thermal image.

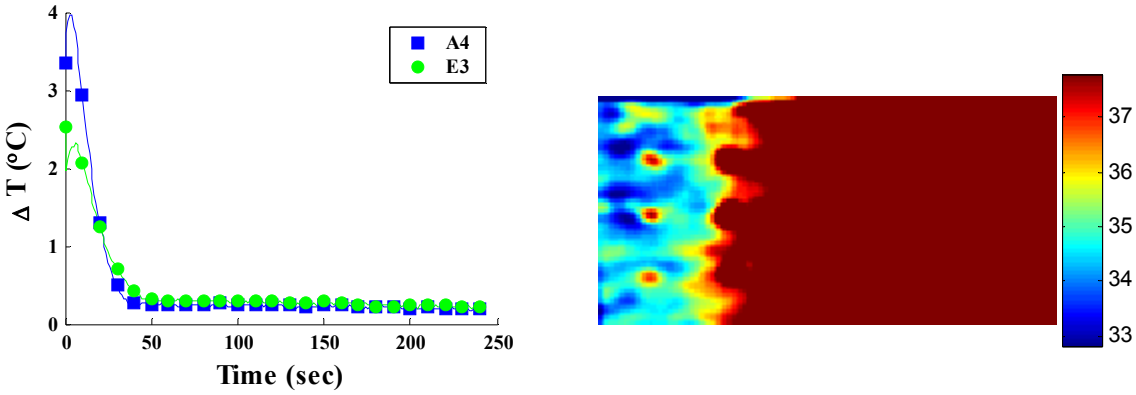

A B Thermal image at t = 5 sec

Figure 6-29. Data for defects A25 and E25 (6.4 mm diameter). A) T_{def} vs. time plot. B) Thermal image at t = 5 sec.

Specimen A-2

All of the defects in Specimen A-2 were detected in the thermal images. Only defects A25 and E25 did not generate sufficient gradient images for area computations. Another noteworthy observation for this specimen is in regards to Defect IB. Recall that this defect contained unintentional defects between the top and second layer of composite. Figure 6-30A provides a thermal image that was collected 2 sec after the heat

source moved passed Defect IB. The two unintentional defects above IB are clearly distinguishable in the thermal image. The image taken at t = 18 sec, however, does not distinguish between the unintentional defects and the interface bubble (see Figure 6-30B). Complete results for Specimen A-2 are provided in the appendix.

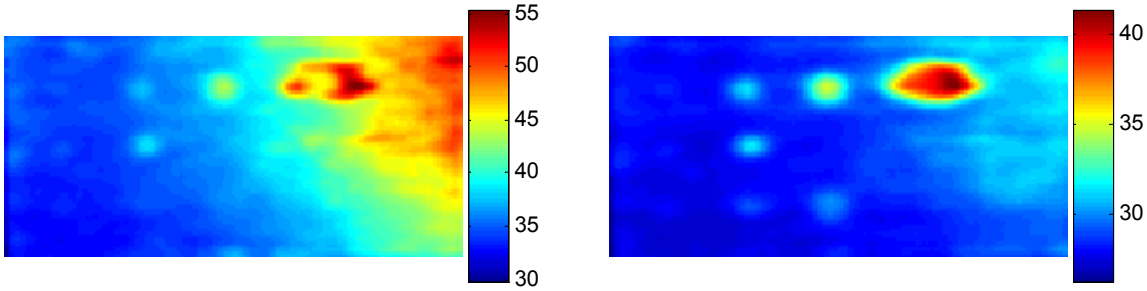

A B

Figure 6-30. Thermal images for Defect IB (Specimen A-2). A) t = 2 sec. B) t = 18 sec.

Specimen A-3

Only defects with a diameter of 6.4 mm (defects A25 and E25) did not develop a signal in the ΔT_{def} vs. time plots. All of the remaining defects were detected in the ΔT_{def} vs. time plots and the gradient images. Complete results for Specimen A-3 are provided in Appendix A.

Specimen A-4

Defects A50, A25, E50, and E25 were not detected in the ΔT_{def} vs. time plots. The remaining defects were detected in the ΔT_{def} vs. time plots and the gradient images. Complete results for Specimen A-4 are provided in Appendix A.

General Detectability

Table 6-12 provides a summary of the general detectability results for all defects implanted in the one, two, three, and four-layer specimens. These data indicate an overall increase in detectability over the flash heating method. The scan heating method also resulted in higher classification levels based on the quality of the defect boundary. In the

pulse heating experiments, a total of 8 defects were classified as Level A. The scan heating experiments resulted in a total of 13 Level A defects. The number of Level B defects also increased from three to six for the pulse and scan heating methods, respectively.

Table 6-12. General detectability results for scan heating

Scan Heating Detectability		Defect						
		IB	A75	A50	A25	E75	E50	E25
Layers	1	I-A	I-A	I-B	I-C	I-A	I-A	I-B
	2	I-A	I-A	II-A	II-B	II-A	II-B	II-C
	3	II-A	II-A	II-A	IV-C	III-A	III-B	IV-C
	4	II-A	II-B	IV-C	IV-C	III-B	IV-C	IV-C

Signal to boundary noise ratio (SBR) results are provided in Table 6-13. For the one and two-layer specimens, it is interesting to note that the SBR for Defect IB is smaller than A75 even though the magnitude of ΔT_{max} is larger. This difference can be attributed to non-uniform heating resulting from moving the heat source from one side of the specimen to the other. When using the scan heating method, a temperature gradient will always be present on the surface of the specimen running parallel to the direction of heat source motion (x-direction). The effect that this gradient has on the SBR calculations is magnified for Defect IB since the length of the rectangle used to define the defect is larger in the x-direction.

Table 6-13. Signal to boundary noise ratio (SBR) results for scan heating

Pulse Heating SBR		Defect						
		IB	A75	A50	A25	E75	E50	E25
Layers	1	14.9	22.8	10.5	4.8	13	7.5	5.5
	2	7.2	13.7	11.4	3.1	10.7	6.2	3.5
	3	14.1	6.1	5.4	-	2.3	3.3	-
	4	10.4	3.8	-	-	3.0	-	-

Defect characterization

Normalized ΔT_{max} is presented in a bar chart for each defect in Figure 6-31. The same general trend that was observed in the pulse heating experiments was also observed in the scan heating results: as the thickness of the FRP system increase, the normalized ΔT_{max} decreases. If the FRP system thickness is held constant, normalized ΔT_{max} decreases as the size of the defect decreases.

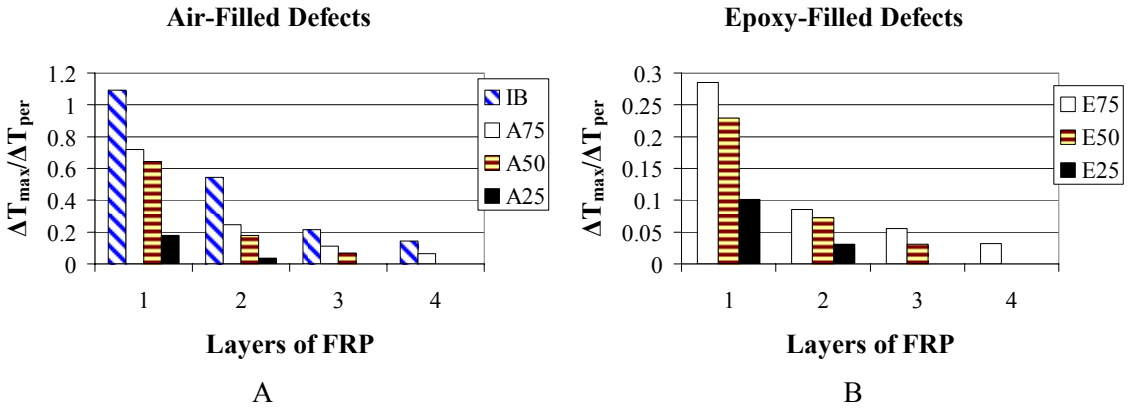

Figure 6-31. Normalized ΔT_{max} for scan heating. A) Air-filled defects. B) Epoxy-filled defects

Figure 6-32 provides bar chart plots for t_{max}. In general, the time required for the maximum ΔT_{def} to develop increases with FRP system thickness. These data, however, do not provide consistent results for defects occurring in the same specimen. For the air-filled defects in Specimen A-1, there is no clearly defined relationship between defect size and t_{max}. The same is true for the air-filled defects in Specimen A-2, but this is likely explained by the unintentional defects between the first and second layer of composite. For specimens A-3 and A-4, the air-filled defects do exhibit a well-defined trend in which t_{max} decreases as the size of the defect decreases. There are insufficient data to compare these results with the pulse heating experiments since none of these quantities were measured for the three and four-layer specimens.

The epoxy-filled defects also show some interesting trends with regards to t_{max}. For specimens A-1 and A-2, the value of t_{max} tends to decrease as the area decreases. For Specimen A-3, however, this trend is not observed. The t_{max} value recorded for the 19 mm diameter defect (E75) was 34 sec while the t_{max} recorded for the 12.7 mm diameter defect was 38 sec. This discrepancy can be explained by a close examination of the ΔT_{def} vs. time plots. For both defects, a large signal develops due to non-uniform heating early in the cooling process. This signal gives way to the true defect signal very slowly resulting in a ΔT_{def} vs. time plot that is extremely flat over the region of the maximum value. Even though the scan heating method was sufficient to generate a signal for each of the defects, it is not possible to determine precisely when the maximum ΔT_{def} occurs.

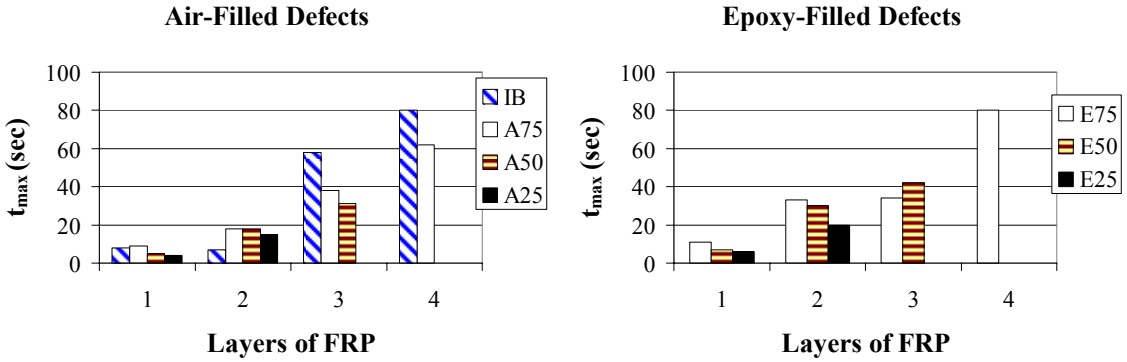

Figure 6-32. Time to maximum signal for scan heating. A) Air-filled defects. B) Epoxy-filled defects

Figure 6-33 provides bar chart plots of $t_{1/2}$. For the air-filled defects, a consistent trend is observed in which $t_{1/2}$ increases with FRP system thickness. Smaller defects also result in consistently lower $t_{1/2}$ values for a constant FRP system thickness. The same trend is observed for the epoxy-filled defects up to the four-layer specimen. The $t_{1/2}$ measured for Defect E75 in Specimen A-4 was 83 sec. The $t_{1/2}$ measured for Defect E75 in the three-layer specimen was 84 sec.

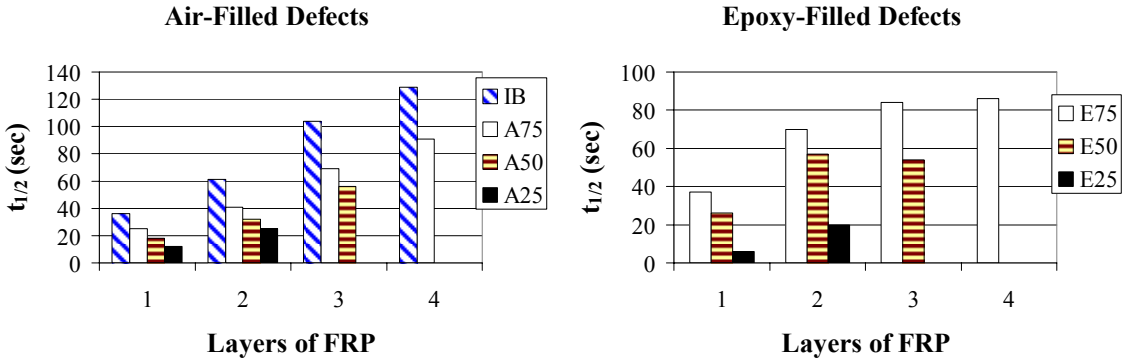

A B

Figure 6-33. Signal half-life for scan heating. A) Air-filled defects. B) Epoxy-filled defects s

The ratios of ΔT_{def} vs. time parameters for epoxy and air-filled defects are provided in Table 6-14. Based on these data, the most promising parameter for distinguishing air and epoxy-filled defects is normalized ΔT_{max} (NDSS). These values are consistently higher for air-filled defects and the smallest recorded ratio for air:epoxy was 1.98. The quantities t_{max} and $t_{1/2}$ are also useful parameters when considering one and two-layer FRP systems. These values are consistently higher for epoxy-filled defects and result in air:epoxy ratios less than one. For three and four-layer systems, however, extracting t_{max} and $t_{1/2}$ from each ΔT_{def} vs. time plot is not possible. The ratios for air:epoxy defects of the same size are not consistent and in some cases have magnitudes greater than 1 (highlighted in Table 6-14).

Table 6-14. Ratio of parameters for air and epoxy-filled defects (scan heating)

		NDSS (Air:Epoxy)		t_{max} (Air:Epoxy)		$t_{1/2}$ (Air:Epoxy)	
Scan Heating		19 mm	12.7 mm	19 mm	12.7 mm	19 mm	12.7 mm
Layers	1	2.53	2.80	0.82	0.71	0.68	0.69
	2	2.87	2.46	0.55	0.60	0.59	0.56
	3	1.98	2.21	1.12	0.74	0.82	1.04
	4	2.06	-	0.89	-	1.05	-

Experimental Results: Long-Pulse Heating (Series A)

Complete results for the long-pulse heating experiments are provided in Appendix A. The following section on general detectability will highlight results from the three pulse durations that were investigated (30 sec, 45 sec, and 60 sec). The section on defect characterization will summarize the results obtained for the 30 sec pulse duration. Results from the 45 sec and 60 sec pulse duration experiments will be discussed in the following section that compares results from all of the heating methods.

General detectability

Table 6-15 provides general detectability results for the three pulse durations that were considered. These results indicate that pulse duration has very little influence on general detectability. For the single-layer specimen, all of the defects were detected in the ΔT_{def} vs. time plots. The gradient images also produced well-defined boundaries for all defects except A25 and E25. For the two-layer specimen, all of the air-filled defects 6.4 mm in diameter or larger were detected in the plots and gradient images. Only epoxy-filled Defect E75 was detected in the plots and gradient images. For Specimen A-3, air-filled defects IB, A75 were detected in the plots and gradient images. Defect A50 and E75 developed very weak signals with a ΔT_{max} of 1.4°C and 1.1°C, respectively. Defects A25, E50, and E75 were not detected. Finally, only defects IB and A75 were detected in the four-layer specimen.

Defect characterization

Figure 6-34 provides data for normalized ΔT_{max} for each of the four specimens. The same general trend that was observed for the flash and scan heating experiments was also observed for the long-pulse heating method:

- Smaller defects have lower normalized ΔTmax

- As FRP system thickness increases, ΔTmax decreases
- Epoxy-filled defects have consistently lower normalized ΔTmax values than air-filled defects

Table 6-15. General detectability results for long-pulse heating

		Defect						
30 Sec Pulse		IB	A75	A50	A25	E75	E50	E25
Layers	1	I-A	I-A	I-A	I-C	I-A	I-A	I-C
	2	I-A	I-A	I-B	IV-C	II-B	III-C	IV-C
	3	II-A	II-A	III-B	IV-C	III-C	IV-C	IV-C
	4	II-B	II-C	IV-C	IV-C	IV-C	IV-C	IV-C
		Defect						
45 sec Pulse		IB	A75	A50	A25	E75	E50	E25
Layers	1	I-A	I-A	I-A	I-C	I-A	I-A	I-C
	2	I-A	I-A	I-A	IV-C	II-A	II-C	IV-C
	3	II-A	II-A	III-B	IV-C	III-B	IV-C	IV-C
	4	II-B	II-B	IV-C	IV-C	IV-C	IV-C	IV-C
		Defect						
60 sec pulse		IB	A75	A50	A25	E75	E50	E25
Layers	1	I-A	I-A	I-A	I-C	I-A	I-A	I-C
	2	I-B	I-A	I-B	IV-C	II-A	IV-C	IV-C
	3	II-A	II-A	III-B	IV-C	III-B	IV-C	IV-C
	4	II-A	II-C	IV-C	IV-C	IV-C	IV-C	IV-C

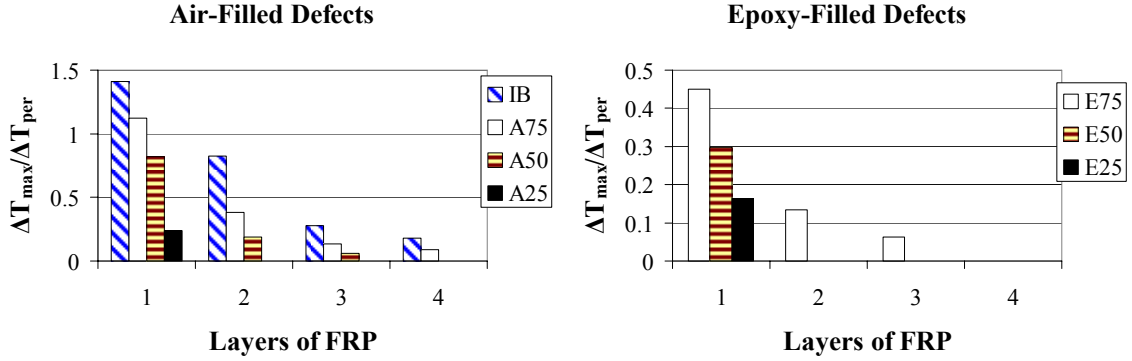

A B

Figure 6-34. Normalized ΔT_{max} for long-pulse heating (30 sec pulse). A) Air-filled defects. B) Epoxy-filled defects.

Data for t_{max} are shown in Figure 6-35 . For the air-filled defects, these data do not indicate a consistent trend with respect to defect size. On average, however, the values for t_{max} increase with FRP system thickness. Figure 6-36 provides a bar chart for defect half-life for each specimen. These results do provide consistent trends for the air-filled defects:

- Smaller defects have shorter half-lives
- As FRP system thickness increases, t1/2 increases

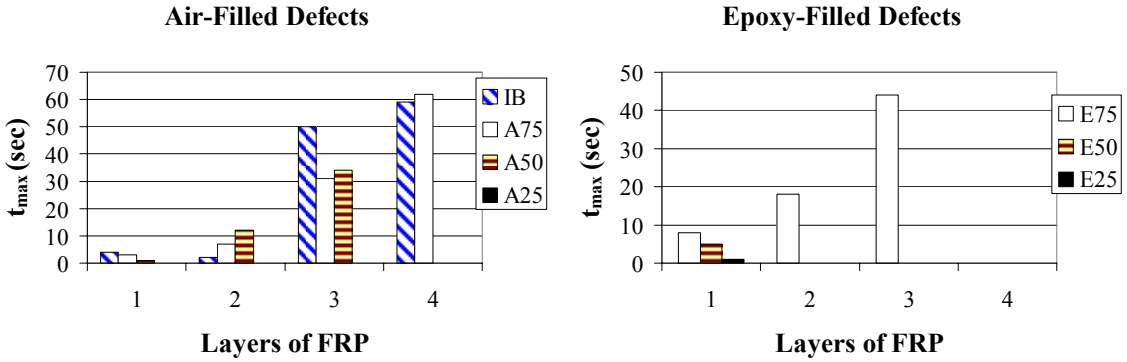

Figure 6-35. Time to maximum signal for long-pulse heating. A) Air-filled defects. B) Epoxy-filled defects.

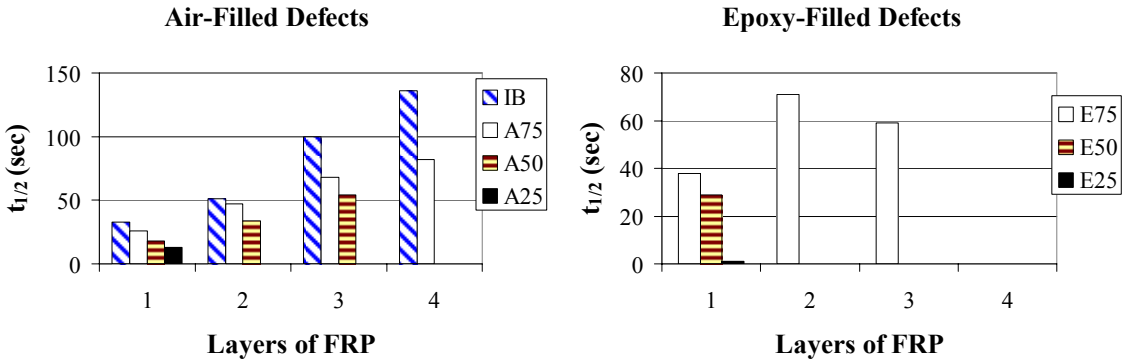

Figure 6-36. Signal half-life for long-pulse heating. A) Air-filled defects. B) Epoxy-filled defects.

Comparison of Heating Methods

Three of the heating methods described in Chapter 4 (flash, scan and long-pulse) were applied to the four specimens in Series A. Three pulse durations were investigated for the long-pulse heating method. Data collection for all heating methods consisted of capturing thermal images at a rate of 1 frame per second for a total of 240 seconds. The start time for recording data occurred immediately after the heat source was removed.

These data were used to compare the performance of each heating method on specimens containing one, two, three or four layers of FRP composite. Each specimen

contained implanted defects of varying size and material composition. The discussion of this analysis will be divided into two parts: (1) general detectability and (2) defect characterization.

General Detectability

Defect detectability is compared for the different heating methods in Figure 6-38 (legend is provided in Figure 6-37). Only eight of the 12 possible detectability levels were encountered. These eight levels were grouped into three categories representing high detectability, medium detectability, and not detected. High detectability was assigned to defects receiving the classification levels I-A, I-B, II-A, and II-B. This category contains defects that were well-defined in ΔT_{def} vs. time plots and at least moderately defined in the gradient images. Medium detectability was assigned to defects classified as I-C, II-C, or III-B. These defects are approaching the limits of detection. The final category, not-detected, was assigned to level IV-C defects.

Based on these criteria, the scan heating method outperformed the flash and long-pulse heating methods from the standpoint of general detectability. For the one and two-layer specimens, all seven defects were categorized as medium or high. For the three-layer specimen, only the 6.4 mm diameter defects were not detected, and for the four-layer specimen only defects with 12.7 mm diameters or smaller were not detected.

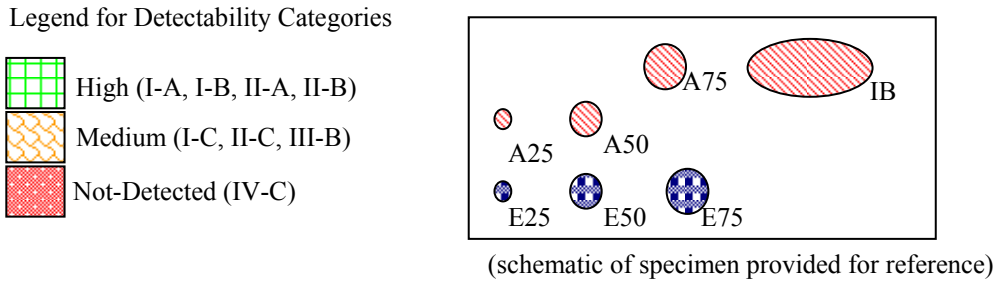

Figure 6-37. Legend for Figure 6-38

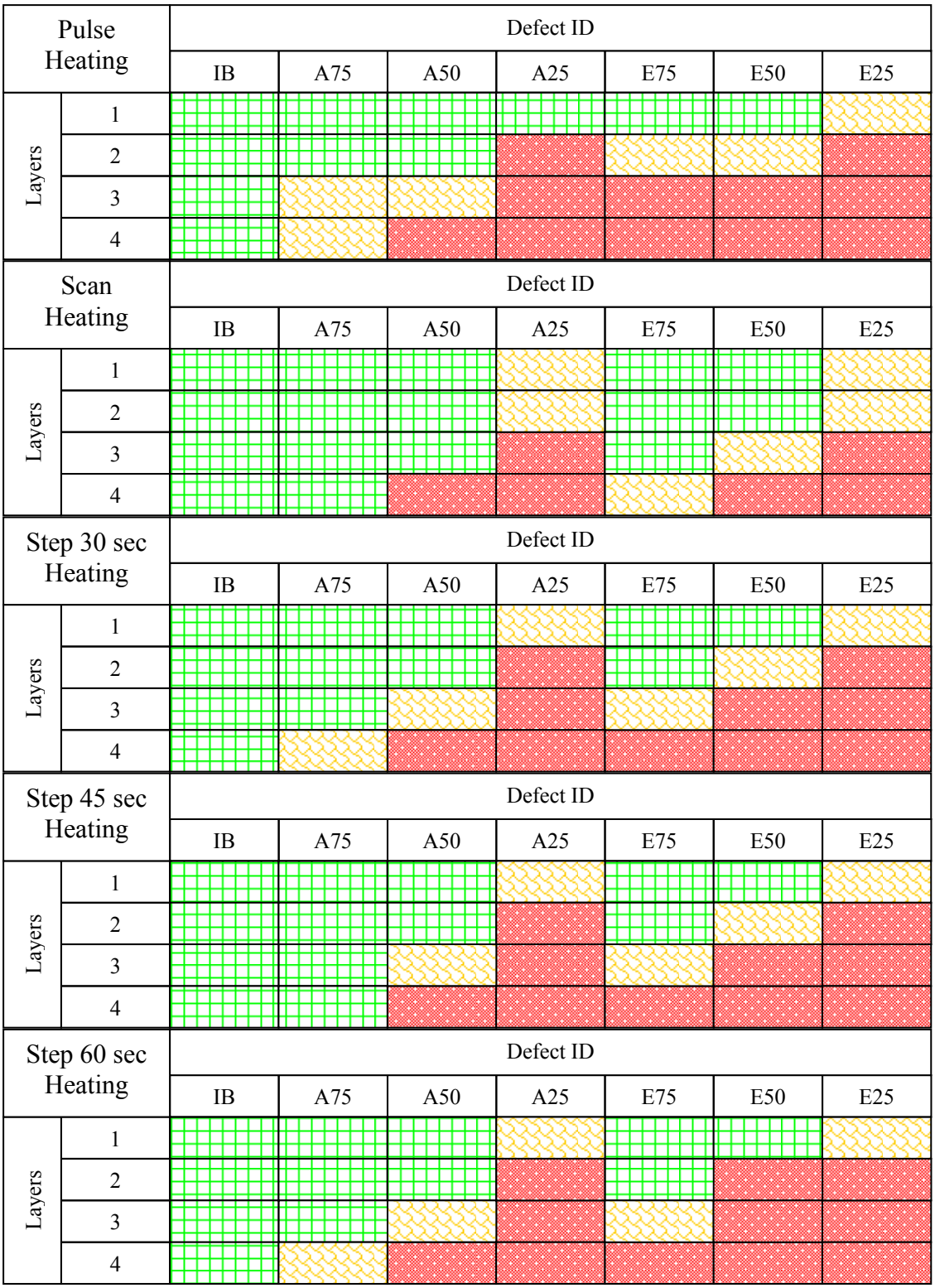

Figure 6-38. Summary of general detectability for flash, scan, and long-pulse heating

Another important measure of detectability is ΔT_{max}. Defects with higher values of ΔT_{max} are more likely to be detected for several reasons:

- Resolution of the camera
- Noise in the image
- Easier to see in color scale

Figure 6-39 provides a series of bar charts for three of the defects that were examined: IB, A75, and E75. These defects were chosen since they provide a reasonable representation of the behavior that was observed for all defects. The x-axis of these charts denotes the heating method and the y-axis provides the measured ΔT_{max} for the defect.

Results for Specimen A-1 are provided in Figure 6-39A. The highest value of ΔT_{max} observed for Defect IB was obtained using the scan heating method (18.8°C). The lowest value for ΔT_{max} was obtained with the pulse heating method (3.3°C). The three different pulse durations that were investigated for the long-pulse heating method provided different results. There is a noticeable trend of increasing ΔT_{max} with increasing pulse duration (ΔT_{max} = 12.7°C, 16.9°C, and 18.1°C for the 30, 45, and 60 sec pulse durations, respectively). The 19 mm diameter defects followed a similar trend.

A similar trend was observed for the two, three, and four-layer specimens.

- The scan heating method produced the highest values for ΔTmax.
- The smaller diameter defects produced lower ΔTmax values
- Epoxy-filled defects produced lower ΔTmax values

It should be mentioned again that the results for Defect IB on Specimen A-2 are influenced by the unintentional defects between the top and second layer of composite. The ΔT_{max} values presented in Figure 6-39B for Defect IB actually represent smaller air-filled defects that are closer to the surface.

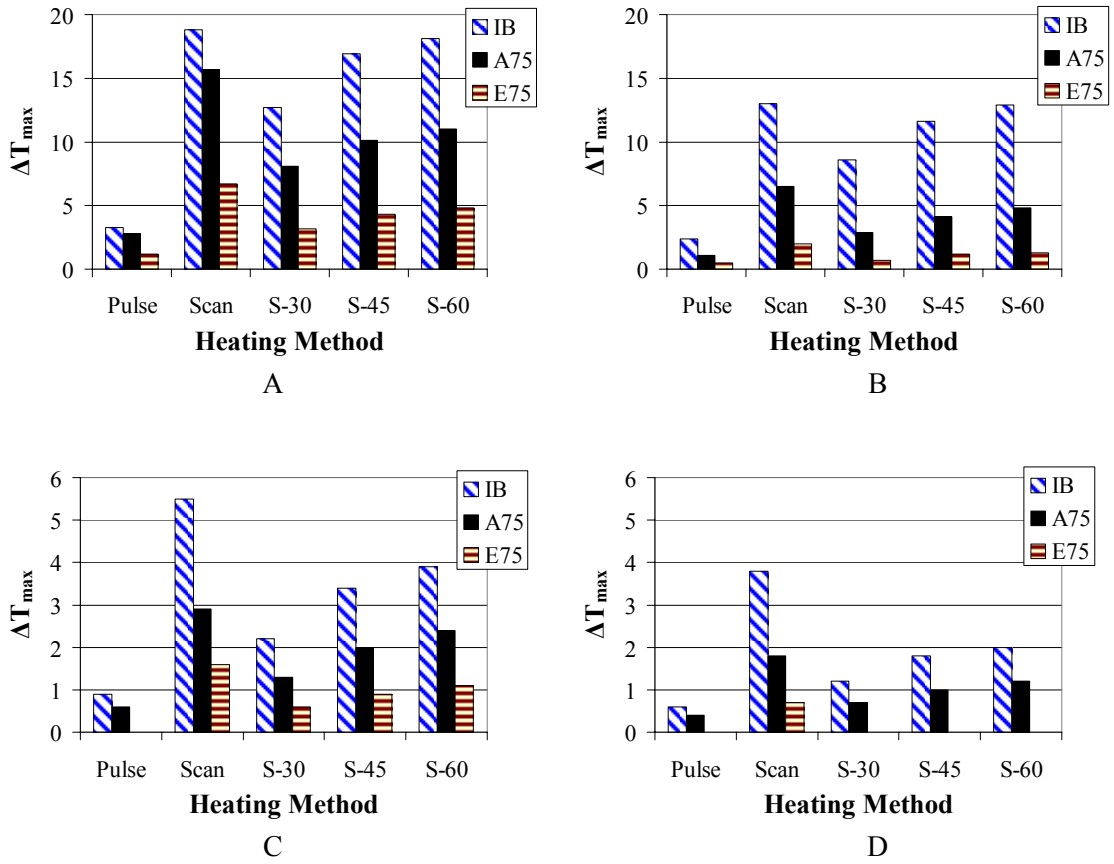

Figure 6-39. Comparison of ΔT_{max} for different heating methods. A) Specimen A-1. B) Specimen A-2. C) Specimen A-3. D) Specimen A-4.

An interesting comparison can be made between the ΔT_{max} results for Specimen A-1 and A-4. For Defect IB on Specimen A-1, the ΔT_{max} values for the scan and step 60 heating methods are very close (relative difference = 3.8%). For Defect IB on Specimen A-4, the relative difference is much larger (62%). The potential significance of this observation is that the scan heating method provides an increasing advantage over the long-pulse heating method as the thickness of the composite increases. This trend is not observed for Defect A75. The relative difference between the scan and step 60 values for Specimen A-1 was 35%. For Specimen A-4, the relative difference was 40%.

For a given defect, ΔT_{max} values are influenced by two factors: intensity of the applied heat flux and heating duration. The relatively high values for ΔT_{max} that were

observed for the scan heating method are due to the high intensity of the applied heat flux. This is an important result because it demonstrates that scan heating is the most effective means for raising the temperature on the surface of a composite in a short period of time. The higher increase in surface temperature then translates into a higher ΔT_{max} for a given defect.

Normalized ΔT_{max} ($\Delta T_{max}/\Delta T_{per}$) is a more useful parameter for investigating the effects of pulse duration on defect detectability. By dividing ΔT_{max} by the average temperature increase that was experienced by the perimeter of the defect boundary, the effects of heat flux intensity are removed. Normalized ΔT_{max} results for defects IB, A75, and E75 are provided in Figure 6-40.

These results indicate that there is an advantage to using longer pulse durations. It is not clear from these data, however, at what point the system reaches steady-state. Consider what would happen if the pulse duration was increased to infinity. At some point in time, the system would achieve a steady-state condition and the normalized ΔT_{max} would reach a maximum value. There are insufficient data to identify how close the 60 sec pulse duration is to a steady-sate condition. For Defect IB on specimens A-1, A-2, A-3 and A-4, normalized ΔT_{max} appears to be leveling off as the pulse duration increases.

These data are insufficient to develop a mathematical relationship for normalized ΔT_{max} as a function of pulse duration, defect depth, defect size, and defect material composition. However, it is possible to use these data to help determine how a particular FRP composite system should be inspected. Results from the following section on defect characterization suggest that a ΔT_{max} of 2.0°C is a reasonable minimum value that is

required to estimate the size and depth of a defect. The normalized ΔT_{max} plots indicate the required ΔT_{per} that must be generated to develop this signal for a specific type of defect. For example, assume that an IRT inspection is going to be conducted on a three-layer carbon FRP system and the smallest defect of interest is 19 mm in diameter. If a long-pulse setup is going to be used with a 30 sec pulse duration, the minimum required temperature increase for the defect-free area (ΔT_{per}) is 14.8°C. Once this quantity has been obtained, it becomes a matter of determining the appropriate lamp intensity and lamp configuration required to generate the 14.8°C temperature increase.

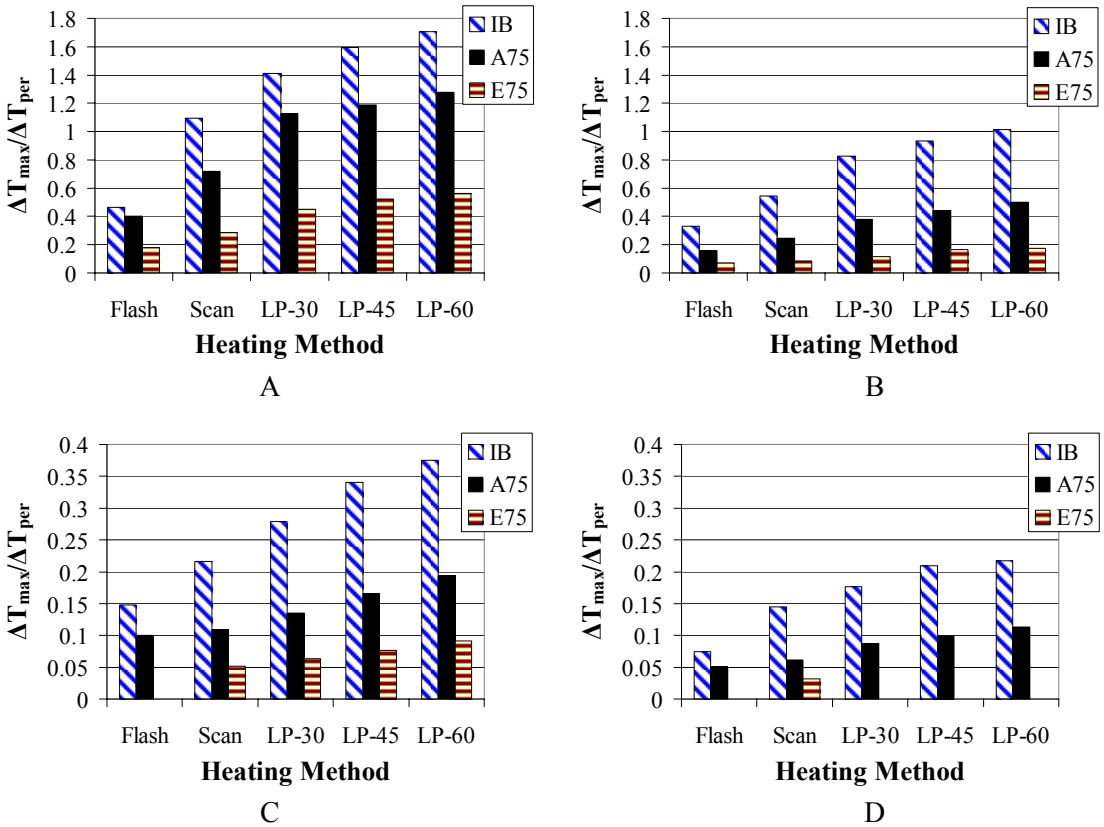

Figure 6-40. Comparison of normalized ΔT_{max} for different heating methods. A) Specimen A-1. B) Specimen A-2. C) Specimen A-3. D) Specimen A-4.

Defect Characterization

Defect size

The gradient area method was previously identified as a means for determining the size of a detected defect. The coefficient of variation of the computed radii was also identified as a means for assessing the quality of the defect boundary in the thermal image. Low COV values indicate a well-defined boundary while high COV values indicate a poorly defined boundary. COV results for the three defects under consideration are provided in Figure 6-41. For the air-filled defects in the single-layer specimen (A-1), each of the heating methods produced a COV of less than 0.1 (indicating high detectability). There does not appear to be any strong advantage afforded to a particular heating method. The highest COV value for the epoxy-filled defect (E75) was 0.2. This value occurred during the pulse heating experiment and is likely a result of the weak signal that developed for this defect (ΔT_{max} = 1.2°C). The general trend for the remaining specimens is that radii COV tends to increase with specimen thickness. This is logical since the overall signal strength for defects tends to decrease with FRP thickness.

Figure 6-42 provides a plot of ΔT_{max} vs. radii COV for each of the detected defects in series A. If all of the defects had been detected for each of the heating methods, this plot would contain a total of 140 data points (7 defects x 4 specimens x 5 heating methods). Since a number of defects were classified as "undetected", ΔT_{max} and COV values were only recorded for 92 points. The plot in Figure 6-42 offers interesting insight into the relationship between ΔT_{max} and radii COV. These data indicate that high radii COV values are most likely to occur if ΔT_{max} is less than 2.0°C. If ΔT_{max} is greater than 2.0°C, the radii COV tends to be less than 0.2 (indicating a well-defined defect boundary). This observation has the potential of simplifying the detectability

classification structure that was developed previously in this chapter. Instead of 12 different detectability levels (four based on ΔT_{def} vs. time plot characteristics and three based on radii COV), it may be more efficient to classify defects as follows:

- Well defined defects have a $\Delta T_{max} > 2.0°C$
- Poorly defined defects have a $\Delta Tmax < 2.0°C$

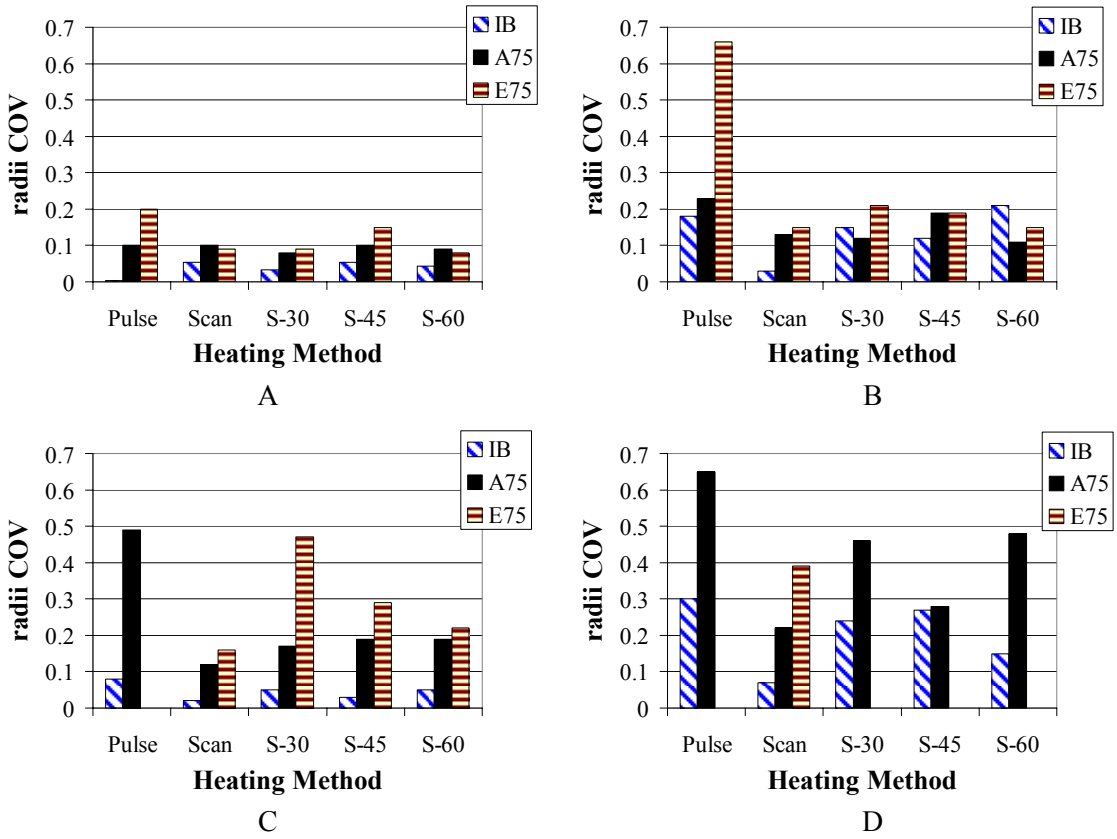

Figure 6-41. Coefficient of variation (COV) of computed radii for different heating methods. A) Specimen A-1. B) Specimen A-2. C) Specimen A-3. D) Specimen A-4.

Using t_{max} to determine depth and material composition

The first ΔT_{def} vs. time plot parameter that will be considered for estimating defect depth is t_{max}. A model for predicting defect depth based on t_{max} is provided in Shepard et al. (2003):

$$circumference * depth = \frac{\alpha}{\sqrt{2}} * t_{max} \qquad (6\text{-}2)$$

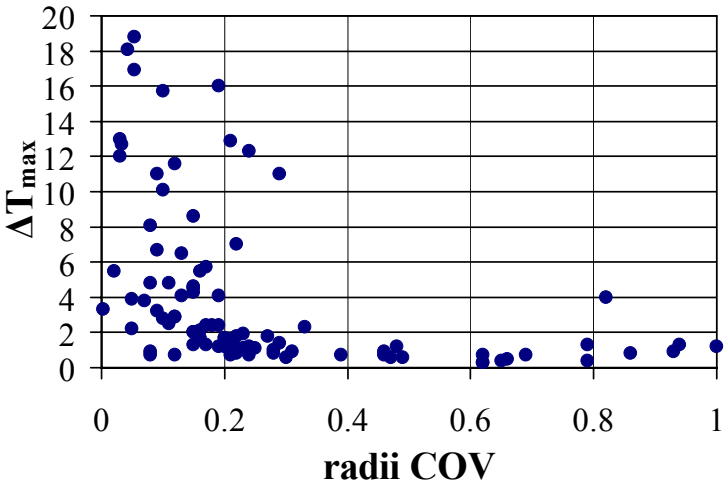

Figure 6-42. Maximum signal vs. radii COV for all detected defects in Series A

In this equation, α is the thermal diffusivity of the material above the defect. This model assumes that the volume of material above the defect acts like a "heat trap". Excess heat that builds up in this volume can only escape through the curved surface of the "imaginary cylinder" above the defect. t_{max} corresponds to the amount of time required to fill-up this volume. As a result, smaller defects at the same depth will have a shorter time to ΔT_{max}. Similarly, if two defects of the same size are considered, the one closer to the surface will have a smaller t_{max}.

Since this model is based on filling a volume above a defect with heat, the time associated with the pulse duration will have an impact on the time at which ΔT_{max} occurs. As a result, the data generated using the different pulse durations can not be analyzed using this model. This is illustrated by the bar charts in Figure 6-43. For the single-layer specimen (Figure 6-43A), the t_{max} recorded for Defect IB during the flash heating experiment was 12 sec. The same defect resulted in a t_{max} of 2 sec for the 60 sec pulse duration. A similar trend is observed for the remaining defects in all four specimens.

The material composition of the defect also may restrict the use of this model. The t_{max} values obtained for epoxy-filled defects were consistently larger than the values obtained for air-filled defects of the same size. This could be a result of the thin layer of thickened epoxy that was used during specimen construction. Even though this layer is relatively thin compared to the FRP, the thermal diffusivity of the epoxy is much lower. This would result in a larger volume of material above the defect that must be filled (and hence more time).

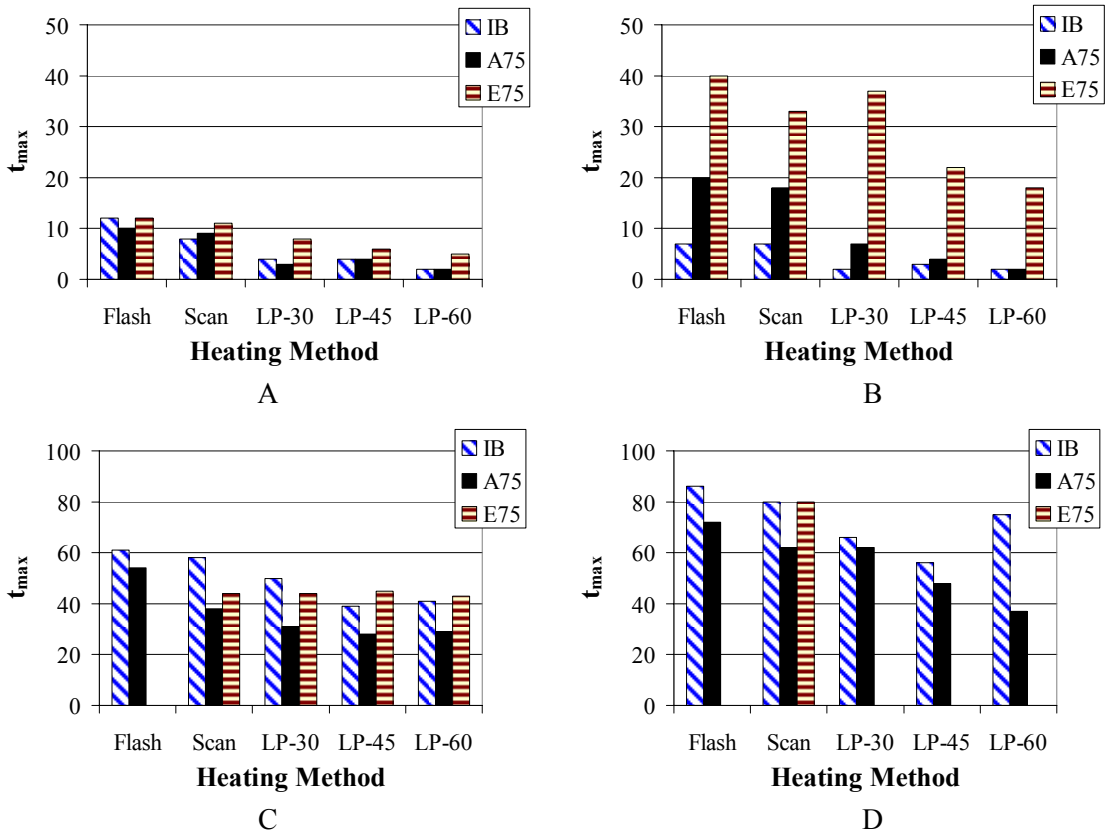

Figure 6-43. Time to maximum signal for different pulse durations (selected defects only). A) Specimen A-1. B) Specimen A-2. C) Specimen A-3. D) Specimen A-4.

The model outlined by Shepard et al (2003) was applied to the data from the flash heating experiments. Only the air-filled defects that were detected in the one, two, three, and four-layer specimens were considered. Defect IB in Specimen A-2 was also removed

from the data set since this defect contained unintentional air voids between the first and second layer of FRP. Figure 6-44 provides a plot of defect circumference C x defect depth D vs. t_{max}. A linear trend is evident, but there is considerable scatter in the data (R^2 = 0.81). The slope of the trend line (4.96 mm^2/sec with 95% confidence interval from 3.18 to 6.75 mm^2/sec) corresponds to a thermal diffusivity (α) of 7.02 mm^2/sec. This value is 3.4 times greater than the value used by Starnes et al (2003) to model the response of an air-filled defect implanted beneath a pre-cured carbon-fiber epoxy laminate and 16.7 times greater than the diffusivity value for carbon FRP provided in Maldague (2001).

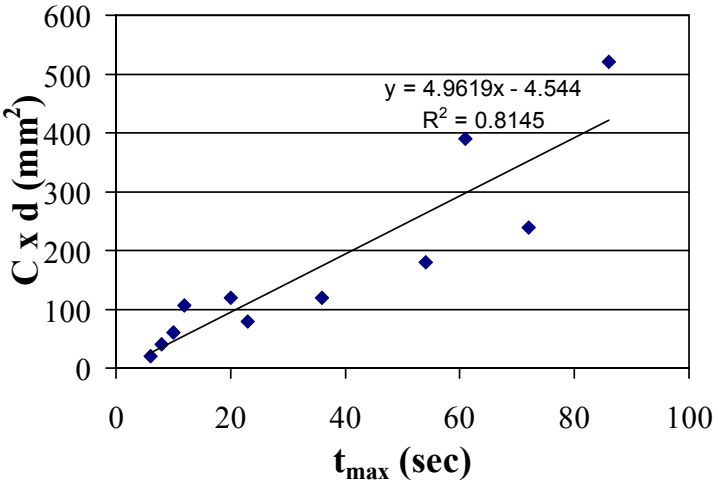

Figure 6-44. Defect circumference (C) x depth (d) vs. t_{max} for flash experiments (air-filled defects only)

It should be noted that the ΔT_{def} vs. time plots that were used to extract the t_{max} values in Figure 6-44 had relatively low ΔT_{max} values (weak signals). Only three of the 11 data points came from signals with ΔT_{max} greater than 2.0°C. It was previously noted that it was not possible to obtain a precise value for t_{max} for these relatively weak signals. This could help to explain some of the scatter in the data.

These data do not support using t_{max} as an indicator of defect depth and material composition. In order to eliminate the effects of pulse duration, the surface should be heated using a flash system. This type of heating resulted in the lowest levels of detectability and the weakest signals for defects. The model proposed by Shepard et al (2003) also fails to account for the material composition of a defect. According to this model, the t_{max} for an air and epoxy-filled defect with the same diameter at the same depth should be the same. Observations from the flash heating experiment do not support this conclusion.

Using $t_{1/2}$ for determining depth and material composition

The second parameter considered for determining depth and material composition was defect half-life ($t_{1/2}$). Unlike t_{max}, $t_{1/2}$ did not appear to be influenced significantly by pulse duration. Results for each of the specimens in Series A are provided in Figure 6-45.

The model presented by Shepard et al (2003) can be modified as follows to accept $t_{1/2}$ as an input:

$$circumference * depth = A * t_{1/2} \qquad (6\text{-}3)$$

In this equation, A represents an unknown constant. In the previous model, t_{max} was described as being proportional to the time required to "fill-up" the volume above the defect. This explanation does not seem correct since the time required to fill-up the volume is independent of the size of the defect (assuming that the surface experiences uniform heating in the vicinity of the defect). If, however, the half-life of the signal can be described as the time required for the excess heat retained above the defect to drain into the surrounding defect-free area, it is logical to include both the depth and size

parameter in the model. In this case, the size parameter is the defect circumference which is directly proportional to the defect diameter.

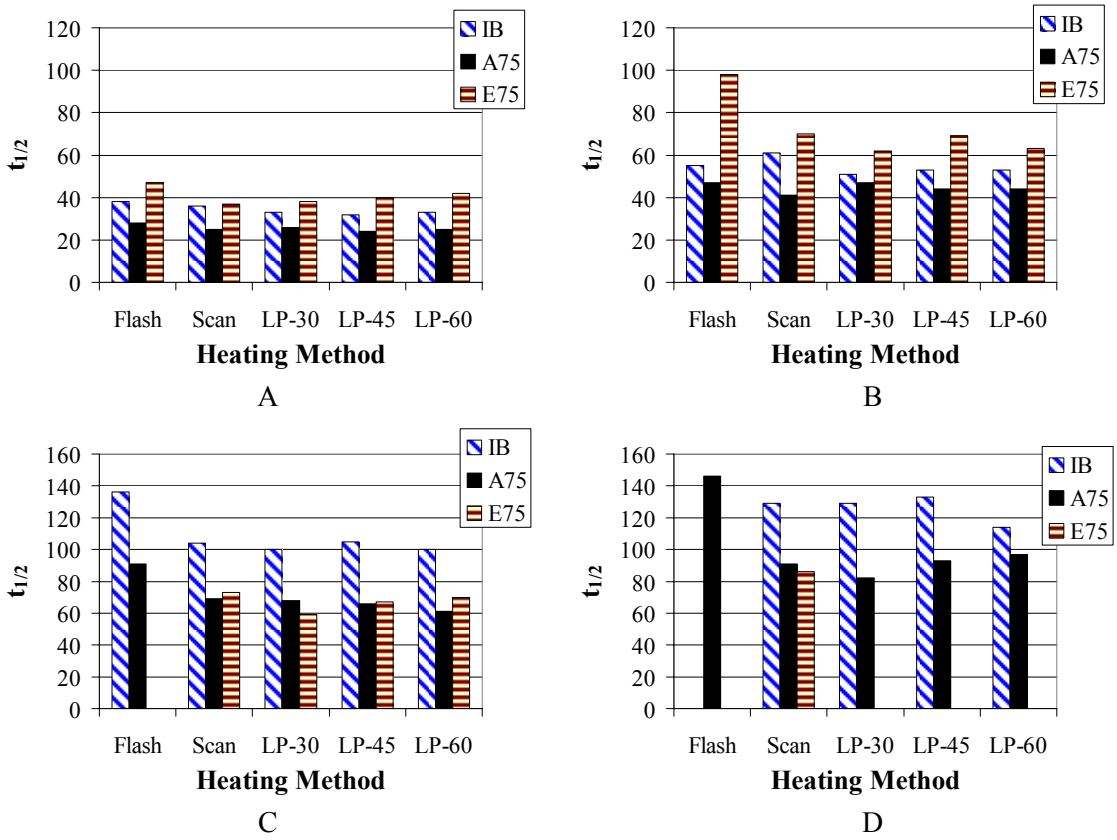

Figure 6-45. Signal half-life for different pulse durations (selected defects only). A) Specimen A-1. B) Specimen A-2. C) Specimen A-3. D) Specimen A-4.

Figure 6-46 provides a plot of defect circumference C x defect depth D vs. $t_{1/2}$. The points on this graph represent data from all of the heating methods for air-filled defects with ΔT_{max} values greater than 2.0°C. The sample size for this analysis was 30. A linear regression analysis resulted in a slope of 4.33 mm^2/sec (R^2 = 0.97, 95% confidence interval = 4.03 to 4.63). This value is surprisingly close to slope obtained in the C x d vs. t_{max} regression analysis. The resulting curve-fit for the $t_{1/2}$ data, however, is much better as evidenced by the higher R^2 value (0.81 vs. 0.97) and narrower 95% confidence interval for the slope. A second regression analysis was performed for the $t_{1/2}$ data in which the

y-intercept was forced to zero. The resulting slope was 3.6 mm^2/sec (R^2 = 0.92, 95% confidence interval = 3.35 to 3.85).

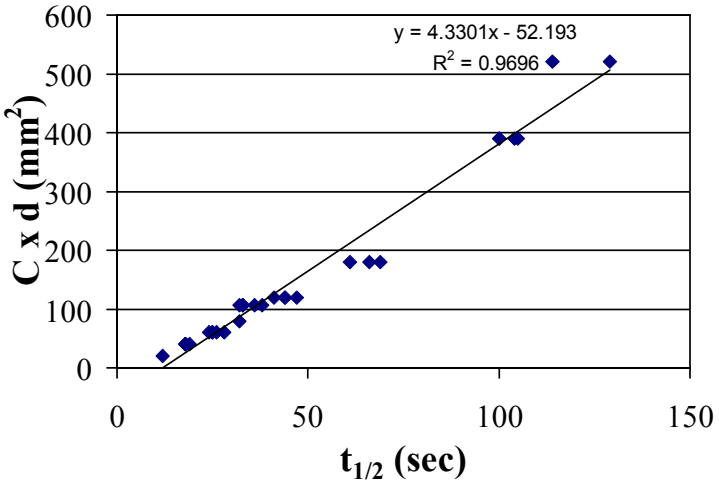

Figure 6-46. Plot of defect circumference C x depth D vs. $t_{1/2}$ for all heating methods (air-filled defects with ΔT_{max} > 2.0°C)

A similar analysis was performed for the epoxy-filled defects in Series A. The plot of C x d vs. $t_{1/2}$ is provided in Figure 6-47. Only defects with ΔT_{max} greater than 2.0°C were considered in the analysis. Since ΔT_{max} values for epoxy-filled defects tend to be lower than air-filled defects, the sample size for this analysis was limited to 9 observations. The slope determined by the linear regression analysis was 1.81 mm^2/sec (R^2 = 0.99, 95% confidence interval = 1.64 to 1.99).

The physical explanation for why epoxy-filled defects have a longer half-life than air-filled defects was not found in the literature. A possible explanation is that epoxy-filled defects store more energy and hence the defect material maintains a higher temperature for longer periods of time than the air-filled defects. Under this scenario, the heated epoxy acts like a heat source after the heat stored in the material above the defect drains away to the perimeter.

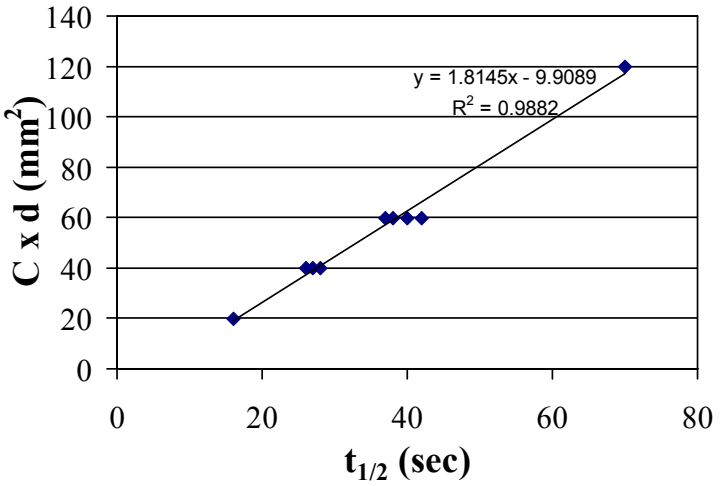

Figure 6-47. Plot of defect circumference C x depth D vs. $t_{1/2}$ for all heating methods (epoxy-filled defects with $\Delta T_{max} > 2.0°C$)

Determining Depth and Material Composition Using Pulse Analysis Data

Data from the pulse analysis experiments suggests that defect half-life ($t_{1/2}$) is a strong indicator of defect depth and material composition. To apply the model described in Equation 5-3, the only quantities that must be known are the size (diameter) of the defect and half-life. It was shown that if a ΔT_{max} value of 2.0°C or greater is obtained for a defect, the gradient area method will provide an accurate estimate of defect size. This minimum ΔT_{max} of 2.0°C also ensures that the $t_{1/2}$ measured for a defect is accurate.

An example will be presented to illustrate how this model can be applied to IRT data. The thermal image provided in Figure 6-48 was collected during a long-pulse heating experiment (60 sec pulse duration) that was conducted for specimens from Series B and Series C. ΔT_{def} vs. time plots were generated for the four defects labeled A1, A2, A3, and A4 using the procedure that was developed for the Series A specimens. The ΔT_{def} vs. time plot is provided in Figure 6-49 and the relevant parameters have been summarized in Table 6-16.

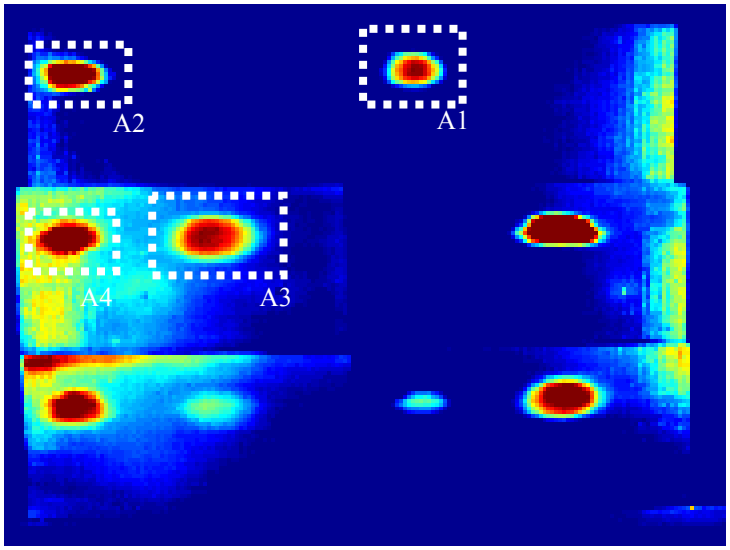

Figure 6-48. Thermal image from long-pulse experiment (Series B and C specimens)

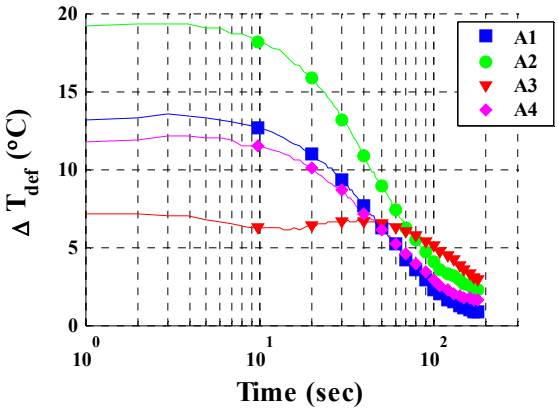

Figure 6-49. Defect signal vs. time plot for defects shown in Figure 6-48

These are sufficient data to enter the plots of C x d vs. $t_{1/2}$. There are two possibilities that must be considered for each defect: (1) the defect is air-filled and (2) the defect is epoxy-filled. To check the air-filled assumption, an estimate of C x d (circumference x depth) is computed using the best-fit line shown in Figure 6-46. Since the defect diameter was also measured from the thermal image, the depth of the defect can be estimated. The process is repeated for the epoxy-filled assumption using the

equation shown in Figure 6-47. The results from both estimates are summarized in the columns labeled "Air Depth" and "Epoxy Depth" in Table 6-16.

At this point, the air vs. epoxy question is still unanswered. Consider the results for Defect A1. Based on the $t_{1/2}$ and defect diameter measured during the long-pulse experiment, this defect is either air-filled with a depth of 0.98 mm OR epoxy-filled at a depth of 0.50 mm. If information about the thickness of each layer in the FRP system is known, it is relatively straightforward to deduce which estimate is accurate. In this case, where 1 mm thick layers were applied, the correct conclusion would be that the defect is air-filled and is 1 mm below the surface. A similar conclusion can be drawn about Defect A2.

Table 6-16. Defect data and predicted depth for defects shown in Figure 6-48

Defect ID	Image Diameter (mm)	ΔT_{per} (°C)	ΔT_{max} (°C)	$\Delta T_{max}/\Delta T_{per}$	$t_{1/2}$ (sec)	Air Depth (mm)	Epoxy Depth (mm)
A1	43	6.3	13.5	2.2	43	0.98	0.50
A2	38	9.0	19.3	2.2	43	1.1	0.56
A3	52	12.1	6.7	0.6	118	2.8	1.24
A4	36	15.0	12.1	0.8	48	1.4	0.68

If no additional information is known about the FRP system, other parameters can be used to assist in the characterization process. It must be noted, however, that the remaining parameters that were extracted from the ΔT_{def} vs. time plots are dependent on pulse duration. The discussion becomes more interesting when Defect A3 is considered. The analysis procedure described above indicates that this defect is either air-filled with depth D = 2.8 mm or epoxy-filled with d = 1.24 mm. For practical purposes, these data can be interpreted as air-filled beneath 3 mm of FRP or epoxy-filled beneath 1 mm of FRP.

Normalized ΔT_{max} was used as an additional parameter to help determine the depth and material composition of the defect. Figure 6-50 provides a plot of normalized ΔT_{max} vs. defect diameter data that were collected during the long-pulse (60 sec) experiments conducted on specimens A-1 and A-3. Only data for the epoxy-filled defects are provided from Specimen A-1. Only data from the air-filled defects are provided for Specimen A-3. The unknown data point is also plotted on the graph as a separate series. The objective of this plot is to investigate which data series the unknown point belongs to. A visual inspection of the graph indicates that the unknown point follows the trend of the 3-layer air specimen. It must be noted, however, that this conclusion requires extrapolation of data and is only based on three observations. The final conclusion then is that the defect is air-filled and is 3 mm below the surface.

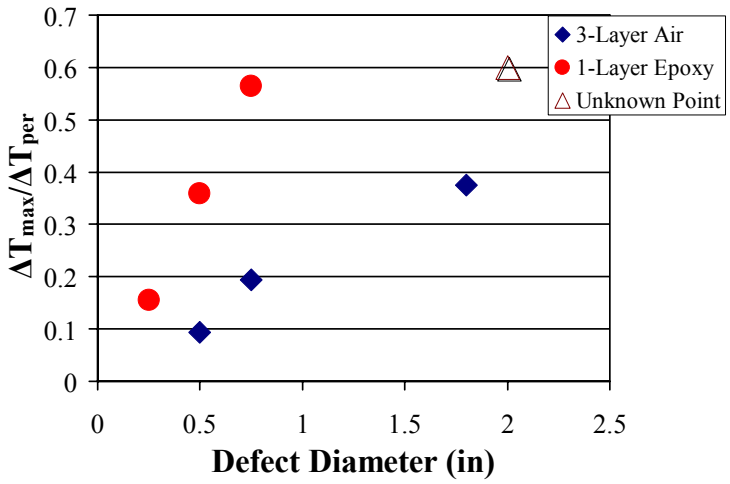

Figure 6-50. Characterization of Defect A3 in Figure 6-48

Defect A4 presents another interesting problem. The C x d vs. $t_{1/2}$ analysis indicates that this defect is either air-filled at a depth of 1.4 mm or epoxy-filled at a depth of 0.67 mm. Neither of these conclusions is consistent with the information known about the FRP system (1 mm thick layers). Once again, normalized ΔT_{max} was investigated to

try and determine which of the following assumptions is correct: (1) the defect is air-filled beneath one layer of FRP or (2) the defect is epoxy-filled beneath one layer of FRP.

Figure 6-51 provides a plot of normalized ΔT_{max} vs. defect diameter data collected for Specimen A-1 during the 60 sec long-pulse experiment. Data for the air-filled and epoxy-filled defects are provided. In this case, a visual inspection of the data indicates that the unknown point follows the trend of the epoxy-filled defects. Again, this requires extrapolation based on three observations.

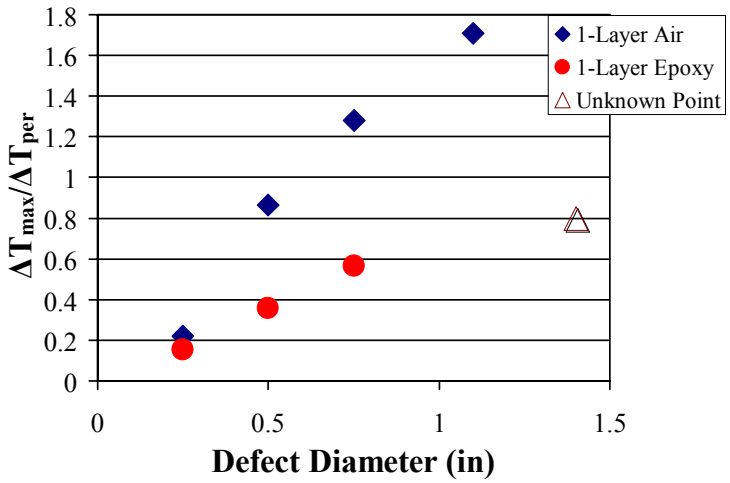

Figure 6-51. Characterization of Defect A4 in Figure 6-48

A comparison of the predicted and actual properties of the defects is provided in Table 6-17. All of the predictions turned out to be correct with the exception of Defect A4. First, defects A1, A2, and A3 were all located at the interface of the FRP and concrete. This defect configuration was identical to the defect configurations used in the development of the model (specimens A-1, A-2, A-3, and A-4). Defect A4, however, was located between the top and second layer of FRP in a three-layer FRP system (inter-lamina bubble on Specimen B-MC-3).

Table 6-17. Predicted and actual properties of defects in Figure 6-48

	Predicted properties		Actual properties	
Defect ID	Depth (mm)	Material	Depth (mm)	Material
A1	1	Air	1	Air
A2	1	Air	1	Air
A3	3	Air	3	Air
A4	1	Epoxy	1	Air

This apparent breakdown of the model can be explained by examining the response of ΔT_{per} while the specimen is being heated. The final value of ΔT_{per} that was achieved due to heating is clearly different among all four defects. This difference is a result of two factors: (1) the location of the perimeter with respect to the heat source and (2) the thickness of the FRP composite. This concept is illustrated in Figure 6-52.

To eliminate the influence of the first factor (proximity to the heat source), four new areas were identified (A1, A2, A3, and A4 in Figure 6-52A). Areas A1, A2, and A3 were all chosen on a specimen with a single layer of FRP. Area A4 was placed on a specimen with three layers of FRP. The location of these areas was selected such that they were all located approximately the same distance from the heat source. Figure 6-52B provides a plot of the average temperature increase experienced by the perimeter of each area vs. the square root of time. A major distinction can be made between the areas that were placed on the single-layer composite (A1, A2, and A3) and the area placed on the three-layer composite (A4). For the three-layer composite, the temperature increase is nearly linear as a function of the square root of time ($t^{1/2}$). For the single-layer systems, the temperature increase exhibits a non-linear trend in which the slope of the line decreases with increasing $t^{1/2}$ (second derivative < 0).

The cause of this change in slope will be investigated in greater detail in the following section on step analysis. For now, it is important to focus on the impact this observation has on the ΔT_{def} vs. time plot for the original A4 defect shown in Figure 6-

48. First, the relative increase in ΔT_{per} experienced by Defect A4 will tend to decrease the computed value of ΔT_{def} and ΔT_{max}. The smaller ΔT_{max} combined with the larger ΔT_{per} will also tend to push the normalized ΔT_{max} lower. The increase in ΔT_{per} will also increase defect half-life since the overall temperature gradient between the middle of the defect (hottest point) and the edge of the defect will be lower (i.e. it will take more time for the excess heat stored above the defect to drain into the surroundings). The resulting decrease in normalized ΔT_{max} and increase in defect half-life give the impression that the defect is either deeper than it actually is or that the defect is filled with something other than air. For the case of Defect A4, this effect was significant enough to result in a misinterpretation of the data.

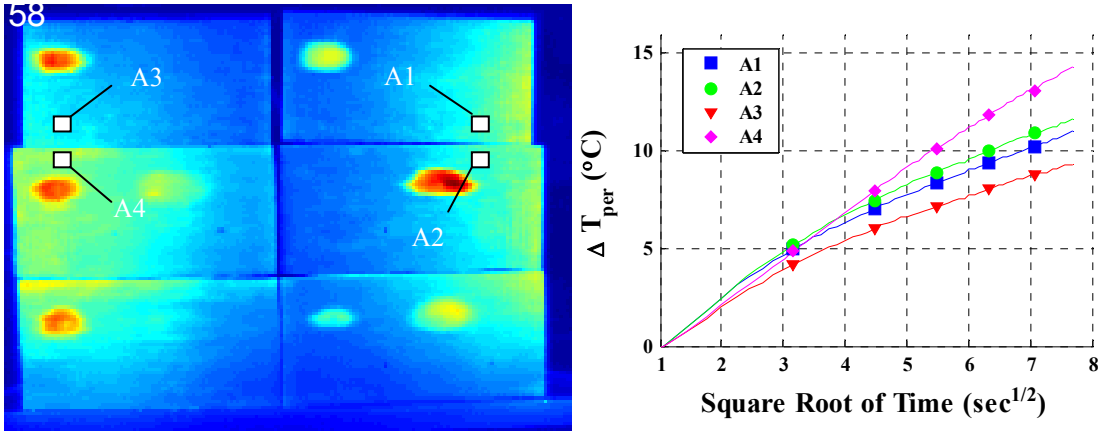

Figure 6-52. Temperature increase for select areas

Summary of Pulse Thermography Results

Three of the heating methods described in Chapter 4 were used to generate data for a pulse thermography analysis of the specimens in Series A. The distinguishing characteristic of the pulse analysis is that data are collected after the heat source is removed. Major conclusions can be summarized as follows:

- Of the three heating methods that were investigated, the scan heating approach resulted in the highest levels of detectability for the greatest number of defects. This heating method generates high temperature increases over the surface of the composite which in turn lead to higher values of ΔT_{max} for detected defects.

- 2.0°C was identified as the minimum value of ΔT_{max} required for defect characterization. Defects with ΔT_{max} values less than 2.0°C did not generate well-defined boundaries when the gradient area method was applied. Defects with weak signals also generated ΔT_{def} vs. time with parameters that could not be extracted with precision (t_{max} and $t_{1/2}$).

- Normalized ΔT_{max} and t_{max} are both dependent on pulse duration. $t_{1/2}$ was shown to be relatively independent of pulse duration.

- The C x d vs. $t_{1/2}$ model can be used as a good starting point in the process of defect characterization. This model generates two possible scenarios for the depth of each detected defect: (1) a depth assuming the defect is air-filled (2) a depth assuming the defect is epoxy-filled.

- The C x d vs. $t_{1/2}$ model was calibrated using specimens in Series A. The implanted defects in these specimens were all located at the FRP/concrete interface. This model was applied to four defects in other specimens (Series B and Series C). For defects occurring at the FRP concrete interface, the predicted depth and material composition were accurate. When this model was applied to a defect that occurred between layers of FRP, the predicted material composition did not match the actual composition. There was also a relatively large error in the predicted depth.

Step Thermography Analysis

Step thermography analysis involves monitoring the surface temperature of a sample during heating. This section contains results for Series A specimens that were heated for 60 seconds using the long-pulse setup described in Chapter 4.

Analysis Procedures

The surface temperature increase (ΔT) as a function of time due to the application of a uniform heat flux is given by the following equation (Maldague 2001):

$$\Delta T = C_c \sqrt{t} \qquad (6\text{-}4)$$

t = time
C_c is a constant that depends on the following:

- Thermal properties of the material

- Emissivity and reflectivity of the surface
- Intensity of the applied heat flux

For a sample containing two layers of material, the temperature increase ΔT is given by the following (Osiander et al. 1996):

$$\Delta T = C_c \sqrt{t}\left\{1 + 2\sum_{n=1}^{\infty}(-\Gamma)^n\left[\exp\left(-\frac{n^2L^2}{\alpha_1 t}\right) - \frac{nL\sqrt{\pi}}{\sqrt{\alpha_1 t}}erfc\left(\frac{nL}{\sqrt{\alpha_1 t}}\right)\right]\right\} \qquad (6\text{-}5)$$

C_c = Constant
t = time
Γ = Thermal mismatch factor
L = Thickness of top layer
α_1 = Thermal diffusivity of top layer

Thermal diffusivity, α, is defined as:

$$\alpha = \frac{k}{\rho c} \quad (6\text{-}6)$$

k = thermal conductivity
ρ = density
c = specific heat

The thermal mismatch factor, Γ, is defined as:

$$\Gamma = \frac{e_2 - e_1}{e_2 + e_1} \qquad (6\text{-}7)$$

e_1 = Thermal effusivity of top layer
e_2 = Thermal effusivity of bottom layer

Thermal effusivity, e, is defined as:

$$e = \sqrt{k\rho c} \qquad (6\text{-}8)$$

Typical thermal properties for materials used in the current study are provided in Table 6-18. It should be noted that different sources provide a range of properties for the materials under consideration. "Carbon FRP" represents a very broad category of composite materials. Different CFRP composites can have varying fiber volume

fractions. CFRP composites that are applied using the wet layup method for field applications to concrete will tend to have lower fiber volume fractions (more epoxy and more voids) than CFRP composites constructed using vacuum bagging and other advanced techniques used in a factory setting. The low thermal conductivity of epoxy will lead to a higher thermal diffusivity and thermal effusivity for CFRP composites applied to concrete than what would normally be expected for an aerospace quality composite.

Table 6-18. Typical thermal properties for materials of interest (Maldague 2001)

Material	k (W/m-K)	ρ (kg/m^3)	c (J/kg-K)	α x 10^6 (m^2/sec)	e (J/m^2-K)	Γ_{FRP}
Concrete (moist)	1.8	2500	1280	0.56	2400	0.38
Concrete (dry)	1.0	2400	800	0.53	1683	0.22
Carbon FRP (⊥ to fibers)	0.8	1600	1200	0.8	1067	0
Epoxy	.2	1300	1700	0.14	795	-0.15
Air	0.024	1.2	700	28	4.5	-1.0

From the standpoint of step thermography analysis, the most important physical property is thermal effusivity. Consider the one-dimensional model of a two-layer sample provided in Figure 6-53. If the two materials have the same thermal effusivity, the thermal mismatch factor, Γ, will be zero. In this case, Equation 6-5 reduces to Equation 6-4 (homogeneous case). The surface temperature increase (ΔT) is plotted as a function of time$^{1/2}$ in Figure 6-53. For Γ = 0, the resulting curve is linear. If Γ is not equal to zero, the surface temperature rise will diverge from the homogenous case at some transit time, t_T, which is the time required for the thermal front to travel from the surface to the second layer. t_T is proportional to the thickness of the top layer squared divided by the thermal diffusivity (L^2/α).

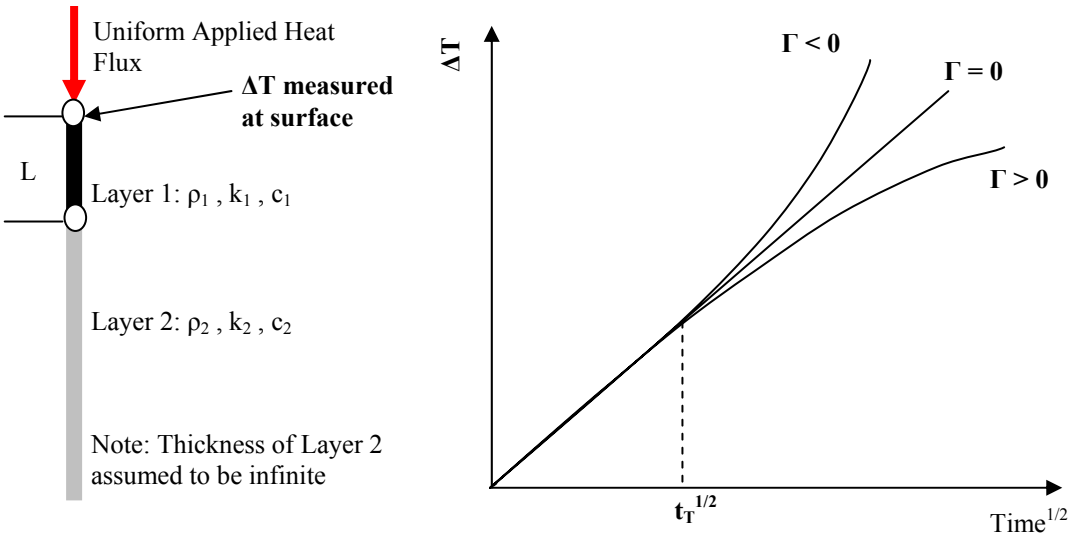

Figure 6-53. Surface temperature increase due to uniform heat flux applied to multi-layer specimen

Based on the values provided in Table 6-18, the thermal mismatch factor for carbon FRP and concrete (assuming the FRP is on the surface) is 0.22. This indicates that once the thermal front reaches the FRP concrete interface, the rate of temperature rise on the surface will decrease (second derivative will become negative).

Since the thermal effusivity of air is significantly smaller than the effusivity of concrete, the thermal mismatch factor for an air-filled defect will always approach -1. This will result in a relative surface temperature increase with respect to the homogeneous case. Epoxy-filled defects also represent a case where the thermal mismatch factor is less than zero ($\Gamma = -0.15$).

It is interesting to compare the relative magnitudes of Γ for a CFRP/concrete interface and a CFRP/epoxy interface. According to the theoretical model (and assuming the material properties provided in Table 6-18 are correct), the concrete beneath the surface of the CFRP will have a larger effect on the surface temperature than the presence of epoxy. Epoxy results in a relative surface temperature increase ($\Gamma = -0.15$) and the

concrete results in a relative surface temperature decrease ($\Gamma = 0.22$). The previous section on pulse thermography analysis was primarily concerned with monitoring the difference in temperature between a defect area and a surrounding defect-free area. The fact that the "defect-free" area actually consists of a multi-layer material that responds differently than a homogeneous material to thermal stimulation was not considered.

Two factors must also be considered when applying the step heating model to results from the current study: two-dimensional heat flow around defects and non-uniform heating. If the thermal front traveling from the surface does encounter a defect, Equation 5-9 will only apply for as long as the heat flow remains one-dimensional (Osiander et al. 1996). If a thermal gradient is present between the defect area and the surrounding defect-free area, the "backed-up" heat that is stored above the defect drain off into the surroundings by traveling around the defect. Once this occurs, the magnitude of the divergence away from the homogeneous case is reduced.

Non-uniform heating can be addressed by applying a normalization procedure to each pixel in the series of thermal images (Osiander et al. 1996). Normalized ΔT is computed with the following equation:

$$\Delta T_{norm}(t) = \frac{\Delta T(t)}{C_c \sqrt{t}} - 1 \qquad (6\text{-}9)$$

ΔT_{norm} = Normalized change in temperature
C_c = Initial slope of ΔT vs. $t^{1/2}$ curve (°C/sec$^{1/2}$)
t = time

ΔT_{norm} provides an indication of how far the change in temperature for a single point has drifted away from what would be expected for a homogeneous material. Note that for a homogeneous material, Equation 6-9 results in a value of zero for ΔT_{norm} at all values of time. For the case of a non-homogeneous material, ΔT_{norm} will equal zero up to

a certain time (t_T in Figure 6-53) and then diverge. The process is illustrated for two points on Specimen A-1 (one-layer FRP) in Figure 6-54. Point 1 is located very close to the heat source and experiences an overall ΔT of 11.5°C after 60 seconds of heating. Point 2 is located farther from the heat source, which results in a lower ΔT of 6°C after the same heating duration. C_c is computed for each curve by measuring the slope of the line through the points collected for $t < t_T$. For both of the curves shown in Figure 6-54A, t_T occurs at some time between $t^{1/2} = 2$ and $t^{1/2} = 3$. Once C_c is known, ΔT_{norm} can be computed using equation 5-9. The resulting curves for ΔT_{norm} are provided in Figure 6-54B. With the exception of some minor deviation that begins at $t^{1/2} = 6$, the two points display a similar ΔT_{norm} response.

It was observed that the initial slope of ΔT vs. $t^{1/2}$ plots did not pass through the origin. This was likely a result of poor synchronization between the time that the lamps were turned on and the time the first image was recorded. If this were the case, the ΔT response would actually be zero for some time interval between t = 0 and t = 1 sec. This observation could also result from the fact that some time is required for the lamps to reach their maximum output level. In this case, the initial slope of the ΔT vs. $t^{1/2}$ curve would start at a lower value and increase as the lamps reach a constant output level.

In order to apply this method to the data collected during each experiment, the initial slope and corresponding y-intercept was determined using a least-squares regression for the data points obtained between t = 1 sec and t = 4 sec. Since the top layer of FRP was essentially the same for all of the specimens, this initial window proved adequate to capture the trend of the initial response for each pixel.

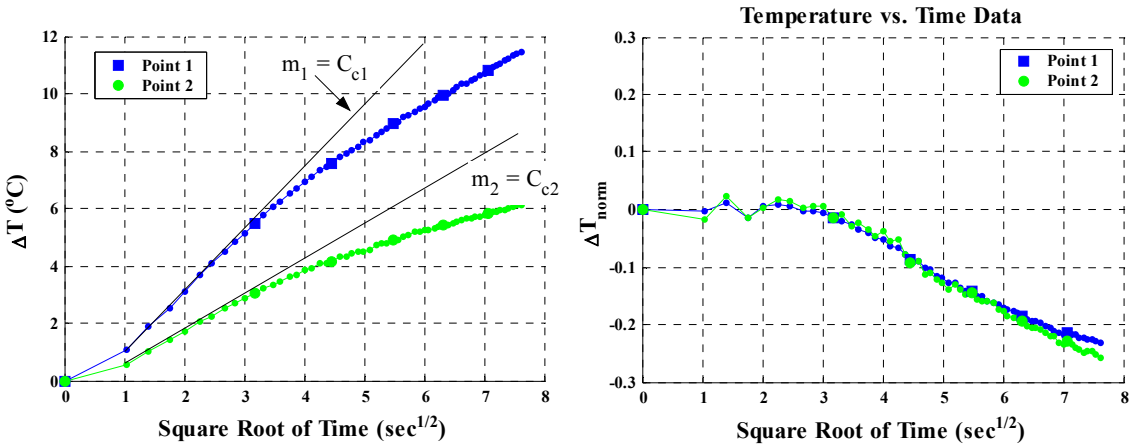

A B

Figure 6-54. Normalizing ΔT for two points on Specimen A-1 for 60 sec pulse duration. A) Raw data. B) Normalized

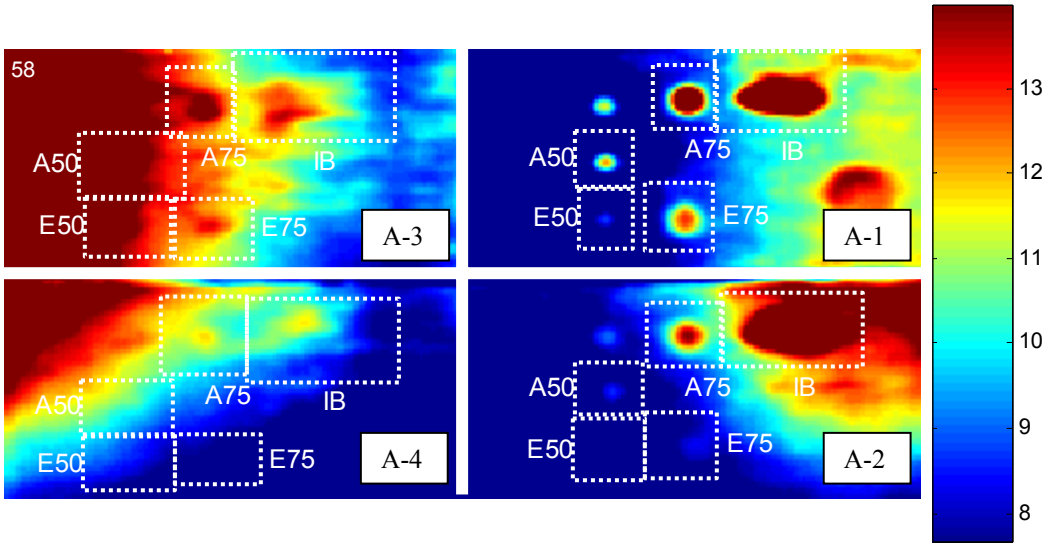

Figure 6-55. ΔT image for Series A specimens (t = 60 sec, long-pulse heating)

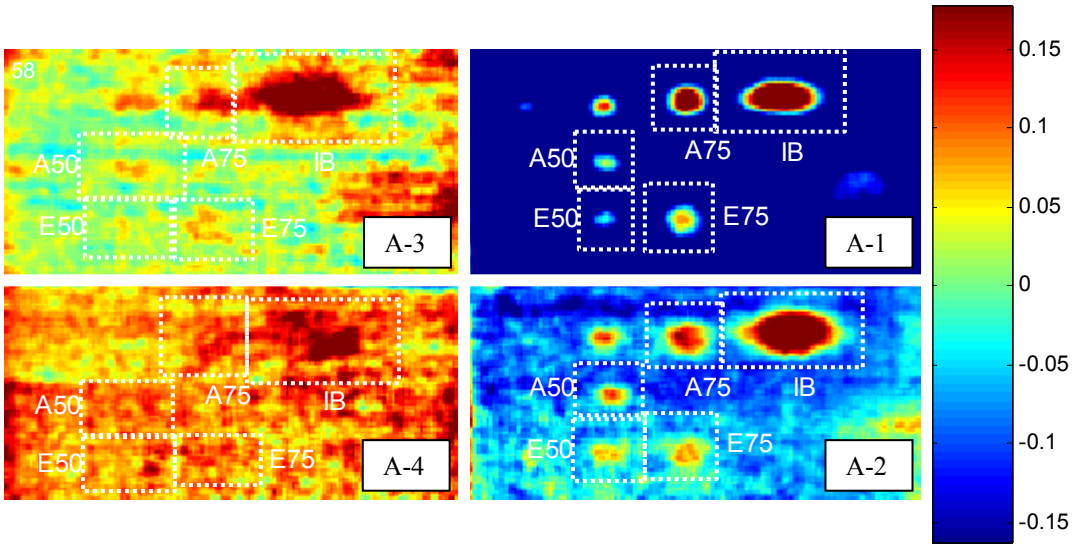

Figure 6-56. Normalized ΔT image for Series A specimens (t = 60 sec, long-pulse heating)

Defect-free areas

One defect-free area was identified on each Series A specimen (labeled DF-1, DF-2, DF-3, and DF-4 in Figure 6-57). The term "defect-free" is used to describe these areas only because there were no implanted defects inside the areas or in the immediate vicinity. Careful inspection of each area, however, did reveal small unintentional defects. The average value of ΔT_{norm} was computed for each area at each time step (NP = total number of pixels inside the area). Outlier pixels due to unintentional defects were removed at each time step. The criterion for discarding a pixel was +/- 2.5 standard deviations away from the mean value. The standard deviation was recomputed after each outlier was removed. After the outlier pixels were removed, the modified mean and standard deviation were computed for each area at each time step. The mean was plotted for each area along with error bars representing +/- 2 σ (Figure 6-58).

The single-layer specimen (A-1) produced similar results to the two points shown in Figure 6-54B: ΔT_{norm} stays close to zero up to $t^{1/2} = 2$ and then decreases as the thermal

front is influenced by the concrete. Ideally, one would expect similar behavior for the remaining specimens with the divergence from zero occurring at a later time depending on the thickness of the FRP composite. This trend, however, was not observed in the two, three, or four-layer specimens. At approximately $t^{1/2} = 2$, the remaining specimens experienced a rise in ΔT_{norm}. At $t^{1/2} = 4.25$, the curve for Specimen A-2 diverges from the trend and the slopes become negative. This curve crosses the $\Delta T_{norm} = 0$ line at $t^{1/2} = 5.75$. The curve for Specimen A-3 assumes a negative slope somewhere between $t^{1/2} = 4$ and $t^{1/2} = 5$. Specimen A-4 does not assume a negative slope until $t^{1/2}$ is approximately 6.75.

One possible explanation for the slight rise in ΔT_{norm} experienced by the multi-layer specimens is contact resistance between layers of FRP composite. This minor thermal resistance could be a result of small air bubbles that may have formed in the thin glass veil present on the bottom side of each layer. This would have the effect of making $\Gamma < 0$ at the interface of two layers (see Figure 6-59). Eventually, the thermal front moves through to the concrete and the normalized ΔT curve assume a negative slope. This behavior might be expected to occur at the interface between the single-layer system and concrete. There are two possibilities as to why this was not observed in the data: (1) the image save rate is insufficient to capture this effect (2) there is adequate epoxy present at the interface of the FRP and concrete.

Table 6-19. Summary statistics for defect-free areas (Series A)

Area ID	Specimen	NP	# of Outliers @ t = 60 sec	Mean @ t=60 sec	Standard Deviation @ t = 60 sec
DF-1	A-1	770	66	-0.29	0.014
DF-2	A-2	780	17	-0.09	0.022
DF-3	A-3	864	32	+0.02	0.024
DF-4	A-4	851	29	+0.08	0.024

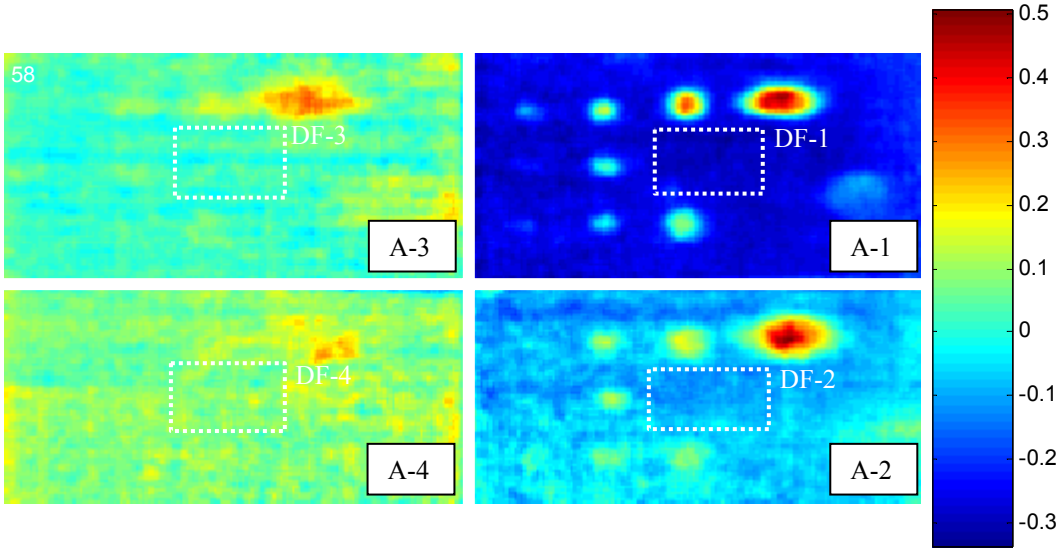

Figure 6-57. Defect-free areas for Series A specimens

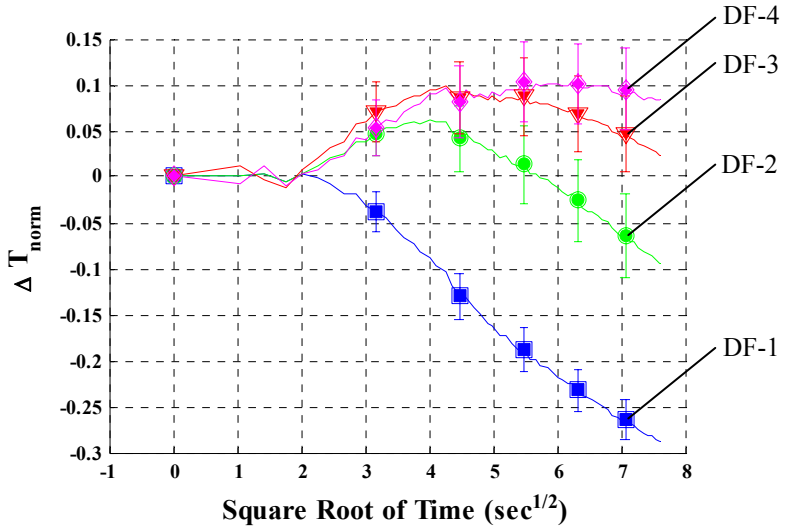

Figure 6-58. Mean value of ΔT_{norm} for defect-free areas on Series A specimens (error bars represent +/- 2 σ)

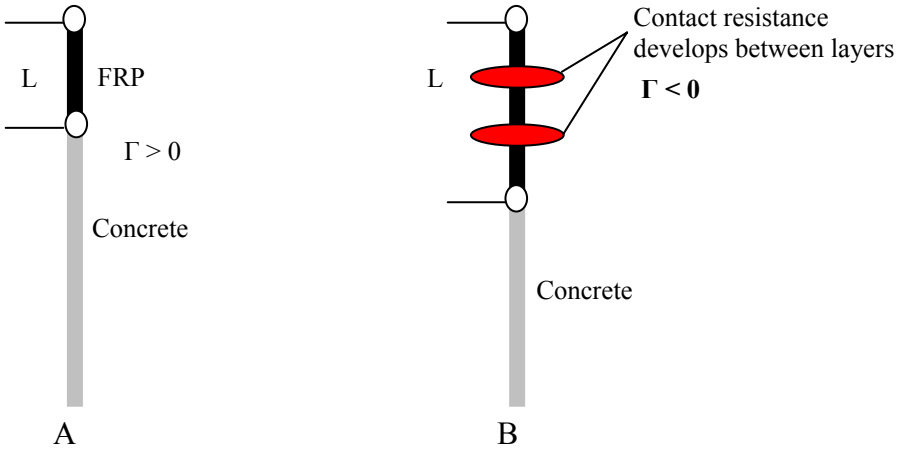

Figure 6-59. One-dimensional model of FRP systems. A) single-layer FRP system. B) multi-layer FRP system with contact resistance

These data indicate that long-pulse heating combined with an analysis of the normalized temperature increase is potentially useful for estimating the thickness of the FRP composite. By the end of heating (t = 60 sec, $t^{1/2}$ = 7.75), the curves for specimens A-1 and A-2 have diverged significantly. The curves for the three and four layer specimens also show signs of divergence; however, there is still substantial overlap in the +/- 2 σ confidence intervals at $t^{1/2}$ = 7.75. It is hypothesized that if the samples were heated for a longer duration, the curves for the three and four-layer systems would also exhibit a statistically significant divergence.

Defect area analysis

The next step in the analysis was to examine the normalized ΔT response of the defect areas (shown in Figure 6-56). ΔT_{def} was computed for each area at each time step using the following equation:

$$\Delta T_{def} = \Delta T_{norm(\max)} - \Delta T_{norm(per_avg)} \qquad (6\text{-}10)$$

ΔT_{def} = Signal strength of defect
$\Delta T_{norm(max)}$ = Maximum ΔT_{norm} bounded by area
$\Delta T_{norm(per_avg)}$ = Average ΔT_{norm} on the perimeter

The process is illustrated for an ideal case in Figure 6-60A and B. Two important parameters that can be used to characterize defects are the time required for ΔT_{def} to become visible, $t_T^{1/2}$, and the rate of increase of the ΔT_{def} curve. $t_T^{1/2}$ is related to the depth of the defect, and rate of increase of the ΔT_{def} curve provides an indication of the material composition of the defect (Maldague 2001). The signal for air-filled defects should increase faster than the signal for epoxy-filled defects.

Figure 6-60C and D provide results from Defect A75 on Specimen A-2. Small, unintentional defects in the FRP system generate a signal for ΔT_{def} for all $t^{1/2} > 2$. This trend was observed for all of the defects that were examined regardless of their actual depth. The ultimate significance of the unintentional defects is that $t_T^{1/2}$ is not a distinct parameter that is easily extracted from a ΔT_{def} vs. $t^{1/2}$ plot. As a result, defining the time at which a defect first becomes "visible" in a series of normalized thermal images requires additional consideration.

Two methods were investigated to assist in defining the time that a defect is first detected. This first method involves establishing a threshold value for ΔT_{def}. The objective of this analysis is to establish a criterion for determining when the signal resulting from the implanted defect is more prominent than the extraneous signal that develops due to background noise. The background noise can be a result of unintentional defects or the natural texture of the composite. It was determined that a plot of the perimeter average +/- 2 standard deviations serves as a good indicator of the overall noise level present in an area. The threshold for detection was then established as the point at which ΔT_{def} exceeds the $\Delta T_{norm(per_avg)} + 2\sigma$.

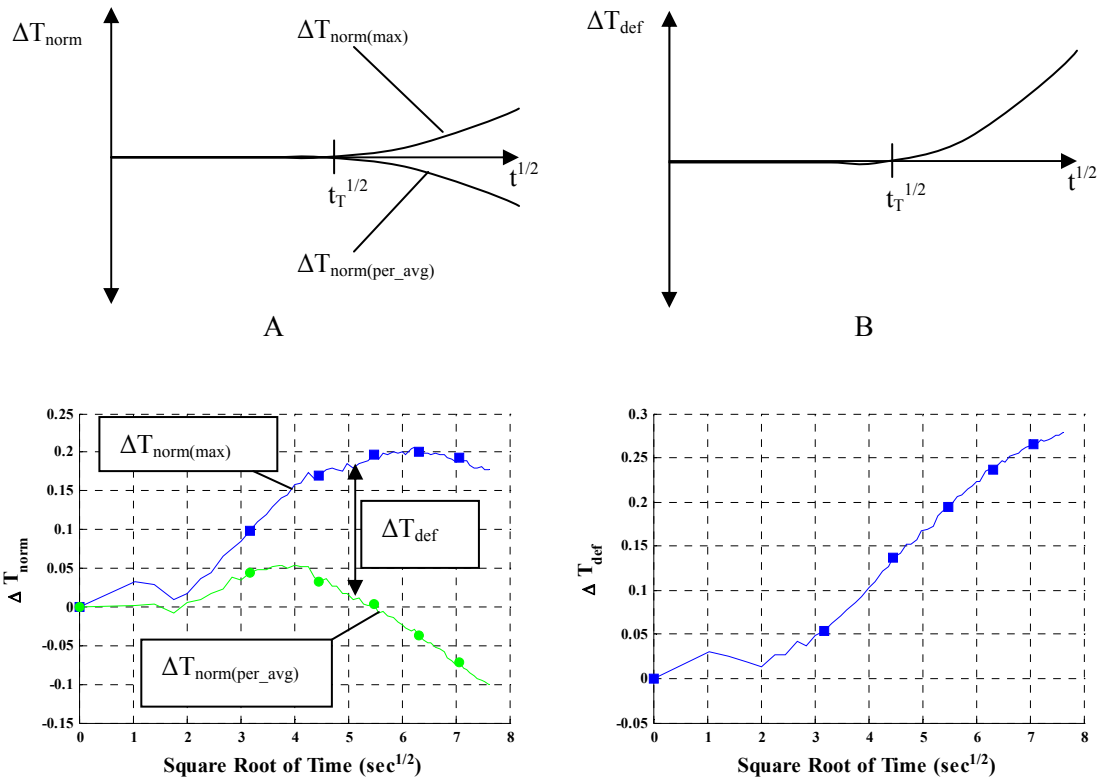

Figure 6-60. Computation of ΔT_{def} from normalized temperature data. A) ΔT_{norm} for idealized case. B) corresponding ΔT_{def} C) ΔT_{norm} for Defect A75, Specimen A-2. D) corresponding ΔT_{def}

The procedure is illustrated for Defect A50 on Specimen A-2 in Figure 6-61. The hatched area in the figure represents the average ΔT_{norm} on the perimeter of the area with a range of +/- 2σ. At $t^{1/2} = 4.2$ (t = 18 sec), ΔT_{def} exceeds the upper boundary defined by $\Delta T_{norm(per_avg)} + 2\sigma$. This point corresponds to $t_T^{1/2}$.

It is important to note that the extracted value for $t_T^{1/2}$ represents a "best-estimate". For the defect described in Figure 6-61, it was determined that the signal for the defect diverged from the surrounding noise at t = 18 sec. Close inspection of the area at t = 13 sec (five seconds before $t_T^{1/2}$) reveals a signal has developed above the implanted defect (Figure 6-62A), but the magnitude is on the same scale as the surrounding noise. At t =

18 sec, the defect is better defined with respect to the surroundings, and by t = 23 sec the defect has risen substantially higher than the surroundings.

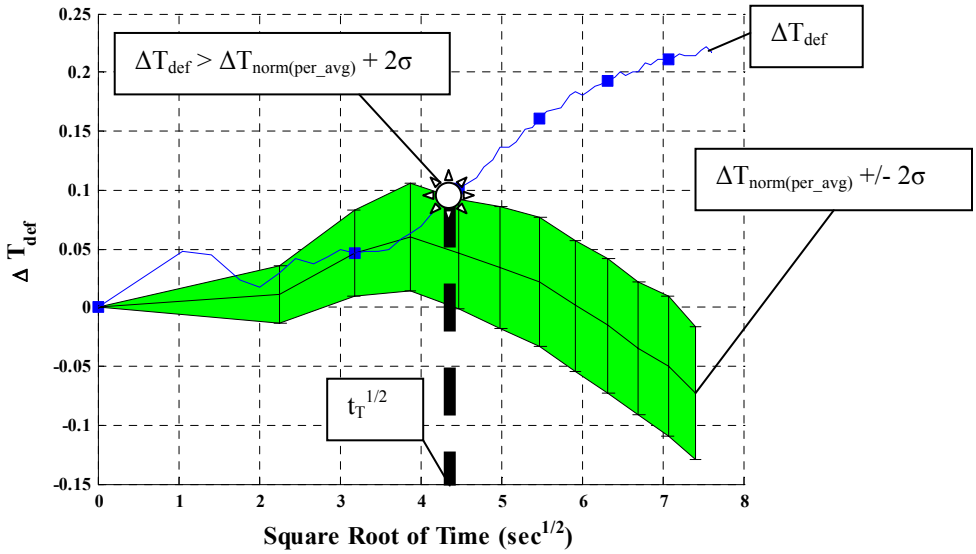

Figure 6-61. Determining point at which defect is detected in ΔT_{def} plots

The second method that was investigated involves computing a two-dimensional cross-correlation coefficient for each defect area at each time step. The two-dimensional cross-correlation coefficient, R, is defined as follows (Matlab User's Guide 2002):

$$R(t) = \frac{\sum_m \sum_n \{[A(t)_{mn} - mean(A(t))] * [B_{mn} - mean(B)]\}}{\sum_m \sum_n [A(t)_{mn} - mean(A(t))]^2 * \sum_m \sum_n [B_{mn} - mean(B)]^2} \quad (6\text{-}11)$$

R(t) = 2-D correlation coefficient at time = t
A(t) = mxn matrix of defect area pixels at time = t
B = mxn matrix of defect area pixels @ time = 60

R provides an indication of similarity between two matrices. The matrix B in Equation 5-11 is populated with the pixel values of the rectangle defining the defect area at t = 60 sec. This matrix represents the "best" image available for the defect of interest. The two-dimensional correlation coefficient is computed at each time step by applying Equation 5-11 to the matrix for the defect area at time t (A(t)) and B. The general

motivation behind performing this computation is that defects close to the surface will correlate more rapidly than deeper defects. Consider the surface plots for Defect A50 (Specimen A-2) provided in Figure 6-62. The R computed at t = 13 sec was 73%. R increases to 87% and 95% for t = 18 sec and t = 23 sec, respectively. R is plotted as a function of time for this defect in Figure 6-63. As long as the defect area at t = 60 sec is used as the reference matrix in Equation 5-11, the resulting R value for all areas will be 1 at t = 60.

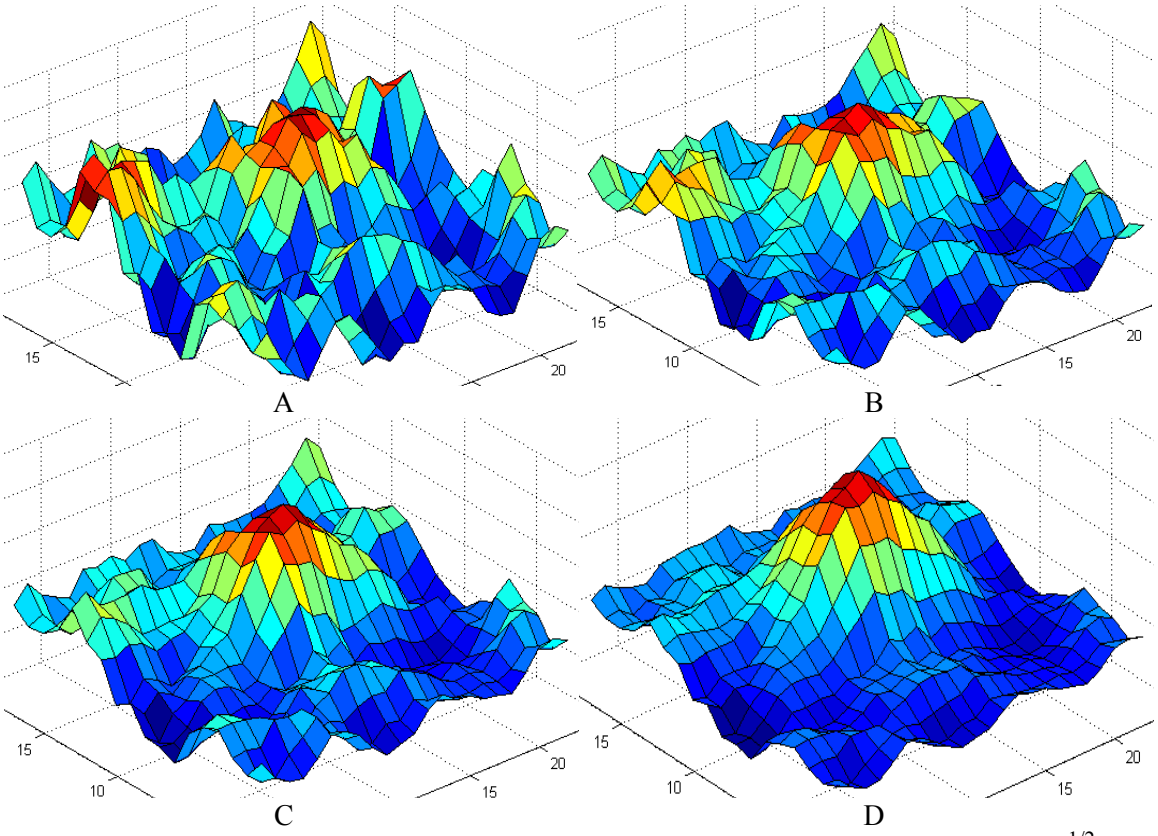

Figure 6-62. Surface plots of Defect A50 (Specimen A-2). A) t = 13 sec. B) $t = t_T^{1/2}$. C) t = 23 sec. D) t = 60 sec.

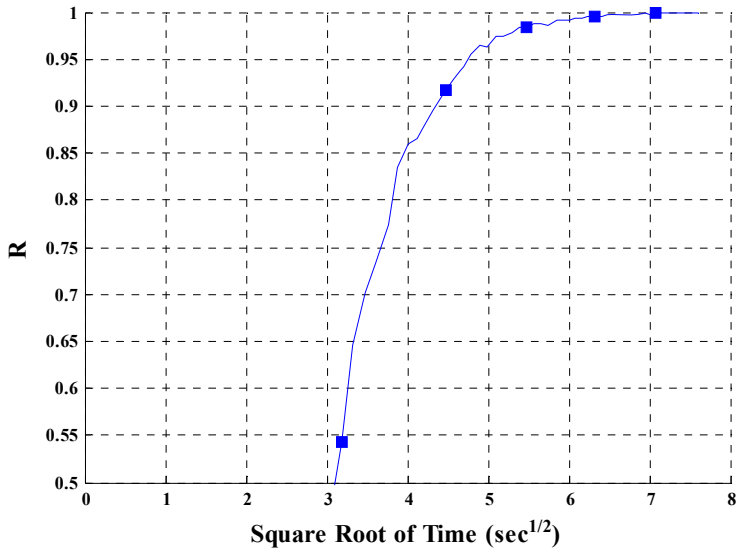

Figure 6-63. Two-dimensional correlation coefficient, R, for Defect A50 (Specimen A-2)

Specimen A-1

Only defects with diameters 12.7 mm or larger were considered in the analysis. A plot of ΔT_{def} vs. $t^{1/2}$ is provided in Figure 6-64. There is a distinct divergence between ΔT_{def} and ΔT_{norm} for the perimeter of each defect area at $t^{1/2} = 2$. Ideally, the initial slopes for the IB, A75, and A50 defects would be the same since Γ at the FRP/defect interface is the same. Defect A50 does not line up with the others. It is also interesting to note how the ΔT_{def} curves begin to level off as time increases. This is a result of two-dimensional effects as the heat flows from the center of the defect towards the edges. The divergence is most pronounced for the smaller defects. The epoxy-filled defects, E75 and E50, follow a similar trend, but the initial slopes of the respective ΔT_{def} curves is less than what was observed for the air-filled defects. This is a result of Γ at the FRP/defect interface being closer to 0 for the epoxy-filled defects.

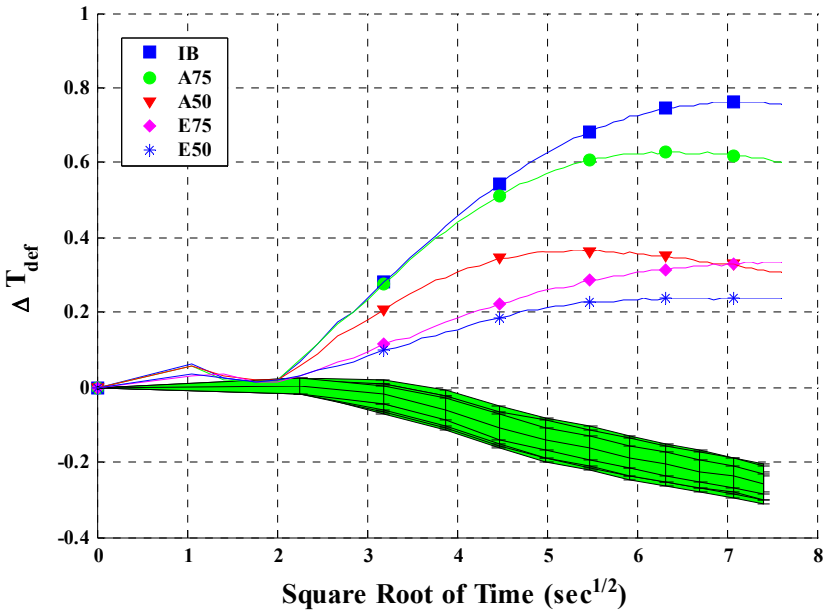

Figure 6-64. Defect signal vs. $t^{1/2}$ for Specimen A-1 defects

The two-dimensional correlation coefficient also provides interesting insight into the behavior of each defect. The time at which each defect reaches a 95% correlation varies from $t^{1/2} = 2.25$ to $t^{1/2} = 3.5$. Defects IB and A75 produce very similar R vs. $t^{1/2}$ curves (Figure 6-65) and Defects A50, E75, and E50 appear to correlate at a slightly lower rate. Careful inspection of the normalized ΔT images generated from $t^{1/2} = 2.25$ to 3.5 confirmed this observation. The ΔT_{norm} image provided on the graph in Figure 6-65 was generated for $t^{1/2} = 3$. First, this image demonstrates that the defects are well defined at this level of correlation (all five defects are between 90% and 98% correlated with their respective defect area at the end of heating). Second, if one was asked to offer a qualitative assessment of the image and rank the defects in order from "most-defined" to "least-defined", it is likely that the three air-filled defects would rank the highest and the smallest epoxy-filled defect would rank the lowest. The computed R for each of the defects at $t^{1/2} = 3$ indicates a similar order.

In summary, the two-dimensional correlation coefficient provides a quantitative measure for how well a defect is defined with respect to some baseline value. In this case, the baseline value was chosen at the end of heating since this represents a point at which the defect is well-defined with respect to the surroundings. For the single-layer specimen, correlation with the baseline image occurs relatively quickly since the time required for the thermal front to reach the defect is small.

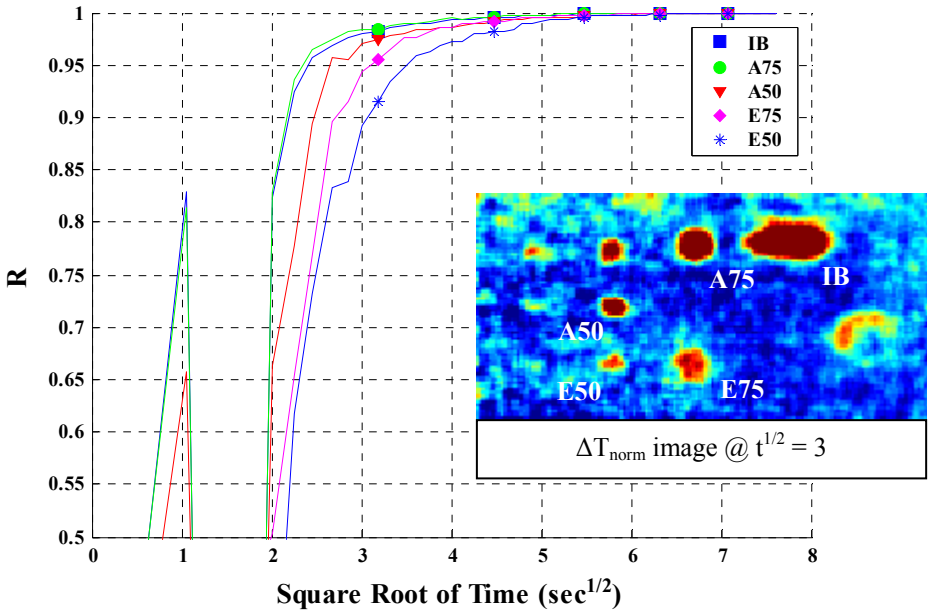

Figure 6-65. Two-dimensional correlation coefficient for Specimen A-1 defects

Specimen A-2

Applying the same analysis procedure to Specimen A-2 generated markedly different results. The threshold value for ΔT_{def} was achieved between $t^{1/2} = 4.3$ and $t^{1/2} = 5.8$ for defects A75, A50, E75, and E50. Data are provided in Figure 6-66. Defect IB achieved the threshold value much earlier at $t^{1/2} = 2.25$. Recall that Defect IB on Specimen A-2 contained rather large unintentional defects between the top and bottom layer of composite. The results contained in the ΔT_{def} vs. $t^{1/2}$ plot are significant for two reasons. First, Defect IB generated a signal at a $t^{1/2}$ value very close to what was

observed for the defects in Specimen A-1. Second, the ΔT_{norm} curve for the perimeter of Defect IB's area is consistent with that of a two-layer FRP composite system. This would suggest that the initial signal generated by Defect IB is a result of a delamination

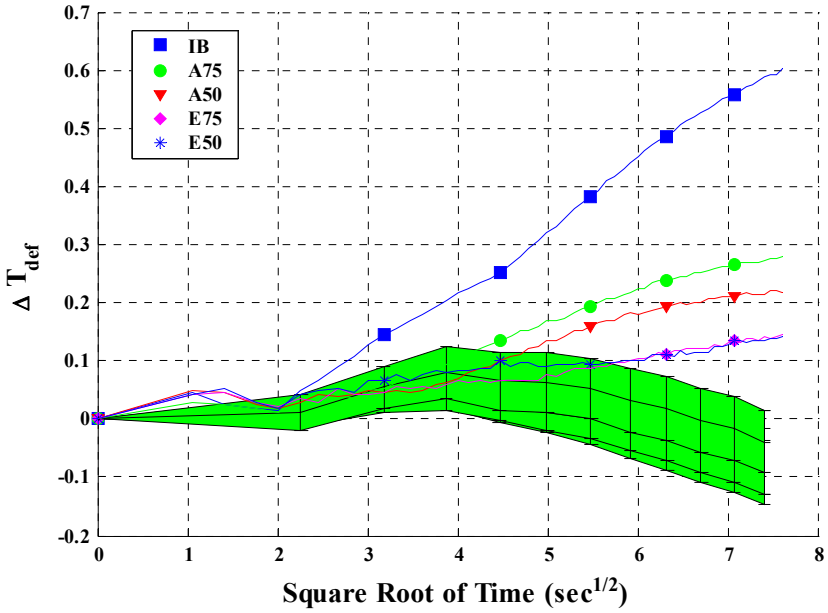

Figure 6-66. Defect signal vs. $t^{1/2}$ for Specimen A-2 defects

The computed two-dimensional correlation coefficient is provided for Specimen A-2 defects in Figure 6-67. For the two layer specimen, a 95% correlation is achieved for all defects between $t^{1/2} = 4.0$ and $t^{1/2} = 5.5$. It is interesting to note how the behavior of R for Defect IB is consistent with the others even though the ΔT_{def} curve for Defect IB diverges. Figure 6-68A provides a ΔT_{norm} image for Defect IB at $t^{1/2} = 2.4$. The unintentional defects are clearly visible in this image and the ΔT_{def} curve has identified the defects at this time. Figure 6-68B provides a ΔT_{norm} image for Defect IB at the end of heating ($t^{1/2} = 7.7$ or t = 60 sec). This image was used as the baseline value in the two-dimensional correlation coefficient computation. At this point, the shape of the defect is consistent with the actual interface bubble. When R is computed at early time steps, the two images are not well correlated (75% at $t^{1/2} = 2.4$). This illustrates the usefulness of

the two-dimensional correlation coefficient for removing the effects of small, unintentional defects that corrupt the ΔT_{def} vs. $t^{1/2}$ curves.

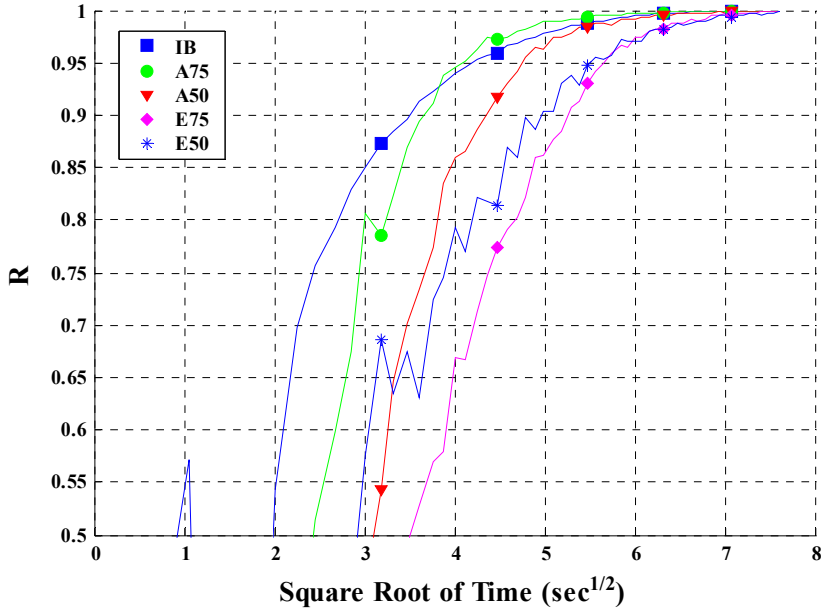

Figure 6-67. Two-dimensional correlation coefficient vs. $t^{1/2}$ for Specimen A-2 defects

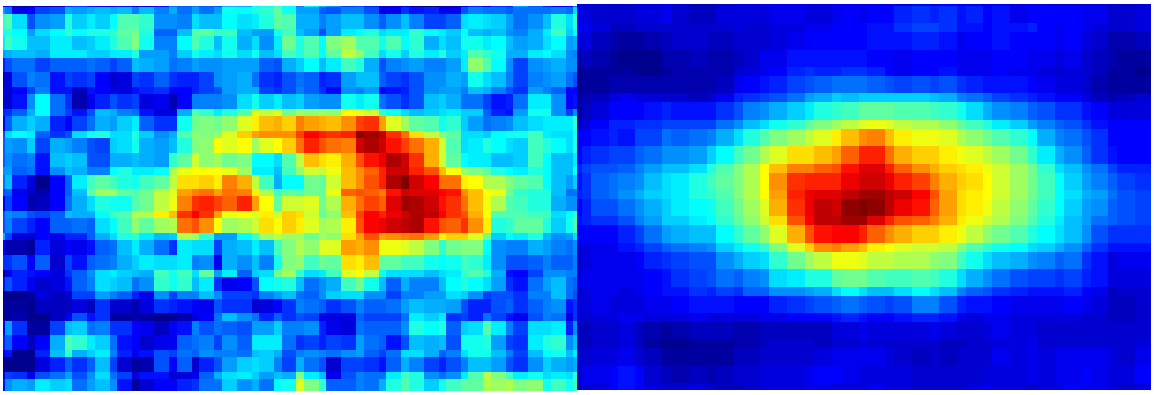

A B

Figure 6-68. Normalized ΔT images for IB defect (Specimen A-2) at A) $t^{1/2} = 2.4$ (t = 6 sec). B) $t^{1/2} = 7.7$ (t = 60 sec)

Specimen A-3 and Specimen A-4

Figure 6-69 provides ΔT_{def} vs. $t^{1/2}$ results for Specimen A-3. The general trend of ΔT_{norm} for the perimeters defining the defect boundaries is consistent with the findings from the defect-free area analysis. Based on these data it is reasonable to conclude that the specimen has three or four layers of composite material. If the total thickness of the

composite was less than three or four layers, the normalized temperature response of each defect boundary should be less than zero at the end of heating.

The ΔT_{def} curves indicate that IB was the only detected defect. The threshold value for ΔT_{def} was reached at $t^{1/2} = 6$. A 95% correlation factor was also achieved at $t^{1/2} = 6$ (see Figure 6-70). This value is suspect, however, since a strong signal for Defect IB never developed. The R vs. $t^{1/2}$ curves for the remaining defects illustrate how an R of 1 will always be achieved at the end of heating even if the defect area contains mostly noise. Based on these data it is not possible to determine if the computed R values for IB reflect the properties of the defect.

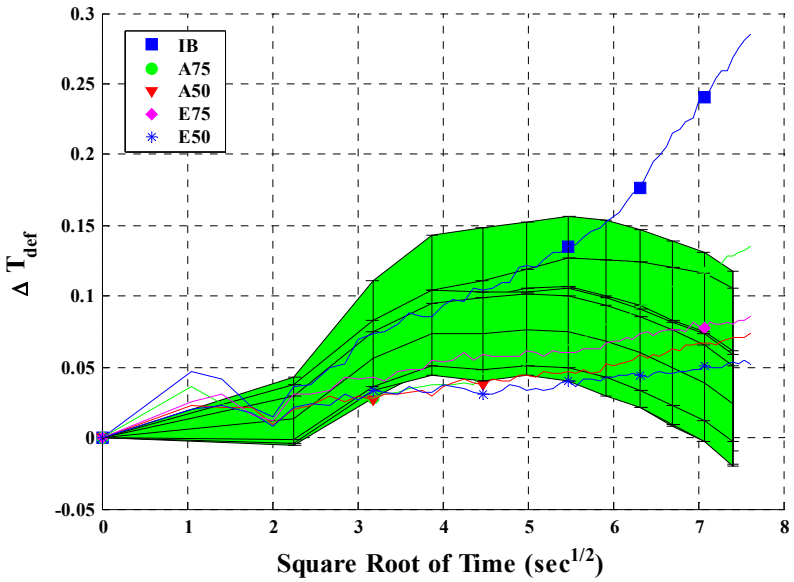

Figure 6-69. Defect signal vs. $t^{1/2}$ for Specimen A-3 defects

Finally, none of the implanted defects were detected for Specimen A-4. This is to be expected since the 60 sec pulse duration was not adequate to reveal all of the defects in the three-layer specimen. The ΔT_{norm} image provided in Figure 6-71 was generated for Specimen A-4 at the end of heating. Even though the implanted defects are not discernable, it is still interesting to note the high degree of variation in the image. The

precise cause of this variation is not known, but it is likely the lack of consistent saturation of the composite during installation or the presence of small, unintentional defects between layers.

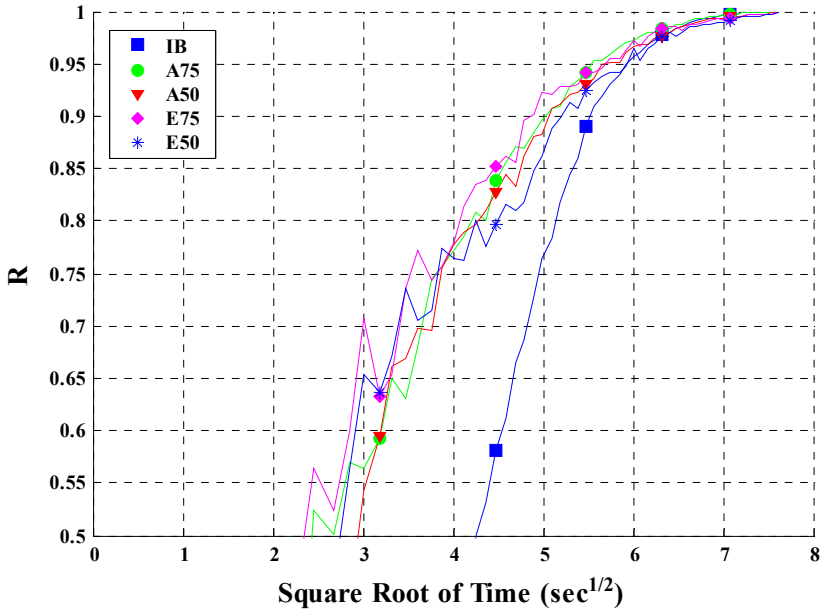

Figure 6-70. Two-dimensional correlation coefficient vs. $t^{1/2}$ for Specimen A-3 defects

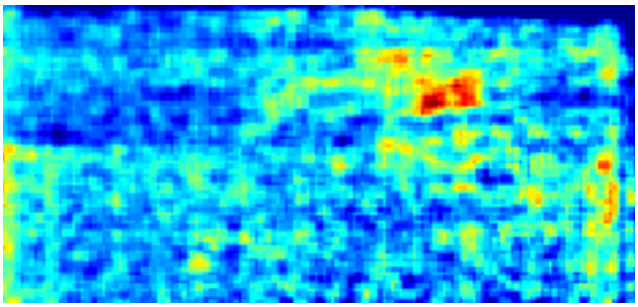

Figure 6-71. ΔT_{norm} image for Specimen A-4 (t = 60 sec)

Summary of Step Thermography Results: Series A Specimens

Thermal images were collected at a rate of 1 frame per second for 60 seconds while specimens in Series A were heated using the long-pulse experimental setup. Data collected during the first 4 seconds of heating were used to normalize each pixel in the series of thermal images. Important findings may be summarized as follows:

- The normalization procedure is useful for reducing the effects of non-uniform heating
- A 60 second pulse duration is adequate for the one and two-layer FRP systems
- Additional heating time is required for three and four-layer FRP systems. The overall effectiveness for three and four layer systems is currently unknown.
- This analysis provides an indication of the thickness of the FRP composite
- It is possible to differentiate defects that occur between layers of FRP and defects that occur at the FRP/concrete interface

There are insufficient data available to develop a mathematical model that estimates defect depth. It is, however, possible to summarize the observations from the analysis of the Series A specimens and identify several parameters that can be used as guidelines for characterizing defects. The first parameter of interest is the time at which ΔT_{def} exceeds a threshold value of ΔT_{norm}. A convenient threshold value was determined as the average of the ΔT_{norm} experienced by the perimeter + 2σ. This value ($t_T^{1/2}$) is provided for each defect that was detected in Table 6-20. If $t_T^{1/2}$ is on the order of 2 – 3, the defect is likely beneath a single layer of composite. For $t_T^{1/2}$ on the order of 4 – 5.5, the defect is likely beneath two layers of composite. There are no data available to support a claim for $t_T^{1/2} > 6$.

The second parameter is the time at which the defect area becomes 95% correlated with a baseline value for the defect that was collected at the end of heating. This parameter is labeled $t^{1/2}$ @ $R_{95\%}$ in Table 6-20. For defects beneath a single layer of FRP, $t^{1/2}$ @ $R_{95\%}$ is between 2 and 3.5, and for defects beneath a two layers of FRP $t^{1/2}$ @ $R_{95\%}$ lies between 4 and 6.

Table 6-20. Parameters of interest for characterizing defects from step thermography data

Specimen	Defect	$t_{T1/2}$ ($sec^{1/2}$)	$t_{1/2}$ @ $R_{95\%}$ ($sec^{1/2}$)
A-1	IB	2	2.4
A-1	A75	2	2.4
A-1	A50	2	2.8
A-1	E75	2	3
A-1	E50	2	3.5
A-2	IB	2.25	4.3
A-2	A75	4.3	4
A-2	A50	4.2	4.8
A-2	E75	5.8	5.3
A-2	E50	5.8	5
A-3	IB	6	6

Frequency Domain Analysis: Series A

Data from the pulse thermography analysis and the step heating analysis indicate that IRT can be used confidently to detect and characterize defects in one and two-layer carbon FRP systems. Furthermore, larger defects (> 10 cm^2) can be detected in the three and four-layer systems, but characterization of these defects is less certain. The objective of this section is to examine two additional heating and analysis techniques that can be used for thicker composite systems. The first method involves heating each specimen using the sinusoidal heating setup described in Chapter 4. Results from these experiments will be processed to generate a series of phase images for each specimen. The second method will utilize the data collected during the pulse heating experiments. This method will also generate a series of phase images by applying a discrete Fourier transform to the cooling curve obtained for each pixel.

Sinusoidal Heating (Lock-In IRT)

Data collection

A total of 10 pulse durations were investigated during the sinusoidal heating experiments. Each pulse duration represents one frequency value (f_{mod}) since the shape

of the pulse was sinusoidal. The specimens were allowed to cool for 10 minutes between pulse durations, and no images were recorded during this cooling period. A summary of the pulse durations that were investigated and the number of images that were collected is provided in Table 6-21.

Table 6-21. Frequencies investigated during sinusoidal heating experiments

Pulse Duration (sec)	f_{mod} (1/sec)	# of images
5	0.2	10
6.25	0.16	10
8.3	0.12	10
12.5	0.08	20
25	0.04	20
100	0.01	20
125	0.008	40
167	0.006	40
250	0.004	40
500	0.002	40

Analysis procedures and results

The general concept behind sinusoidal heating is that defects closer to the surface will appear when the pulse duration is short (frequency is high) and deeper defects will appear when the pulse duration is long (frequency is low). A least squares sinusoidal curve fit was applied to the temperature vs. time response for each pulse duration that was investigated. The quantity of interest in this analysis is the phase shift experienced by each pixel. By focusing on phase (as opposed to amplitude), the effects of non-uniform heating are minimized and defects with weak signals are accentuated.

Consider the three points shown in the thermal image provided in Figure 6-72A. These points are all located on Specimen A-4 with Point 1 positioned above Defect IB, and Point 2 and Point 3 positioned above defect-free areas. The temperature vs. time results for the 500 sec pulse duration indicates that the overall amplitude of the temperature response is highly dependent on the location of the point with respect to the

heat source. The general form of the sinusoidal curve fit that was applied to each point is as follows:

$$T(t) = A + B * \cos(2\pi ft + \pi - \Phi) \qquad 6\text{-}12)$$

T = Temperature
t = Time
f = Frequency of heat source modulation (1/pulse duration)
Φ = Phase shift (measured in radians)
A = Average offset
B = Amplitude of sine wave

Note that when the phase shift is zero, the temperature response is a scaled function of the modulated heat input. For the case of a 500 second pulse duration, the peak output of the heat source occurs at 250 sec. The resulting phase shift for Point 1 (above the defect area) was -0.86 rad. This quantity indicates that the peak value of the sinusoidal curve-fit occurs 68 seconds later at t = 318 sec. The phase shift for each of the defect free pixels was -0.73 rad which corresponds to a lag in the peak response of 58 sec. The important thing to recognize is that the computed phase shift is independent of amplitude. In the example provided, the defect-free region described by Point 3 has greater amplitude than the defect area throughout the entire pulse duration. The phase shift, however, is less for the defect-free area since the flow of heat from the surface into the concrete is not interrupted (slowed down) by the defect. By applying this procedure to each pixel in a series of thermal images, it is possible to generate a single phase image that is independent of amplitude.

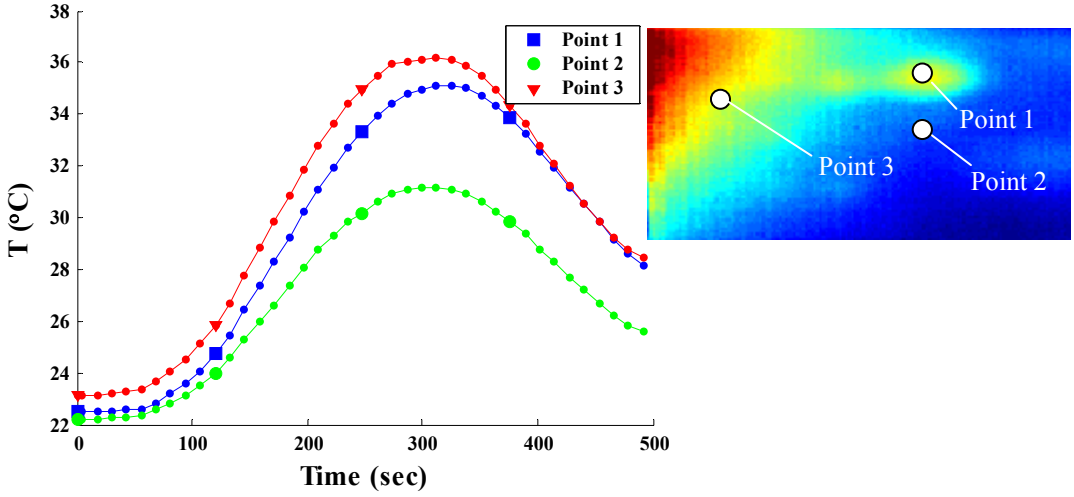

A

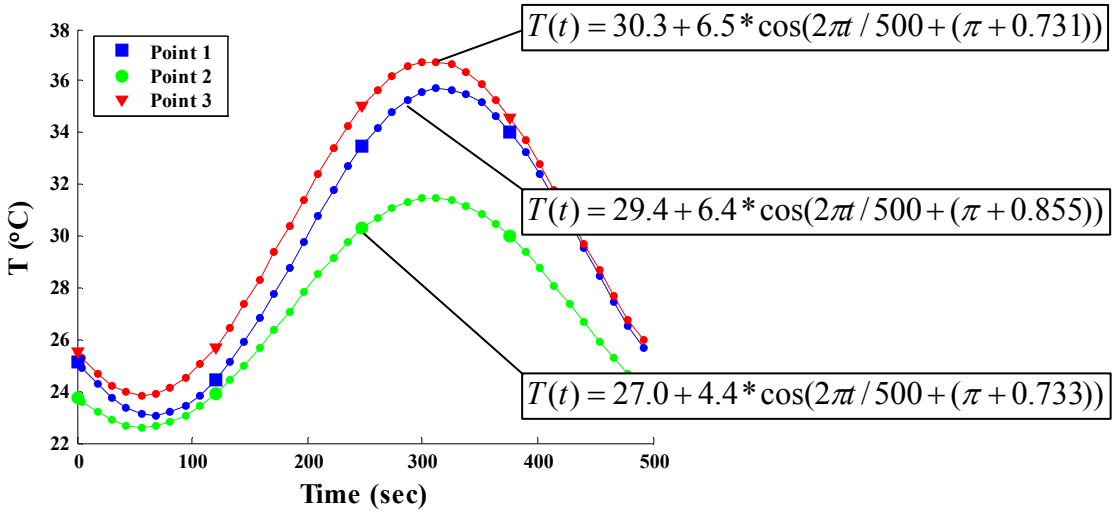

B

Figure 6-72. Data analysis for sinusoidal heating (pulse duration = 500 sec). A) Temperature vs. time response for three points on Specimen A-4. B) Results of sinusoidal curve-fit

Results for the 8.33 sec pulse duration are provided in Figure 6-73. During this short pulse duration, the thermal front is only affected by features that occur near the surface. Most of the implanted defects in Specimen A-1 are visible in the surface plot as

well as the large unintentional defects present above Defect IB in Specimen A-2. Significant non-uniformities are also observed in the region of Defect IB in specimens A-3 and A-4. Ideally, the phase images for specimens A-2, A-3, and A-4 would show little or no variation.

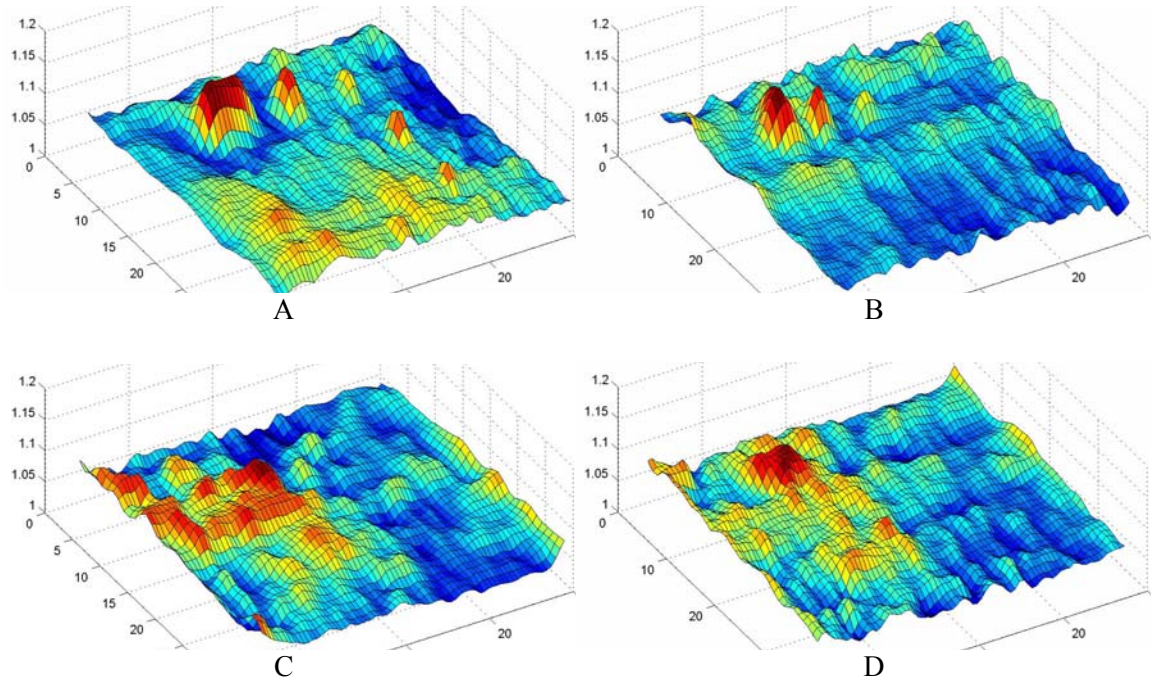

Figure 6-73. Sinusoidal heating results for Series A specimens (Pulse Duration = 8.33 sec). A) Specimen A-1. B) Specimen A-2. C) Specimen A-3. D) Specimen A-4

For the 25 sec pulse duration (shown in Figure 6-74), all of the implanted defects in Specimen A-1 develop a significant signal. Only the air-filled defects (IB, A75, and A50) are clearly detected in Specimen A-2. It is interesting to compare these results with the ΔT_{def} vs. $t^{1/2}$ plot that was generated for Specimen A-2 during the step thermography analysis (shown in Figure 6-66). At $t^{1/2} = 5$ (t = 25 sec), the ΔT_{def} plot indicates that defects IB, A75, and A50 have exceeded the threshold value for detectability. The epoxy-filled defects, however, have not yet developed a significant signal with respect to

the surrounding areas. A similar conclusion can be drawn from the sinusoidal heating results.

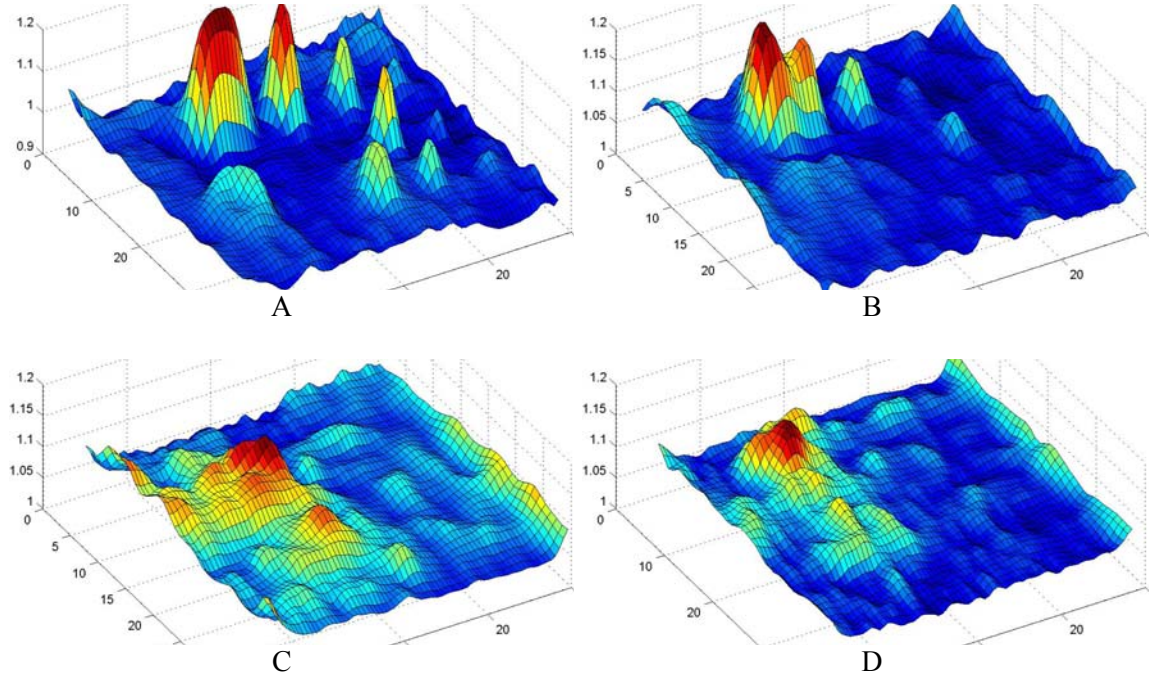

Figure 6-74. Sinusoidal heating results for Series A specimens (Pulse Duration = 25 sec) A) Specimen A-1. B) Specimen A-2. C) Specimen A-3. D) Specimen A-4.

Results for the 100 sec pulse duration experiment are shown in Figure 6-75. All implanted defects in Specimen A-1 and A-2 are clearly defined, and the interface defects in Specimen A-3 are beginning to dominate the phase response. The fact that the IB and A75 defects appear to blend together is an indication that these defects were placed too close together. The overall pattern of the phase shift response for the three-layer specimen does indicate that the thermal front is influenced by the implanted defects. Without a destructive inspection of the specimen, it is not possible to determine how much of the signal that has developed for the three and four-layer specimens is due to the implanted defects and how much results from non-uniformities in the composite above the defect.

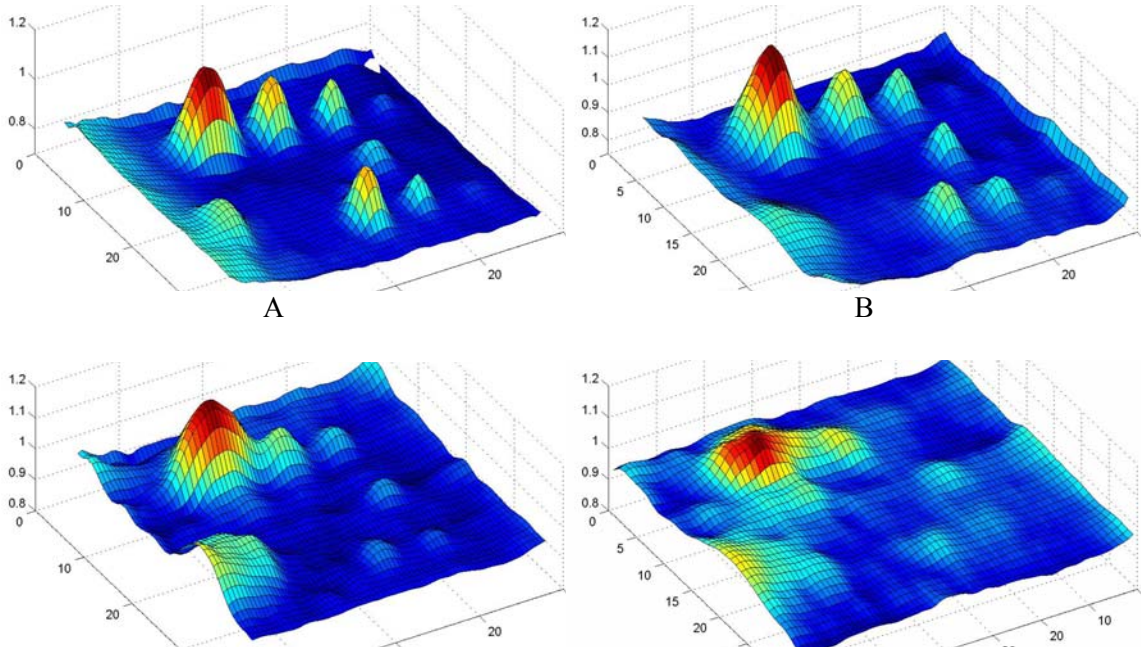

Figure 6-75. Sinusoidal heating results for Series A specimens (Pulse Duration = 125 sec) A) Specimen A-1. B) Specimen A-2. C) Specimen A-3. D) Specimen A-4.

Results for the 500 second pulse duration experiment are provided in Figure 6-76. Specimen A-1 exhibited a very interesting phase response. For this pulse duration, the phase shift above the air-filled defect areas was actually smaller in magnitude than the phase shift above the defect-free areas. The epoxy-filled defects are can not be distinguished. For the two-layer specimen, the phase response of the air-filled defects was essentially the same as the surrounding areas (no signal developed) and the epoxy-filled defects display a slightly larger phase shift than the surroundings. Bai and Wong (2001) reported this phenomenon and referred to the frequency (inverse of pulse duration) at which defects blend in with the surroundings as the "blind frequency". Bai and Wong do not offer a physical explanation for this phenomenon but they do suggest that this frequency be avoided.

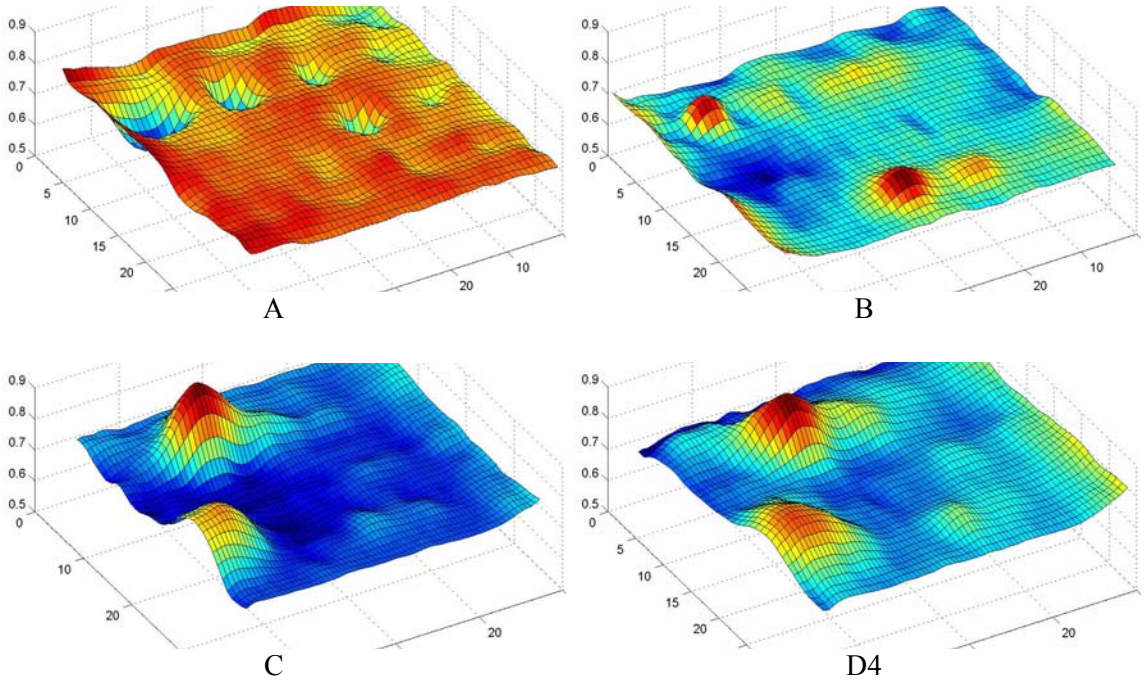

Figure 6-76. Sinusoidal heating results for Series A specimens (Pulse Duration = 500 sec) A) Specimen A-1. B) Specimen A-2. C) Specimen A-3. D) Specimen A-4.

Summary of sinusoidal heating results

Results from this investigation into sinusoidal heating highlight the major downside to method: multiple inspections must be performed in order to detect defects at different depths in an FRP system. On the other hand, the pulse duration at which a defect is first detected can be correlated to the defect's depth. The original intent was to investigate a large number of pulse durations and establish a relationship between defect depth and "blind" pulse duration. This was accomplished to a certain extent for the one and two-layer specimens, but unintentional defects and other non-homogeneities in the composite system do not support establishing a precise relationship for the three and four-layer systems. Nonetheless, results from this study can be used to make recommendations for suitable pulse durations depending on the thickness of the FRP composite and/or the desired depth of the inspection.

The proposed guidelines are summarized in Table 6-22. These guidelines cover a range of depths from 1 mm to 4 mm. The second column in the table represents the recommended pulse duration for inspecting a desired depth. The third column provides an acceptable range of values for pulse duration. The idea behind the acceptable range for pulse duration is to identify an upper and lower boundary for a specific inspection depth. The lower boundary represents the minimum required pulse duration for a defect at that depth to become visible in the phase image. The upper boundary is intended to provide some guidance in avoiding the "blind" pulse duration at which the phase shift for the defect and defect-free regions are equal. These values were chosen based on an inspection of $\Delta\Phi_{def}$ vs. frequency plots that were generated for the five defects (IB, A75, A50, E75, and E50) in each of the four specimens. $\Delta\Phi_{def}$ was computed the same way that ΔT_{def} was computed in the time domain analysis. These results are provided in Appendix B.

Table 6-22. Recommended pulse durations and detection limits for sinusoidal heating (carbon-FRP systems)

Depth of inspection (mm)	Recommended pulse duration (sec)	Acceptable range for pulse duration (sec)	Dimension of smallest detectable defect (mm)
1	30	10 – 100	12.7
2	60	45 – 150	12.7
3	120	100 – 250	19
4	240	200 - 500	25.4

It must be noted that these recommendations are made based on results from four specimens. It remains to be seen whether the effects of fiber saturation levels, fiber type (glass vs. carbon), and surface preparation methods have any significant impact on IRT results. These effects will be investigated with the specimens contained in Series B, Series C, and Series D.

Pulse Phase Thermography

Pulse phase thermography (PPT) is a heating and data analysis method that can be used to reduce the effects of non-uniform heating (Maldague et al. 2002). In this method, a high energy heat pulse is applied using a photography flash and thermal images are recorded while the surface cools. The discrete Fourier transform (DFT) is computed for the temperature vs. time response of each pixel in the series of thermal images using the following:

$$F_{k=0\ldots N-1} = \frac{1}{N}\sum_{n=0}^{N}\left[T_n\left(\cos\left(\frac{2\pi kn}{N}\right) - i\sin\left(\frac{2\pi kn}{N}\right)\right)\right] \qquad (6\text{-}13)$$

N = Number of time steps
T_n = Temperature value of pixel at each time step

The output of the DFT includes real and imaginary components that vary as a function of frequency. The phase angle is determined at each frequency interval using the following:

$$\Phi_{k=0\ldots N-1} = \arctan\left[\frac{-\mathrm{Im}(F_k)}{\mathrm{Re}(F_k)}\right] \qquad (6\text{-}14)$$

$Im(F_k)$ = Imaginary component of DFT output
$Re(F_k)$ = Real component of DFT output

This procedure generates a new series of phase images in the frequency domain. The first value in the DFT output, F_0, corresponds to the average value of the temperature response (dc-component). The corresponding phase angle, Φ_0, is zero. The second value in the DFT, F_1, corresponds to the lowest frequency. The lowest frequency value can be determined as follows:

$$f_1 = \frac{1}{t_N} \qquad (6\text{-}15)$$

t_N = duration of the record

The final value in the DFT output corresponds to the highest frequency, f_{max}, and is equal to the image save rate. The DFT operation generates a unique set of values for frequencies between 0 and $f_{max}/2$. The values generated by the DFT for frequencies between $f_{max}/2$ and f_{max} are the complex conjugates of the values generated between 0 and $f_{max}/2$.

Data collection

The data used to investigate the PPT method were collected during the pulse analysis experiments (time domain) that were described previously. Each of the four specimens in Series A was heated using the photography flash setup and the long-pulse setup. Three pulse durations were considered from the long-pulse data set: 30 sec, 45 sec, and 60 sec. Only data recorded after the heat source was removed were considered.

This section will only consider results from Specimen A-3 and Specimen A-4 (three and four-layer FRP systems). Specimen A-1 and Specimen A-2 were omitted based on the findings of the time domain analysis and the lock-in analysis. The heating methods and analysis procedures previously described were shown to be effective for detecting defects in one and two-layer FRP systems.

Previous research by others (Ibarra-Castanedo and Maldague 2004, Avdelidas et al. 2004, Woolard and Cramer 2005, Ibarra-Castanedo and Maldague 2005) involved heating the surface of FRP composites using a high powered photography flash. This approach was attempted in the current study but was only moderately successful for Specimen A-3 and Specimen A-4. The flash system used in the current study was not powerful enough to develop strong signals for defects in three and four-layer FRP systems. When the PPT method was applied to the data collected using the photography

flash, the resulting phase images were very noisy. There was no observable advantage gained by applying the PPT method to flash heating data.

The output of the DFT operation depends on the image save rate and the duration for which data are recorded. Several experiments were conducted where thermal images were collected for up to 15 minutes after the heat source was removed. Results from these trials indicated that after 240 sec the surface temperature of each specimen was uniform and had returned to its initial value before the heat was applied. No additional information was gained by recording data for longer than 240 sec.

Experiments were also conducted in which the image save rate was varied from the maximum possible (5 frames per second = 5 Hz) to 1 frame per 2 seconds (0.5 Hz). Results from these trials indicated that a capture rate of 1 Hz is adequate. Phase images that were generated for frequencies higher than 0.5 Hz contained mostly noise and were not considered.

Analysis procedures and results

The general concept behind PPT is similar to the lock-in analysis procedure: defects close to the surface appear at high frequencies while deeper defects appear at lower frequencies. The fundamental difference between the two methods is that lock-in analysis requires multiple experiments for each frequency of interest. PPT examines all frequencies based on results from one experiment.

The objective of this analysis for Specimen A-3 and Specimen A-4 is to investigate using PPT to remove the effects of non-uniform heating. Data were collected using the long-pulse setup with a 60 sec pulse duration. Temperatures vs. time results for three points on Specimen A-3 are shown in Figure 6-77 A. Point 1 was selected directly above Defect IB. Point 2 and Point 3 were selected above defect-free areas. Point 2 was

located relatively close to the defect and experienced similar heat intensity. Point 3 was located very close to the heat source. The thermal image shown in Figure 6-77 A was collected at the time of maximum defect signal strength. This image shows the effects of non-uniform heating.

The phase response of each point is provided in Figure 6-77 B. Between 0.05 and 0.5 Hz, It is not possible to distinguish the phase response of each point. Between 0 and 0.05 Hz, the phase shift for the point above the defect is larger than the phase shift for the defect-free regions. The important thing to notice about these curves is that the phase response for the defect-free points is nearly identical for all frequencies. The effects of non-uniform heating have been removed.

Figure 6-78 A contains a surface plot of the phase shift for Specimen A-3. The maximum phase difference occurred at a frequency value of 0.0042 Hz. This was the lowest frequency generated by the DFT since the total duration of the record was 240 sec (1/240 sec = 0.0042 Hz). All of the defects 12.7 mm in diameter or larger can be seen in the surface plot. A surface plot of the temperature profile at time = 41 sec (t_{max} for Defect IB) is shown in Figure 6-78 B. The same defects that can be seen in the phase profile are also visible in the temperature profile. The only major advantage of the phase image is that the response of the defect-free region is uniform.

A similar analysis was conducted for three points on Specimen A-4. The frequency at which the point above the defect diverged with the defect-free regions was approximately 0.05 Hz. This is consistent with the overall concept of PPT analysis: deeper defects appear at lower frequencies while defects closer to the surface appear at

higher frequencies. The increased detectability over the time domain results is shown in Figure 6-79.

The next step in the analysis was to construct $\Delta\Phi_{def}$ vs. frequency plots (Figure 6-80). The rectangular areas used to define the defects for the pulse analysis (time domain) were also used in the PPT analysis (frequency domain). $\Delta\Phi_{def}$ was calculated by taking the difference of the maximum value for phase shift inside the area and the average value of phase shift measured along the perimeter. A rigorous analysis of the resulting $\Delta\Phi_{def}$ vs. frequency plots was not performed in the current study. General observations were made for the air-filled defects in Specimens A-1, A-2, A-3, and A-4:

- The maximum value of $\Delta\Phi_{def}$ ($\Delta\Phi_{max}$) decreases as the size of the defect decreases
- There was no observable trend between defect depth and $\Delta\Phi_{max}$ for Defect IB. This is likely a result of the unintentional defects that occurred in the multilayer systems
- $\Delta\Phi_{max}$ decreased as depth increased for defects of the same size.
- A visual inspection of the $\Delta\Phi_{def}$ vs. frequency plots indicated that the blind frequency (frequency at which a defect first becomes visible in a series of phase images) for air-filled defects in Specimen A-1 occurred at approximately 0.15 Hz. The blind frequency for Specimen A-2 defects occurred at approximately 0.075 Hz. The blind frequency for Specimens A-3 and A-4 occurred at 0.035 Hz and 0.015 Hz, respectively.

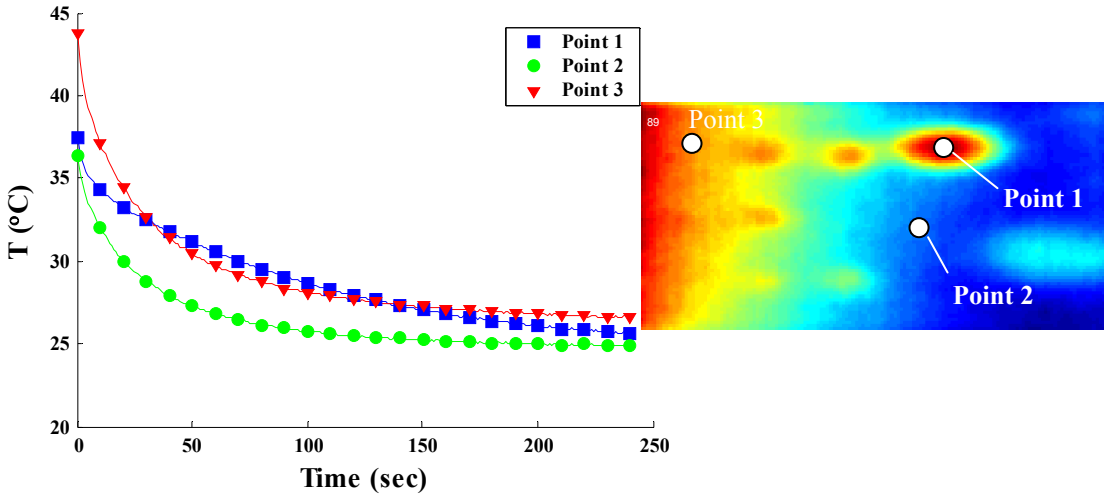

A

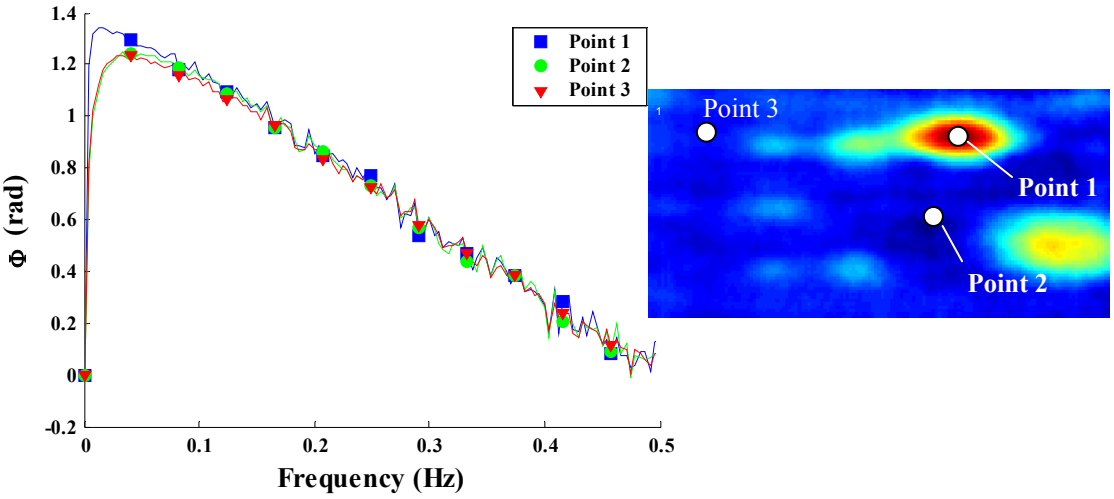

B

Figure 6-77. Application of PPT method to Specimen A-3. A) Time domain results and thermal image. B) Frequency domain results and phase image

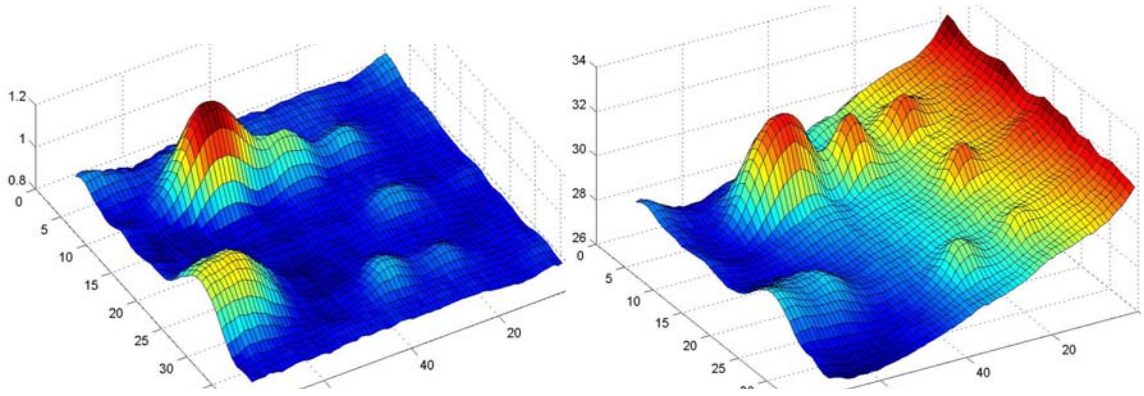

Figure 6-78. Comparison of time domain and frequency domain (PPT) results for Specimen A-3. A) Phase angle surface plot at f = 0.0042 Hz. B) Temperature surface plot at t = 41 sec.

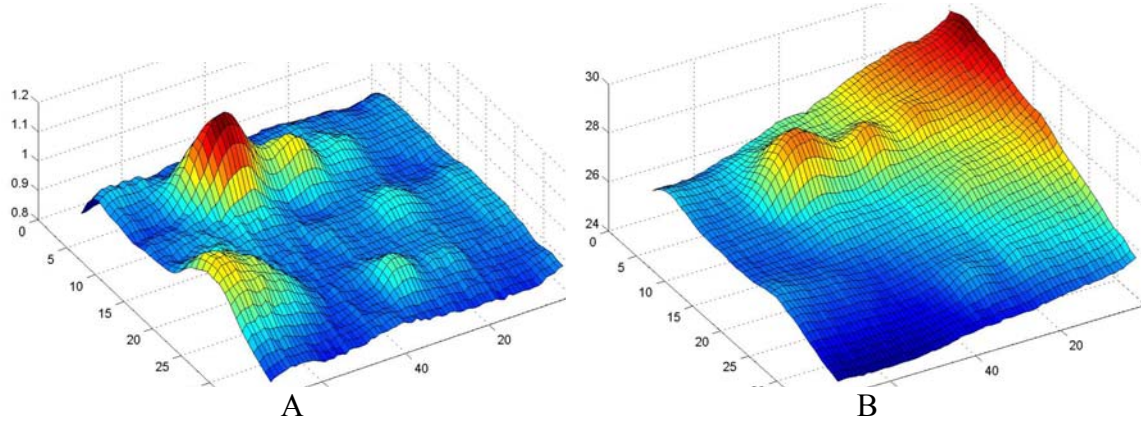

Figure 6-79. Comparison of time domain and frequency domain (PPT) results for Specimen A-4. A) Phase angle surface plot at f = 0.0042 Hz. B) Temperature surface plot at t = 75 sec.

Summary of PPT results

It was shown in the previous section on sinusoidal heating that computing phase angle from a series thermal of images can reduce the effects of non-uniform heating. Similar results were obtained with the PPT method. The primary advantage of the PPT method is that phase angle can be computed for multiple frequencies using data obtained from one experiment. The long-pulse experimental setup was used with a 60 sec pulse duration and data were recorded for 240 seconds while the specimens cooled. A visual comparison of the phase response for Specimen A-3 using the PPT method (Figure 6-81

A) and the sinusoidal heating method (Figure 6-81 B) indicates that both methods are suitable for detecting defects. From a qualitative perspective, the two results are identical.

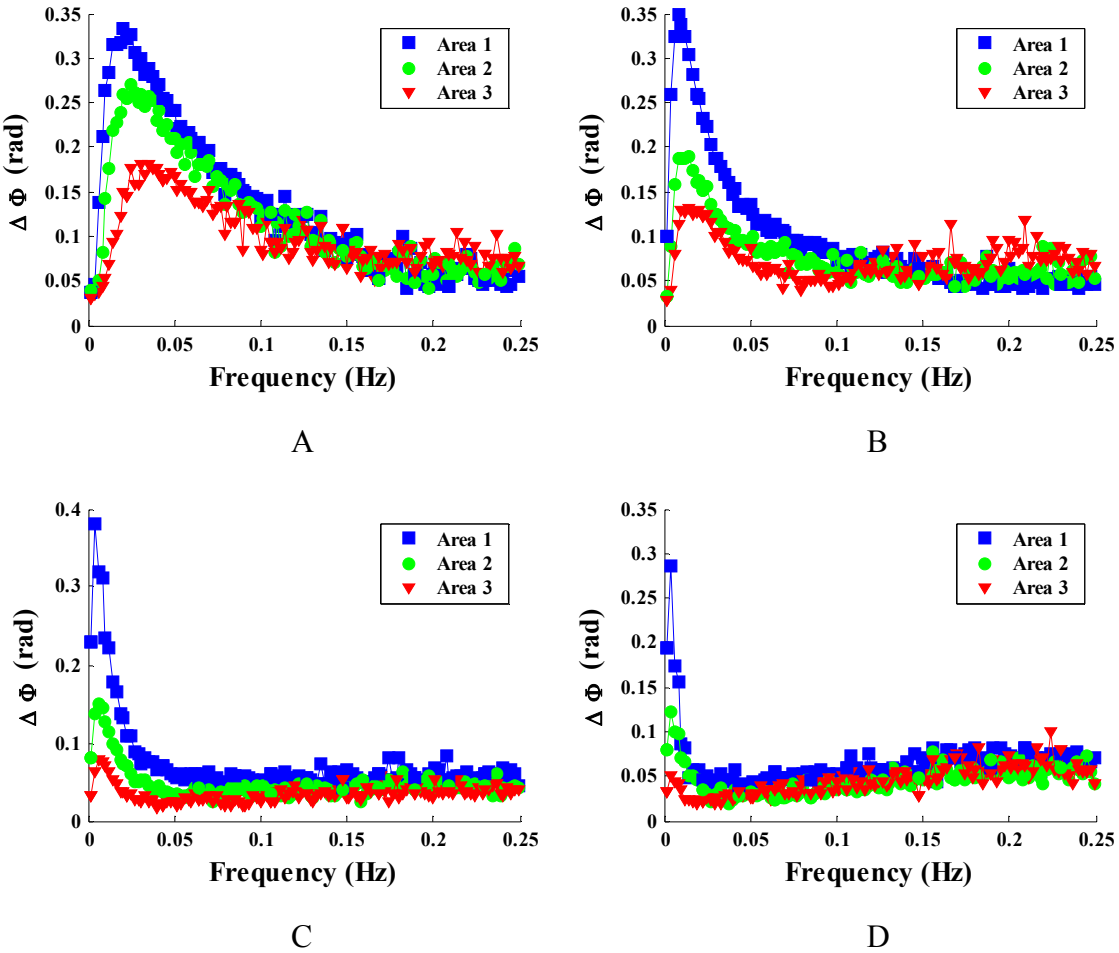

Figure 6-80. Defect signal (phase) vs. frequency plots for air-filled defects.
A) Specimen A-1. B) Specimen A-2. C) Specimen A-3.
D) Specimen A-4

This issue of determining material composition based on PPT results was not addressed in the current study. Additional work is also needed to investigate the relationship between blind frequency and defect depth.

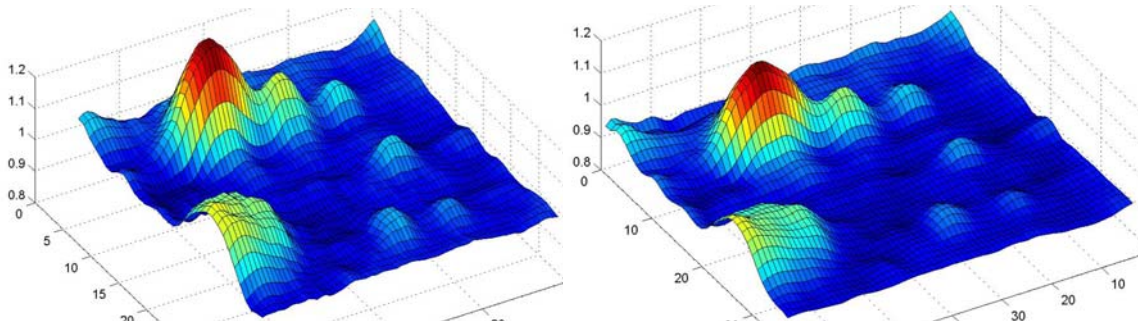

A B

Figure 6-81. Frequency domain results for Specimen A-3. A) PPT method @ f = 0.0083 Hz. B) Sinusoidal heating @ pulse duration = 125 sec (f = .008 Hz)

Comparison of Heating Methods and Analysis Techniques

General Detectability

Four heating methods were investigated:

- Flash heating
- Scan heating
- Long-pulse heating
- Sinusoidal heating

From the standpoint of general detectability, the scan heating method was the most effective. This method generated a ΔT_{max} of nearly 3.8°C for Defect IB in Specimen A-4 (four-layer carbon FRP). This value is nearly double the quantity obtained from the long-pulse heating setup with a 60 sec pulse duration (ΔT_{max} = 2.0°C). The flash heating method only generated a ΔT_{max} of 0.6°C for Defect IB in Specimen A-4.

Scan heating was also the most efficient means for heating the surface of the FRP composite. It was possible to adequately heat an area of 1858 cm^2 in 25 sec using two 500 W halogen lamps. To generate the ΔT_{max} of 2.0°C in Specimen A-4, the long-pulse heating method required 60 sec and four 500 W halogen lamps (total area = 2787 cm^2).

The flash heating method was not efficient. Only 0.5 ft^2 could be heated each time the flash was fired. It may be possible to improve the efficiency of flash heating by using a higher powered flash system. It should be noted, however, that the system used in the

current study (two Godard 3.6 kJ power packs for a total of 6.4 kJ) was valued at over $6000. Increasing the total power supplied by the flash heads will only increase the cost of the system. The flash system also may not be suitable for field applications. Each lamp head requires its own power pack and associated cabling. Gaining access to the FRP composite may be difficult if all of this equipment must be repositioned to heat a small area. The flash bulbs themselves are also quite delicate and can easily be broken ($150 each).

The major disadvantage of the scan heating method is that it is difficult for a person to control the rate at which the heat source is moved. The final scanning rate that was adopted in the current study was approximately 2.2 cm/sec. This corresponded to a heating duration of 12 sec for each specimen. The targeted heating duration was 15 sec, but after multiple attempts to achieve this duration it was determined that 12 sec would have to suffice. Without employing some type of mechanical means for moving the heat source across the surface it would be very difficult to reproduce the same results from one inspection to the next.

The final justification for choosing the scan heating method as the best approach for general detectability is based on a side by side comparison of results from the four heating methods (Figure 6-82). A defect must be identified in a series of thermal images before a quantitative analysis can be performed. This identification entails a certain degree of subjectivity. A defect is more likely to be recognized if the difference between the defect temperature and the background temperature is large.

It is also desirable for the background temperature to be uniform. Thermal images are formed by assigning a color or grayscale intensity to a pixel based on temperature

measurements. The range of temperatures within an image is typically divided into 64 (Matlab standard color maps) or 120 bins (Thermacam Researcher 2001 color maps). Ideally, the temperature above the defects will be the hottest areas in an image and the temperature above the background will be the coolest. The thermal images generated with the long-pulse heating setup do not display this feature (Figure 6-82 C). Defect IB in Specimen A-4 is detectable using the long-pulse setup; however, the maximum temperature in the thermal image appears in the corner closest to the heat source. There is the potential for misinterpretation of this feature.

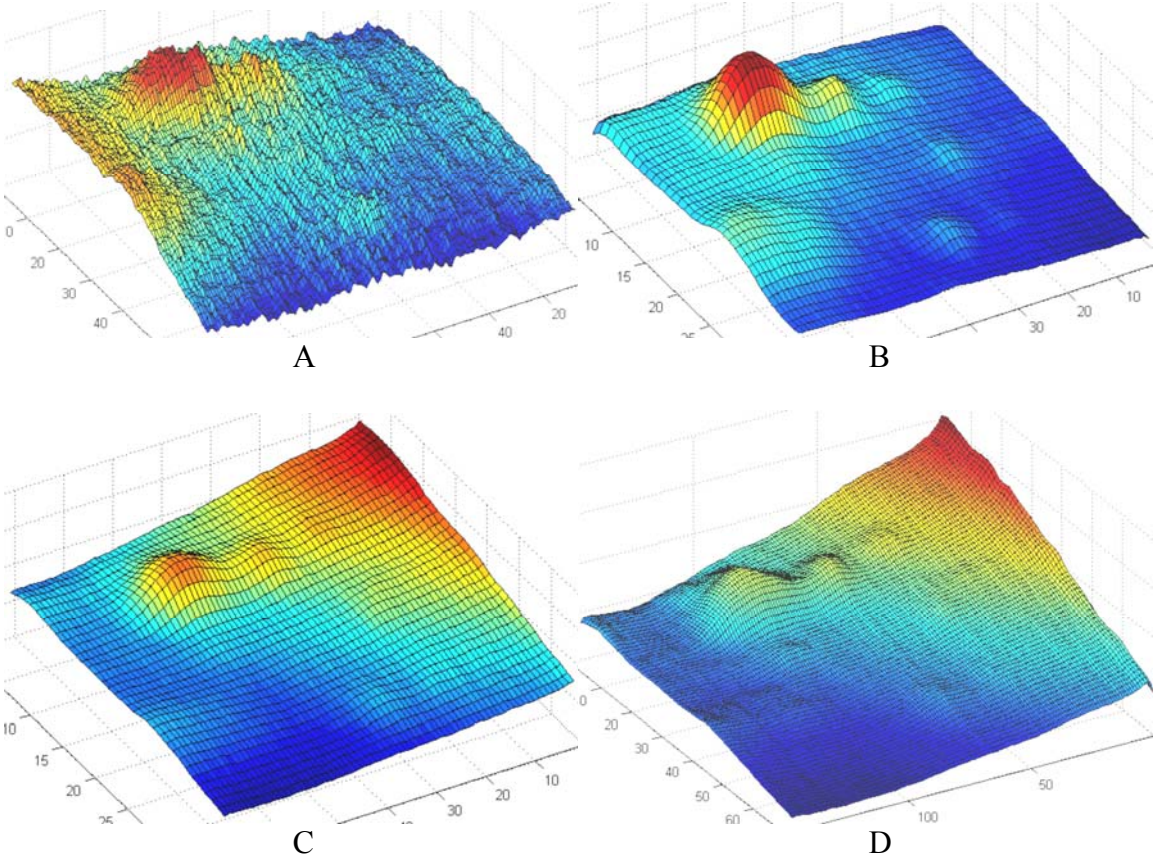

Figure 6-82. Comparison of heating methods for Specimen A-4. A) Flash heating. B) Scan heating. C) Long-pulse heating. D) Sinusoidal heating

Defect Characterization

Four data analysis techniques were also investigated:

- Pulse (time domain)
- Step (time domain)
- Lock-in (frequency domain)
- Pulse-phase (frequency domain)

The pulse analysis procedure utilized data that were collected while the surface cooled. Five different pulse durations were investigated. The signal half-life ($t_{1/2}$) was the most useful parameter for determining defect depth. Two models were calibrated using data from the Series A specimens. The following relationship was established for air-filled defects:

$$C \times d = 4.33 \times t_{1/2} - 52.2 \qquad (6\text{-}16)$$

For epoxy-filled defects:

$$C \times d = 1.81 \times t_{1/2} - 9.9 \qquad (6\text{-}17)$$

C = Circumference of defect (mm)
d = Depth of defect (mm)
$t_{1/2}$ = Defect signal half-life

The size of the defect and the signal half-life are obtained from the series of thermal images. Once these parameters are established, two possible values for defect depth can be determined. One value assumes that the defect is air-filled. The second value assumes the defect is epoxy-filled.

This model was calibrated using specimens containing fabricated defects at the FRP/concrete interface. When the model was applied to data collected from three different specimens, it was shown that good agreement exists for other defects that occur at the FRP/concrete interface. The model was shown to be ineffective when applied to a defect located between layers of FRP in a multi-layer system.

Step analysis involved analyzing data that were collected while the specimens were heated. A normalization process was applied to each pixel in the thermal images and the effects of non-uniform heating were reduced. This method also demonstrated that the normalized temperature response on the surface of the FRP is strongly influenced by the thickness of the FRP system. The concrete substrate acts like a large heat sink and reduces the rate of surface temperature increase.

The heating time for step analysis was limited to 60 sec in the current study. This pulse duration was shown to be sufficient for detecting defects in the one and two-layer FRP systems. It was possible to differentiate between defects that occurred at the FRP/concrete interface and defects that occurred between layers. This was accomplished by examining the ΔT_{def} signal generated by a defect and the normalized temperature response of the adjacent defect-free region.

The 60 sec pulse duration was not sufficient to detect and characterize defects in the three and four-layer specimens. It was later determined that the normalized temperature response (ΔT_{norm}) could also be computed for each pixel while the specimen cooled. Even though the absolute magnitude of ΔT_{norm} decreases rapidly after the heat source is removed. The relative rate of cooling between defect and defect-free areas is still different. A sample surface is for Specimen A-3 is shown in Figure 6-83 A. This surface plot of ΔT_{norm} was generated 100 sec after the 60 sec heat pulse was terminated. The effects of non-uniform heating have been removed

The two remaining data analysis techniques, lock-in and pulse phase, were also shown to limit the effects of non-uniform heating. It is interesting to make a side by side comparison of the ΔT_{norm} results (time domain) and the frequency domain results (Figure

6-83 B and C). The first result shown in Figure 6-83 A was obtained by normalizing the series of thermal images using the initial slope of the temperature vs. $t^{1/2}$ response. The second result (Figure 6-83 B) was obtained by applying a least squares sinusoidal curve fit to temperature vs. time data and examining the phase response. The final result, Figure 6-83 C, was obtained by applying a discrete Fourier transform to the data collected during cooling. All three results are very similar. Most importantly, the results are independent of the intensity of the heat flux that was used to heat the surface.

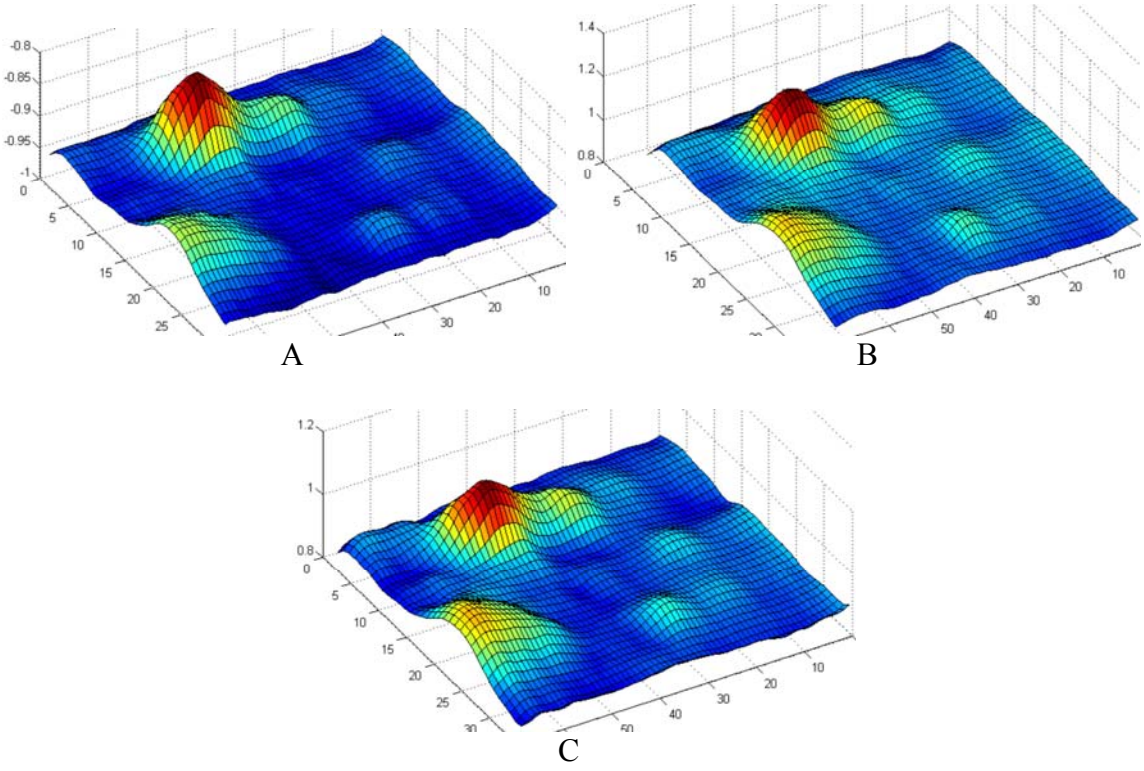

Figure 6-83. Comparison of data analysis techniques for Specimen A-3. A) Normalized temperature result at t = 160 sec. B) Lock-in results for pulse duration = 250 sec. C) Pulse phase result at f = 0.0083 Hz.

Series B, C, D, and E Specimens

The specimens in Series B, C, D, and E were constructed to investigate the effects of the following FRP system properties on IRT results:

- Matrix saturation levels
- Fiber type
- Surface preparation methods
- Fabric saturation methods
- Lap splices

The original intent was to evaluate the response of implanted defects that were placed in specimens with different FRP system properties. All of the implanted defects in Series B and C were created as interface bubbles using the procedure outlined in Chapter 5. This defect configuration produced poor results for the specimens in Series A. The large number of unintentional defects and other non homogeneities in the FRP composite made the characterization process difficult. Initial investigations into the Series B specimens produced similar results. It was not possible to compare results for the defects in multi-layer FRP systems. Rather than focus on the IRT results for the different defects in Series B and Series C, it was determined that an investigation into the response of the defect-free areas would provide more useful information.

The step analysis procedure was shown to provide an indication of the thickness of the FRP composite. This is the most important parameter to consider when trying to decide how an FRP composite should be inspected using IRT. If the composite is thin (i.e. the effects of the concrete are observed at early times in the heating process), the duration of heating and the observation time can be short. Thicker composites require longer heating and observation times.

"Thick" and "thin" are relative terms. Decisions regarding heating and observation times should be based on the observed response of the FRP composite to applied heating. In this section, the step analysis procedure was used to investigate the response of defect-free regions in Series B to E specimens. The objective of this investigation was to

determine if the parameters that were varied between each specimen in these series have an impact on the normalized temperature response.

Data Collection

Each specimen in Series B, C, D, and E was heated for 60 sec using the long-pulse experimental setup described in Chapter 5. Thermal images were collected at a rate of one frame per second while the specimens were heated. The data were normalized based on the slope of the temperature vs. $t^{1/2}$ response for $1 \leq t^{1/2} \leq 2$. A defect-free area was identified near the center of each specimen. The exact size and orientation of the defect-free areas were not the same on each specimen because of the implanted defects. The size of each area varied between 22.6 cm^2 and 55.5 cm^2.

The mean and standard deviation (σ) of ΔT_{norm} were computed for each area at each time step. These results were plotted against the square root of time ($t^{1/2}$) with error bars representing +/- 2 σ. ΔT_{norm} vs. $t^{1/2}$ plots and summary statistics for each curve at t = 60 sec are provided in Appendix C. The following sections contain a summary of these results.

Series B

Series B contained a total of 18 specimens with different matrix saturation levels (low, medium, and high). Twelve specimens were constructed using carbon-fibers and six specimens were constructed using glass-fibers.

Low saturation (carbon-fibers)

Under saturation of the carbon-fibers was expected to result in small air voids throughout the FRP composite. These air voids should have the following effects on the normalized temperature response:

- The overall rate of heat transfer through the FRP composite and into the concrete will be less than for a properly saturated composite. The effects of the concrete substrate should be observed at a later time.
- The normalized temperature distribution will have greater variation across the surface of the composite.

Defect-free areas on the one and two-layer specimens (B-LC-1 and B-LC-2) responded similarly to the one and two-layer specimens in Series A. The mean value of ΔT_{norm} at the end of heating was -0.27 and -0.10 for B-LC-1 and B-LC-2, respectively. The corresponding values for the properly saturated systems in Series A were -0.29 and -0.9. Specimens B-LC-3 and B-LC-4 behaved differently than the corresponding three and four-layer specimens in Series A. The mean values for the defect-free areas at the end of heating were higher in the Series B specimens (+0.14 and +0.23 for B-LC-3 and B-LC-4, respectively). This would indicate that the thermal front requires more time to reach the FRP/concrete interface.

The observations made for the three and four-layer specimens are consistent with the expected behavior. The standard deviations computed for each area were also higher than what was observed for Series A. Careful examination of surface plots for normalized temperature did indicate some variability in the temperature response across the three and four-layer specimens, but not nearly to the extent that was expected. It is not possible to ascertain the cause of this variability without a destructive inspection of the FRP composite through the cross-section.

Medium saturation (carbon-fibers)

The four specimens contained in the medium saturation subset were expected to behave the same as the four specimens in Series A. The Series A specimens and the

medium saturation specimens in Series B were constructed using the amount of epoxy recommended by the FRP system manufacturer.

Normalized temperature results for the single-layer specimens appear to be very similar. The mean value of ΔT_{norm} for Specimen B-MC-1 was -0.277 ($\sigma = 0.023$). The mean value of ΔT_{norm} for Specimen A-1 was -0.283 ($\sigma = 0.018$). A Student t-test was performed to validate the hypothesis that the two means are equal (Table 6-23). The corresponding t-test value was 6.66. This value exceeds the tabulated t-value for p = 0.001 (degrees of freedom = ∞), which indicates that the means are significantly different. The t-test value obtained when comparing the two means for the two-layer specimens was 0.99, which indicates that the means are essentially the same.

Table 6-23. Normalized temperature response @ t = 60 sec for properly saturated specimens

	Series B: medium saturation			Series A: medium saturation			
Layers	NP	Mean @ t=60 sec	Standard deviation @ t = 60 sec	NP	Mean @ t=60 sec	Standard deviation @ t = 60 sec	t-test value
1	1350	-0.277	0.023	770	-0.283	.018	6.66
1[a]	50	-0.277	0.022	50	-0.279	.019	0.49
2	1196	-0.093	0.023	780	-0.092	.021	0.99
3	1092	+0.008	0.017	864	+0.023	.019	18.16
4	990	+0.027	0.025	851	+0.084	.020	54.31

[a] Defect free areas on Specimen A-1 and Specimen B-MC-1 were randomly sampled for 50 data points

The requirements for claiming significance based on Student's t-test are very stringent if a large number of data points are considered. A better test for significance may be to randomly sample each of the areas for 50 data points and then compute the mean and standard deviation of the sample. This operation was performed for the defect-free areas on Specimen A-1 and Specimen B-MC-1. The resulting means and standard deviations were essentially the same but the t-value was reduced to 0.48. This t-value indicates that the means are not significantly different. Additional investigation is needed

to determine an appropriate method for sampling the defect-free regions in a specimen and comparing the normalized temperature response.

High saturation (carbon-fibers)

Applying excess epoxy during fiber saturation was expected to slow down the rate of heat transfer though the composite. This behavior was observed. The single-layer specimen (B-HC-1) generated a ΔT_{norm} response that was similar to the two-layer specimens that were properly saturated. The ΔT_{norm} at t = 60 sec for Specimen B-HC-1 was only -0.15 (σ = 0.042). The two-layer specimen with heavy saturation displayed similar behavior to a three-layer specimen that was properly saturated. At the end of heating, the two, three, and four-layer specimens were still grouped together with ΔT_{norm} values greater than 0.05. These data support the finding from the Phase I study that highly saturated FRP composites will require longer heating and observation times than properly saturated composites.

Glass-fiber specimens

Analysis of the defect-free area in each glass-fiber specimen showed that heat is transferred from the surface of the composite to the concrete more slowly than for carbon-fiber FRP systems. This suggests that glass-fiber FRP systems require longer heating durations and longer observation times than carbon-fiber FRP systems of the same thickness. For the two-layer specimen, the maximum value of ΔT_{norm} (+0.38) occurred at $t^{1/2}$ = 6.5. At the end of heating, ΔT_{norm} was still positive (+0.35). The four-layer specimen did not achive a local maximum and the ΔT_{norm} at the end of heating was +0.55. This indicates that the thermal front had not yet reached the FRP/concrete interface.

Specimens with low and high matrix saturation levels produced different ΔT_{norm} results than the properly saturated specimens. The ΔT_{norm} was influenced by the concrete at an earlier time for the undersaturated specimens. The ΔT_{norm} response of the oversaturated specimens was not influenced by the concrete.

Series C

Series C contained six specimens. Two variables were investigated with this series:

- Surface preparation methods: none, light blast, or heavy blast
- Use of thickened-epoxy tack-coat

No significant difference was observed in the normalized temperature response based on the surface preparation method. A consistent trend was observed with respect to specimens constructed with and without thickened-epoxy tack-coat. The three specimens constructed without tack-coat moved heat away from the surface faster than the three specimens constructed with tack-coat. The mean value of ΔT_{norm} at t = 60 sec for the three specimens containing the thickened epoxy was 0.296 (σ = 0.006). These values are consistent with the other single-layer specimens that were properly saturated and constructed with tack-coat. The mean value for the three specimens without tack-coat was 0.329 (σ = 0.003). The two means were compared using Student's t-test. The resulting t-value of 9.31 shows that the means are significantly different (degrees of freedom = 4, p = 0.001, t_{sig} = 8.61).

Series D

Series D contained three specimens. Three different fiber saturation techniques were used during specimen construction:

- Surface saturation (D-1)
- Heavy pressure with roller (D-2)
- Light pressure with roller (D-3)

The first two cases, surface saturation and heavy pressure with the roller, resulted in composites with fiber weight fractions of 0.50 and 0.51, respectively. The final layer of epoxy top-coat was omitted from Specimen D-1. The third saturation method, light roller, resulted in a fiber weight fraction of 0.40 (i.e. a larger percentage of the composite was epoxy). The total amount of epoxy used to construct each specimen (including saturant, tack-coat and top coat) was:

- D-1: 43.7 g
- D-2: 50.6 g
- D-3: 72.5 g

The ΔT_{norm} response for this series of specimens followed a trend that consistent with the total amount of epoxy that was used to construct each specimen. The composite containing the least amount of epoxy (D-1) was shown to move heat away from the surface more rapidly than the other three specimens with more epoxy.

Series E

The final series contained three specimens. The objective of these specimens was to investigate whether or not IRT could be used to determine the location of lap splices in FRP systems. All three specimens were constructed using properly proportioned composites. The lap splices were designed such that the middle third of each specimen contained the thickest portion of the lap splice. It was shown in the previous sections that the step analysis method was capable of distinguishing between FRP systems with different thicknesses. The only thing unique about this set of specimens is that the FRP thickness varies within each specimen. In all cases the lap splices were detected. The normalized temperature response for each area was also consistent with results from other

specimens having the same thickness. Surface plots of normalized temperature at t = 60 sec are provided in Appendix C.

CHAPTER 7
SUMMARY AND RECOMMENDATIONS FOR FUTURE RESEARCH

Summary

The use of fiber-reinforced polymer (FRP) composites for strengthening existing civil infrastructure is expanding rapidly. This research investigated using infrared thermography (IRT) to evaluate bond in FRP systems. Current guidelines provided by ACI, NCHRP, and ICBO specify allowable defect sizes in FRP systems, and IRT is cited as a possible nondestructive evaluation (NDE) technique. There are currently no standardized inspection procedures for applying IRT to FRP composites bonded to concrete.

Results from the current study indicate that IRT is a potentially useful tool for evaluating bond in FRP systems applied to concrete. It was shown that defects as small as 6.4 mm in diameter can be detected in 1 mm thick carbon FRP composites. For the thickest carbon FRP composite systems investigated in the current study (4 mm), defects as small as 19 mm in diameter were detected. The experimental data generated by this research is an important first step towards the development of standardized inspection procedures.

This chapter contains a summary of the findings from Phase I and Phase II of the current study as well as recommendations for future research. Finally, recommendations are provided for the deployment of IRT for inspecting FRP composites applied to concrete.

Phase I

In Phase I of this research, IRT was used to inspect full-scale AASHTO pretensioned concrete bridge girders that were strengthened with FRP composites. The first part of this phase involved an FDOT study on using FRP composites to strengthen bridges that had been hit by over height vehicles. Four full-scale AASHTO girders with simulated vehicle impact damage were repaired and strengthened with FRP composites in a laboratory environment. Each FRP system was designed and installed by the FRP system manufacturer. In the second part of Phase I, an in service bridge that had been damaged by vehicle impact and repaired with FRP composites was inspected using IRT. Significant findings and conclusions are highlighted in the following sections.

Laboratory Study

- IRT results were found to vary considerably with FRP composite characteristics.
- The measured thickness of the installed FRP systems, on average, was two times the manufacturer's reported thickness for the carbon-fiber systems.
- Infrared thermography was not effective for the FRP system that contained polyurethane matrix material. This type of matrix material acts as a strong thermal insulator that prevents heat from traveling through the FRP composite. IRT is not recommended for use with these types of FRP systems.
- Thermal images collected using a hand-propelled cart resulted in non-uniform heating of the FRP composite due to the variation in cart speed. As a result, quantitative data that was collected for defects could not be compared.
- The average IRT data collection period was 20 sec, which was found to be too short to identify defects that occurred at depths greater than 1 mm. The scanning procedure, however, did detect defects located within 1mm of the surface.
- Constant motion of the camera created images in which the relative position of the subject was constantly changing. Consequently it was necessary to extract the data for each defect frame by frame from a series of thermal images. If a quantitative analysis is desired, the IR camera should remain stationary throughout the duration of heating and cooling.

Field Study

- Applying IRT in the field presented several unanticipated challenges. In the current study, a scissor lift was used to gain access to the FRP composite. The IR camera, the IR camera operator, the heat source, and the heat source operator were all confined to a 6 ft. x 12 ft. area that was lifted 12 ft above the ground, which inhibited both heating and image collection activity. Furthermore, noise from the generators and adjacent highway traffic inhibited verbal communication. Positioning the camera with respect to the surface being inspected was also challenging.

- Installation defects were detected using IRT in the original FRP system used to strengthen the bridge. The IRT results could be verified for large defects (on the order of 25 cm^2) with a combination of visual inspection and acoustic sounding. Defects smaller than 10 cm^2, however, were not detected visually or with acoustic sounding.

- Damage sustained by the FRP composite system due to vehicle impact was limited to the immediate vicinity of the impact. This was verified with acoustic sounding (coin-tap) and IRT.

Phase II

Results from Phase I indicated that additional research was needed to develop a standardized approach for inspecting FRP composites applied to concrete. Thirty-four small-scale specimens were constructed. These specimens contained fabricated defects of varying size and depth. The effects of matrix saturation level were also investigated. The overall objective of Phase II was to investigate different heating methods and quantitative IRT analysis techniques that can be used detect and characterize defects (i.e. determine the size, depth, and material composition).

Heating Methods

- Flash heating was effective for detecting air-filled defects in single-layer (1 mm) carbon FRP systems. Defects larger than 12.8 mm in diameter developed a strong signal ($\Delta T_{max} > 2.0°C$) that could be used to estimate size. Flash heating produced weak signals for implanted defects in carbon FRP systems 2 mm thick or greater.

- Scan heating was effective for detecting air-filled and epoxy-filled defects in carbon FRP systems up to 4 mm thick. Scan heating also produced higher values for ΔT_{max} compared to flash and long-pulse heating.

- Long-pulse heating was also effective for detecting air and epoxy-filled defects that occurred up to 4 mm beneath the surface. One disadvantage of the long-pulse method was that the surface was not heated uniformly. It was shown, however, that several data analysis techniques can be employed to reduce the effects of non-uniform heating.

Data Analysis Methods

Pulse analysis

- The defect signal strength (ΔT_{def}) vs. time response for implanted defects depended on the following parameters: heat source intensity; duration of heating; thickness of the FRP composite system; and the size, depth, and material composition of the defect.

- The pulse analysis model based on signal half-life ($t_{1/2}$) provided a good estimate of defect depth for carbon FRP systems up to 3 mm thick.

- Signal half-life could also be used to determine if a defect was air-filled or epoxy-filled for carbon FRP composite systems up to 2 mm thick.

- A model was developed to estimate depth and material composition of defects based on data collected during cooling. This model was calibrated using data from defects that occurred at the FRP/concrete interface. When this model was applied to defects that occurred between layers of FRP, the resulting estimates for depth and composition were not accurate.

Step analysis

- The normalized surface temperature increase (ΔT_{norm}) that was measured during heating was strongly influenced by the thickness of the FRP composite system. These data could be used to provide an estimate of the thickness and matrix saturation level of the FRP composite system.

- A 60 sec pulse duration was sufficient to detect implanted defects to a depth of 2 mm in properly saturated carbon FRP composites. Deeper defects were not detected with the 60 sec pulse duration.

- It was possible to distinguish between defects that occurred between layers and defects that occurred at the FRP/concrete interface.

Lock-in analysis

- Lock-in analysis requires sinusoidal heating. Unique experiments involving different pulse durations are required to inspect FRP composites with different thicknesses.

- Lock-in analysis was shown to reduce the effects of non-uniform heating and increase detectability for defects in three and four-layer FRP systems.

Pulse phase analysis

- The pulse phase analysis procedure was used on data that were collected during cooling. A discrete Fourier transform was applied to each pixel in a series of thermal images to generate a series of phase images.

- The phase response of defect-free areas was not affected by non-uniform heating. This increased detectability for defects in three and four-layer FRP systems.

- Defects that are close to the surface appear over a wide range of frequencies while deeper defects only appear in low-frequency phase images.

FRP System Properties and IRT Results

- Oversaturated composites increase the amount of time required for the thermal front to reach the concrete substrate. A 1 mm thick carbon FRP lamina that was oversaturated by 50% displayed a normalized temperature response similar to a 2 mm thick carbon laminate that was properly saturated.

- On average, the standard deviation of the normalized temperature response was larger for undersaturated composites ($\sigma = 0.035$) than for properly saturated composites ($\sigma = 0.022$).

- Concrete surface preparation levels had no noticeable affect on the normalized temperature response of specimens in Series C.

- It was possible to identify the location and length of lap splices using the normalized temperature response of defect-free areas.

Recommendations for Deployment of IRT

Guidelines for Qualitative IRT Inspections

- The scan heating method (described in Chapter 5) is recommended for qualitative IRT inspections.

- The IR camera should be positioned with respect to the surface under consideration such that at least 10 pixels occupy the dimension of the smallest defect of interest in the thermal images.

- The heat source configuration should be adjusted such that an average temperature increase of 20 °C is obtained after 15 sec of exposure.

- A reflective shield should be used to limit the amount of heat energy reflected by the surface of the composite back to the IR camera.

- The heat source should be moved from one side of the camera's field of view (FOV) to the other at a constant velocity (same speed and same direction). The heat source should not be waved back and forth across an area (Figure 7-1).

- If multiple passes are required to heat the entire area within the IR camera's FOV, the surface temperature of the heated area should return to the initial conditions before the next pass is made. This will avoid overlap of heated areas.

- Thermal images should be stored at a minimum rate of one frame per second for carbon FRP systems less than 2 mm thick. The image save rate may be decreased to one frame per two seconds for carbon FRP systems greater than 2 mm thick.

- The observation time for carbon FRP systems less than 2 mm thick should be from 3 to 4 minutes. The observation time for FRP systems greater than 2 mm thick should be from 4 to 6 minutes. Longer observation times increase certainty that all defects have been detected.

- Defect size can be estimated using the gradient area method. The temperature difference between the defect and defect-free area should be at least 2.0 °C

Figure 7-1. Field inspection (scan heating method) of FRP system applied to AASHTO girder. IR Camera was located on the ground (9 feet from surface being heated). A 2x telephoto lens was used to narrow the IR camera's field of view.

Quantitative Analysis

- The long-pulse heating method (described in Chapter 5) is recommended for quantitative IRT inspections. The heat source and camera should remain fixed throughout the duration of heating and cooling.

- The heat lamps should be configured such that a minimum temperature increase of 5°C is experienced by all areas within the IR camera's FOV.

- Thermal images should be collected at a minimum rate of one frame per second during heating and cooling. Additional research may support increasing the minimum image save rate during the initial stages of heating. This increase in image save rate may improve the estimate of the initial slope used in the step analysis procedure.

- The duration of the heat pulse and required observation time is dictated by the thickness of the FRP system and the amount of matrix material that was used to saturate the composite. A minimum pulse duration of 60 sec is recommended for carbon FRP systems less than 2 mm thick.

Future Research

- The guidelines for performing qualitative IRT inspections were based primarily on experience. A rational method for determining the required heating duration, heating intensity and observation time is still needed.

- The step analysis method generated normalized temperature results that could be related to the thickness of the FRP composite. It may be possible to relate these data to heating intensity and duration requirements for thicker FRP systems.

- Additional research is needed to refine the data collection procedure for the step analysis method. Experiments should be conducted using homogenous samples, such as acrylic or polyethylene. Variables to be considered include the image acquisition rate during the initial stages of heating and the uniformity of the heat pulse as a function of time.

- Additional research is needed to evaluate the effect of FRP system properties on the response of defect areas.

- Finite element modeling would be useful for describing the fundamental heat transfer mechanisms that generate temperature differences above defects. These models would help to provide a better understanding of the temperature distribution below the surface of the FRP composite.

- Further research is needed into the effects of convection on IRT results.

- Further research is needed to describe the physical meaning of frequency domain results. Of particular interest is the case where near surface defects generate a relative phase response that is smaller than what was observed for defect-free regions.

- The implanted defects that were discussed in the current study all occurred between layers of FRP or at the FRP concrete interface. Additional research is required to establish inspection procedures and detection limits for defects that occur below the FRP /concrete bond line.

- All of the implanted defects used in the current study were round or elliptical. Further experimental and/or analytical work is needed to investigate the effects of long defects that can not be reasonably contained by a rectangle.

- Further investigation is needed to verify that the temperature gradients induced by IRT inspections are not harmful to FRP composites.

APPENDIX A
TIME DOMAIN RESULTS: SERIES A

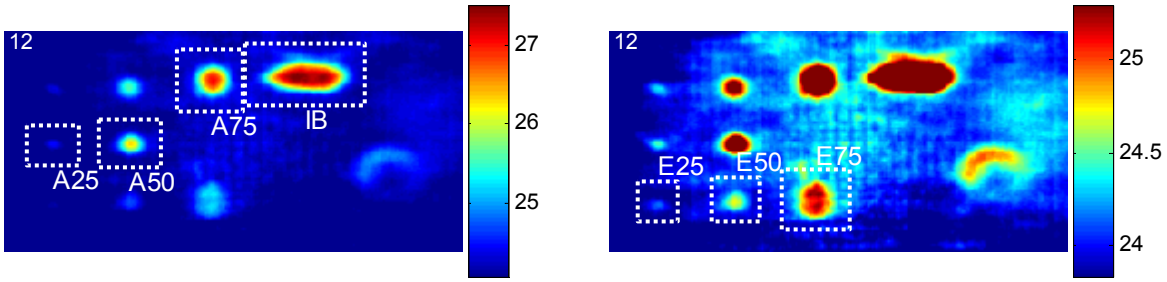

(A) A-1 (air-filled)

(B) A-1 (epoxy-filled)

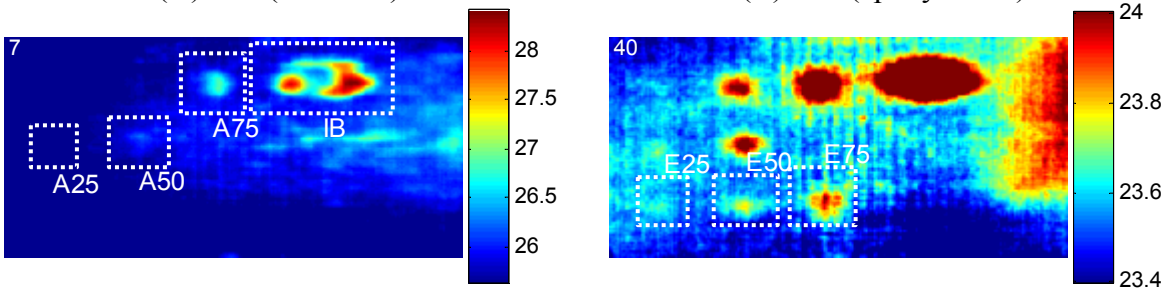

(C) A-2 (air-filled)

(D) A-2 (epoxy-filled)

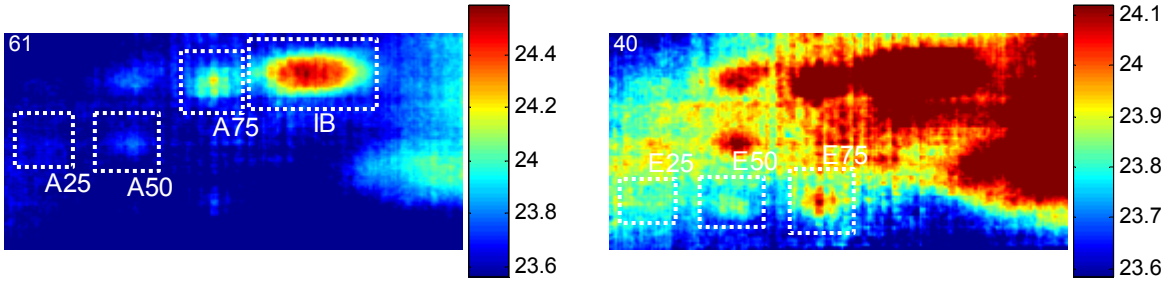

(E) A-3 (air-filled)

(F) A-3 (epoxy-filled)

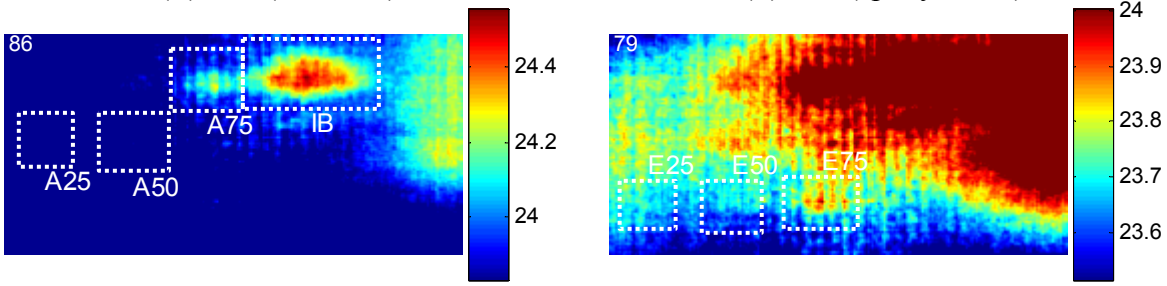

(G) A-4 (air-filled)

(H) A-4 (epoxy-filled)

Figure A-1. Flash heating results: Thermal images for Series A.

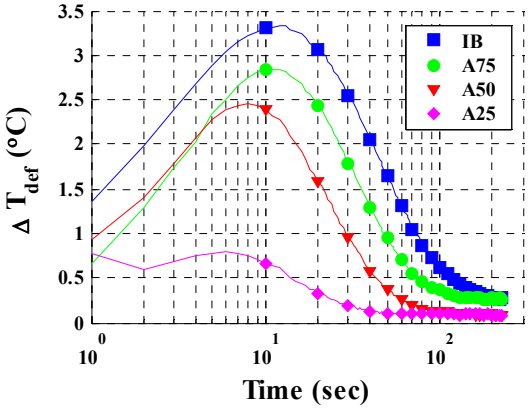

(A) A-1 (air-filled)

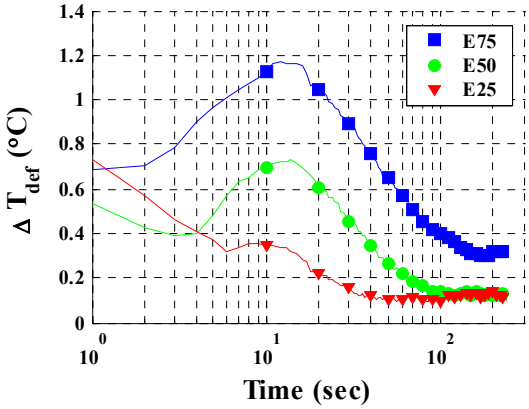

(B) A-1 (epoxy-filled)

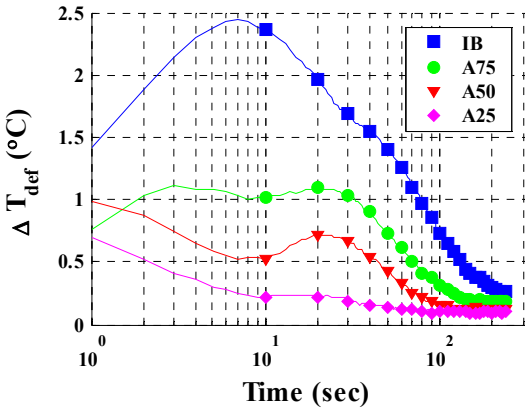

(C) A-2 (air-filled)

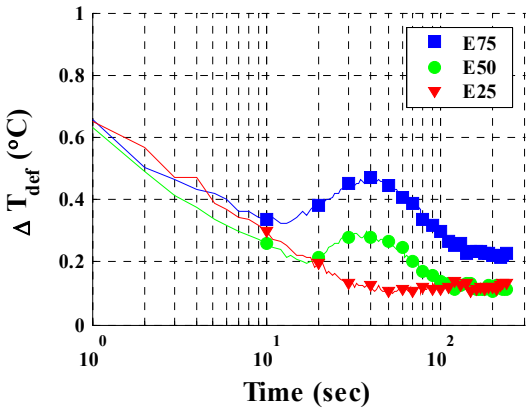

(D) A-2 (epoxy-filled)

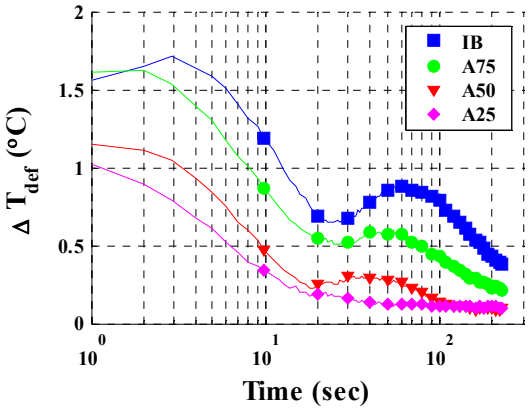

(E) A-3 (air-filled)

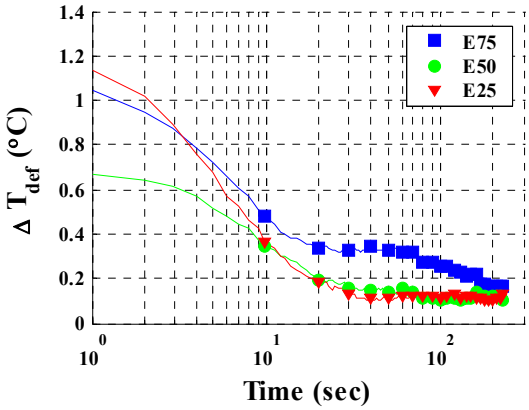

(F) A-3 (epoxy-filled)

Figure A-2. Flash heating results: ΔT_{def} vs. time plots for Series A.

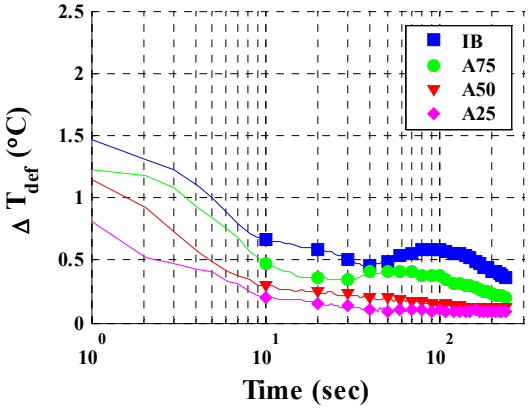

(G) A-4 (air-filled)

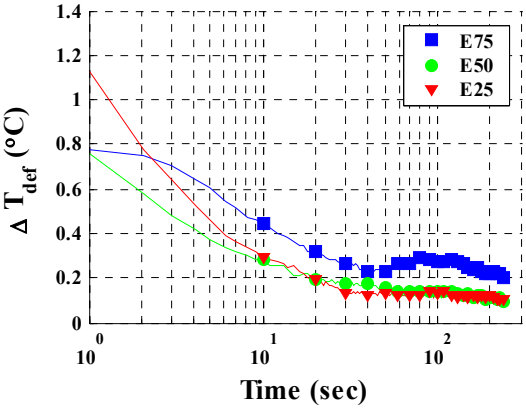

(H) A-4 (epoxy-filled)

Figure A-2. Continued

Table A-1. Flash heating results for Series A

	Defect	Defect material	ΔT_{per} (°C)	ΔT_{max} (°C)	t_b (sec)	t_{max} (sec)	$t_{1/2}$ (sec)	SBR	Actual diameter (in)	Image diameter (in)	COV
Specimen A-1	IB	Air	7.1	3.3	0	12	38	40.9	1.34	1.15	0.33
	A75	Air	7.0	2.8	1	10	28	33.5	0.75	0.72	0.10
	A50	Air	7.0	2.5	0	8	18	23.3	0.50	0.48	0.11
	A25	Air	5.8	0.8	2	6	12	3.5	0.25	0.27	0.28
	E75	Epoxy	6.7	1.2	1	12	47	6.6	0.75	0.84	0.20
	E50	Epoxy	6.4	0.7	3	14	25	6.2	0.50	0.49	0.08
	E25	Epoxy	5.3	0.4	6	5	20	1.9	0.25	0.34	0.79

	Defect	Defect material	ΔT_{per} (°C)	ΔT_{max} (°C)	t_b (sec)	t_{max} (sec)	$t_{1/2}$ (sec)	SBR	Actual diameter (in)	Image diameter (in)	COV
Specimen A-2	IB	Air	7.3	2.4	0	7	55	19.1	1.69	1.46	0.40
	A75	Air	7.1	1.1	8	20	47	12.4	0.75	0.74	0.23
	A50	Air	7.1	0.7	7	23	35	16.4	0.50	0.56	0.12
	A25	Air	5.8	-	-	-	-	-	0.25	-	-
	E75	Epoxy	6.9	0.5	13	40	98	8.6	0.75	0.72	0.66
	E50	Epoxy	6.5	0.3	17	38	50	6.7	0.50	0.83	0.62
	E25	Epoxy	5.3	-	-	-	-	-	0.25	-	-

	Defect	Defect material	ΔT_{per} (°C)	ΔT_{max} (°C)	t_b (sec)	t_{max} (sec)	$t_{1/2}$ (sec)	SBR	Actual diameter (in)	Image diameter (in)	COV
Specimen A-3	IB	Air	6.1	0.9	25	61	136	12.7	1.63	1.56	0.33
	A75	Air	6.0	0.6	27	54	91	9.5	0.75	0.75	0.49
	A50	Air	5.9	0.3	18	36	60	7.3	0.50	0.85	0.62
	A25	Air	4.9	-	-	-	-	-	0.25	-	-
	E75	Epoxy	5.9	-	-	-	-	-	0.75	-	-
	E50	Epoxy	5.4	-	-	-	-	-	0.50	-	-
	E25	Epoxy	4.3	-	-	-	-	-	0.25	-	-

	Defect	Defect material	ΔT_{per} (°C)	ΔT_{max} (°C)	t_b (sec)	t_{max} (sec)	$t_{1/2}$ (sec)	SBR	Actual diameter (in)	Image diameter (in)	COV
Specimen A-4	IB	Air	8.1	0.6	37	86	-	10.8	1.63	1.69	0.47
	A75	Air	7.9	0.4	25	72	146	5.1	0.75	0.87	0.65
	A50	Air	7.9	-	-	-	-	-	0.50	-	-
	A25	Air	6.4	-	-	-	-	-	0.25	-	-
	E75	Epoxy	7.4	-	-	-	-	-	0.75	-	-
	E50	Epoxy	7.0	-	-	-	-	-	0.50	-	-
	E25	Epoxy	5.6	-	-	-	-	-	0.25	-	-

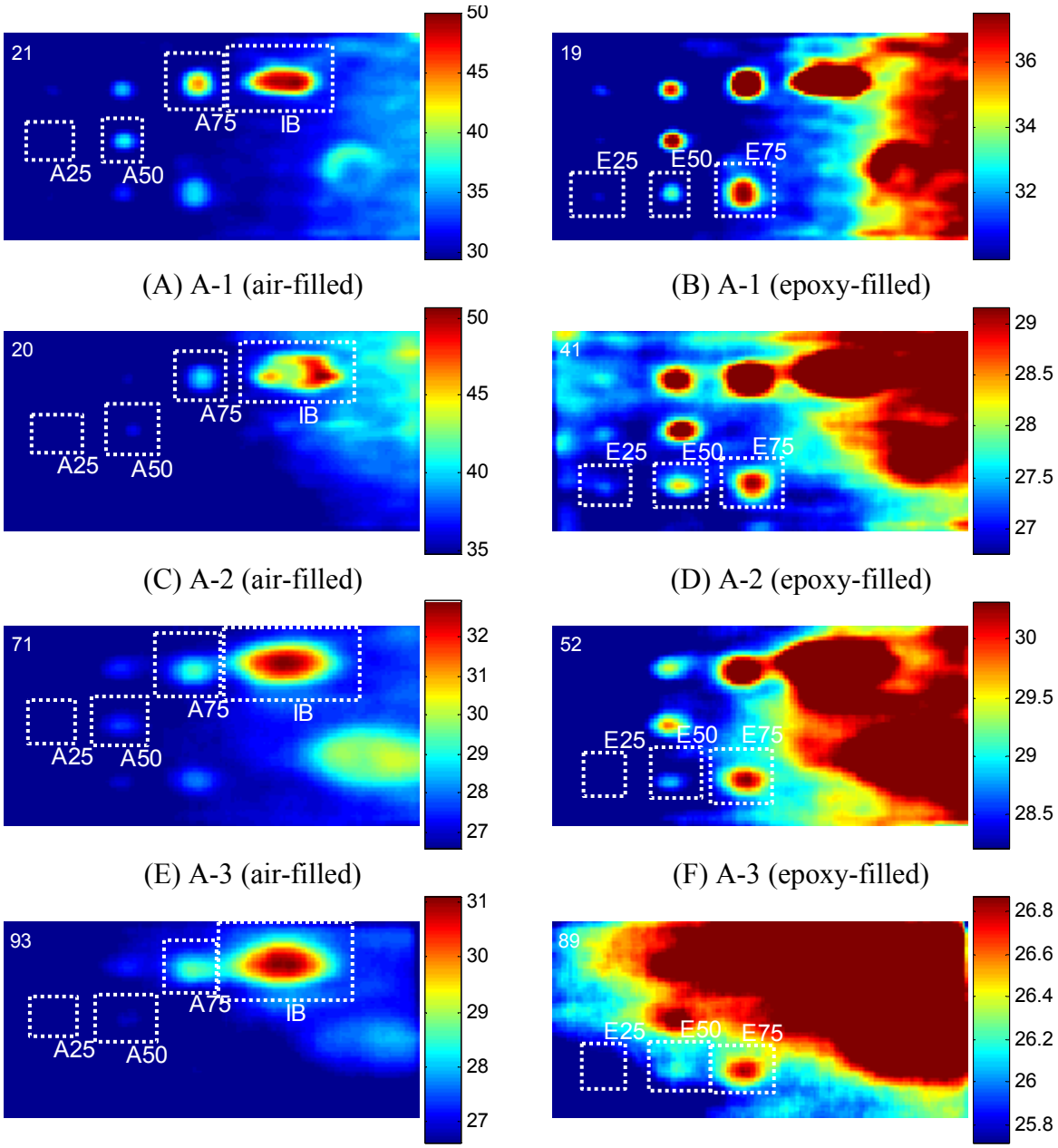

(A) A-1 (air-filled) (B) A-1 (epoxy-filled)

(C) A-2 (air-filled) (D) A-2 (epoxy-filled)

(E) A-3 (air-filled) (F) A-3 (epoxy-filled)

(G) A-4 (air-filled) (H) A-4 (epoxy-filled)

Figure A-3. Scan heating results: Thermal images for Series A.

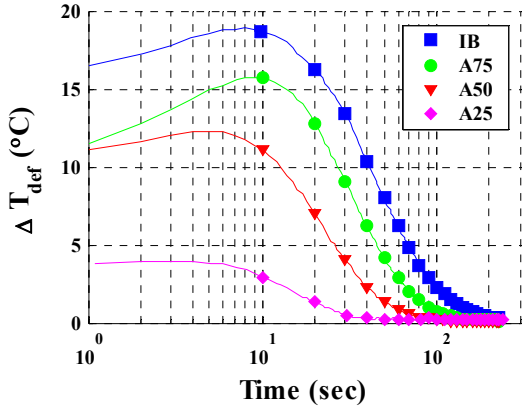

(A) A-1 (air-filled)

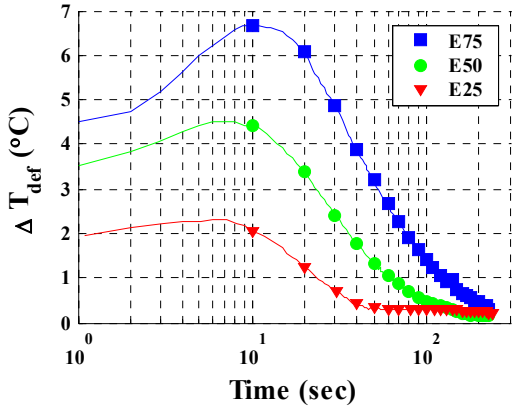

(B) A-1 (epoxy-filled)

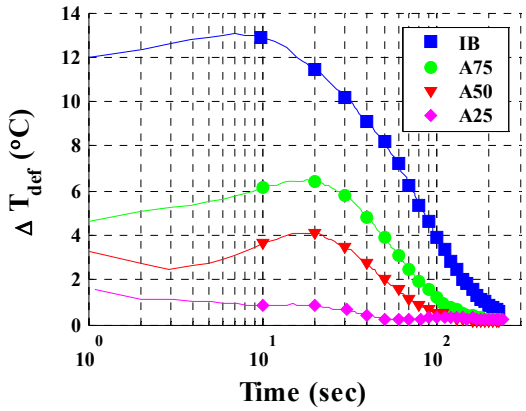

(C) A-2 (air-filled)

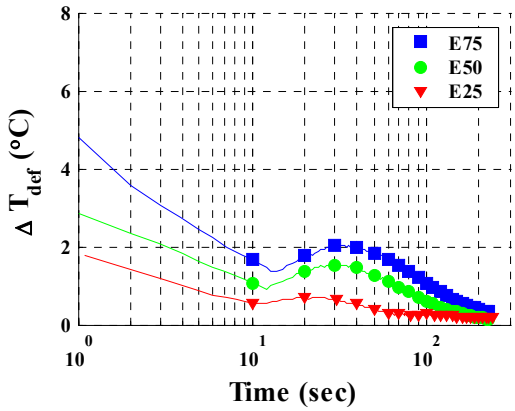

(D) A-2 (epoxy-filled)

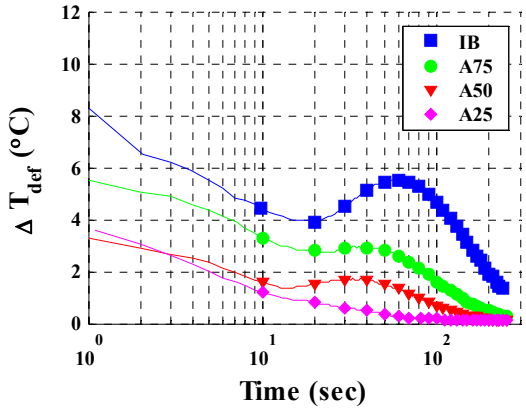

(E) A-3 (air-filled)

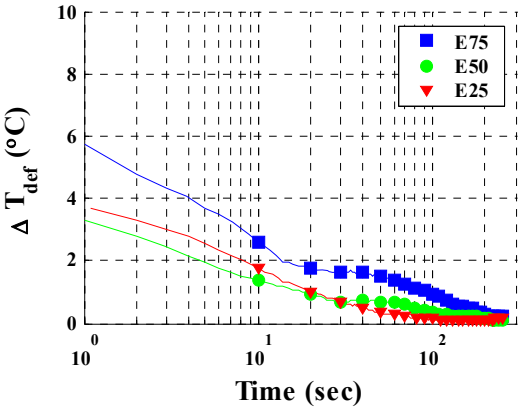

(F) A-3 (epoxy-filled)

Figure A-4. Scan heating results: ΔT_{def} vs. time plots for Series A.

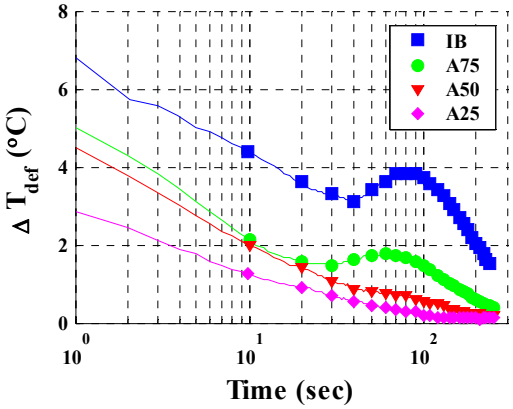

(G) A-4 (air-filled)

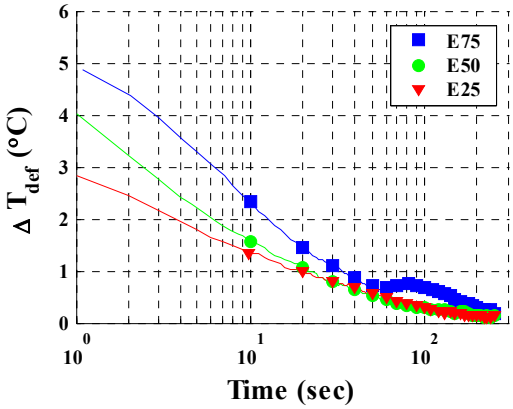

(H) A-4 (epoxy-filled)

Figure A-4. Continued

Table A-2. Scan heating results for Series A

	Defect	Defect material	ΔT_{per} (°C)	ΔT_{max} (°C)	t_b (sec)	t_{max} (sec)	$t_{1/2}$ (sec)	SBR	Actual diameter (in)	Image diameter (in)	COV
Specimen A-1	IB	Air	17.2	18.8	0	8	36	14.9	1.34	1.08	0.28
	A75	Air	21.8	15.7	0	9	25	22.8	0.75	0.69	0.10
	A50	Air	19.1	12.3	0	5	18	10.5	0.50	0.47	0.24
	A25	Air	22.3	4.0	0	4	12	4.8	0.25	0.29	0.82
	E75	Epoxy	23.5	6.7	1	11	37	13.0	0.75	0.79	0.09
	E50	Epoxy	19.6	4.5	0	7	26	7.5	0.50	0.50	0.15
	E25	Epoxy	22.8	2.3	1	6	16	5.5	0.25	0.39	0.33

	Defect	Defect material	ΔT_{per} (°C)	ΔT_{max} (°C)	t_b (sec)	t_{max} (sec)	$t_{1/2}$ (sec)	SBR	Actual diameter (in)	Image diameter (in)	COV
Specimen A-2	IB	Air	23.8	13.0	0	7	61	7.2	1.69	1.51	0.25
	A75	Air	26.4	6.5	1	18	41	13.7	0.75	0.71	0.13
	A50	Air	22.9	4.1	3	18	32	11.4	0.50	0.54	0.13
	A25	Air	25.6	0.9	9	15	25	3.1	0.25	0.36	0.31
	E75	Epoxy	23.3	2.0	14	33	70	10.7	0.75	0.78	0.15
	E50	Epoxy	20.6	1.5	12	30	57	6.2	0.50	0.56	0.21
	E25	Epoxy	23.1	0.7	11	20	34	3.5	0.25	0.45	0.69

	Defect	Defect material	ΔT_{per} (°C)	ΔT_{max} (°C)	t_b (sec)	t_{max} (sec)	$t_{1/2}$ (sec)	SBR	Actual diameter (in)	Image diameter (in)	COV
Specimen A-3	IB	Air	25.4	5.5	20	58	104	14.1	1.63	1.51	0.27
	A75	Air	26.5	2.9	23	38	69	6.1	0.75	0.80	0.12
	A50	Air	25.2	1.7	14	31	56	5.4	0.50	0.57	0.20
	A25	Air	28.0	-	-	-	-	-	0.25	-	-
	E75	Epoxy	30.8	1.6	21	44	73	5.2	0.75	0.77	0.16
	E50	Epoxy	26.2	0.8	30	42	54	3.3	0.50	0.49	0.22
	E25	Epoxy	29.0	-	-	-	-	-	0.25	-	-

	Defect	Defect material	ΔT_{per} (°C)	ΔT_{max} (°C)	t_b (sec)	t_{max} (sec)	$t_{1/2}$ (sec)	SBR	Actual diameter (in)	Image diameter (in)	COV
Specimen A-4	IB	Air	26.3	3.8	40	80	129	10.4	1.63	1.55	0.24
	A75	Air	29.2	1.8	30	62	91	3.8	0.75	0.86	0.22
	A50	Air	24.1	-	-	-	-	-	0.50	0.98	0.46
	A25	Air	-	-	-	-	-	-	0.25	-	-
	E75	Epoxy	22.1	0.7	52	80	86	3.5	0.75	0.79	0.39
	E50	Epoxy	-	-	-	-	-	-	0.50	-	-
	E25	Epoxy	-	-	-	-	-	-	0.25	-	-

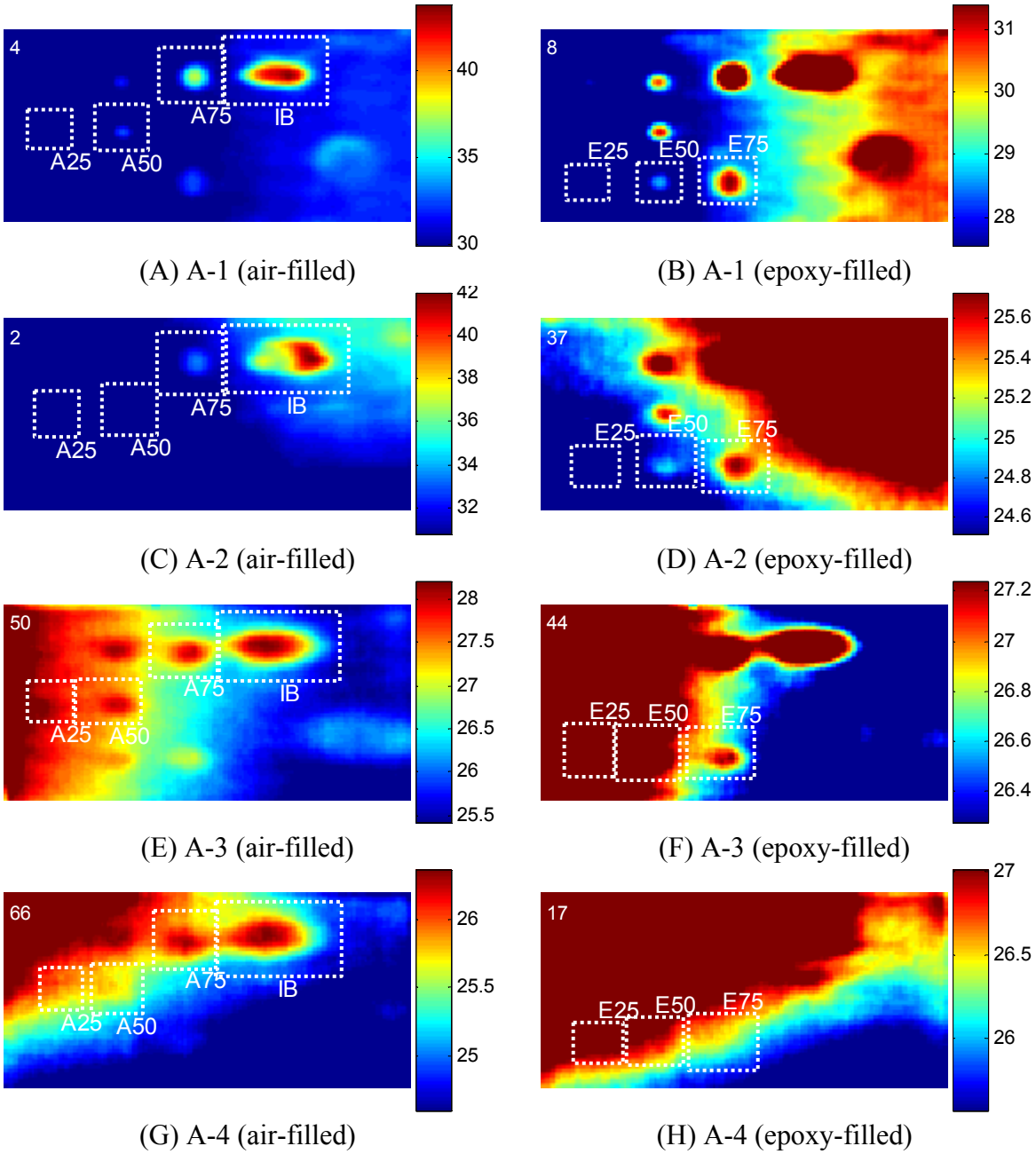

(A) A-1 (air-filled) (B) A-1 (epoxy-filled)

(C) A-2 (air-filled) (D) A-2 (epoxy-filled)

(E) A-3 (air-filled) (F) A-3 (epoxy-filled)

(G) A-4 (air-filled) (H) A-4 (epoxy-filled)

Figure A-5. Long-pulse (30 sec) heating results: Thermal images for Series A.

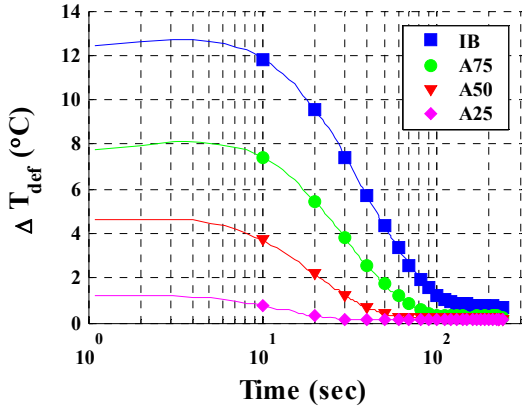

(A) A-1 (air-filled)

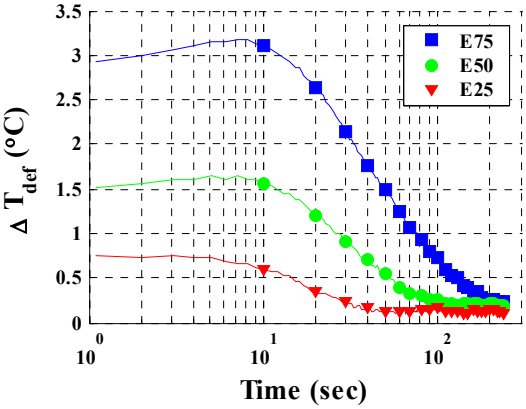

(B) A-1 (epoxy-filled)

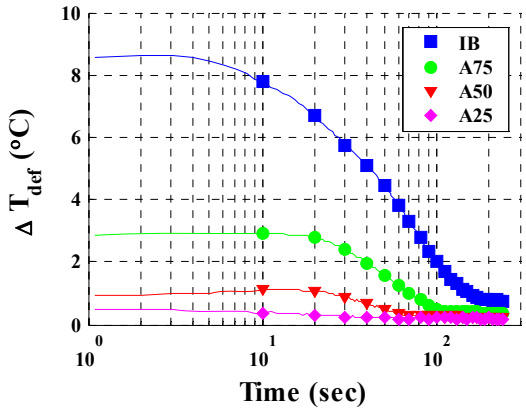

(C) A-2 (air-filled)

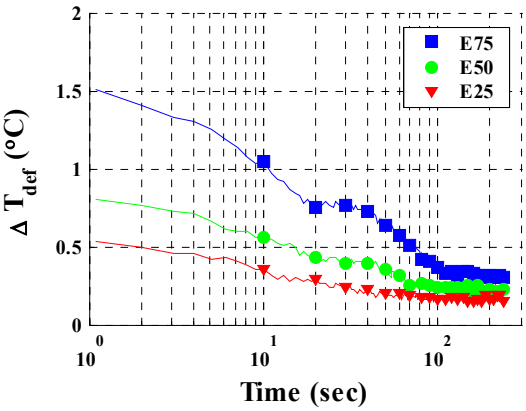

(D) A-2 (epoxy-filled)

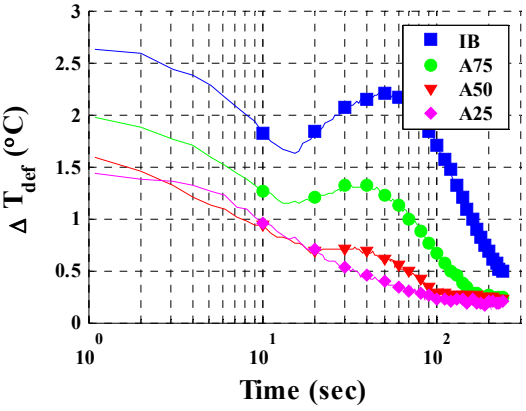

(E) A-3 (air-filled)

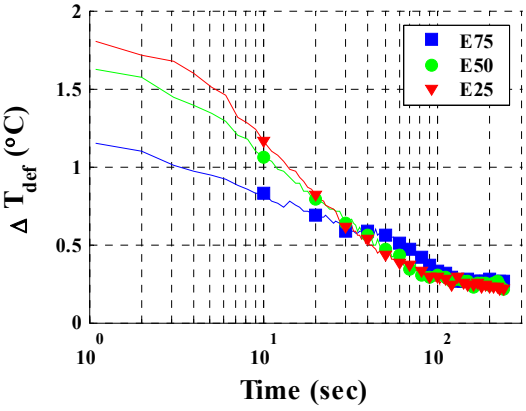

(F) A-3 (epoxy-filled)

Figure A-6. Long-pulse (30 sec) heating results: ΔT_{def} vs. time plots for Series A.

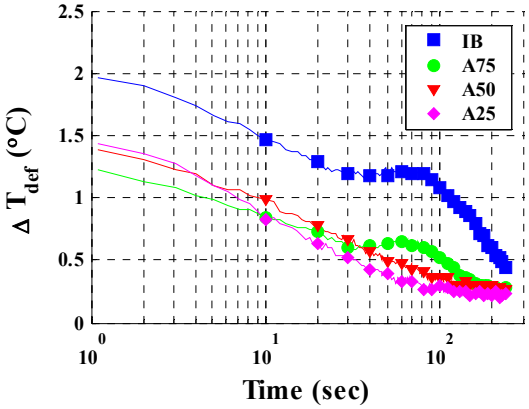

(G) A-4 (air-filled)

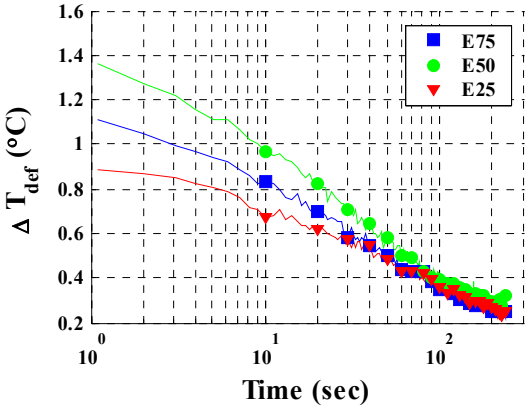

(H) A-4 (epoxy-filled)

Figure A-6. Continued

Table A-3. Long-pulse (30 sec) heating results for Series A

	Defect	Defect material	ΔT_{per} (°C)	ΔT_{max} (°C)	t_b (sec)	t_{max} (sec)	$t_{1/2}$ (sec)	SBR	Actual diameter (in)	Image diameter (in)	COV
Specimen A-1	IB	Air	9.0	12.7	0	4	33	17.7	1.34	1.07	0.30
	A75	Air	7.2	8.1	0	3	26	12.5	0.75	0.72	0.08
	A50	Air	5.6	4.6	0	1	18	11.1	0.50	0.48	0.15
	A25	Air	5.0	1.2	3	0	13	5.0	0.25	0.25	1.00
	E75	Epoxy	7.1	3.2	0	8	38	7.4	0.75	0.80	0.09
	E50	Epoxy	5.7	1.7	0	5	29	7.5	0.50	0.47	0.16
	E25	Epoxy	4.9	0.8	0	1	18	5.0	0.25	0.33	0.86

	Defect	Defect material	ΔT_{per} (°C)	ΔT_{max} (°C)	t_b (sec)	t_{max} (sec)	$t_{1/2}$ (sec)	SBR	Actual diameter (in)	Image diameter (in)	COV
Specimen A-2	IB	Air	10.4	8.6	0	2	51	5.8	1.69	1.55	0.37
	A75	Air	7.6	2.9	0	7	47	4.2	0.75	0.74	0.12
	A50	Air	5.8	1.1	2	12	34	3.4	0.50	0.56	0.25
	A25	Air	5.0	-	-	-	-	-	0.25	-	-
	E75	Epoxy	6.0	0.7	20	37	62	2.7	0.75	0.81	0.21
	E50	Epoxy	5.0	-	-	-	-	-	0.50	-	-
	E25	Epoxy	4.3	-	-	-	-	-	0.25	-	-

	Defect	Defect material	ΔT_{per} (°C)	ΔT_{max} (°C)	t_b (sec)	t_{max} (sec)	$t_{1/2}$ (sec)	SBR	Actual diameter (in)	Image diameter (in)	COV
Specimen A-3	IB	Air	7.9	2.2	15	50	100	5.7	1.63	1.52	0.30
	A75	Air	9.6	1.3	16	31	68	3.9	0.75	0.83	0.17
	A50	Air	11.9	0.7	19	39	50	2.4	0.50	0.57	0.24
	A25	Air	13.9	-	-	-	-	-	0.25	-	-
	E75	Epoxy	9.5	0.6	30	44	59	2.2	0.75	0.78	0.47
	E50	Epoxy	11.4	-	-	-	-	-	0.50	-	-
	E25	Epoxy	13.3	-	-	-	-	-	0.25	-	-

	Defect	Defect material	ΔT_{per} (°C)	ΔT_{max} (°C)	t_b (sec)	t_{max} (sec)	$t_{1/2}$ (sec)	SBR	Actual diameter (in)	Image diameter (in)	COV
Specimen A-4	IB	Air	6.8	1.2	30	66	129	3.4	1.63	1.58	0.41
	A75	Air	8.0	0.7	33	62	82	2.2	0.75	0.94	0.46
	A50	Air	7.9	-	-	-	-	-	0.50	-	-
	A25	Air	9.0	-	-	-	-	-	0.25	-	-
	E75	Epoxy	5.6	-	-	-	-	-	0.75	-	-
	E50	Epoxy	6.4	-	-	-	-	-	0.50	-	-
	E25	Epoxy	7.0	-	-	-	-	-	0.25	-	-

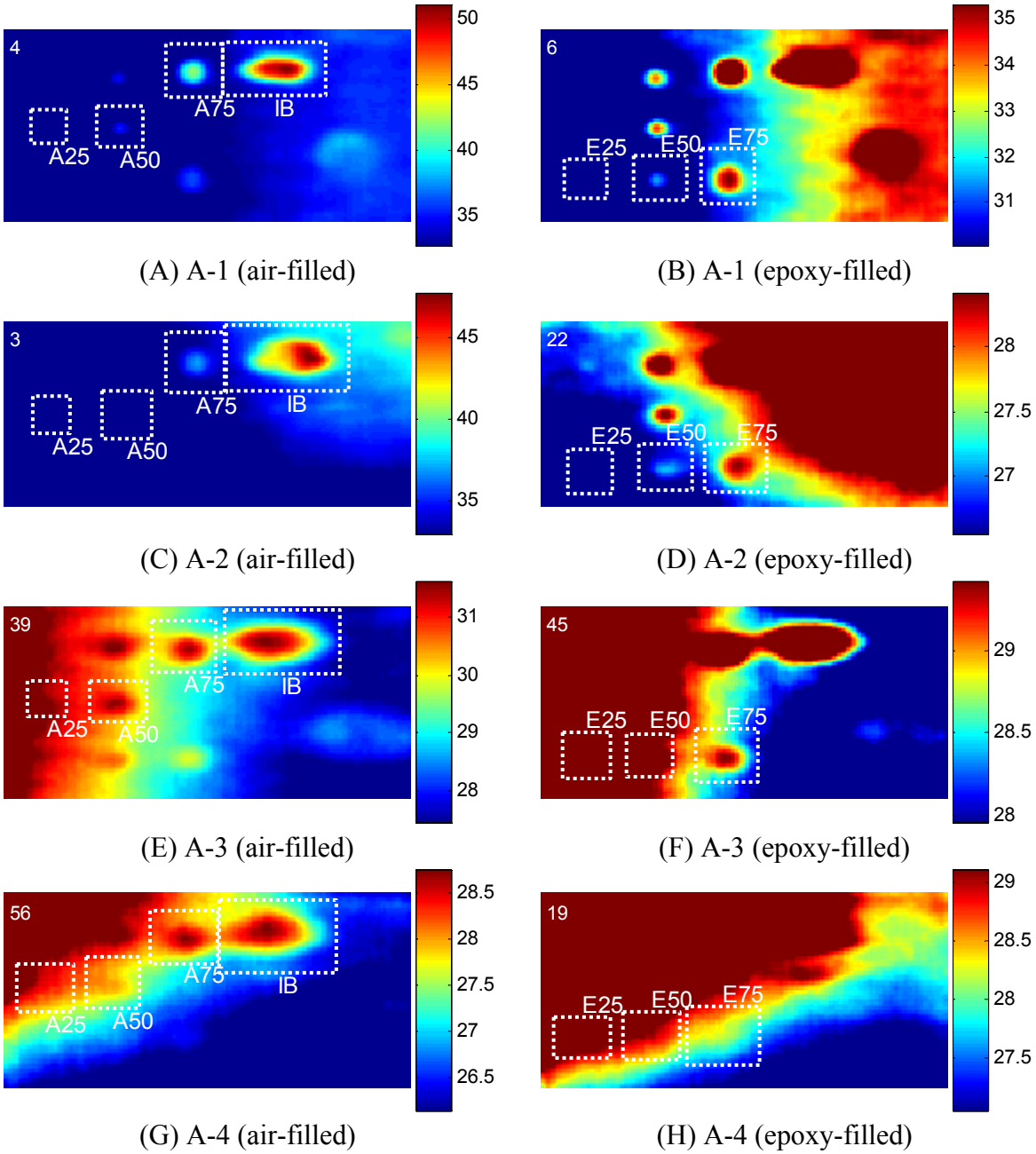

(A) A-1 (air-filled) (B) A-1 (epoxy-filled)

(C) A-2 (air-filled) (D) A-2 (epoxy-filled)

(E) A-3 (air-filled) (F) A-3 (epoxy-filled)

(G) A-4 (air-filled) (H) A-4 (epoxy-filled)

Figure A-7. Long-pulse (45 sec) heating results: Thermal images for Series A.

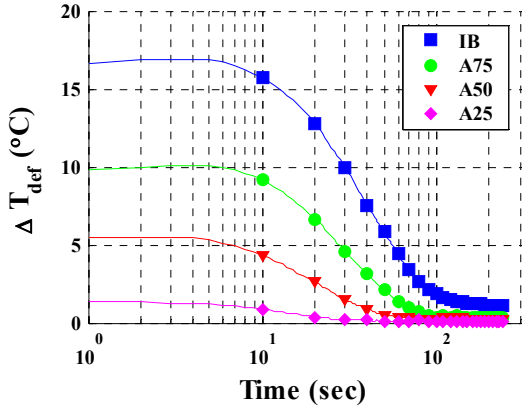

(A) A-1 (air-filled)

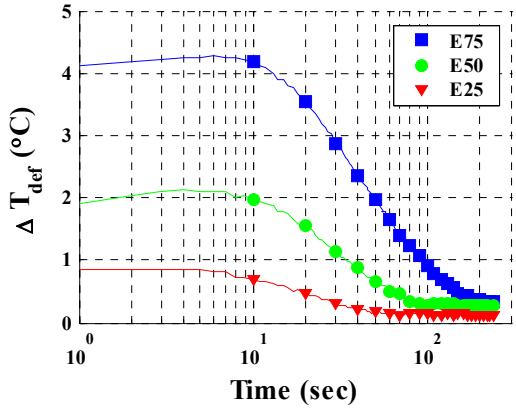

(B) A-1 (epoxy-filled)

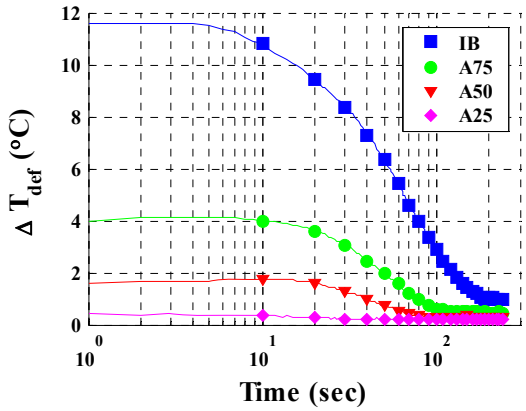

(C) A-2 (air-filled)

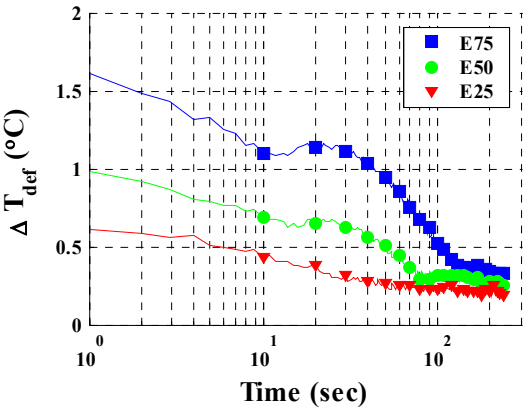

(D) A-2 (epoxy-filled)

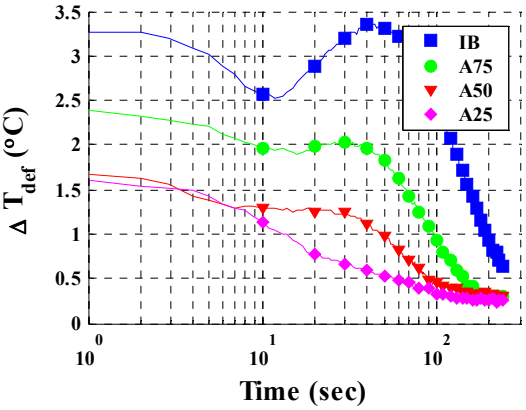

(E) A-3 (air-filled)

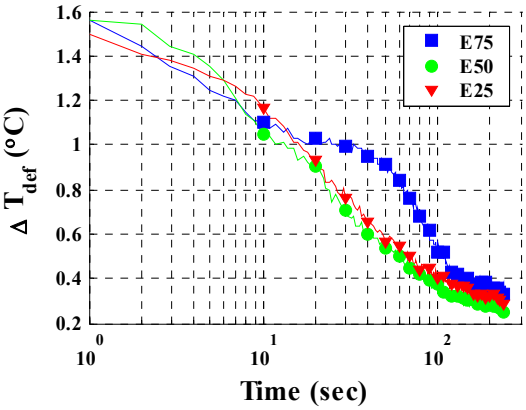

(F) A-3 (epoxy-filled)

Figure A-8. Long-pulse (45 sec) heating results: ΔT_{def} vs. time plots for Series A.

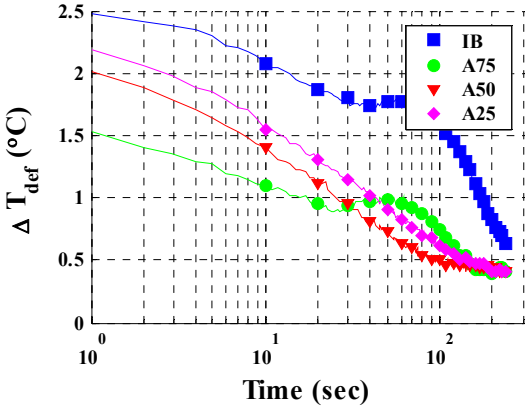

(G) A-4 (air-filled)

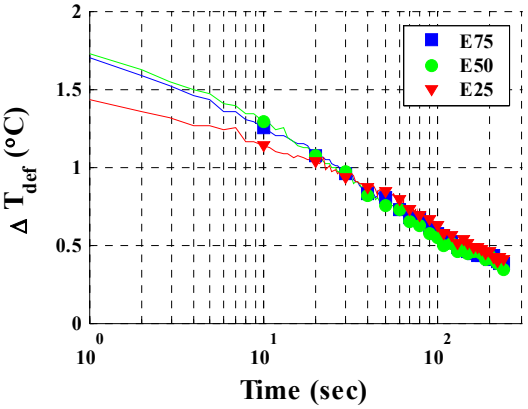

(H) A-4 (epoxy-filled)

Figure A-8. Continued

Table A-4. Long-pulse (45 sec) heating results for Series A

	Defect	Defect material	ΔT_{per} (°C)	ΔT_{max} (°C)	t_b (sec)	t_{max} (sec)	$t_{1/2}$ (sec)	SBR	Actual diameter (in)	Image diameter (in)	COV
Specimen A-1	IB	Air	10.6	16.9	0	4	32	18.6	1.34	1.07	0.28
	A75	Air	8.5	10.1	0	4	24	14.5	0.75	0.70	0.10
	A50	Air	6.5	5.5	0	1	19	10.3	0.50	0.48	0.16
	A25	Air	5.7	1.3	0	0	14	5.1	0.25	0.31	0.79
	E75	Epoxy	8.2	4.3	0	6	40	7.1	0.75	0.77	0.15
	E50	Epoxy	6.5	2.1	0	4	28	5.3	0.50	0.49	0.16
	E25	Epoxy	5.6	0.9	0	4	19	4.8	0.25	0.30	0.93

	Defect	Defect material	ΔT_{per} (°C)	ΔT_{max} (°C)	t_b (sec)	t_{max} (sec)	$t_{1/2}$ (sec)	SBR	Actual diameter (in)	Image diameter (in)	COV
Specimen A-2	IB	Air	12.4	11.6	0	3	53	6.4	1.69	1.54	0.34
	A75	Air	9.3	4.1	0	4	44	4.5	0.75	0.73	0.19
	A50	Air	6.7	1.7	0	11	33	4.7	0.50	0.58	0.20
	A25	Air	5.8	-	-	-	-	-	0.25	-	-
	E75	Epoxy	7.2	1.2	11	22	69	2.9	0.75	0.80	0.19
	E50	Epoxy	6.0	0.7	14	19	57	2.2	0.50	0.63	0.62
	E25	Epoxy	5.1	-	-	-	-	-	0.25	-	-

	Defect	Defect material	ΔT_{per} (°C)	ΔT_{max} (°C)	t_b (sec)	t_{max} (sec)	$t_{1/2}$ (sec)	SBR	Actual diameter (in)	Image diameter (in)	COV
Specimen A-3	IB	Air	10	3.4	12	39	105	5.9	1.63	1.51	0.28
	A75	Air	12.1	2	16	28	66	4.4	0.75	0.81	0.19
	A50	Air	14.4	1.2	7	30	50	2.5	0.50	0.61	0.22
	A25	Air	17.1	-	-	-	-	-	0.25	-	-
	E75	Epoxy	11.7	0.9	11	45	67	2.5	0.75	0.76	0.29
	E50	Epoxy	14.1	-	-	-	-	-	0.50	-	-
	E25	Epoxy	16.4	-	-	-	-	-	0.25	-	-

	Defect	Defect material	ΔT_{per} (°C)	ΔT_{max} (°C)	t_b (sec)	t_{max} (sec)	$t_{1/2}$ (sec)	SBR	Actual diameter (in)	Image diameter (in)	COV
Specimen A-4	IB	Air	8.6	1.8	41	56	133	3.4	1.63	1.66	0.44
	A75	Air	10.1	1.0	27	48	93	2.3	0.75	0.86	0.28
	A50	Air	10.3	-	-	-	-	-	0.50	-	-
	A25	Air	11.6	-	-	-	-	-	0.25	-	-
	E75	Epoxy	7.2	-	-	-	-	-	0.75	-	-
	E50	Epoxy	8.3	-	-	-	-	-	0.50	-	-
	E25	Epoxy	9.2	-	-	-	-	-	0.25	-	-

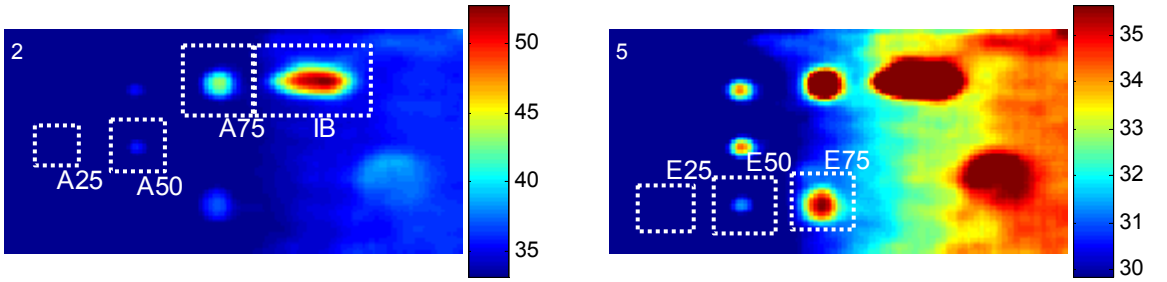

(A) A-1 (air-filled) (B) A-1 (epoxy-filled)

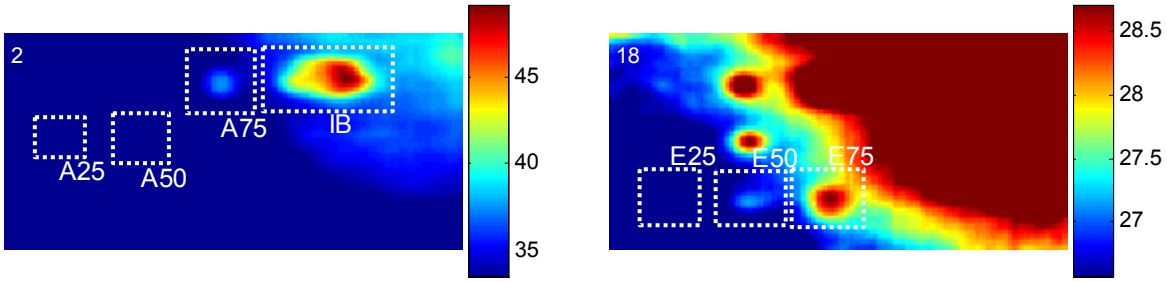

(C) A-2 (air-filled) (D) A-2 (epoxy-filled)

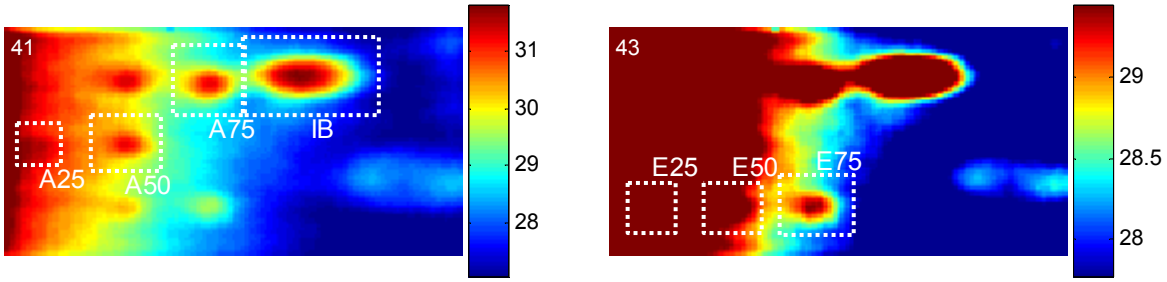

(E) A-3 (air-filled) (F) A-3 (epoxy-filled)

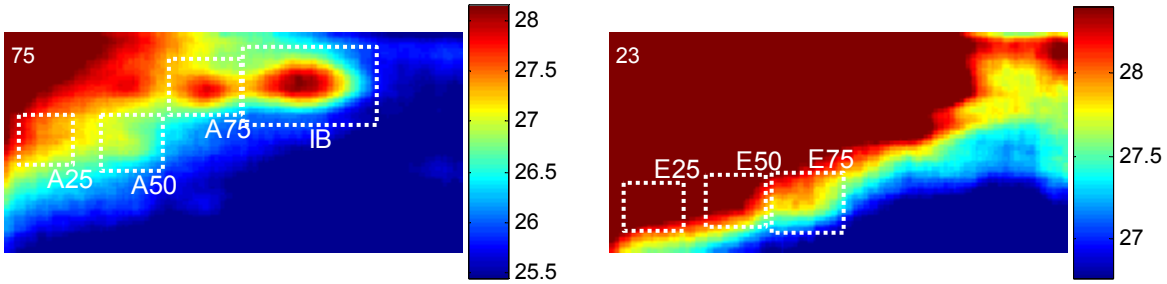

(G) A-4 (air-filled) (H) A-4 (epoxy-filled)

Figure A-9. Long-pulse (60 sec) heating results: Thermal images for Series A.

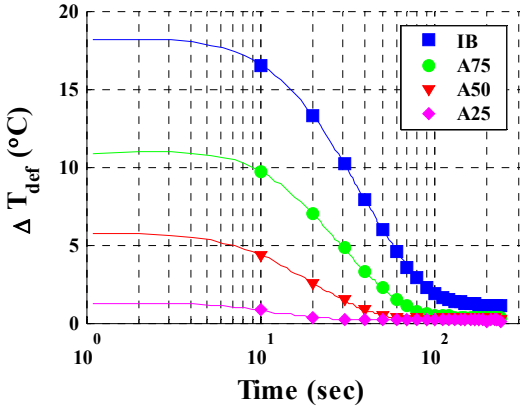

(A) A-1 (air-filled)

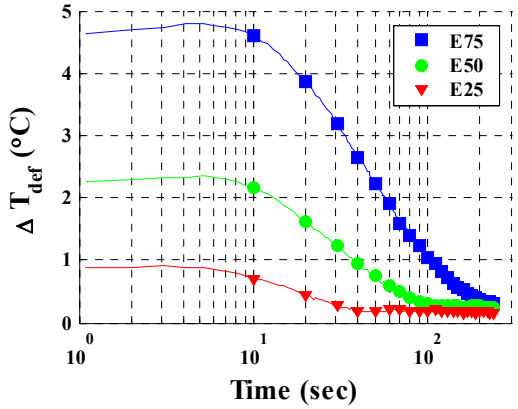

(B) A-1 (epoxy-filled)

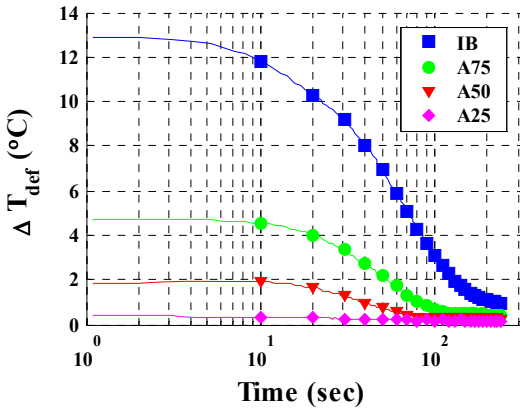

(C) A-2 (air-filled)

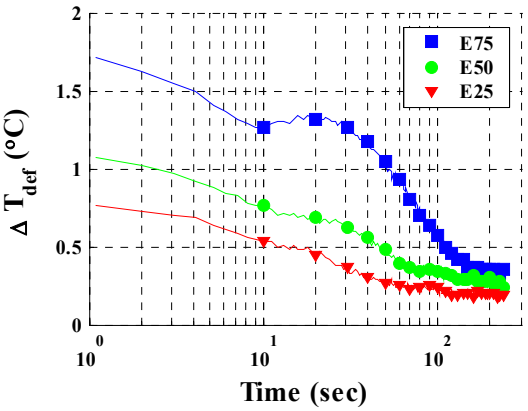

(D) A-2 (epoxy-filled)

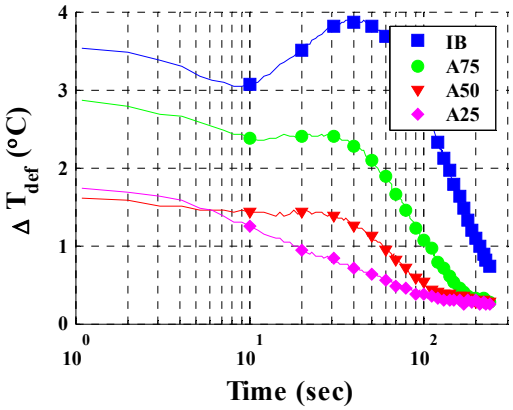

(E) A-3 (air-filled)

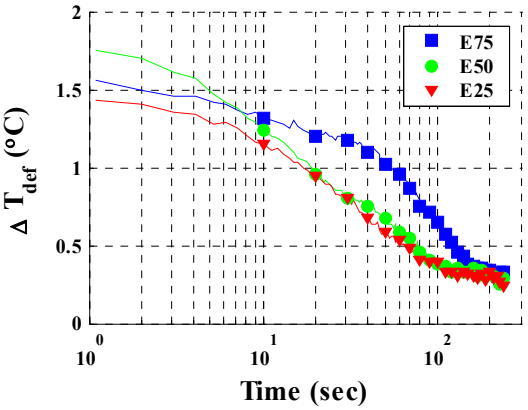

(F) A-3 (epoxy-filled)

Figure A-10. Long-pulse (60 sec) heating results: ΔT_{def} vs. time plots for Series A.

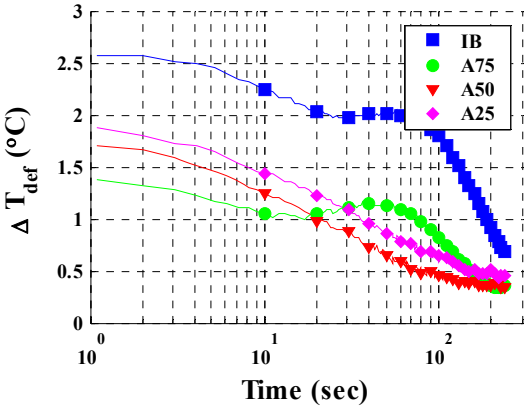

(G) A-4 (air-filled)

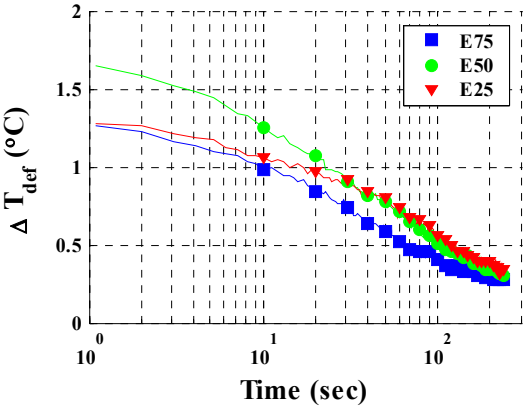

(H) A-4 (epoxy-filled)

Figure A-10. Continued

Table A-5. Long-pulse (60 sec) heating results for Series A

	Defect	Defect material	ΔT_{per} (°C)	ΔT_{max} (°C)	t_b (sec)	t_{max} (sec)	$t_{1/2}$ (sec)	SBR	Actual diameter (in)	Image diameter (in)	COV
Specimen A-1	IB	Air	10.6	18.1	0	2	33	20.6	1.34	1.05	0.29
	A75	Air	8.6	11.0	0	2	25	13.6	0.75	0.71	0.09
	A50	Air	6.6	5.7	2	0	18	10.5	0.50	0.49	0.17
	A25	Air	5.9	1.3	2	0	12	4.8	0.25	0.21	0.94
	E75	Epoxy	8.5	4.8	0	5	42	8.2	0.75	0.79	0.08
	E50	Epoxy	6.7	2.4	0	5	27	5.8	0.50	0.47	0.17
	E25	Epoxy	5.8	0.9	2	3	17	3.9	0.25	0.22	1.43

	Defect	Defect material	ΔT_{per} (°C)	ΔT_{max} (°C)	t_b (sec)	t_{max} (sec)	$t_{1/2}$ (sec)	SBR	Actual diameter (in)	Image diameter (in)	COV
Specimen A-2	IB	Air	12.7	12.9	0	2	53	8.0	1.69	1.57	0.43
	A75	Air	9.6	4.8	0	2	44	4.9	0.75	0.73	0.11
	A50	Air	7.0	1.9	0	5	37	4.1	0.50	0.56	0.23
	A25	Air	-	-	-	-	-	-	0.25	-	-
	E75	Epoxy	7.5	1.3	9	18	63	2.8	0.75	0.83	0.15
	E50	Epoxy	-	-	-	-	-	-	0.50	-	-
	E25	Epoxy	-	-	-	-	-	-	0.25	-	-

	Defect	Defect material	ΔT_{per} (°C)	ΔT_{max} (°C)	t_b (sec)	t_{max} (sec)	$t_{1/2}$ (sec)	SBR	Actual diameter (in)	Image diameter (in)	COV
Specimen A-3	IB	Air	10.4	3.9	8	41	100	6.5	1.63	1.49	0.30
	A75	Air	12.4	2.4	11	29	61	5.0	0.75	0.82	0.19
	A50	Air	15.0	1.4	14	26	53	2.6	0.50	0.61	0.29
	A25	Air	18.2	-	-	-	-	-	0.25	-	-
	E75	Epoxy	12.1	1.1	20	43	70	2.9	0.75	0.77	0.22
	E50	Epoxy	14.4	-	-	-	-	-	0.50	-	-
	E25	Epoxy	17.1	-	-	-	-	-	0.25	-	-

	Defect	Defect material	ΔT_{per} (°C)	ΔT_{max} (°C)	t_b (sec)	t_{max} (sec)	$t_{1/2}$ (sec)	SBR	Actual diameter (in)	Image diameter (in)	COV
Specimen A-4	IB	Air	9.2	2.0	27	75	114	4.1	1.63	1.52	0.32
	A75	Air	10.6	1.2	17	37	97	2.5	0.75	0.83	0.48
	A50	Air	10.5	-	-	-	-	-	0.50	-	-
	A25	Air	12.4	-	-	-	-	-	0.25	-	-
	E75	Epoxy	7.6	-	-	-	-	-	0.75	-	-
	E50	Epoxy	8.6	-	-	-	-	-	0.50	-	-
	E25	Epoxy	9.5	-	-	-	-	-	0.25	-	-

APPENDIX B
SINUSOIDAL HEATING RESULTS: SERIES A

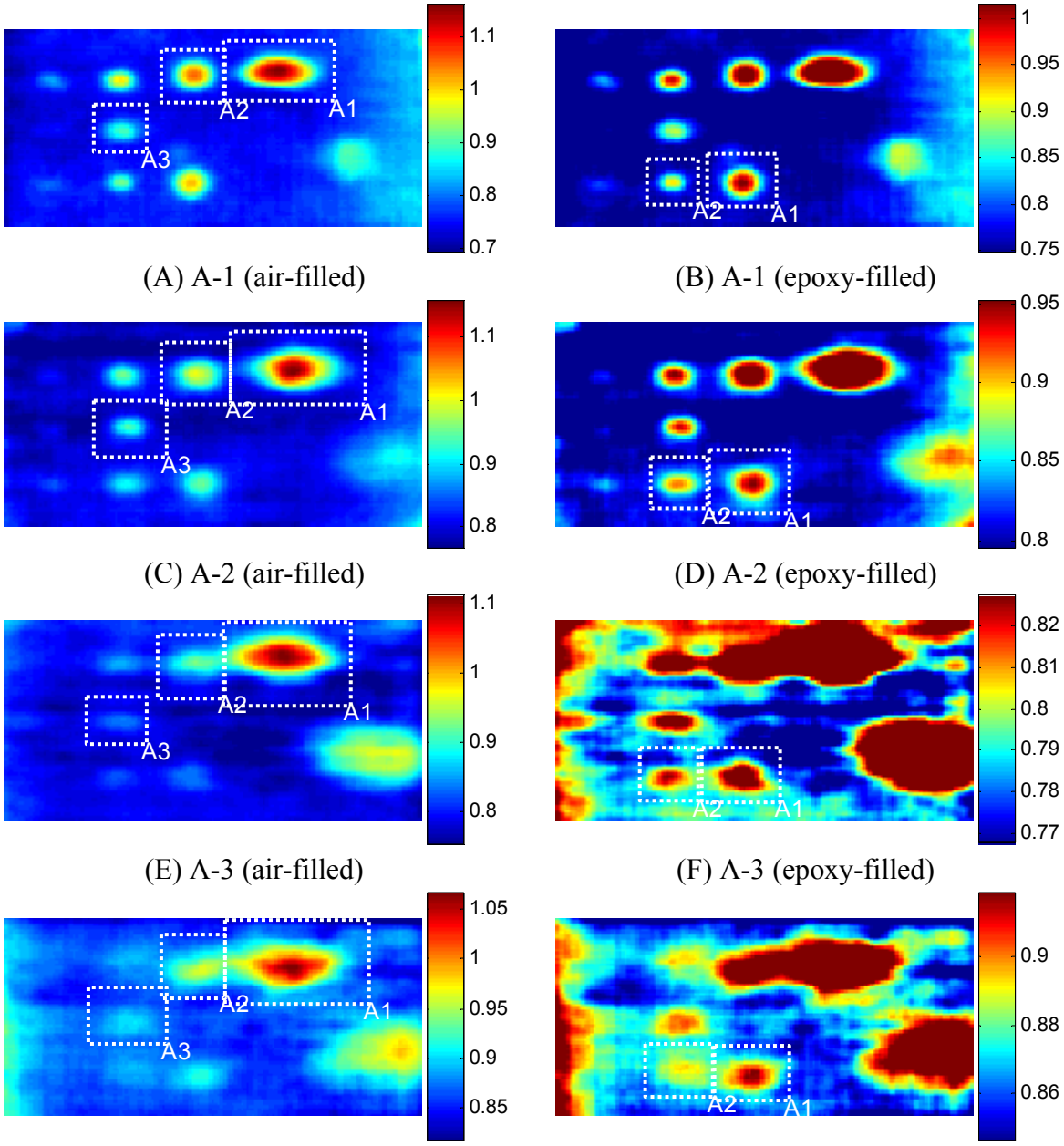

(A) A-1 (air-filled)

(B) A-1 (epoxy-filled)

(C) A-2 (air-filled)

(D) A-2 (epoxy-filled)

(E) A-3 (air-filled)

(F) A-3 (epoxy-filled)

(G) A-4 (air-filled)

(H) A-4 (epoxy-filled)

Figure B-1. Sinusoidal heating results: Phase images for Series A.

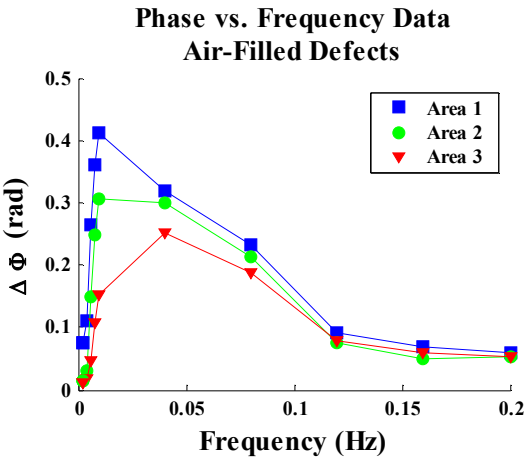

(A) A-1 (air-filled)

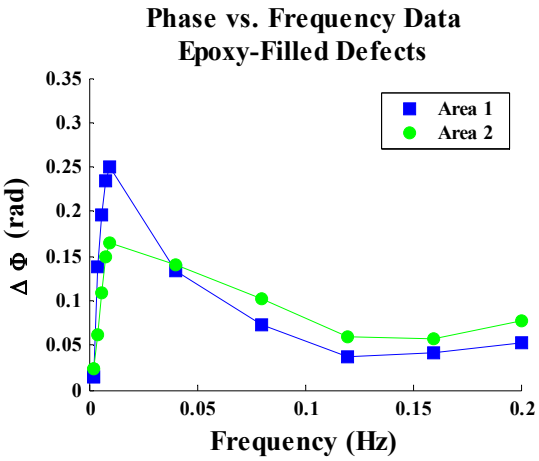

(B) A-1 (epoxy-filled)

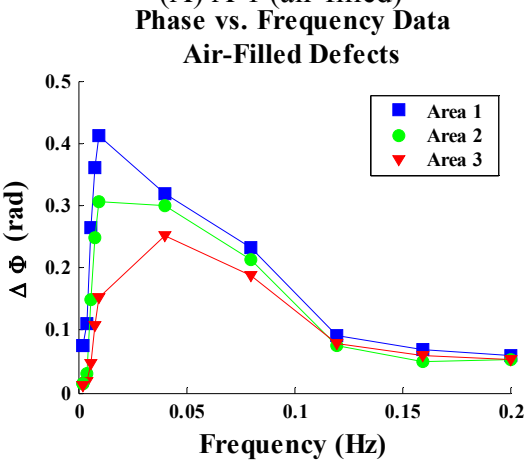

(C) A-2 (air-filled)

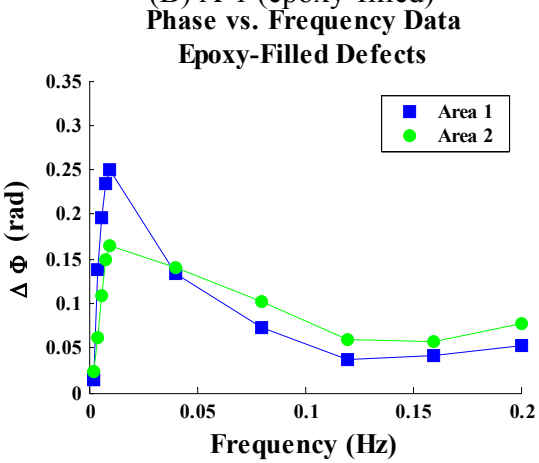

(D) A-2 (epoxy-filled)

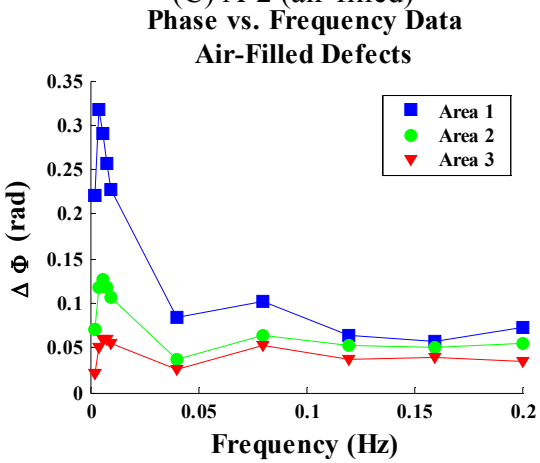

(E) A-3 (air-filled)

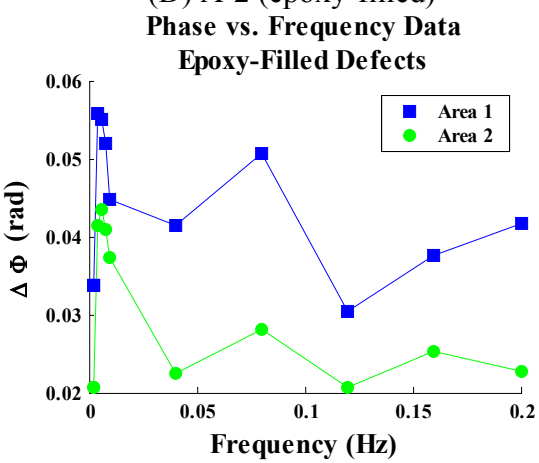

(F) A-3 (epoxy-filled)

Figure B-2. Sinusoidal heating results: ΔΦ vs. frequency plots for Series A.

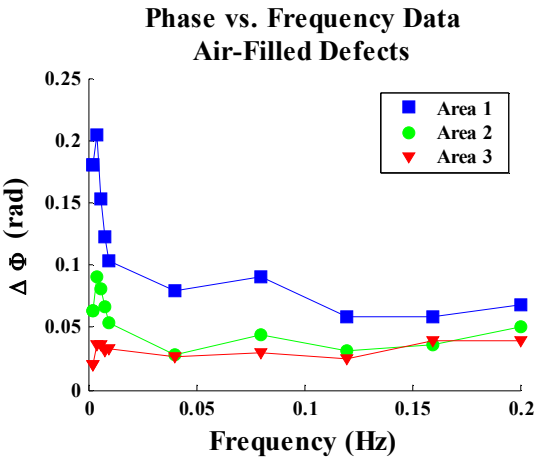

(G) A-4 (air-filled)

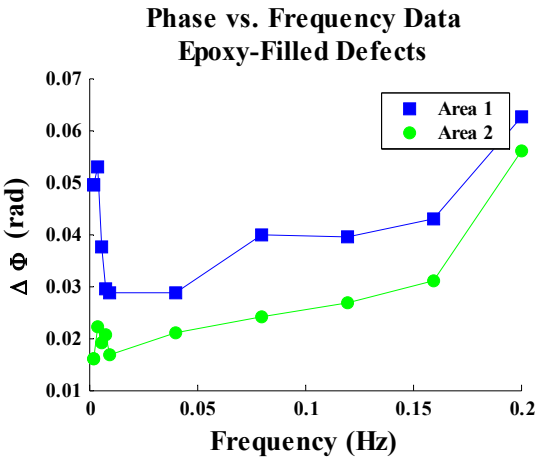

(H) A-4 (epoxy-filled)

Figure B-2. Continued

Table B-1. Sinusoidal heating results: ΔΦ vs. frequency plot parameters for Series A.

	Defect	Defect material	Actual size (in^2)	Image size (Pixels)	Image size (in^2)	$\Delta\Phi_{max}$ (rad)	SBR
Specimen A-1	IB	Air	1.1	173	1.16	0.41	24.6
	A75	Air	0.44	84	0.56	0.31	22.8
	A50	Air	0.20	37	0.25	0.25	15.5
	E75	Epoxy	0.44	80	0.54	0.25	23.5
	E50	Epoxy	0.20	36	0.24	0.16	29.0

	Defect	Defect material	Actual size (in^2)	Image size (Pixels)	Image size (in^2)	$\Delta\Phi_{max}$ (rad)	SBR
Specimen A-2	IB	Air	2.0	143	0.96	0.36	24.2
	A75	Air	0.44	99	0.66	0.22	13.6
	A50	Air	0.20	45	0.30	0.15	17.1
	E75	Epoxy	0.44	76	0.51	0.14	18.8
	E50	Epoxy	0.20	50	0.34	0.10	11.9

	Defect	Defect material	Actual size (in^2)	Image size (Pixels)	Image size (in^2)	$\Delta\Phi_{max}$ (rad)	SBR
Specimen A-3	A1	Air	2.0	243	1.63	0.31	13.1
	A2	Air	0.44	74	0.50	0.12	5.4
	A3	Air	0.20	66	0.44	0.06	9.8
	E1	Epoxy	0.44	109	0.73	0.06	7.0
	E2	Epoxy	-	55	0.37	0.04	7.2

	Defect	Defect material	Actual size (in^2)	Image size (Pixels)	Image size (in^2)	$\Delta\Phi_{max}$ (rad)	SBR
Specimen A-4	A1	Air	2.0	226	1.52	0.21	8.0
	A2	Air	0.44	96	0.64	0.09	4.2
	A3	Air	0.20	98	0.66	0.04	5.0
	E1	Epoxy	0.44	88	0.59	0.05	7.6
	E2	Epoxy	0.20	-	-	-	-

APPENDIX C
SERIES B, C, D, AND E RESULTS

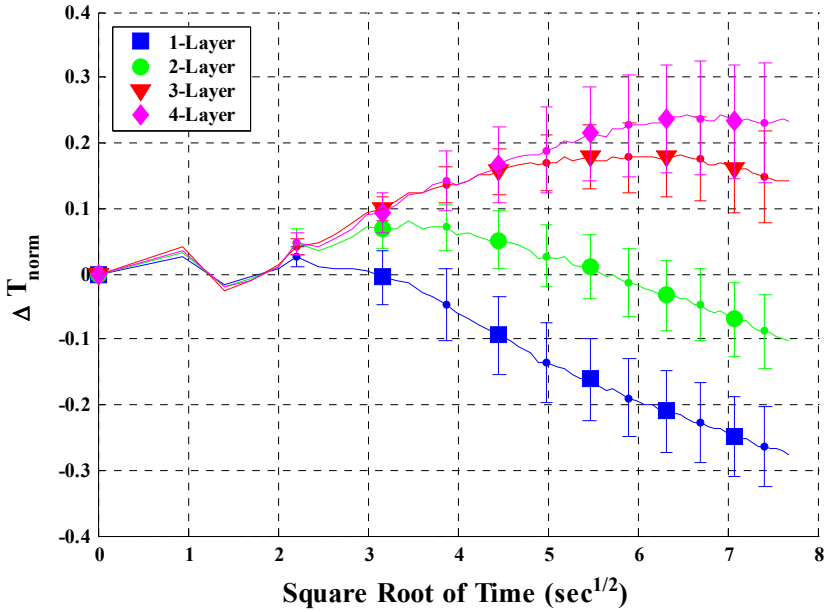

Figure C-1. Low matrix saturation (Series B carbon-fibers)

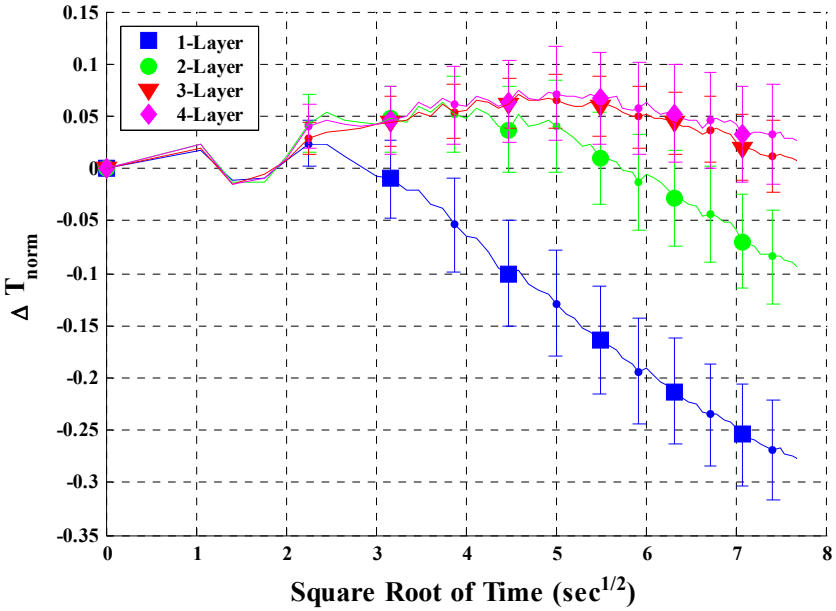

Figure C-2. Medium matrix saturation (Series B carbon-fibers)

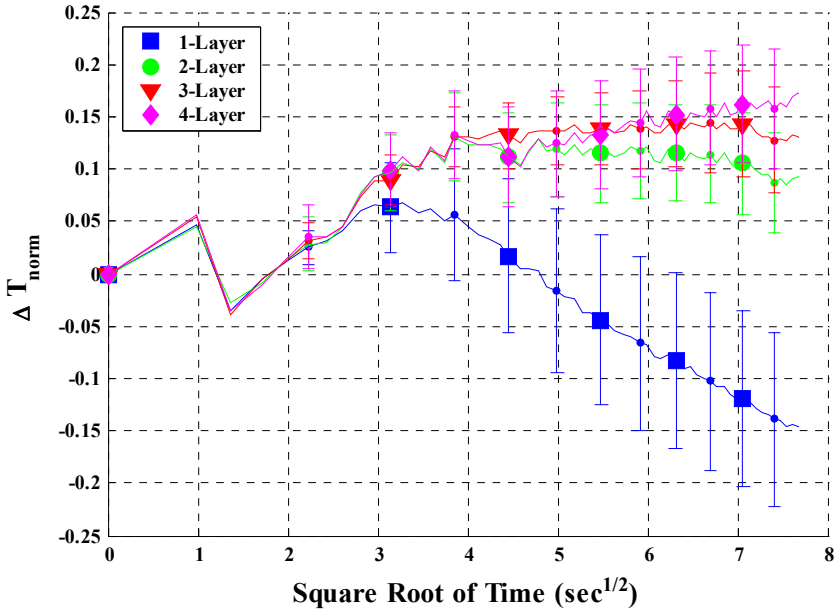

Figure C-3. High matrix saturation (Series B carbon-fibers)

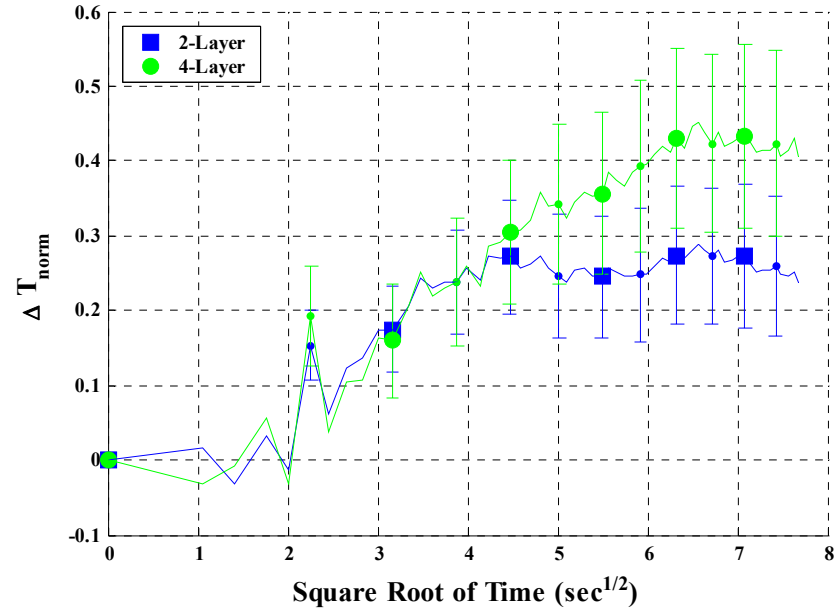

Figure C-4. Low matrix saturation (Series B glass-fibers)

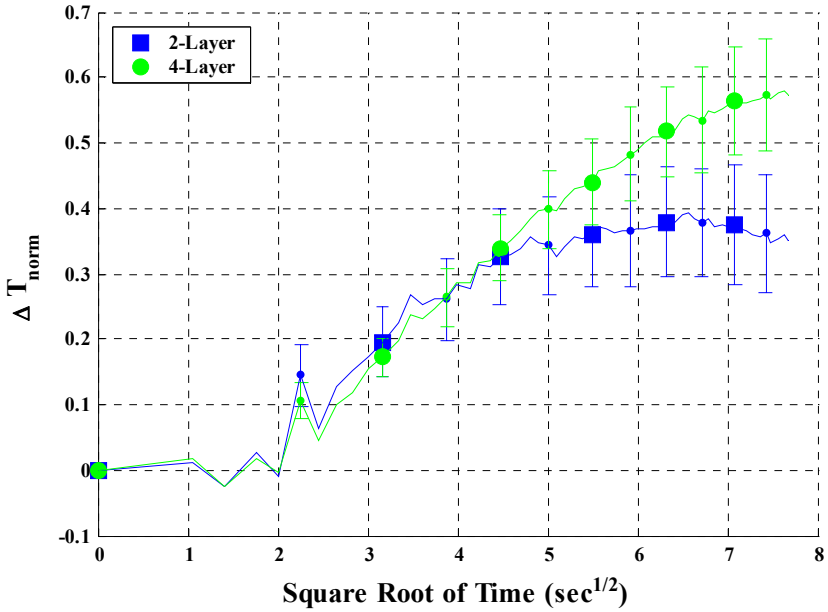

Figure C-5. Medium matrix saturation (Series B glass-fibers)

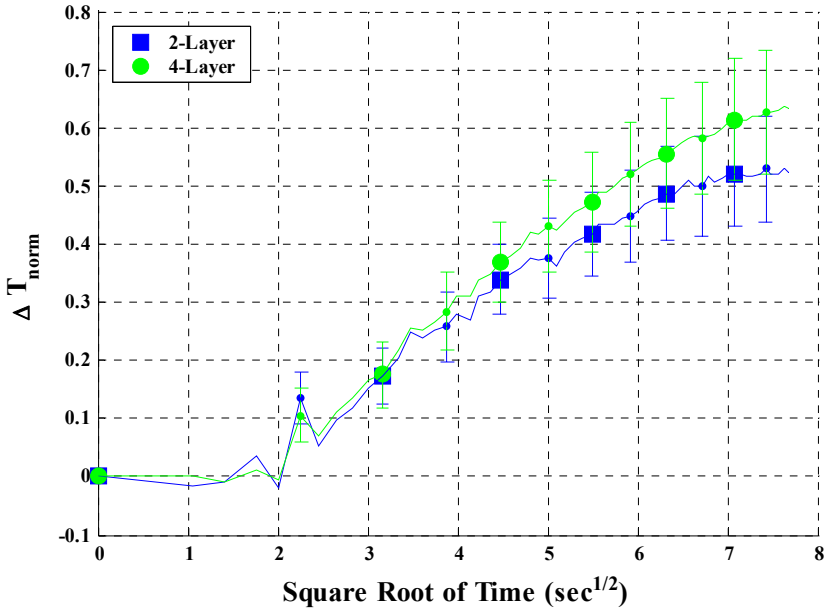

Figure C-6. High matrix saturation (Series B glass-fibers)

Table C-1. Series B (low saturation) summary statistics for defect-free areas

	Specimen	NP	Mean @ t=60 sec	Standard deviation @ t = 60 sec
Carbon FRP (low saturation)	B-LC-1	1350	-.27	0.030
	B-LC-2	1196	-0.10	0.028
	B-LC-3	1092	+0.14	0.036
	B-LC-4	990	+0.23	0.047
	Specimen	NP	Mean @ t=60 sec	Standard Deviation @ t = 60 sec
Carbon FRP (med saturation)	B-MC-1	1350	-.28	0.023
	B-MC-2	1196	-0.09	0.023
	B-MC-3	1092	+0.01	0.017
	B-MC-4	990	+0.03	0.025
	Specimen	NP	Mean @ t=60 sec	Standard Deviation @ t = 60 sec
Carbon FRP (high saturation)	B-HC-1	780	-.15	0.042
	B-HC-2	1196	+0.09	0.025
	B-HC-3	1092	+0.13	0.028
	B-HC-4	990	+0.17	0.028
	Specimen	NP	Mean @ t=60 sec	Standard Deviation @ t = 60 sec
Glass FRP	B-LG-2	1088	+.236	.048
	B-MG-2	621	+.350	.044
	B-HG-2	621	+.525	.048
	B-LG-4	1036	+.406	.065
	B-MG-4	575	+.507	.044
	B-HG-4	575	+.634	.056

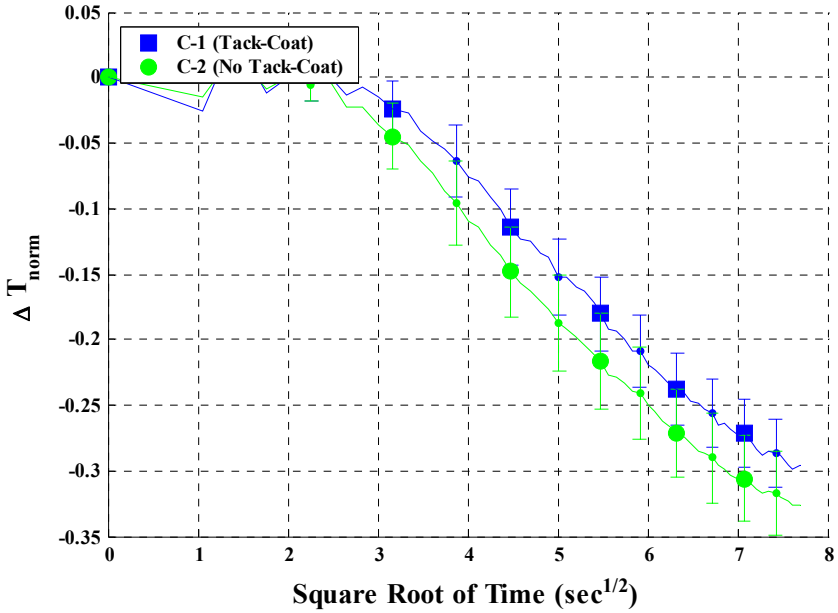

Figure C-7. No surface preparation (Series C carbon-fibers)

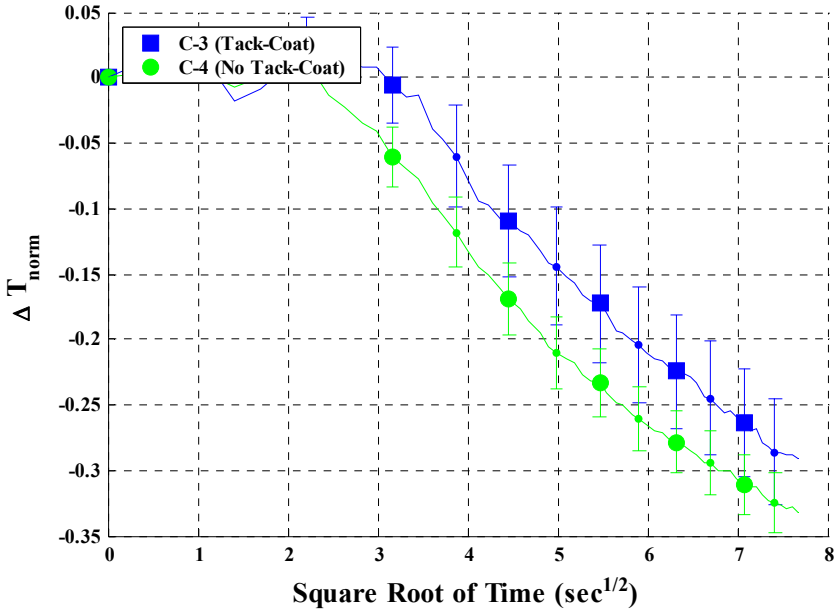

Figure C-8. Light blast surface preparation (Series C carbon-fibers)

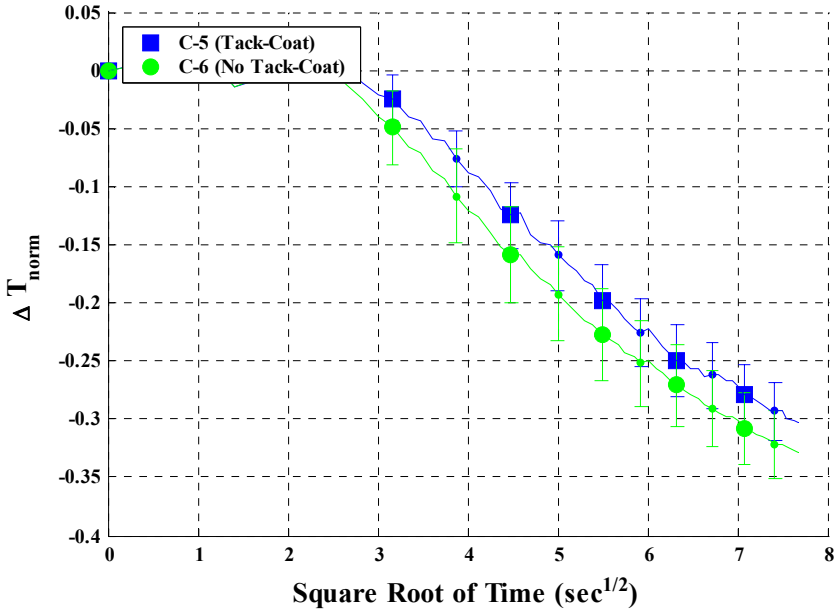

Figure C-9. Heavy blast surface preparation (Series C carbon-fibers)

Table C-2. Series C (surface prep) summary statistics for defect-free areas

Specimen	Tack-Coat	NP	Mean @ t=60 sec	Standard Deviation @ t = 60 sec
C-1	Yes	621	-.296	.012
C-3	Yes	621	-.291	.020
C-5	Yes	621	-.302	.013
C-2	No	575	-.327	.016
C-4	No	575	-.332	.011
C-6	No	575	-.328	.014

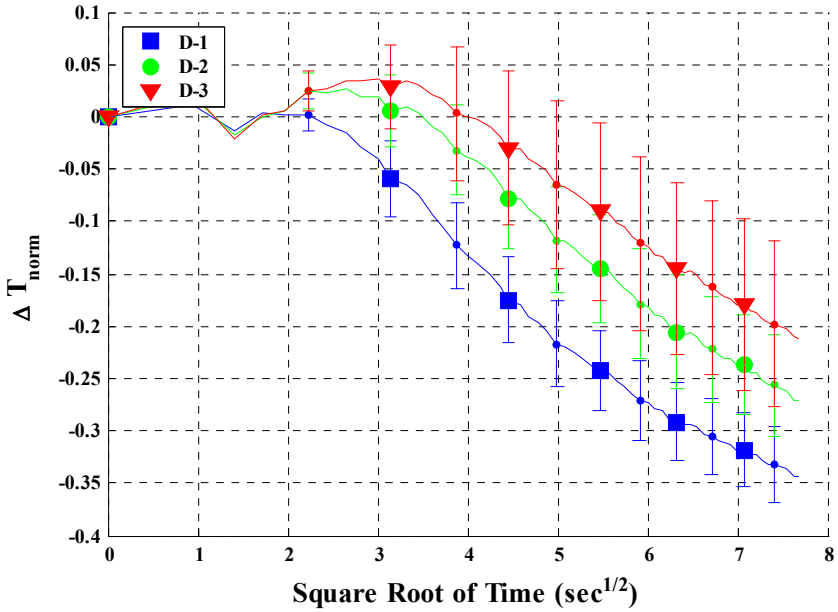

Figure C-10. Different fiber saturation methods (Series D carbon-fibers)

Table C-3. Series D (fiber saturation methods) summary statistics for defect-free areas

Specimen	NP	Mean @ t=60 sec	Standard Deviation @ t = 60 sec
D-1	1088	-.343	.018
D-2	621	-.271	.024
D-3	621	-.212	.038

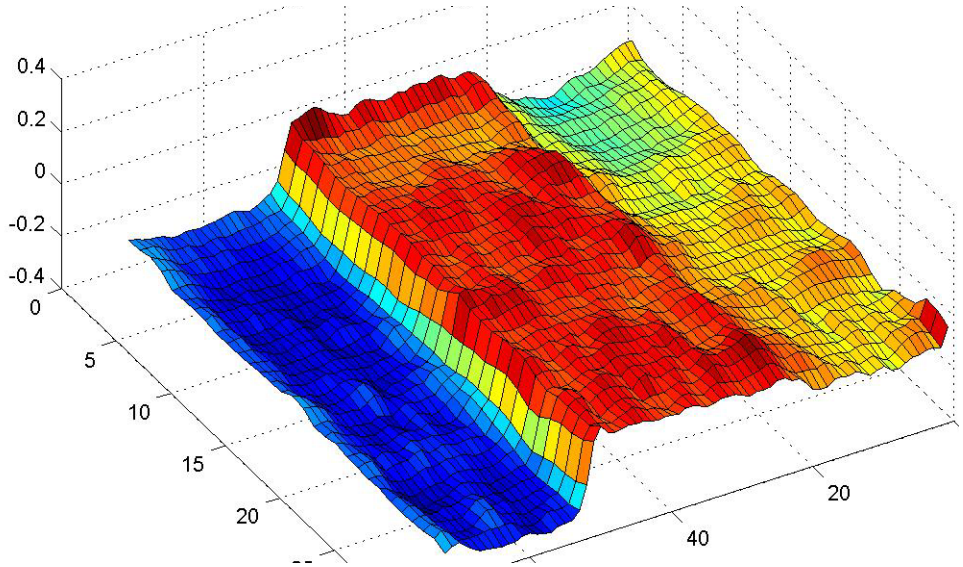

Figure C-11. Specimen E-1 (1-layer/3-layer/2-layer)

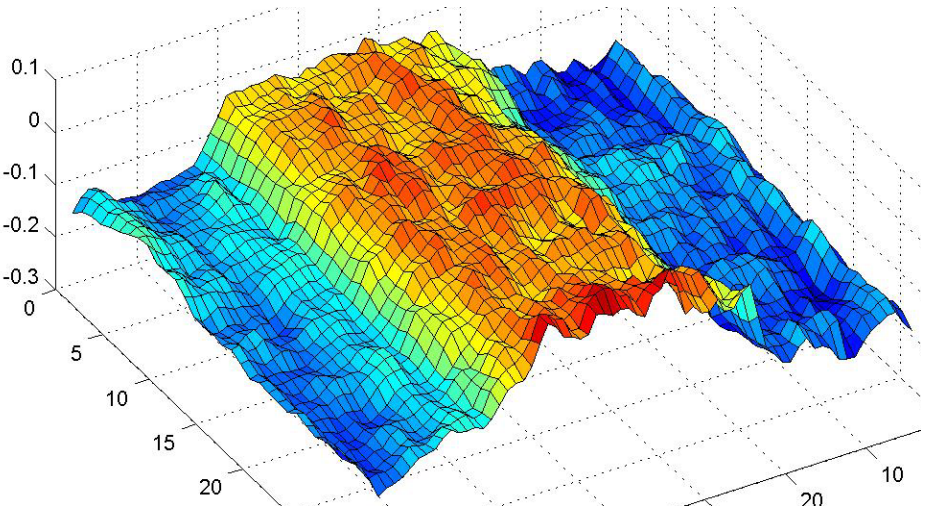

Figure C-12. Specimen E-2 (2-layer/3-layer/2-layer)

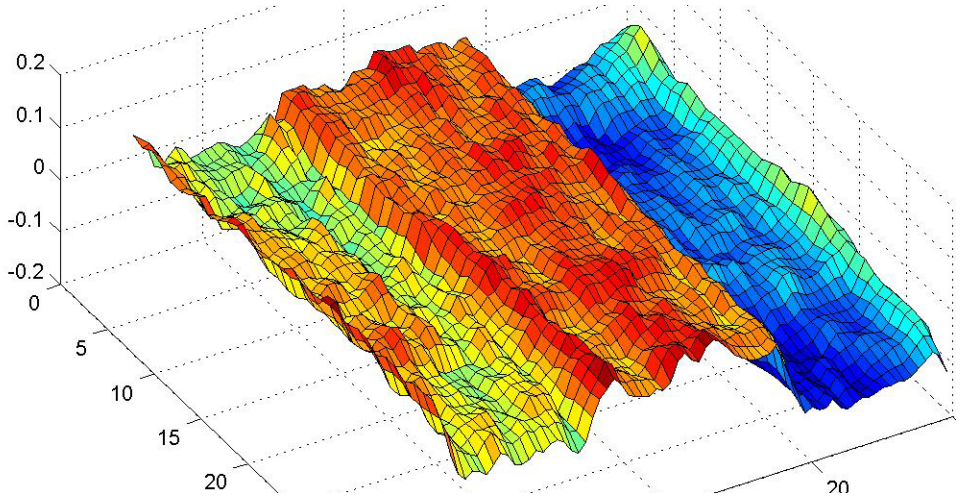

Figure C-13. Specimen E-3 (3-layer/4-layer/2-layer)

APPENDIX D
COMPOSITE PROPERTIES FOR SMALL-SCALE SPECIMENS

Table D-1. Series A composite properties

Specimen ID	Layers	Surface prep	Saturant (g)	Tack coat (g)	Fibers (g)	Matrix (g)	Top coat (g)	w_f[a]
A-1	1	LB	6	11	31	31	9	0.50
A-2	2	LB	5	11	62	62	11	0.50
A-3	3	LB	6	10	93	93	9	0.50
A-4	4	LB	6	12	124	124	11	0.50

[a] w_f is weight fraction of fibers

Table D-2. Series B composite properties

Specimen ID	Layers	Surface prep	Saturant (g)	Tack coat (g)	Fibers (g)	Matrix (g)	Top coat (g)	wf
B-GL-2	1	LB	8	9	88	43	7	0.67
B-GL-4	2	LB	8	10	181	85	10	0.68
B-CL-1	1	LB	7	7	32	16	9	0.67
B-CL-2	2	LB	7	11	63	30	7	0.68
B-CL-3	3	LB	7	9	97	48	11	0.67
B-CL-4	4	LB	7	10	127	70	8	0.64
B-GM-2	1	LB	6	7	88	74	9	0.54
B-GM-4	2	LB	5	10	179	159	9	0.53
B-CM-1	1	LB	6	9	33	31	9	0.52
B-CM-2	2	LB	6	7	63	67	7	0.48
B-CM-3	3	LB	7	11	96	96	9	0.50
B-CM-4	4	LB	8	8	125	125	8	0.50
B-GH-2	1	LB	6	7	90	106	9	0.44
B-GH-4	2	LB	5	10	176	236	9	0.43
B-CH-1	1	LB	6	9	33	44	9	0.43
B-CH-2	2	LB	6	7	63	109	7	0.37
B-CH-3	3	LB	7	11	92	127	9	0.42
B-CH-4	4	LB	8	8	124	180	8	0.41

Table D-3. Series C composite properties

Specimen ID	Layers	Surface prep	Saturant (g)	Tack coat (g)	Fibers (g)	Matrix (g)	Top coat (g)	wf
C-1	1	None	6.3	11.0	28.7	36.7	0	0.44
C-2	1	None	6.1	NA	29.4	40.1	0	0.42
C-3	1	LB	6.5	8.0	29.1	36.3	0	0.45
C-4	1	LB	7.9	NA	28.8	36.4	0	0.44
C-5	1	HB	7.0	12.8	28.3	33.8	0	0.46
C-6	1	HB	6.5	NA	28.2	37.1	0	0.43

Table D-4. Series D composite properties

Specimen ID	Layers	Surface prep	Saturant (g)	Tack coat (g)	Fibers (g)	Matrix (g)	Top coat (g)	wf
D-1	1	LB	5.7	10.0	28.3	28.0	0	0.50
D-2	1	LB	6.5	11.0	29.8	28.4	11.2	0.51
D-3	1	LB	7.1	10.5	28.7	43.4	11.5	0.40

Table D-5. Series E composite properties

Specimen ID	Layers	Surface prep	Saturant (g)	Tack coat (g)	Fibers (g)	Matrix (g)	Top coat (g)	wf
E-1	2/3/1	LB	7	8	65	51	7	0.56
E-2	2/3/2	LB	9	7	78	74	11	0.51
E-3	2/4/3	LB	6	11	94	111	9	0.46

LIST OF REFERENCES

American Concrete Institute (ACI) Committee 440 (2002). "Guide for the design and construction of externally bonded FRP systems for strengthening concrete structures." American Concrete Institute, ACI 440.2R-02, Farmington Hills, Michigan.

American Society for Testing and Materials (ASTM) (1997). "Standard practice for location of wet insulation in roofing systems using infrared imaging." C 1153-97. ASTM, West Conshohocken, Pennsylvania.

American Society for Testing and Materials (ASTM) (2003). "Standard test method for detecting delaminations in bridge decks using infrared thermography." D 4788. ASTM, West Conshohocken, Pennsylvania.

ASM Materials Handbook (2005). ASM Handbooks Online. ASM International, 9639 Kinsman Road, Materials Park, OH. http://products.asminternational.org.

Avdelidis, N. P., D. P. Almond, Dobbinson, A., Hawtin, B., Ibarra-Castanedo, Clemente, Maldague, Xavier P. (2004). "Thermal transient thermographic NDT and E of composites." Thermosense XXVI, Edited by D.D. Burleigh, Eliot Cramer, G. Raymond, Peacock. Proceedings of SPIE, Vol. 5405, pp. 403-413.

Bai, W. and B. S. Wong (2001). "Photothermal models for lock-in thermographic evaluation of plates with finite thickness under convection conditions." Journal of Applied Physics 89(6): 3275.

Carlomagno, G. M. and C. Meola (2002). "Comparison between thermographic techniques for frescoes NDT." NDT & E International 35(8): 559-565.

CERF (2001). "Gap analysis for durability of fiber reinforced polymer composites in civil infrastructure." Civil Engineering Research Foundation, Reston, Virginia.

Cytec Industries (2005). http://www.cytec.com/business/EngineeredMaterials/CFInternet/cfthornelpitch.shtm. Cytec Industries Inc., 5 Garret Mountain Plaza, West Paterson, NJ

Edge Structural Composites (2005). http://www.edgest.com/edgedataintro.html. 145 Park Place Point, Richmond, CA.

Fyfe Co. LLC (2005). http://www.fyfeco.com/products/compositesystems.html. Nancy Ridge Technology Center, 6310 Nancy Ridge Drive, Suite 103,San Diego, CA.

Gibson, R. F. (1994). “Principles of composite material mechanics.” McGraw-Hill, Inc., 1994.

Hexcel (2005). http://www.hexcel.com/Products. Hexcel, 6400 West 5400 South, Salt Lake City, UT

ICC Evaluation Services (2003) “Acceptance criteria for concrete and unreinforced masonry strengthening using fiber-reinforced composite systems.” AC125, Whittier, California.

Ibarra-Castanedo, C. and X. P. Maldague (2004). “Defect depth retrieval from pulsed phase thermographic data on Plexiglas and aluminum samples.” Thermosense XXVI, Edited by D.D. Burleigh, Eliot Cramer, G. Raymond, Peacock. Proceedings of SPIE, Vol. 5405, pp. 348-356.

Ibarra-Castanedo, C. and X. P. Maldague (2005). “Pulsed phase thermography inversion procedure using normalized parameters to account for defect size variations.” Thermosense XXVII, Edited by D.D. Burleigh, Eliot Cramer, J. Miles. Proceedings of SPIE, Vol. 5782, pp. 334-341.

Kaiser, H. and Kharbari, V. (2001a). “Quality and Monitoring of Structural Rehabilitation Measures (Part I: Description of Potential Defects).” Report Submitted to the Oregon Department of Transportation under Contract Number 18347.

Kaiser, H. and Kharbari, V. (2001b). “Quality and Monitoring of Structural Rehabilitation Measures (Part II: Review and Assessment of Non-destructive Testing (NDT) Techniques).” Report Submitted to the Oregon Department of Transportation under Contract Number 18347.

Kharbari, V. M., J. W. Chin, Hunston, D., Benmokrane, B., Juska, T., Morgan, R., Lesko, J. J., Sorathia, U., Reynaud, D. (2003). “Durability gap analysis for fiber-reinforced polymer composites in civil infrastructure.” Journal of Composites for Construction 7(3): 238-247.

Kulowitch, P. J., I. M. Perez, Granata, D., (1995). Flash infrared thermography for nondestructive testing (NDT) I/E of naval aircraft. Thermosense XVI, Edited by Sharon A. Semanovich, Proceedings of SPIE, Vol. 2473, pp. 252-262.

Lammert, K. A. (2003). “Structural evaluation of impact damaged prestressed concrete I girders repaired with fiber reinforced polymer (FRP) materials.” Masters Thesis, University of Florida, Gainesville, FL.

Levar, J. M. and H. R. Hamilton (2003). “Nondestructive evaluation of carbon fiber-reinforced polymer-concrete bond using infrared thermography.” ACI Materials Journal 100(1): 63-72.

Maierhofer, C., A. Brink, Rollig, M., Wiggenhauser, H. (2003). "Detection of shallow voids in concrete structures with impulse thermography and radar." NDT & E International 36(4): 257-263.

Maldague, X., F. Galmiche, Ziadi, A. (2002). "Advances in pulsed phase thermography." Infrared Physics & Technology 43(3-5): 175-181.

Maldague, X. P. V. (2001). "Theory and Practice of Infrared Technology for Nondestructive Testing." John Wiley & Sons, Inc.

Matlab User's Guide. (2002). On-line reference manual. The MathWorks, Inc., 3 Apple Hill Drive, Natick, MA.

Nanni, A. (2003). "North American design guidelines for concrete reinforcement and strengthening using FRP: principles, applications and unresolved issues." Construction and Building Materials 17(6-7): 439-446.

Mirmiran, A., Shawhawy, M., Nanni, A., and Kharbari, V. (2004). NCHRP Report 514. "Bonded repair and retrofit of concrete structures using FRP composites." National Cooperative Highway Research Program, Washington, D.C.

Osiander, R., J. W. M. Spicer, Maclachlan, J.W., and Murphy, J. C. (1996). "Analysis methods for full-field time-resolved infrared radiometry." Thermosense XVI, Edited by Douglas D. Burleigh, Jane W. Maclachlan Spicer, Proceedings of SPIE, Vol. 2766, pp. 218-227.

Sebastian, W. M. (2001). "Significance of midspan debonding failure in FRP-plated concrete beams." Journal of Structural Engineering-ASCE 127(7): 792-798.

Shepard, S. M., J. R. Lhota, Hou, Y. L., Ahmed, T. (2004). "Blind characterization of materials using single-sided thermography." Thermosense XXVI, Edited by D.D. Burleigh, Eliot Cramer, G. Raymond, Peacock. Proceedings of SPIE, Vol. 5405, pp. 442-446.

Starnes, M. A., N. J. Carino, and Kausel, E.A. (2003). "Preliminary thermography studies for quality control of concrete structures strengthened with fiber-reinforced polymer composites." Journal of Materials in Civil Engineering 15(3): 266-273.

VSL (2005). http://www.vsl.net/strengthening_products/vsl_frp_composites.html. 7455 New Ridge Road, Suite T, Hanover, MD.

William D. Callister, J. (1997). "Materials science and engineering an introduction." John Wiley & Sons, Inc.

Woolard, D. F. and K. E. Cramer (2005). "Line scan versus flash thermography: comparative study on reinforced carbon-carbon." Thermosense XXVII, Edited by D.D. Burleigh, Eliot Cramer, J. Miles. Proceedings of SPIE, Vol. 5782, pp. 334-341.

BIOGRAPHICAL SKETCH

Jeff Brown completed high school in Daytona Beach, Florida. In August 1996, he was awarded the degree of Bachelor of Science in Civil Engineering from the University of Central Florida and received top honors from the College of Engineering. He began his graduate studies at the University of Central Florida that same year and was awarded a masters degree in Structures and Foundations Engineering in May 1998. Upon completion of his masters degree, he served for two years as a Peace Corps volunteer in the East African nation of Tanzania. In January 2002, he entered the Graduate School of the University of Florida.